TENSILE STRAIN CAPACITY OF ENERGY PIPELINES

by

Celal Cakiroglu

A thesis submitted in partial fulfillment of the requirements for the degree of

Doctor of Philosophy

in
STRUCTURAL ENGINEERING

Department of Civil and Environmental Engineering
University of Alberta

ABSTRACT

Pipeline structures can be subjected to excessive tensile strains due to a variety of environmental agents including but not limited to slope instabilities, seismic forces, freezing and thawing cycle of the permafrost in arctic regions. In addition to environmental and geotechnical effects, large strains can also occur during offshore pipe laying operations using reeling. Another occasion where the increase of the tensile strains can cause damage to pipelines and the environment is the accumulation of strains in the vicinity of cold bends. Experimental research showed that tension side fracture of cold bends is a probable mode of failure albeit being mostly overlooked in practice. This mode of failure due to tensile strain is highly dangerous because of the explosion associated with it in case of gas carrying pipelines. Therefore further study of that failure mode is necessary in order to identify the conditions leading to it.

In the recent years a strain based design approach is increasingly adopted in the management of pipeline systems in order to guarantee a safe and economical pipeline operation. An integral part of the strain based design methodology is the prediction of the tensile strain capacity of pipeline structures under a combination of external forces, in the presence of defects in the pipe wall which can be caused due to corrosion or imperfections in the manually or automatically manufactured girth welds. The presence of pipe wall flaws due to corrosion is especially critical in case of vintage pipes which constitute a large portion of the Canadian pipeline network. On the other hand the tensile strain capacity prediction equations currently available in the literature are not applicable to vintage pipes with low yield strength. Therefore, there is a dire need for the study of vintage pipes in order to have

a better understanding of their structural response under tensile strain.

In the scope of this research program the tensile strain capacity of energy pipelines is investigated both experimentally and using finite element analysis. In the experimental part of the research program eight full scale tests are carried out with vintage pipes having X52 steel grade and flaws of different length and height in the pipe wall. Each full scale test specimen is prepared in order to have a unique combination of the internal pressure and the flaw dimensions. The specimens are subjected to axial tensile force up to the point of rupture at the flaw location. The test results showed that, the tensile strain capacity of the pipes greatly vary not only due to the changes in the flaw height and length but also due to the level of the internal pressure. This condition shows that the effect of the internal pressure should not be ignored despite not being included in the CSA code for the oil and gas pipeline systems as one of the parameters affecting the tensile strain capacity.

The second part of the research program is focused on the finite element analysis and classification of failure modes of cold bends under large tensile strains. In order to have a better understanding of the tension side fracture of cold bends under excessive tensile strain, the effects of the internal pressure level and the pipe steel grade on the structural response of cold bends are investigated. Parametric studies are carried out which span a range of internal pressure values causing hoop stresses between 20% and 80% of the pipe yield strength. The parametric study of the internal pressure is repeated for X60, X65, X70 and X80 steel grades. The results of these finite element simulations showed that, two different types of structural response can be observed depending on the level of the internal pressure and the steel grade. In order to develop a rigorous decision making procedure for the mode of the structural behaviour, a linear classification algorithm is utilized based on the

results of the finite element simulations.

ACKNOWLEDGEMENTS

I would like to acknowledge the Natural Sciences and Engineering Research Council and Enbridge Pipelines Inc. for their financial support. In addition to the financial support I would like to thank Dr. Millan Sen of Enbridge Pipelines Inc., for the technical guidance and assistance that he provided throughout this research project. The pipe specimens used for this research were supplied by Enbridge Pipelines Inc., and the full scale experiments were carried out in the I.F. Morrison Structural Engineering Laboratory of the University of Alberta. I would like to thank the technicians at the I.F. Morrison Structural Laboratory, Greg Miller and Cameron West for their technical support and cooperation.

I would like to thank Dr. Muntaseer Kainat, Meng Lin, Diana Abdulhameed, Dr. Amin Komeili, Behzad Vafaeian, and the rest of the former and current members of our research group for supporting this experimental program. Special thanks to Dr. J. J. Roger Cheng for his valuable advice and directions throughout this research work. His guidance and suggestions improved my overall understanding of the research topic.

I would like to express my utmost gratitude to my supervisor Dr. Samer Adeeb. He has been supportive and helpful during each and every step. I am grateful to him for sharing with me his expertise in topics as diverse as simulation of engineering systems and mathematical analysis.

The support and encouragement of my friends and family are deeply appreciated.

Contents

1 INTRODUCTION **1**

2 LITERATURE REVIEW **5**
2.1 CSA Z662-11 Annex C 5
2.1.1 Material Modelling 6
2.1.2 Rupture Limit State 6
2.2 Tensile Strain Capacity Equations Developed by PRCI 11
2.3 Research Conducted on the Tensile Strain Capacity of Pipelines using Curved Wide Plate Tests 16
2.4 Research Conducted on Tensile Strain Capacity of Pressurized Pipelines 21
2.5 Research Conducted on Cold Bent Pipes 27
2.6 State of the Art in the Buckling Analysis of Line Pipes 30
2.7 Current Design Provisions for the Prevention of Local Failure of Steel Pipes 34

3 SENSITIVITY ANALYSIS OF THE TENSILE STRAIN CAPACITY PREDICTION EQUATIONS **37**
3.1 CSA Equations 37
3.2 PRCI Equations 42
3.3 Closing Remarks 44

4 DESIGN OF THE FULL SCALE TESTS **48**
4.1 Test Setup and Instrumentation 48
4.1.1 Positioning of the Strain Gauges 52
4.2 End Plate Design 54
4.2.1 First iteration of bolt design calculations based on an initial assumption for the number of bolts and their diameter 56
4.2.2 Second iteration of bolt design calculations 58
4.3 Finite Element Analysis and Machining of Flaws in the Pipe Wall 61
4.4 High-Low Misalignment Measurements 71

5 RESULTS OF THE FULL SCALE TESTS **73**
5.1 Material properties of the X52 Specimens 73
5.2 Strain Measurements and their Cross Correlation 75

5.2.1 Analysis of the Strain Measurements for the First Full Scale Experiment . . . 77
5.2.2 Analysis of the Strain Measurements for the Second Full Scale Experiment . . . 88
5.2.3 Analysis of the Strain Measurements for the Third Full Scale Experiment . . . 94
5.2.4 Analysis of the Strain Measurements for the Fourth Full Scale Experiment . . . 100
5.2.5 Analysis of the Strain Gauge Measurements for the Fifth Full Scale Experiment . . . 106
5.2.6 Analysis of the Strain Gauge Measurements in the Sixth Full Scale Experiment . . . 111
5.2.7 Analysis of the Strain Gauge Measurements in the Seventh Full Scale Experiment . . . 115
5.2.8 Analysis of the Strain Gauge Measurements in the Eighth Full Scale Experiment . . . 119
5.3 Load-Displacement Response . . . 124
5.4 Closing Remarks . . . 128

6 TENSION SIDE FRACTURE OF PIPES 133
6.1 TENSION SIDE FRACTURE OF COLD BENDS . . . 133
6.1.1 Extension of the Parametric Study to X60 and X80 Steel Grades . . . 147
6.2 CLASSIFICATION OF FAILURE MODES . . . 154
6.3 Closing Remarks . . . 166

7 ERROR ANALYSIS AND LIMITATIONS OF THE STUDY 168

8 SUMMARY AND CONCLUSIONS 175

A APPENDIX 193
A.1 Matlab code for computing the cross correlation of strain gauges 193
A.2 Matlab code for computing the tensile strain capacity according to the equations of CSA Z662-11 . . . 193
A.3 Matlab code for computing the tensile strain capacity according to the equations of the PRCI report . . . 193
A.4 Java code for factorial analysis . . . 194
A.5 The Application of the Curvature Concept to Cold Bends . . . 217
A.6 Matlab code for the classification of cold bends using the perceptron algorithm . . . 219

List of Figures

2.1 Ramberg−Osgood material model for different values of n [9] . 7
2.2 A planar surface-breaking defect in the pipe wall [9] 10
2.3 A planar buried defect in the pipe wall [9] 11
2.4 Position of a curved wide plate specimen [24] 16
2.5 Variation of the CTOD with respect to the remote strain as a function of a/t [25] 17
2.6 Division of the curved wide plate into uniform and non−uniform strain regions [24] 19
2.7 Variation of tensile strain capacity with respect to flaw size [29] 20
2.8 The validation of Eq. 2.16 using experimental results [31] . . . 21
2.9 Silicone replicas of the flaw showing CMOD, CTOD and crack growth(Δa) at different stages of the test [32] 22
2.10 Comparison of the crack growth resistance curves from small scale(SENT) and full scale tests [32] 23
2.11 Placement of girth weld flaws [33] 25
2.12 Longitudinal cross section of the flaw [34] 26
2.13 Calculation of the tensile strain capacity using finite element analysis and SENT tests [34] 27
2.14 Experimental setup of the cold bend[16] 30
2.15 Variation of the failure curvature with respect to the Y/T ratio for the steel grade X65 and the circumferential stress of 80% SMYS 36
3.1 Combinations of three parameters (Factor A, Factor B, Factor C) at three different levels (0, 1, 2) [20] 38
3.2 Sensitivity analysis for surface defects 40
3.3 Sensitivity analysis for buried defects 42
3.4 Sensitivity analysis for GMAW 43
3.5 Sensitivity analysis for SMAW/FCAW 43
4.1 End plates and the lug pieces 49
4.2 Pin-yoke assembly 50
4.3 DIC areas of interest in the first two tests (left) and in Test 3 to Test 8 (right) 51
4.4 Speckle patterns [52] 51
4.5 Strain gauge positions around the pipe circumference 52
4.6 Experimental setup 54
4.7 Iterative process of end plate dimensioning 55
4.8 Distribution of the von Mises stress on the finite element model 60

4.9 Von Mises stress distribution at the crack location with the end plate configuration with 14 bolt holes and 1 in. (25.4 mm) bolt hole diameter 60
4.10 Force−displacement response with 14 bolts of 1 in. (25.4 mm) diameter 61
4.11 Flaw machining equipment 62
4.12 A close-up of the blade assembly 64
4.13 Flaw dimensions (height), undesired (left), desired (right) . . . 64
4.14 Von Mises stress distribution for 1.7 mm crack height 65
4.15 Von Mises stress distribution for 1.7 mm crack height with the initial 1 mm cut wider on one side 65
4.16 Von Mises stress distribution for 1.7 mm crack height with the initial 1 mm cut wider on both sides 66
4.17 Von Mises stress distribution for 3.4 mm crack height 66
4.18 Von Mises stress distribution for 3.4 mm crack height with the initial 1.7 mm cut wider on one side 67
4.19 Von Mises stress distribution for 3.4 mm crack height with the initial 1.7 mm cut wider on both sides 67
4.20 The variation of the flaw tip von Mises stress with respect to the applied displacement 68
4.21 Determination of the high−low misalignment for the first full scale specimen 72
5.1 X52 pipe base metal stress-strain variation [51] 74
5.2 Bottom side of the pipe in the first test 77
5.3 Top side of the pipe in the first test 78
5.4 Digital image correlation showing the critical strain distribution close to the bottom end plate (Test 1) 82
5.5 Digital image correlation showing the critical strain distribution close to the heat affected zone (Test 1) 84
5.6 Development of the strain profile in the first full scale test . . 85
5.7 Measurements of the strain gauges with good correlation (Test 1) 86
5.8 Measurements of the strain gauges with no correlation (Test 1) 86
5.9 Highest axial strain gauge measurements in Test 1 87
5.10 Load-displacement response of the first test 87
5.11 Bottom side of the pipe in the second test 90
5.12 Top side of the pipe in the second test 91
5.13 Strain measurements of the gauges 180° away from the flaw in Test 2 92
5.14 Strain measurements of the gauges aligned with the flaw in Test 2 92

5.15 Load-displacement response of the second test 93
5.16 Development of the strain profile in the second full scale test . 93
5.17 Bottom side of the pipe in the third test 95
5.18 Top side of the pipe in the third test 95
5.19 Hoop strain measurements in Test 3 96
5.20 Load-displacement response of the third test 97
5.21 Axial strain measurements in Test 3 98
5.22 Axial strain field prior to rupture in Test 3 99
5.23 Development of the strain profile in the third full scale test . . 99
5.24 Bottom side of the pipe in the fourth test 101
5.25 Top side of the pipe in the fourth test 101
5.26 Hoop strain measurements in Test 4 102
5.27 Load-displacement response of the fourth test 103
5.28 Axial strain measurements in Test 4 104
5.29 Axial strain field prior to rupture in Test 4 105
5.30 Development of the strain profile in the fourth full scale test . 105
5.31 Bottom side of the pipe in the fifth to eighth tests 106
5.32 Top side of the pipe in the fifth to eighth tests 107
5.33 Hoop strain measurements in Test 5 108
5.34 Load-displacement response of the fifth test 108
5.35 Axial strain measurements in Test 5 109
5.36 Axial strain field prior to rupture in Test 5 110
5.37 Development of the strain profile in the fifth full scale test . . 110
5.38 Hoop direction strain gauge measurements in Test 6 112
5.39 Load-displacement response of the sixth test 112
5.40 Axial strain gauge measurements in Test 6 113
5.41 Axial strain field prior to rupture in Test 6 114
5.42 Development of the strain profile in the sixth full scale test . . 115
5.43 Hoop strain gauge measurements in Test 7 116
5.44 Load-displacement response of the seventh test 116
5.45 Axial strain gauge measurements in Test 7 117
5.46 Axial strain field prior to rupture in Test 7 118
5.47 Development of the strain profile in the seventh full scale test 119
5.48 Hoop strain gauge measurements in Test 8 120
5.49 Load-displacement response of the eighth test 120
5.50 Axial strain gauge measurements in Test 8 121
5.51 Axial strain field prior to rupture in Test 8 122
5.52 Development of the strain profile in the eighth full scale test . 122
5.53 Load-displacement response of all full scale tests 125
6.1 Test setup used in the cold bend experiments[16] 135
6.2 Tension side fracture[54] 136

6.3 Material and geometic properties of the specimen in Figure 6.2[55] 136
6.4 Distribution of the equivalent plastic strain for un-pressurized X65 cold bend . . . 138
6.5 Distribution of the equivalent plastic strain for pressurized X65 cold bend . . . 138
6.6 The original (undeformed) cold bend with an initial radius of curvature R_0 (dotted lines) versus the deformed cold bend after applying a horizontal displacement u and the new radius of curvature R[55]. . . . 141
6.7 The relationship between the curvature κ and the applied displacement u . . . 142
6.8 Development of the equivalent plastic strain at the intrados (X65) . . . 142
6.9 Development of the equivalent plastic strain at the extrados (X65) . . . 143
6.10 Compression side (solid) and tension side (dotted) variations of PEEQ (X65, 55% SMYS) . . . 145
6.11 Compression side (solid) and tension side (dotted) variations of PEEQ (X65, 58% SMYS) . . . 145
6.12 Transition of the failure mode in the $(\Delta\kappa, p_i)$ space (X65) . . . 146
6.13 Development of the equivalent plastic strain at the intrados (X60) . . . 148
6.14 Development of the equivalent plastic strain at the extrados (X60) . . . 148
6.15 Compression side (solid) and tension side (dotted) variations of PEEQ (X60, 50% SMYS) . . . 150
6.16 Compression side (solid) and tension side (dotted) variations of PEEQ (X60, 53% SMYS) . . . 150
6.17 Transition of the failure mode in the $(\Delta\kappa, p_i)$ space (X60) . . . 151
6.18 Development of the equivalent plastic strain at the intrados (X80) . . . 152
6.19 Development of the equivalent plastic strain at the extrados (X80) . . . 153
6.20 Compression side (solid) and tension side (dotted) variations of PEEQ (X80, 65% SMYS) . . . 154
6.21 Geometry of the training set and the decision boundary in $\mathbb{R}^2$ 157
6.22 Training set of cold bends separated by a decision boundary (x_1 :steel grade, x_2 :internal pressure) . . . 162
6.23 Training set of cold bends separated by a decision boundary (x_1 :internal pressure, x_2 :steel grade) . . . 163
6.24 Variation of PEEQ at the intrados for X70 steel grade . . . 164

6.25 Variation of PEEQ at the extrados for X70 steel grade 164
6.26 Variation of PEEQ at the extrados (dotten) and intrados (solid) for 60% SMYS internal pressure and X70 steel grade 165
6.27 Relationship between the steel grade and the transition pressure 167
7.1 Frequency distribution of the wall thickness 171
7.2 Fractography results of the machined flaw 172
7.3 Flaw after the rupture (left hand side) and the location of the fractography specimen (right hand side) 173
8.1 Average tensile strain capacities for short and long flaws . . . 180
8.2 Average tensile strain capacities for shallow and deep flaws . . 180
8.3 Average tensile strain capacities for low and high levels of the internal pressure 181
8.4 Combined training set of the steel grades X60, X65, X70 and X80 182
A.1 Description of the curvature as an infinitesimal deviation [56] . 218

List of Tables

1.1 Full Scale Test Matrix 4
2.1 Description of the parameters in Eq. 2.3 and Eq. 2.5 10
2.2 Parameter ranges for Eq. 2.3 and Eq. 2.5 11
2.3 Coefficients of the tensile strain capacity equation for GMAW 14
2.4 Coefficients of the tensile strain capacity equation for SMAW/F-CAW 14
2.5 Parameter ranges for Eq. 2.3 and Eq. 2.5 15
2.6 Measured Tensile Strain Capacities [33] 25
2.7 Mechanical properties before and after cold bending [35] . . . 28
2.8 Computation of the uniaxial strain limit ε_{Lu} 35
3.1 Parameter ranges for the tensile strain capacity prediction equations in CSA Z662-11 39
4.1 Comparison of the bolt hole configurations of the first and second iterations 58
5.1 Average Charpy impact energies [51] 75
5.2 Cross correlation of strain gauge measurements from Test 1 . . 79
5.3 Cross correlation of strain gauge measurements from Test 1 . . 80
5.4 Development of the strain profile in Test 1 84
5.5 The ratio between the strain gauge measurement and the image correlation strains 85
5.6 Cross correlation of strain gauge measurements from Test 2 . . 89
5.7 Cross correlation of strain gauge measurements from Test 2 . . 89
5.8 Cross correlation of strain gauge measurements from Test 3 . . 94
5.9 Cross correlation of strain gauge measurements from Test 4 . . 102
5.10 Cross correlation of strain gauge measurements from Test 5 . . 106
5.11 Cross correlation of strain gauge measurements from Test 6 . . 111
5.12 Cross correlation of strain gauge measurements from Test 7 . . 115
5.13 Cross correlation of strain gauge measurements from Test 8 . . 119
5.14 The comparison of the tensile strain capacity measurements by the DIC and the strain gauges 123
5.15 Maximum tensile force and strain in the experiments 124
5.16 Difference in the maximum tensile force due to increasing flaw height 126
5.17 Difference in the maximum tensile force due to increasing flaw length 127
5.18 Difference in the maximum tensile force due to internal pressure 128
5.19 The comparison of the tensile strain capacity measurements and the predicted values 130

6.1 Failure curvature values for X65 147
6.2 Failure curvature values for X60 152
6.3 Failure curvature values for X80 155
6.4 Failure curvature values for X70 165
7.1 Comparison of the theoretical and experimental hoop strain values 170

Nomenclature

δ	Crack tip opening displacement (CTOD) toughness
$\Delta\kappa$	Difference between the curvature values necessary to cause the fracture of the pipe intrados and extrados
η	Ratio of the pipe wall flaw height to the pipe wall thickness
γ_F	Functional margin of the decision boundary
γ_G	Geometric margin of the decision boundary
γ_t	Functional margin of a training sample $\mathbf{x}_t$
κ	Curvature of the pipe axis
λ	Ratio of the yield strength to the ultimate tensile strength (Y/T)
$\mathbb{R}$	The set of real numbers
$\mathbf{w}$	Weight vector of the linear classifier function
$\mathbf{x}_t$	Training sample vector with index t
μ_x	The mean value of the signal $x(n)$
ϕ	Ratio of the girth weld ultimate strength to the pipe base metal ultimate strength
ϕ_{et}	Tensile strain resistance factor
ψ	Ratio of the pipe wall flaw depth (measured from the inner pipe surface) to the pipe wall thickness
ψ_1	Ratio of the high-low misalignment of the girth weld to the pipe wall thickness
ρ_{xy}	The cross correlation coefficient between the signals $x(n)$ and $y(n)$
σ	Uniaxial stress
σ_x	The standard deviation of the signal $x(n)$
ε	Uniaxial strain

$\varepsilon_t^{crit}(t)$ Tensile strain capacity predicted by the PRCI equations after the wall thickness adjustment

$\varepsilon_t^{crit}(t,p)$ Tensile strain capacity predicted by the PRCI equations after the wall thickness and pressure effect adjustments

ε_{py} Proportional strain limit

ε_t^{crit} Tensile strain capacity of the pipe wall or weldment

ξ Ratio of the pipe wall flaw length to the pipe wall thickness

A_b Cross section area of a single bolt

b Bias coefficient of the linear classifier function

d_1 pipe wall flaw depth, which is the distance from the internal pipe surface to the buried flaw

d_O Distance of the decision boundary from the origin

DB The set of vectors building the decision boundary of the training set

e Load eccentricity

E_s Young's modulus of steel

f_p Ratio of the hoop stress caused by the internal pressure to the specified minimum yield strength of the pipe

f_t Tensile stress per bolt

F_y Effective specified minimum yield strength

H_0 Initial horizontal length of the cold bend

I Total area moment of inertia of bolt cross sections

k_t The temperature derating factor which accounts for the reduction in the yield strength of the pipe base metal due to an increase in the operating temperature beyond 120°C

L Total length of the cold bend

l Total number of training samples

p_i Internal pressure of the pipeline

R_0 Initial radius of curvature of the cold bend

T The operating temperature of the pipeline

t Pipe wall thickness

t_0 15.9 mm wall thickness used in the development of the PRCI equations

y_t Label of the training sample $\mathbf{x}_t$ indicating its class. Equal to 1 for intrados fracture and -1 for extrados fracture

CMOD Crack mouth opening displacement

CTOD Crack tip opening displacement

DIC Digital image correlation

FCAW Flux-cored arc welding

GMAW Gas metal arc welding

HAZ Heat affected zone of the girth weld

OD Outer diameter of the pipe

PEEQ Equivalent plastic strain

PRCI Pipeline Research Council International

SENT Single edge notch tension

SMAW Shielded metal arc welding

SMYS Specified minimum yield strength

1 INTRODUCTION

Steel pipelines are used for the efficient transportation of oil and natural gas from remote regions like sub-Arctic region of North America to the place of consumption. These pipelines are often subjected to excessive bending, tensile loading and high longitudinal strains due to temperature differences, internal pressure and unfavourable geotechnical conditions. The latter include slope instability, seismic activity or discontinuous permafrost which causes differential settlement of the pipeline due to the freezing and thawing cycle of the permafrost. To date the research on pipeline structures mostly focused on the buckling of different pipe configurations under compressive forces. Such research projects were carried out to investigate the buckling and fracture of pipe walls under compressive loading. The research projects [1], [2], [3] are some examples of experimental studies which analyzed the occurrence of local buckling in the form of wrinkles in the pipe wall due to bending. On the other hand there is a limited amount of research projects studying the tensile strain capacity of pipelines that consider the effect of the internal pressure.

Girth welded pipelines can be subjected to large amounts of longitudinal deformation due to a variety of conditions. In case of onshore pipelines the main causes of high longitudinal deformations are seismic activity, slope instability, frost heave and the gradual sinking of landforms to a lower level as a result of mining operations. In case of offshore pipelines the highest deformations occur in the process of pipe laying by reeling where the girth welded segments of a pipeline are wound onto a spool and therefore experience high bending strains.

In the presence of girth weld flaws, pressurized pipelines exhibit a reduc-

tion in their tensile strain capacity under axial tension and bending loads. In case of excessive tensile strain, manual and automatic welding errors in the girth welds can lead to the failure of a pipeline. In order to prevent the failure of a pipeline due to these high strain levels the inevitable flaws in and around the girth welds have to be kept within acceptable limits. The lack of knowledge about the effects of flaw sizes, internal pressure and material properties on the structural behaviour of a pipeline can have detrimental economical and environmental effects. In order to understand the structural behaviour of a pipeline in the presence of flaws in the pipe wall and internal pressure it is necessary to conduct full scale tests of the pipe for different crack sizes and internal pressure levels. The research conducted in this field in the recent years focused on pipelines with steel grades having a specified minimum yield strength of at least 450 MPa (X65). Extensive research is conducted by Wang, et al [4], [5], [6], [7], [8] to understand the reduction of the tensile strain capacity due to girth weld flaws which culminated in equations for the prediction of the tensile strain capacity of steel pipes. These equations (Eq. 2.3, Eq. 2.5) are included in the CSA Z662−11 code [9]. However since these equations are developed based on experiments conducted with pipes having at least 450 MPa yield strength, it is not recommended to apply them for the prediction of the tensile strain capacity if the pipe base metal has lower yield strength values. This restriction also applies in case of pipes with steel grade X52 which is the subject of the current work. Furthermore the effect of internal pressure on the tensile strain capacity is not included in the current code equations. In the scope of this research project a total of 8 full scale tests are conducted (Table 1.1). For each one of these experiments a defect is machined into the pipe wall having a predefined height and length. Also in each experiment the full scale specimen is pressurized

with water pressure up to a predefined level of internal pressure before the application of the tensile strain. For each test, the pipe wall defect size and the internal pressure are chosen in such a way that each one of the 8 full scale tests has a unique combination of defect length, defect height and internal pressure. The steel grade of the pipe base metal is X52 in all full scale tests. The outcome of this experimental study is expected to provide new insights about the acceptability of pipe wall flaw sizes and structural behaviour under excessive tensile loading in case of X52 vintage pipes.

Another important load case where pipeline failure due to tensile strains can occur is the application of bending strains on cold bent pipes. Experimental studies of Sen et al. [1],[16] showed that there is a likelihood of pipe body tension side failure in load cases of cold bends under internal pressure and bending. While the main focus of the study by Sen et al. was investigating the compressive strain capacity of cold bends, in one of the experiments the pipe specimen failed on the tension side due to the high level of internal pressure. In this current research project, the experimental studies of Sen et al. are further investigated using finite element analysis in order to have a better understanding of the conditions which lead to a tension side failure of cold bent pipes. The finite element simulations extended the experimental study of Sen et al. by simulating different levels of internal pressure by incrementally increasing the level of internal pressure between 10% SMYS and 80% SMYS. In this way the effect of internal pressure on the failure mode of the cold bend is investigated. Moreover, different levels of the pipe base metal yield strength are analyzed in order to understand the effect of this material property on the failure mode.

Table 1.1: Full Scale Test Matrix

Test number	Specimen length (inches)	Internal pressure (%SMYS)	Flaw length [mm]	Flaw height [mm]
1	72	80	50	1.7
2	72	30	50	1.7
3	72	80	50	3.4
4	72	30	50	3.4
5	48	80	150	1.7
6	48	30	150	1.7
7	48	80	150	3.4
8	48	30	150	3.4

2 LITERATURE REVIEW

Traditional allowable stress based design methods of pipelines only address situations where the pipe material response stays in the elastic range. However experimental research results showed that longitudinal strains in pipelines can greatly exceed the yield strains prior to ultimate limit states. Therefore there is a need to develop new strain based design methods for pipelines. In this section the most relevant research techniques and research findings in the field of strain based design of pipelines are summarized. The section starts with the review of the limit states design concepts from CSA Z662-11 Annex C. Afterwards curved wide plate test based research results about the tensile strain capacity of pipelines are reviewed. The section continues with research results which consider the effect of the internal pressure on the tensile strain capacity. Finally cold bend related research results are summarized.

2.1 CSA Z662-11 Annex C

In pipeline design limit states are categorized as ultimate limit states and serviceability limit states. The ultimate limit states have four subcategories which are rupture, yielding caused by primary loads, buckling resulting in collapse or rupture and fatigue. The focus of this research project is the rupture ultimate limit state. Also in the analysis of cold bend failure, yielding caused by primary loads and buckling are relevant ultimate limit states. Internal pressure and applied strain are the primary loads analyzed in this project.

2.1.1 Material Modelling

For the modelling of the stress−strain response of the pipe base metal two different methods are mentioned in CSA Z662-11 Annex C. These methods are a bilinear elastic−plastic stress−strain model and the Ramberg−Osgood material model. The RambergOsgood model is described as in Eq. 2.1

$$\varepsilon = \frac{\sigma}{E_s} + \varepsilon_{py}\Big(\frac{\sigma}{F_y}\Big)^n \tag{2.1}$$

In Eq. 2.1 $\varepsilon_{py} = 0.005 - F_y/E_s$ is the proportional limit and $F_y = k_t \cdot SMYS$ is the effective specified minimum yield strength. The parameter n is in practice equal to or greater than 5. Figure 2.1 shows that with increasing values of n, the stress−strain model converges to its limit. The parameter k_t is the temperature derating factor for F_y and it accounts for the reduction in the yield strength due to an increase of the operating temperature beyond $120°C$. For operating temperatures less than $120°C$, k_t is taken as 1.0. The relationship between k_t and the operating temperature (T) is given in Eq. 2.2

$$k_t = 1.14 - \frac{T}{850} \tag{2.2}$$

2.1.2 Rupture Limit State

In order to prevent the rupture of the pipe membrane due to longitudinal tensile strain, the factored tensile strain ε_{tf} should not exceed the factored tensile resistance $\phi_{et}\varepsilon_t^{crit}$ where ϕ_{et} is the tensile strain resistance factor and is equal to 0.7 (Table C.3 Annex C). ε_t^{crit} is the ultimate tensile strain capacity of the pipe wall or weldment. In the absence of test data ε_t^{crit} can

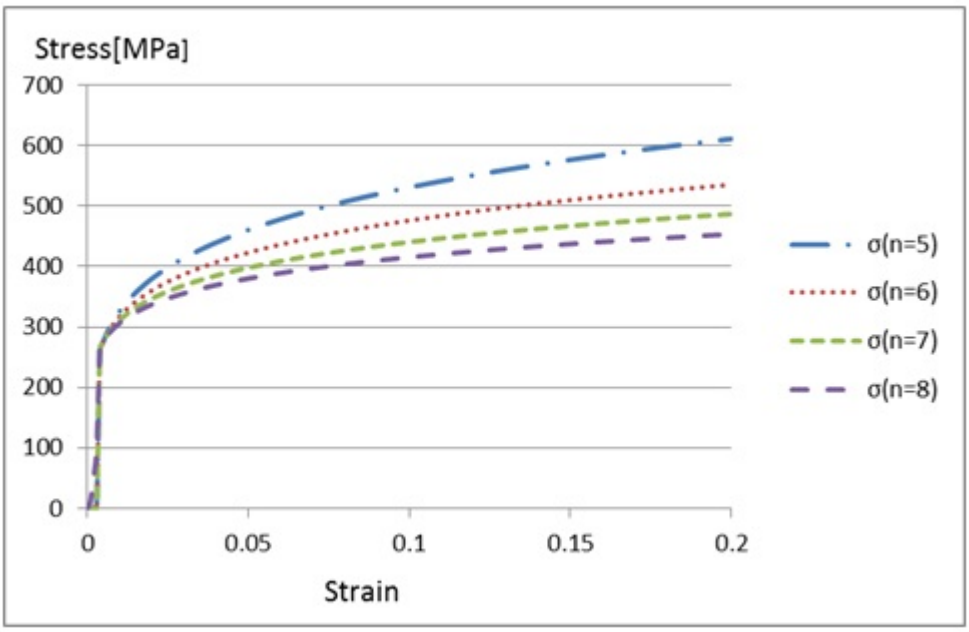

Figure 2.1: Ramberg−Osgood material model for different values of n [9]

be calculated as in Eq. 2.3 and Eq. 2.5 for surface−breaking defects and buried defects respectively[9]:

$$\varepsilon_t^{crit} = \delta^{(2.36-1.58\lambda-0.101\xi\eta)}(1+16.1\lambda^{-4.45})(-0.157+0.239\xi^{-0.241}\eta^{-0.315}) \tag{2.3}$$

$$\varepsilon_t^{crit} = \varepsilon_t^{crit}(\delta,\xi,\eta,\lambda) \tag{2.4}$$

$$\begin{aligned}\varepsilon_t^{crit} = \quad & \delta^{(1.08-0.612\eta-0.0735\xi+0.364\psi)}(12.3-4.65\sqrt{t}+0.495t) \\ & (11.8-10.6\lambda)(-5.14+\frac{0.992}{\psi}+20.1\psi)(-3.63+11.0\sqrt{\eta}-8.44\eta) \\ & (-0.836+0.733\eta+0.0483\xi+\frac{3.49-14.6\eta-12.9\psi}{1+\xi^{1.84}})\end{aligned} \tag{2.5}$$

$$\varepsilon_t^{crit} = \varepsilon_t^{crit}(\delta,\xi,\eta,\lambda,\psi,t) \tag{2.6}$$

In CSA Z662-11 surface-breaking defects are defined as defects on the pipe wall that are connected to the surface of the pipe whereas buried defects are

defined as defects on the pipe wall that are not connected to the surface of the pipe. Both of these defect types are assumed to have sizes in macro scale so that their dimensions are comparable to the pipe wall thickness and are in the circumferential direction of the pipe wall. These defects can be present due to different reasons such as imperfections in the girth welding procedures, entrapment of gas within the solidified weld and formation of porosity or coalescence of micro scaled slag inclusions or dislocations into larger sized flaws. Welding defects can be present in both manually and automatically welded girth welds. The difference between the automatic and manual welding procedures is that in automatic welding, parameters such as welding current, the distance of the arc from metals which affects the current and heat going into the joint and welding voltage are controlled automatically whereas in manual welding these parameters are controlled manually [10]. Research conducted on the failure assessment of pipeline weld defects showed that failure of pipeline welds occurs mostly due to the weld defects of lack of fusion and lack of penetration [11], [12]. In the long term these weld defects lead to the formation of cracks [13]. Lack of fusion occurs when there is no fusion between the weld metal and the base metal. Some of the conditions leading to lack of fusion can be summarized as too large weld puddle and the use of a very wide weld joint [14]. The lack of penetration is associated with an incomplete penetration of the weld bead into the base metal. The main cause of lack of penetration is insufficient welding current [15]. Clearly, these conditions can occur both in manual and automatic welding procedures. Therefore, regardless of the welding being done automatically or manually, defects can occur in the pipeline welds.

Eq. 2.3 and Eq. 2.5 are developed based on the extensive experimental work conducted by Wang et al[4],[5],[6],[7],[8] on curved wide plates with

machined defects. However, the code specifies high values of toughness which occur in X52 vintage pipes as a limitation to using these equations, indicating that these equations were developed for modern high strength steel pipelines. In addition, the code specifically warns that the effect of internal pressure on the longitudinal tensile strain capacity is not considered in the equations Eq. 2.3, Eq. 2.5 and experienced judgement needs to be used or testing needs to be conducted to verify the behaviour under the effect of internal pressure. Thus, in order to predict the longitudinal tensile strain capacity of Enbridge X52 vintage pipeline it is imperative to conduct full scale experiments and toughness tests for a possible range of pipe wall defects under the effects of both internal pressure and longitudinal tensile strain.

The equations (Eq. 2.3 and Eq. 2.5) predict the tensile strain capacity of a pipeline in the presence of a flaw in the pipe wall or weldment as a function of flaw dimensions and pipe base metal mechanical properties. Possible defect shapes in the pipe wall are classified in [9] as surface−breaking defects and buried defects. Surface breaking defects are those that resemble a crack that is connected to the surface of the pipe, while buried defects are those that are not connected to the surface of the pipe. The geometric descriptions of surface−breaking defects and buried defects are shown in Figure 2.2 and Figure 2.3 respectively. Although the surface breaking defect is depicted in Figure 2.2 on the inner surface of the pipe wall, the CSA code does not distinguish between surface flaws on the inner surface and those on the outer surface. Wang et al [4] demonstrated that despite being considered as a less harmful type of pipe wall defect compared to surface defects, buried defects can still be detrimental. Therefore for each type of pipe wall defect suitable equations are developed in order to predict ε_t^{crit} as a function of δ, η, λ, ξ for surface−breaking defects and as a function of δ, η, λ, ξ, ψ for buried defects.

A description of these parameters is given in Table 2.1.

Table 2.1: Description of the parameters in Eq. 2.3 and Eq. 2.5

δ	Crack−tip opening displacement (CTOD) toughness
λ	Ratio of yield strength to tensile strength (Y/T). If the material behaviour is nonlinear elastic (round - house), the stress at 0.5% strain can under−represent the yield strength. This would result in an overly low Y/T ratio and a non−conservative prediction of ε_t^{crit}. In order to prevent this, if the slope of the stress−strain curve is greater than 10000 MPa at 0.5% strain, then the Y value of the Y/T ratio is obtained as the stress value at the point where the slope of the stress−strain curve begins to be less than 10000 MPa
ξ	Ratio of defect length to pipe wall thickness
η	Ratio of defect height to pipe wall thickness
ψ	Ratio of defect depth (d_1 in Figure 2.3) to pipe wall thickness
t	Pipe wall thickness

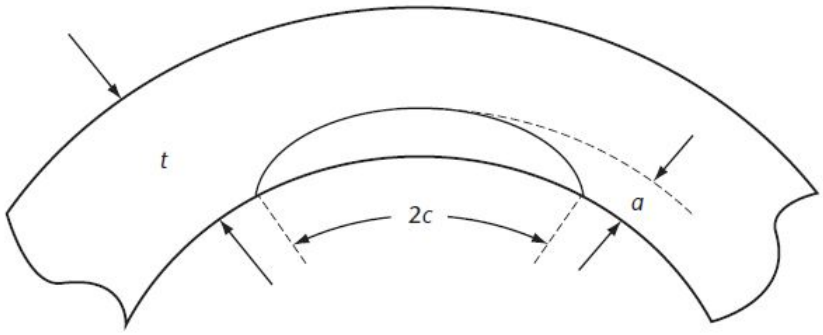

Figure 2.2: A planar surface-breaking defect in the pipe wall [9]

CSA Z662−11 Annex C defines certain boundaries of applicability for the parameters listed in Table 2.1. For parameter values falling outside of these boundaries the usage of Eq. 2.3 and Eq. 2.5 is not recommended. Table 2.2 lists these parameters with their corresponding ranges of applicability. In Table 2.2, D denotes the nominal pipe diameter.

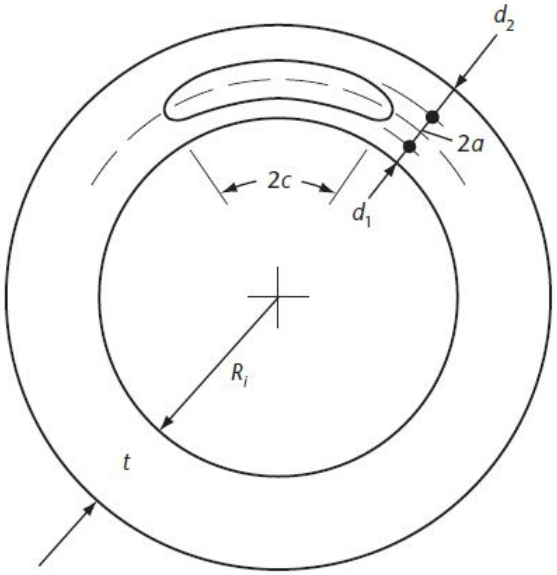

Figure 2.3: A planar buried defect in the pipe wall [9]

Table 2.2: Parameter ranges for Eq. 2.3 and Eq. 2.5

$0.1 \leq \delta \leq 0.3$
$0.7 \leq \lambda \leq 0.95$
$1 \leq \xi \leq 10$
$\eta \leq 0.5$
$t \leq D/32$

2.2 Tensile Strain Capacity Equations Developed by PRCI

Further research conducted by the Pipeline Research Council International (PRCI) culminated in a new set of equations that predict the tensile strain capacity as a function of various material and geometric properties. Also, the effect of internal pressure on the tensile strain capacity is considered in these equations. In addition to the parameters used in Eq. 2.3 and Eq. 2.5 and internal pressure, the effects of the girth weld high-low misalignment and

the weld metal strength mismatch ratio are included in the equations. Two separate equations are developed for three different welding methods used in the manufacturing of girth welds. These three different welding methods are gas metal arc welding (GMAW), shielded metal arc welding (SMAW) and flux-cored arc welding (FCAW). The first of the equations is developed for GMAW and the second equation is developed for SMAW or FCAW. The equations are developed using curve fitting techniques based on the results of experimental studies enriched by finite element analysis for a wide range of material and geometry configurations. The method of calculating ε_t^{crit} consists of several steps. In the first of these steps ε_t^{crit} is calculated for a pipe with 15.9 mm wall thickness and an internal pressure that causes 72% SMYS hoop stress ($f_p = 0.72$) for any given combination of material and geometric parameters. This equation has the same format for both GMAW and SMAW/FCAW which is given in Eq. 2.7. In Eq. 2.7 the letters A,B,C,D are functions of different geometric and material parameters. Among these parameters $\delta, \lambda, \xi, \eta$ have the same meaning as described in Table 2.1. In addition to these parameters also, the ratio of the high-low misalignment to the pipe wall thickness (ψ_1) and the girth weld metal strength mismatch ratio (ϕ) are included in the equations. The strength mismatch ratio is calculated by dividing the ultimate strength of the girth weld metal by the ultimate strength of the pipe base metal. The functions B and C have the same format for both GMAW and SMAW/FCAW whereas the functions A and D differ as shown in Eq. 2.8 to Eq. 2.13.

$$\varepsilon_t^{crit} = A\frac{(C\delta)^{B\delta^D}}{1+(C\delta)^{B\delta^D}} \tag{2.7}$$

$$A_{GMAW} = a_1 e^{a_2/\xi} e^{a_3 \eta \xi e^{a_4/\xi}} \Big[1 + a_5 \psi_1^{a_6} + a_7 \psi_1 (\eta\xi)^{a_8}\Big] \cdot \Big(1 + a_9 \lambda^{a_{10}} \phi^{a_{11}} + a_{12} \psi_1^{a_{13}} \lambda^{a_{14}}\Big) \tag{2.8}$$

$$A_{SMAW} = a_1 e^{a_2/\xi} e^{a_3 \eta \xi e^{a_4/\xi}} \Big[1 + a_5 \psi_1^{a_6} + a_7 \psi_1^{a_8} (\eta\xi)^{a_9}\Big] \cdot \Big(1 + a_{10} \lambda^{a_{11}} \phi^{a_{12}}\Big) \tag{2.9}$$

$$B_{GMAW,SMAW} = \xi^{b_1} \eta^{b_2 \xi^{b_3}/\eta} \Big[b_4 \phi^{b_5} \Big(b_6 \phi^{b_7}\Big)^{\lambda} + b_8 \psi_1^{b_9}\Big] \tag{2.10}$$

$$C_{GMAW,SMAW} = e^{c_1/\xi} e^{\frac{c_2 \xi}{(1+c_3\xi)\eta}} \Big(1 + c_4 \psi_1^{c_5} + c_6 \psi_1 e^{-\eta} + c_7 \psi_1 e^{-\xi}\Big) \cdot \Big(c_8 + c_9 \phi^{c_{10}} + c_{11} \lambda^{c_{12}} \phi\Big) \tag{2.11}$$

$$D_{GMAW} = d_1 \xi^{d_2} \eta^{\frac{d_3 \xi}{(1+d_4\xi)}} \Big(1 + d_5 \psi_1^{d_6}\Big) \Big(1 + d_7 \lambda^{d_8} + d_9 \phi^{d_{10}}\Big) \tag{2.12}$$

$$D_{SMAW} = d_1 \xi^{d_2} \eta^{d_3} \Big(1 + d_4 \psi_1^{d_5} + d_6 \eta\xi\psi_1\Big) \Big(1 + d_7 \lambda^{d_8} + d_9 \phi^{d_{10}}\Big) \tag{2.13}$$

In Eq. 2.8 to Eq. 2.13 the coefficients a_1 to a_{14}, b_1 to b_9, c_1 to c_{12}, d_1 to d_{10} are obtained from curve fitting procedures and have different values for GMAW and SMAW/FCAW type girth welds. These coefficients are listed in Table 2.3 and Table 2.4. In the next step ε_t^{crit} is adjusted to the actual wall thickness by multiplying ε_t^{crit} with a wall thickness adjustment function as shown in Eq. 2.14 where t_0 is equal to 15.9 mm, t is the actual wall thickness and ψ_1 is the ratio of the high-low misalignment to the wall thickness.

$$\varepsilon_t^{crit}(t) = \varepsilon_t^{crit} \Big(\frac{t_0}{t}\Big)^{0.8096(1+1.503\psi_1^{1.229})} \tag{2.14}$$

In order for the adjustment in Eq. 2.14 to be valid, the actual wall thickness t has to be between 12.7 mm and 25.4 mm. Also, $\varepsilon_t^{crit}(t)$ is not allowed to be greater than the uniform strain whereby the concept of the uniform strain is not well defined in [17]. Another restriction on the use of the equations is that the pipe material yield strength has to be between 386 MPa and 690

Table 2.3: Coefficients of the tensile strain capacity equation for GMAW

a1=2.084	b1=-0.05005	c1=1.409	d1=0.02209
a2=0.2812	b2=-0.005139	c2=0.2345	d2=1.156
a3=-0.495	b3=0.4485	c3=1.125	d3=1.601
a4=0.7373	b4=1.417	c4=4.181	d4=0.8964
a5=-5.005	b5=2.217	c5=1.201	d5=1.383
a6=1.186	b6=1.029	c6=-5.384	d6=1.333
a7=1.644	b7=-2.598	c7=2.406	d7=0.09313
a8=0.7374	b8=-2.679	c8=-0.2154	d8=-2.24
a9=-0.9829	b9=1.694	c9=-0.005237	d9=8.559
a10=0.08655		c10=9.889	d10=-3.719
a11=-0.1029		c11=0.3547	
a12=-0.15		c12=-0.7513	
a13=1.025			
a14=5.557			

Table 2.4: Coefficients of the tensile strain capacity equation for SMAW/F-CAW

a1=0.9281	b1=-0.05578	c1=1.609	d1=0.006822
a2=0.09573	b2=0.01112	c2=0.1138	d2=1.014
a3=-0.5053	b3=-0.1735	c3=0.6729	d3=1.746
a4=0.3718	b4=1.675	c4=2.357	d4=2.378
a5=-2.023	b5=0.2603	c5=1.057	d5=0.9434
a6=0.7585	b6=1.106	c6=-4.444	d6=-1.243
a7=0.6299	b7=-1.073	c7=0.01727	d7=35.79
a8=0.5168	b8=-1.519	c8=-0.01354	d8=7.5
a9=0.7168	b9=1.965	c9=-0.01224	d9=62.94
a10=-0.9815		c10=8.128	d10=-6.93
a11=0.2909		c11=0.2007	
a12=-0.3141		c12=-1.594	

MPa.

The next step in the calculation of the tensile strain capacity is the pressure effect adjustment. The results of parametric finite element studies with f_p ranging between 0 and 0.8 [18] showed that the internal pressure has an increasingly detrimental effect on the tensile strain capacity up to the point of 60% SMYS hoop stress. For internal pressure values causing hoop stresses greater than 60% SMYS no significant change in the effect of the internal pressure on the tensile strain capacity was observed. Based on this finding, the pressure effect adjustment on the tensile strain capacity is made as shown in Eq. 2.15 where $\varepsilon_t^{crit}(0)$ stands for the tensile strain capacity of an unpressurized pipe and $\varepsilon_t^{crit}(t,p)$ is the tensile strain capacity after the wall thickness and internal pressure adjustments. $\varepsilon_t^{crit}(0)$ is conservatively estimated as $1.5\varepsilon_t^{crit}(t)$.

$$\varepsilon_t^{crit}(t,p) = \begin{cases} \varepsilon_t^{crit}(t) & \text{if } 0.6 \leq f_p \leq 0.8 \\ \varepsilon_t^{crit}(0) + \dfrac{5f_p}{3}\Big(\varepsilon_t^{crit}(t) - \varepsilon_t^{crit}(0)\Big) & \text{if } f_p < 0.6 \end{cases} \tag{2.15}$$

The parametric studies during the development of the PRCI equations are carried out for certain ranges of the parameters effecting the tensile strain capacity. These ranges are listed in Table 2.5.

Table 2.5: Parameter ranges for Eq. 2.3 and Eq. 2.5

$0.2 \leq \delta \leq 2.5$
$0.75 \leq \lambda \leq 0.94$
$1 \leq \xi \leq 20$
$0.05 \leq \eta \leq 0.5$
$12.7mm \leq t \leq 25.4mm$
$0 \leq \psi_1 \leq 0.2$
$1 \leq \phi \leq 1.3$
$0 \leq f_p \leq 0.8$

2.3 Research Conducted on the Tensile Strain Capacity of Pipelines using Curved Wide Plate Tests

Due to the difficulty associated with full scale testing of pressurized pipes, full scale tests are usually conducted on curved wide plates (Figure 2.4) with machined defects. Wang et al. [25] developed a methodology of establishing strain based design criteria using the concept of crack tip opening displacement (CTOD). In this methodology the CTOD toughness of the pipe base metal from small scale material tests is compared to the CTOD value observed in the full scale tests. In this work CTOD of the full scale tests is also referred to as the crack driving strain. The critical strain is defined as the longitudinal strain value at the point where the CTOD in the full scale tests or finite element models reaches the CTOD toughness of the material. The location of the critical strain is chosen to be remote from the girth weld. Therefore this strain value is also called the remote strain. Wang et al [25] simulated numerous finite element models having surface defects with a variation of defect depth and weld strength mismatch ratio levels.

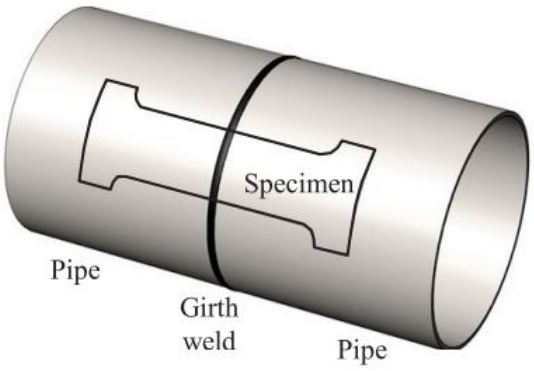

Figure 2.4: Position of a curved wide plate specimen [24]

Figure 2.5 shows typical CTOD variations with respect to remote strain

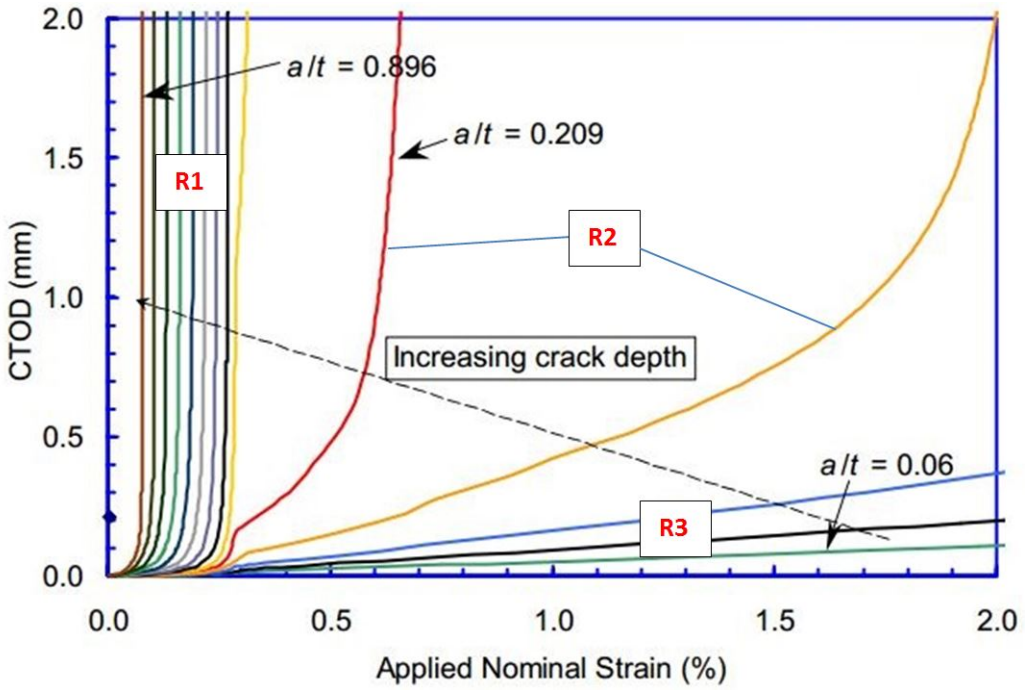

Figure 2.5: Variation of the CTOD with respect to the remote strain as a function of a/t [25]

for different crack depth to pipe wall thickness ratios (a/t). In Figure 2.5 the CTOD variations are classified into the groups R1, R2, R3. These three groups are classified as unstable, stable−nonlinear and stable−linear variations of CTOD respectively. The outcome of these simulations was verified with an experimental program on curved wide plate tests performed by the University of Waterloo and the Welding Institute of Canada and published by Pick et al and Glover et al.[26], [27], [28]. It was concluded that the defect size is the most influential parameter affecting the tensile strain capacity. Also the results of the simulations were used to develop strain capacity prediction equations by curve fitting techniques.

In practice the remote strain in curved wide plate tests is measured using strain gauges. As a result the outcome and validity of these experiments are

highly dependent on the chosen location for the strain measuring sensors. Hertele et al. [24] analyzed the effect of the remote strain sensor location in a study which includes curved wide plate tests as well as finite element simulations. In this study each side of the weld in the curved wide plate is assumed to be divided into three regions. The first of these regions is the vicinity of the weld. In order to define the boundaries of these regions a $z_{45}-$coordinate system is introduced which has its origin at the point where a line starting from the crack center with 45° angle from the plate midline intersects the plate edge. The second region is where $0 \leq z_{45} \leq 100mm$ and the third region is where $100mm < z_{45}$. The first and third regions are assumed to have non$-$uniform strain distributions and the second region is divided into four partitions each being 25 mm wide. The uniformity of the longitudinal strain is investigated for the second region at five different cross sections corresponding to $z_{45} = 0mm, 25mm, 50mm, 75mm, 100mm$. For each of these cross sections a dimensionless coefficient of variance c_v is defined as the ratio of the standard deviation of the longitudinal strain along the cross section to the average longitudinal strain along the same cross section. Since c_v changes as more deformation is applied on the specimen, another variable $\bar{c}_v$ is defined which is the average value of c_v over the entire test. Finally the cross section which exhibits the lowest value of $\bar{c}_v$ is considered to have the most uniform longitudinal strain distribution. The results of three curved wide plate experiments showed that the cross section with the most uniform longitudinal strain distribution was the cross section corresponding to $z_{45} = 25mm$ which showed $\bar{c}_v$ values less than 0.02. On the other hand different strain values were observed on both sides of the girth weld for the same magnitude of z_{45} which can be attributed to a heterogeneous distribution of material properties. This condition strengthens the assumption that the

remote strain is not a well defined quantity and therefore it is necessary to capture the strain field with digital image correlation in each experiment.

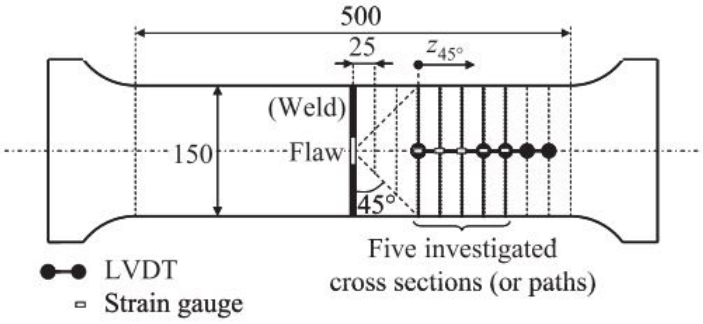

Figure 2.6: Division of the curved wide plate into uniform and non−uniform strain regions [24]

Wang et al.[29] discussed the overview of tensile strain capacity prediction methodology developed by ExxonMobil[30]. This methodology is based on full scale tests, enrichment of strain capacity database with finite element simulations and small scale SENT (single edge notched tensile) tests for the measurement of the material CTOD toughness. Using these results and curve fitting techniques the following tensile strain capacity prediction equation is developed [30]:

$$\varepsilon_t^{crit} = \beta_1 ln \frac{aC}{(t-a)^2} + \beta_2 \tag{2.16}$$

In Eq. 2.16 a, C, t are the flaw height, the half flaw length and pipe wall thickness respectively(Figure 2.2, Figure 2.3). The quantity $aC/(t-a)^2$ represents the ratio of the flaw cross section area to the uncracked ligament cross section area. This dimensionless quantity provides a convenient way of visualizing the variation of the tensile strain capacity with respect to increasing flaw size (Figure 2.7). β_1 and β_2 in Eq. 2.16 are functions of flaw length, girth weld high low misalignment, weld metal−base metal strength mismatch ratio, Y/T ratio of the pipe base metal and the fracture toughness

of the pipe base metal. Eq. 2.16 is developed for pipe grades X65 to X80. Wang et al.[31] compared the predictions of Eq. 2.16 with the results of full scale experiments with pressurized specimens for a variety of crack geometry and pipe material properties. The result of this comparison proved the validity of Eq. 2.16 in the cases of pipe base metal grades between X65 and X80 and internal pressure values causing hoop stresses between 40% SMYS and 80% SMYS (Figure 2.8).

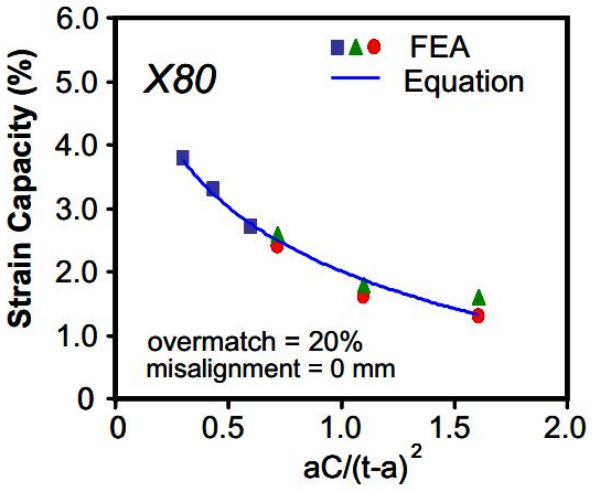

Figure 2.7: Variation of tensile strain capacity with respect to flaw size [29]

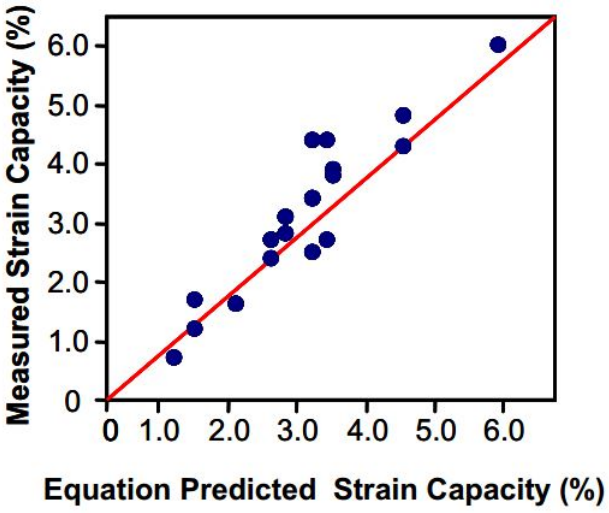

Figure 2.8: The validation of Eq. 2.16 using experimental results [31]

2.4 Research Conducted on Tensile Strain Capacity of Pressurized Pipelines

Østby et al[32] carried out a full scale test program which included 6 pipe specimens. In these experiments a crack with 100 mm circumferential length was placed at the location of the pipe where the wall thickness was smallest. The crack depth to pipe wall thickness ratio was kept constant in all tests. Two of the experiments were carried out without internal pressure and in the remaining tests two different levels of internal pressure were tested corresponding to 25% SMYS and 60% SMYS hoop stresses. 4-point bending was applied in all tests. The steel grade was X65 for all tests. The strain measurements were made using strain gauges located 0.5 OD, 1 OD and 2 OD away from the center of the pipe. The CMOD of the flaw was measured using clip gauges with an attack point 0.2 mm below the external pipe surface. In order to measure the CTOD and crack growth(Δa), silicone replicas of the flaws were made at different stages of the experiments(Figure 2.9).

In this way the clip gauge measurements and the actual CTOD could be related to each other. At the end of the experiments it was observed that the

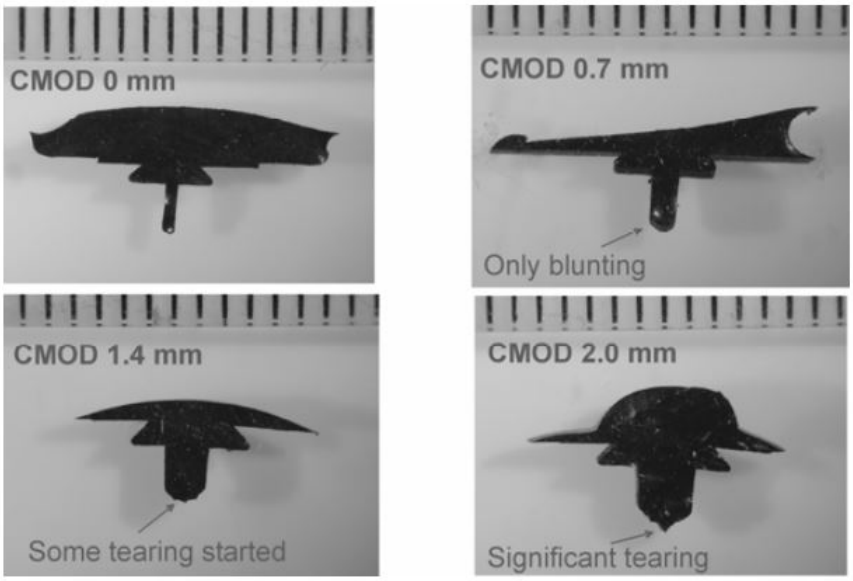

Figure 2.9: Silicone replicas of the flaw showing CMOD, CTOD and crack growth(Δa) at different stages of the test [32]

internal pressure significantly reduces the tensile strain capacity of the pipe from a level of 3.5 - 4% to a level of 1.5 - 2%. Another observation was that the unpressurized specimens failed due to local buckling at the compression side whereas the pressurized specimens failed due to fracture at the flawed locations at the tension side. Østby et al[32] also introduced an alternative method to strain gauge measurements in order to obtain the bending strain. This method calculates the bending strain as $\varepsilon = r/R$ where ε is the bending strain, r is the outer radius of the pipe and R is the radius of curvature. The comparison of the strain values calculated using this method with the average of measured strain values showed that the obtained strain values are consistent with each other.

Using the silicone replicas and numerical analysis, Østby et al[32] were

able to create the crack growth resistance curves(curves showing the variation of CTOD with respect to Δa) of the full scale tests. The crack growth resistance curves of the full scale tests were compared to the curves obtained from small scale SENT tests. It was observed that the crack growth resistance curves obtained using these two methods are close to each other(Figure 2.10). This finding also justifies the determination of the tensile strain capacity as the strain at the point where CTOD (or CMOD) reaches the material toughness measured in the small scale tests.

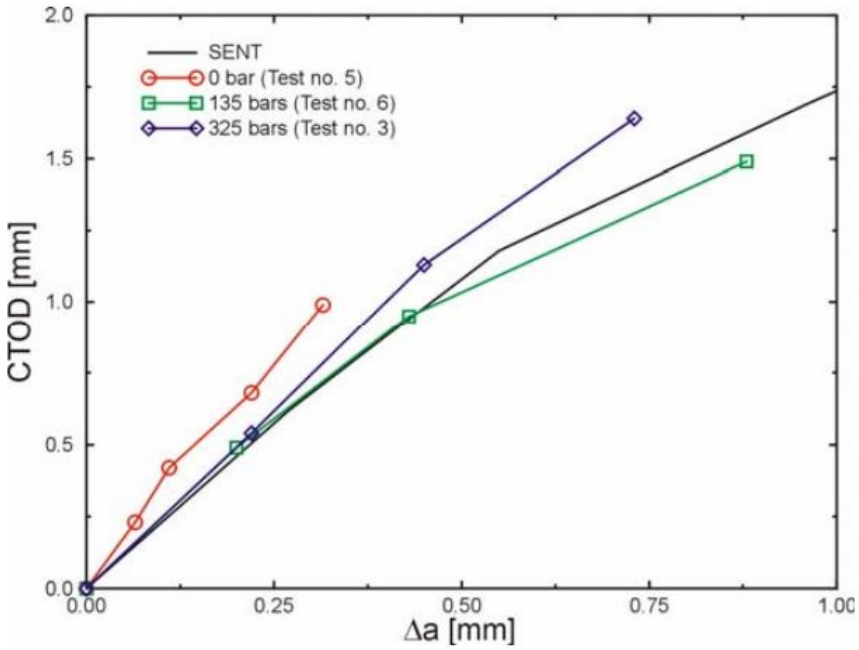

Figure 2.10: Comparison of the crack growth resistance curves from small scale(SENT) and full scale tests [32]

Gioielli et al[33] carried out pressurized and unpressurized full scale tests with six pipe specimens in order to investigate the effect of internal pressure on the tensile strain capacity of a pipeline. The specimens were grouped as three pairs and each pair had a different girth weld strength overmatch ratio. In each pair, one of the specimens was used for a pressurized test and the

other one was used for an unpressurized test. The pressurized specimens had an internal pressure equivalent to 80% SMYS hoop stress and the unpressurized specimens had a negligible amount of internal pressure equivalent to 2% SMYS hoop stress which was applied in order to facilitate the leak detection. The girth weld strength overmatch ratios of the specimen pairs were 0%, 5% and 20%. All specimens had the steel grade X65, outer diameter of 12.75 inches(325 mm) and wall thickness of 0.562 inches(14.3 mm). Surface defects were machined on all specimens using electrical discharge machining(EDM) with equal crack dimensions of 3 mm depth and 50 mm length. Girth weld flaws were machined at three locations 120° separated from each other at the girth weld centerline(Figure 2.11). The data collected in these experiments consists of the axial tensile load applied on the specimens, the overall elongation of the pipe due to axial loading, local strain measurements in longitudinal and hoop directions, crack mouth opening displacement (CMOD) and the internal pressure. The overall pipe elongation was measured using linear variable displacement transducers (LVDT). For the local strain measurements biaxial strain gauges were used at multiple locations on the pipe surface. The CMOD was measured using clip gauges. Acoustic emission monitoring was used to determine the point at which the ductile tearing of the crack initiated. The tensile strain capacities in these experiments were measured by dividing the total LVDT displacement at the moment of failure by the initial LVDT length. In the tests where the pipe failed away from the weld the tensile strain capacity was defined as the strain value at the point of maximum applied axial load. The test pairs with 0% and 5% strength overmatch exhibited tensile strain capacity decreases of 44% and 47% respectively due to internal pressure. In the tests with 20% strength overmatch the failure occurred away from the girth weld and the decrease of the tensile strain

capacity due to internal pressure was 16%. The tensile strain capacities observed in this study are listed in Table 2.6. It was concluded that increasing girth weld strength overmatch ratio leads to a transition of the failure mode from ductile tearing at the girth weld flaw to plastic collapse away from the girth weld.

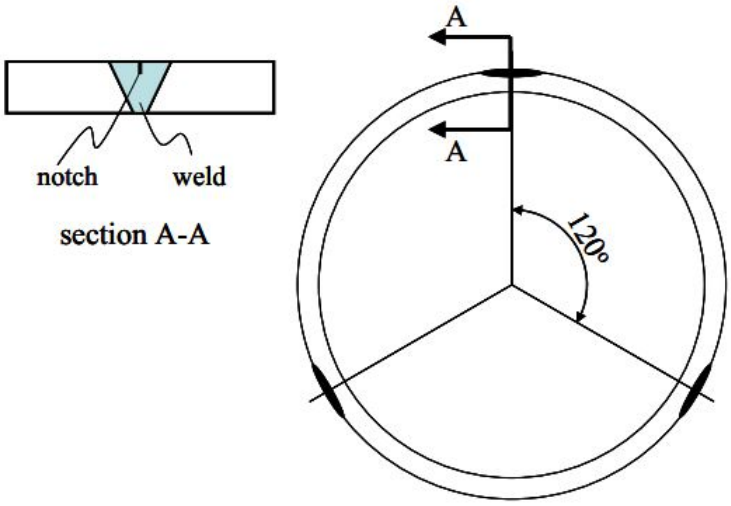

Figure 2.11: Placement of girth weld flaws [33]

Table 2.6: Measured Tensile Strain Capacities [33]

Girth Weld strength overmatch ratio (%)	Tensile Strain Capacity (%) Pressurized	Unpressurized	Reduction of the tensile strain capacity due to internal pressure (%)
0	1.9	3.4	44
5	1.9	3.6	47
20	4.6	5.5	16

Igi et al [34] conducted a pressurized full scale test, a curved wide plate test which represents the unpressurized load case, small scale single edge notch tension (SENT) tests as well as finite element analyses in order to develop a methodology for the prediction of the tensile strain capacity in the

presence of internal pressure and surface defects. The specimens were taken from X80 pipeline with an outside diameter of 508 mm (20in.) and a wall thickness of 14.3mm (0.563in.). The surface defects were machined into the heat affected zone (HAZ) of the girth weld using EDM. The SENT tests were used to determine the variation of the effective crack opening displacement (δ_{eff}) with respect to ductile crack growth (Δa). This variation is denoted as the material resistance curve (R−curve). The finite element simulations were used to plot the variation of δ_{eff} with respect to global strain. The global strain was calculated from the increase of axial distance between two points in the finite element models. A series of finite element simulations were carried

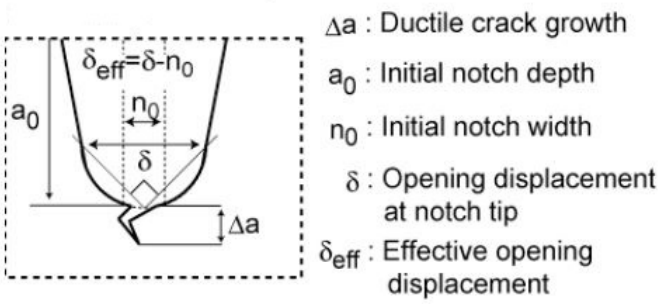

Figure 2.12: Longitudinal cross section of the flaw [34]

out with predefined Δa dimensions. For each finite element simulation a curve showing the variation of δ_{eff} with respect to global strain was plotted. In the next step on each of these curves a point was marked which shows the δ_{eff} value that was observed in the SENT test for the corresponding level of Δa. Once all curves are marked with a point, these points are joined which gives another curve with increasing slope. Finally the tensile strain capacity is defined as the global strain at the point where the curve which joined the marked points seems to have infinite slope. The procedure of calculating the tensile strain capacity from finite element simulations is also illustrated in

Figure 2.13 The effect of internal pressure was investigated by comparing the

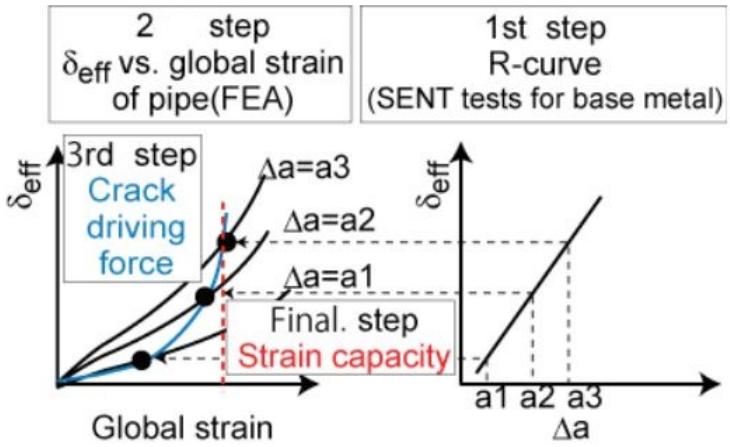

Figure 2.13: Calculation of the tensile strain capacity using finite element analysis and SENT tests [34]

results of the pressurized full scale test to the results of a curved wide plate test. It was observed that the tensile strain capacity decreases approximately 50% due to the internal pressure.

2.5 Research Conducted on Cold Bent Pipes

Fukuda et al [35] investigated the longitudinal strain distribution of cold bends and the decrease in the yield stress due to cold bending experimentally and numerically. Full scale cold bending experiments were carried out with two different pipes (denoted Pipe A and Pipe B in the rest of the text) of steel grade X60 and X80. The residual strains were measured using strain gauges on the line of maximum compressive strain in the longitudinal direction. It was found that the length of the longitudinal range where the compressive strain exceeds 0.2% is almost equal to the outer diameter of the pipe. The mechanical properties of the pipes were tested before and after cold bending (Table 2.7). As shown in Table 2.7, due to cold bending the yield stresses

of the pipe materials were reduced 6% and 27% for Pipe A(X60) and Pipe B(X80) respectively.

Table 2.7: Mechanical properties before and after cold bending [35]

Pipe	Before and after bending	Yield stress [Mpa]	Tensile strength [Mpa]
A	Before	465	527
	After	437	529
B	Before	633	670
	After	461	656

Caminada et al[36] investigated the mechanical properties at extrados and intrados of cold bends. These mechanical properties are compared to those of straight pipes. Pipes with ASTM grade T23, T91 and T92 were cold bent by industrial rotary bending machines in form of U bends with a bending angle of 180°. A total of 21 cold bends were tested with R[1]/OD ratio ranging between 1.0 and 4.5. For the assessment of the mechanical properties, tension tests, Charpy impact tests and creep−rupture tests were conducted. The specimens for material testing were cut out of a cold bend with an outer diameter of 76 mm(3in.) and a wall thickness of 12.5 mm(0.5in.). Specimens were cut out of intrados, extrados and unbent portions of the pipe. The results of the tension tests showed that the yield stress at the extrados was on average 40% higher than the yield stress of the unbent pipe. On the other hand the yield stress at the intrados was on average 20% lower than the yield stress of the unbent pipe. From the results of the Charpy impact tests no correlation was observed between the locations where the test specimens were cut from and the absorbed energy in the tests. The tubes with grade T23 exhibited lower Charpy toughness than the grades T91 and T92. The results of the creep−rupture tests showed that the intrados and extrados have similar

[1]Radius of curvature of the cold bend

creep−rupture strength, whereas the specimens from the intrados exhibited higher creep−rupture ductility than the specimens from the extrados.

Sen et al.[16] tested one straight pipe and seven cold bend pipes under internal pressure and bending loads in order to have a better understanding of the allowable strains that a cold bend can undergo before local buckling occurs. Also the post−buckling behaviour of the cold bends were investigated. The steel grades of the specimens were X60, X65 and X80. 40%, 60% and 80% SMYS internal pressure levels were tested. In these experiments the bending load was applied in form of an eccentric compressive force which increases the curvature of the cold bend longitudinal axis. The curvature was applied after filling the pipe with water and bringing the internal pressure to the maximum level with a pneumatic pump. Both ends of the cold bends were closed with end plates welded to the pipe wall. These end plates were also connected to moment arms used for the application of the eccentric load(Figure 2.14). The portions of the cold bends adjacent to the end plates were prevented from ovalization. This condition was causing a stress concentration adjacent to the end plates making the pipe prone to local buckling at these locations. In order to prevent local buckling near the end plates, collars were installed at the ends of the specimen after the internal pressure was at the desired level. The test results showed that in the post−buckling phase of the experiments, the load carrying capacity of the unpressurized specimens decreased more severely than the pressurized ones. Also the peak moments of the unpressurized specimens were less than the peak moments of the pressurized specimens. It was also demonstrated that the maximum curvature that the unpressurized specimens could undergo prior to buckling was in average 71% of the maximum curvature that the pressurized specimens could undergo prior to buckling. The comparison of the peak moments

measured in two unpressurized tests showed that the effect of the OD/t ratio of the cold bend on the peak moment is greater than the effect of the yield stress of the pipe base metal on the peak moment since the specimen with lower OD/t ratio and lower yield stress exhibited higher peak moment. The comparison of the maximum moment and corresponding curvature of cold bent and straight pipes showed that these quantities decreased due to cold bending. The average critical strain (the maximum strain prior to the formation of local buckling) of a cold bent specimen was measured as 48% of the critical strain of the straight specimen where all specimens have similar dimensions.

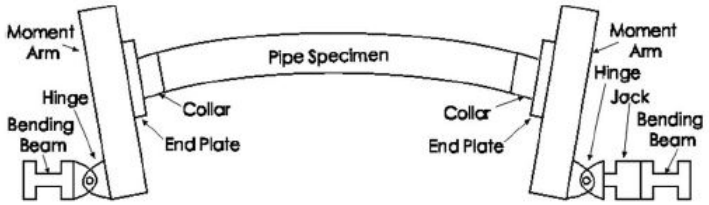

Figure 2.14: Experimental setup of the cold bend[16]

2.6 State of the Art in the Buckling Analysis of Line Pipes

A significant part of the research projects on the post−buckling response of the line pipes is concerned with the strain corresponding to the peak moment. The importance of strain analysis of pipeline systems stems from the fact that especially pipelines crossing northern areas can be subjected to large deformations due to the freezing and thawing cycle of the permafrost. In this section some of the research carried out in this area is summarized. It should be pointed out that none of the numerical studies carried out in

these research projects deals with the possible local failure of a line pipe due to a fracture at the tension side.

Fatemi et al. [37],[38],[39] investigated the influence of internal pressure, girth weld high-low misalignment and pipe diameter on the moment-curvature and buckling response of high strength pipelines. A parametric study was carried out for internal pressure and high-low misalignment using finite element analysis. It was found that the peak moment that the pipe can reach, is inversely proportional to the level of internal pressure and the high−low misalignment of the girth weld. On the other hand, the maximum curvature that can be applied was found to increase with increasing internal pressure and decrease with increasing high-low misalignment. Also in [39], the effect of the length to diameter ratio on the local buckling behaviour was examined. The focus of that work was to establish allowable compressive strain limits as a function of pipe length, diameter, wall thickness and initial geometric imperfections. These studies do not include any account of a tension side failure in a load case where the curvature is progressively increased.

Zimmerman et al. [40] carried out an experimental research program to investigate the compressive buckling resistance of spiral welded, large diameter pipelines. Combined internal pressure, axial force and bending moment was applied on full scale pipe specimens with X70 and X80 steel grade. The purpose of the applied axial force was to counteract the axial tensile forces caused by the internal pressure acting on the end plates of the pipe. It was concluded that the spiral welding method does not lower the buckling capacity of the line pipe in comparison to longitudinal welds. In all the full scale tests of this experimental program the specimen failed at the compression side due to excessive bending.

Suzuki et al. [41] demonstrated the performance of a newly developed line pipe called stress-strain curve controlled high−strain line pipe (SSLP) using full scale test results. The strain capacity of SSLP was shown to be 3.2 times and 1.7 times greater than that of standard line pipe under compression and bending respectively. The main characteristic of the material of this line pipe is a round−house type stress−strain curve. The strain capacity was determined using the compressive strain measurements corresponding to the maximum value of the bending moment.

Mitsuya et al. [42] examined the beam−mode buckling of line pipes, where the pipe bends similar to the bending of an Euler beam. This is a mostly overlooked mode of buckling compared to the shell−mode buckling which results in the formation of local wrinkles. On the other hand this buckling mode was observed to have a considerable likelihood under seismic loading. In [42] two different seismic assessment methods were developed with respect to beam−mode buckling in order to predict the critical buckling strain using analytical techniques and finite element analysis. It was shown that as the pipe diameter increases, the critical strain increases for beam−mode buckling while the opposite is true for shell−mode buckling. The critical strain was defined as the strain at the peak load, and did not distinguish between the tension side and compression side strain.

Das et al. [43] experimentally investigated a fracture at the wrinkle location of an NPS10 pipe in the post-buckling phase that took place in the field. In order to better understand the conditions leading to the fracture at the wrinkle location, two full scale experiments were carried out at the University of Alberta. In these experiments, compressive axial forces and transverse shear forces were applied on NPS12 specimens. The compressive axial force was applied concentrically up until the formation of an outward bulge and

starting from this point a combination of axial compressive force and transverse shear force was applied in order to create a load case and structural response which resembles the wrinkle location fracture of the NPS10 pipe. In order to obtain a failure mode that resembles the one that occurred in the field, it was necessary to modify the boundary conditions of the specimen such that after the formation of the wrinkle the clamped supports at the pipe ends were replaced with knife edge supports allowing the rotation of the end plates. Once the top part of the specimen was sufficiently offset from the bottom part due to the transverse shear force, the boundary conditions were brought back to their initial state and further axial compression was applied. As a result the specimen was brought to fracture at the compression side.

The main outcome of the experimental study carried out by Das et al. [43] was that monotonic loading conditions can lead to fracture at the wrinkle location. In order to further investigate the structural behaviour of the NPS10 pipe that failed in site, Ahmed et al. [44] carried out a finite element analysis of this pipe configuration. The load-displacement response obtained from the finite element analysis was in good agreement with the experiments carried out by Das et al. [43]. A close resemblance between the post-wrinkling deformed configurations of the finite element model and the tested specimens was observed. It was found that strain reversals can occur at the compression side of the wrinkles under monotonic loading which eventually lead to the fracture of the pipe wall at the compression side.

A common denominator of all the studies reviewed in this section is that the experiments or numerical analyses carried out to determine the tensile strain capacity of steel pipes, focused on the compression side failure of the specimens.

2.7 Current Design Provisions for the Prevention of Local Failure of Steel Pipes

API 579−1 Fitness for Service Standard [45] provides an assessment methodology using a strain limit criterion for the protection of the pipe wall against local failure in form of a fracture. This provided methodology is based on an elastic−plastic analysis of the structure for any given load combination including internal pressure and bending. Once a structural analysis, which also considers the effect of geometric nonlinearities, is completed, the principal stress values $\sigma_1, \sigma_2, \sigma_3$, the von Mises equivalent stress σ_{VM} and the equivalent plastic strain ε_{eq}^{p} are computed for the location of the pipe wall to be evaluated. The limiting triaxial strain ε_L is computed using Eq. 2.17

$$\varepsilon_L = \varepsilon_{Lu} \cdot \exp\Big[- \Big(\frac{\alpha_{sl}}{1+m_2}\Big)\Big(\Big\{\frac{(\sigma_1+\sigma_2+\sigma_3)}{3\sigma_{VM}}\Big\} - \frac{1}{3}\Big)\Big] \tag{2.17}$$

In Eq. 2.17, m_2 is the strain hardening limit and can be calculated as $0.6(1.0-R)$ for ferritic steels, $0.75(1.0-R)$ for stainless steels/nickel base alloys and $0.75(0.95-R)$ for duplex stainless steels, where R is the ratio of the specified minimum yield stress to the specified minimum ultimate stress(the Y/T ratio). The uniaxial strain limit ε_{Lu} is taken as equal to m_2 if the specified percent elongation and specified percent area reduction of the material are unknown. If these two material properties are known, then ε_{Lu} is taken as the minimum of m_2 and the two values given in Table 2.8 for each steel type. In the expressions in Table 2.8, E denotes the specified percent elongation of the material and RA denotes the specified percent reduction in area of the material. If only one of these two properties is known, then the smaller of m_2 and the value computed using the corresponding expression in Table 2.8 is used. The variable α_{sl} in Eq. 2.17 is equal to 2.2,0.6 and 2.2 for ferritic steels,

Table 2.8: Computation of the uniaxial strain limit ε_{Lu}

Material	ε_{Lu}	
Ferritic steels	$2 \cdot \ln\left[1 + \frac{E}{100}\right]$	$\ln\left[\frac{100}{100 - RA}\right]$
Stainless steels/nickel base alloys	$3 \cdot ln\left[1 + \frac{E}{100}\right]$	$\ln\left[\frac{100}{100 - RA}\right]$
Duplex stainless steels	$2 \cdot \ln\left[1 + \frac{E}{100}\right]$	$\ln\left[\frac{100}{100 - RA}\right]$

stainless steels/nickel base alloys and duplex stainless steels respectively.

Once the limiting triaxial strain ε_L is computed, it is compared to the sum of the equivalent plastic strain ε^p_{eq} and the forming strain ε_{cf}. The forming strain can be determined based on the steel grade and the method of fabrication or assumed to be zero if heat treatment is performed according to the applicable construction code. If the inequality given in Eq. 2.18 is not satisfied, then the pipe is deemed to be in risk of local failure due to fracture.

$$\varepsilon^p_{eq} + \varepsilon_{cf} \leq \varepsilon_L \tag{2.18}$$

As an example for the application of Eq. 2.17, a load case with a cold bent pipe is analysed. The steel grade of the cold bent pipe is X65 which is one of the steel grades experimentally tested in [1]. Later in this work, a more detailed numerical analysis of cold bent pipes is presented. At this point for the demonstration purposes the variation of predicted failure curvature values is visualized with respect to changing Y/T ratios of the pipe material(Figure 2.15). The example curve in Figure 2.15 is obtained from the simulation of the cold bent pipe with an internal pressure which causes 80% SMYS hoop stress. At this level of internal pressure as the simulation results later in the text show, for this particular pipe material and geometry there is a high probability of tension side fracture. Therefore the principal stress

and equivalent plastic strain values are taken from an element at the tension side of the finite element model of the cold bend. One information about

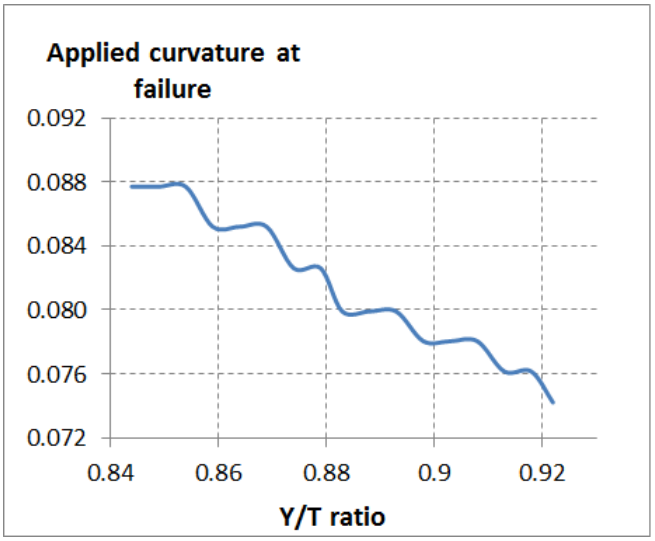

Figure 2.15: Variation of the failure curvature with respect to the Y/T ratio for the steel grade X65 and the circumferential stress of 80% SMYS

the nature of Eq. 2.17 that Figure 2.15 imparts is that Eq. 2.17 is highly sensitive with respect to variatons in the (Y/T) ratio. The range of the Y/T ratios in Figure 2.15 is selected based on the API requirements for the upper and lower bounds for the specified Y/T ratio listed in [4]. In Figure 2.15, the forming strain which is part of Eq. 2.18, is assumed to be zero. Furthermore, the value of the uniaxial strain limit ε_{Lu} is taken as equal to m_2. The values of m_2 and α_{sl} are computed as appropriate for duplex stainless steels. It was observed that, as the Y/T ratio increases from its lower bound to its upper bound, the applied curvature at the tension side failure increases 18%. This confirms the high sensitivity of Eq. 2.17 with respect to the Y/T ratio.

3 SENSITIVITY ANALYSIS OF THE TENSILE STRAIN CAPACITY PREDICTION EQUATIONS

Tensile strain capacity prediction equations are developed in such a way that they can estimate the maximum tensile strain that can be sustained by the pipeline structure in the presence of flaws in the pipe wall. These flaws have a reducing effect on the tensile strain capacity which becomes more detrimental with growing flaw sizes. The tensile strain capacity prediction equations in the literature consider the effect of the flaw size on the tensile strain capacity. In addition to that some of these equations also quantify the effect of the internal pressure on the tensile strain capacity. However due to the complex nature of these empirical equations it is difficult for the practitioners in the field to develop an intuition about the effect of different parameters on the tensile strain capacity. The analysis presented in this chapter aims at clarifying the effects of different parameters on the tensile strain capacity. For this purpose the sensitivity of the equations in the CSA Z662-11 code[9] and the equations presented in the PRCI report[17] with respect to different parameters is analyzed using factorial analysis. In this way the effects of the parameters like flaw length, flaw height, wall thickness etc. on the tensile strain capacity are quantified.

3.1 CSA Equations

The tensile strain capacity prediction equations (Eq. 2.3, Eq. 2.5) of the CSA Z662-11 code[9] are reviewed in Section 2.1. In the current section these equations are analyzed using 3^4 and 3^6 factorial analysis respectively.

In the 3^k notation for factorial designs, the base 3 denotes that the tensile strain capacity is evaluated at 3 different levels (low, intermediate, high) of each parameter affecting the tensile strain capacity, and k denotes the total number of parameters. In case of surface defects k is equal to 4 and in case of buried defects k is equal to 6. The geometry of the 3^k factorial analysis can be visualized as in Figure 3.1.

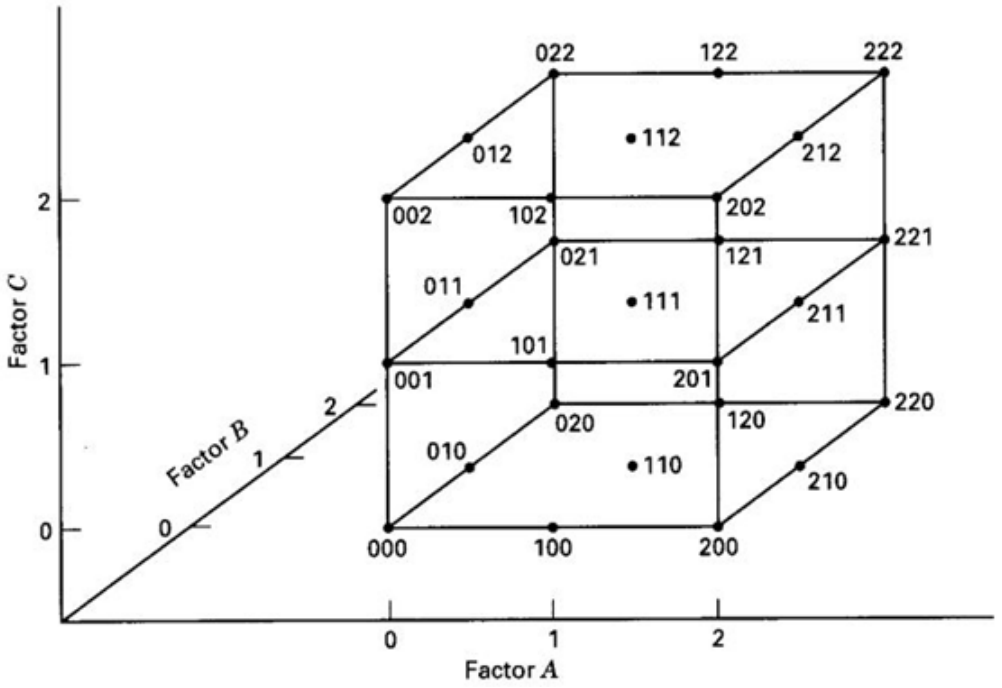

Figure 3.1: Combinations of three parameters (Factor A, Factor B, Factor C) at three different levels (0, 1, 2) [20]

In Figure 3.1, each of the three coordinate axes represents a different parameter. The three digit numbers at the corners and side mid-lengths of the cube represent the combinations of the parameters for which the output quantity is evaluated. In each three digit number the first second and third digits denote the levels of the parameters Factor A, Factor B and Factor C respectively. The digits 0,1,2 represent the low, intermediate and high levels

respectively.

The outcome of the factorial analysis gives insights about the parameters having the greatest effect on the tensile strain capacity (ε_t^{crit}) of a pipe in the presence of pipe wall flaws. In Eq. 2.3 and Eq. 2.5, the parameters effecting ε_t^{crit} are material properties such as the Y/T ratio of the base metal (λ), the fracture toughness of the pipe base metal in terms of the crack tip opening displacement (δ) and geometric properties such as the ratio of the flaw length to pipe wall thickness (ξ), the ratio of the flaw height to pipe wall thickness(η), the wall thickness (t), The ratio of the buried defect depth (measured from the interior pipe wall) to pipe wall thickness (ψ). For each of these parameters there are certain ranges defined in the CSA code such that the equations only deliver reliable results within these ranges. The parameters and their corresponding ranges of applicability are listed in Table 3.1, where the lower bound for η is an assumed value for the purpose of the factorial analysis, since for this parameter no lower bound is defined in CSA Z662-11.

Table 3.1: Parameter ranges for the tensile strain capacity prediction equations in CSA Z662-11

$0.1 \leq \delta \leq 0.3$
$0.7 \leq \lambda \leq 0.95$
$1 \leq \xi \leq 10$
$\eta \leq 0.5$
$t \leq D/32$

In case of surface defects, the parameters affecting the tensile strain capacity are η, ξ, λ and δ such that $\varepsilon_t^{crit} = f(\eta, \xi, \lambda, \delta)$. In the 3^4 factorial analysis, ε_t^{crit} is evaluated for all combinations of the four parameters at the low, intermediate and high levels which results in 81 different predictions for ε_t^{crit}. In order to determine the sensitivity of ε_t^{crit} to the changes in a

particular parameter, ε_t^{crit} is evaluated when this parameter is kept fixed at low, intermediate and high levels for all possible combinations of the rest of the parameters. This analysis results in 27 different ε_t^{crit} predictions for each fixed level of the parameter in the analysis of the equation for the surface defects. The next step of the analysis is to take the average of the 27 predictions for each level which gives a single real number for each level of the parameter. The final step of the analysis is to plot the variation of these averages with respect to the level at which the parameter is fixed and to repeat this procedure for all of the parameters.

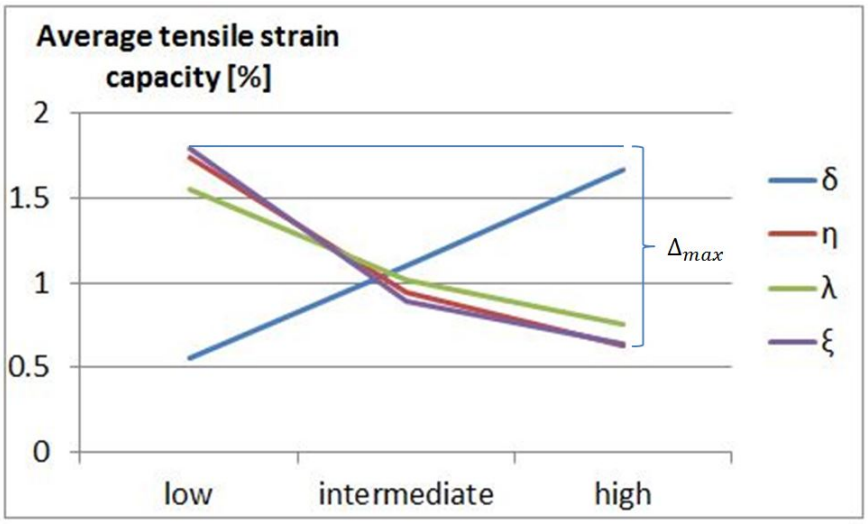

Figure 3.2: Sensitivity analysis for surface defects

Figure 3.2 shows the results of the factorial analysis for surface defects. The low and high levels in Figure 3.2 correspond to the lower and upper bounds for the parameters given in Table 2.2 whereas the intermediate level is the middle point of these two boundaries. In Figure 3.2, Δ_{max} is the maximum difference between the highest and the lowest average ε_t^{crit} value that a parameter takes. A high value of this difference for any particular parameter indicates a high sensitivity of the equation with respect to that

parameter. In case of surface defects the highest value of these differences is observed for the parameter ξ as 1.18%.

According to Figure 3.2 the increasing values of the geometric parameters ξ and η lead to lower average ε_t^{crit} values as expected. Also, an increase of the fracture toughness parameter δ leads to higher average ε_t^{crit} values. Figure 3.2 shows that low values of the Y/T ratio (λ) have a favorable effect on ε_t^{crit}. The geometric parameters ξ and η are seen to have a clearly non-linear effect on ε_t^{crit} whereas the effect of δ is seen to be perfectly linear and the Y/T ratio has only a slightly non-linear effect on ε_t^{crit}. It should be noted that the linear relationship between δ and ε_t^{crit} is not clearly discernable from the format of Eq. 2.3 and could only be revealed by a factorial analysis.

In addition to η, ξ, λ and δ, the equation for buried defects includes the parameters ψ and t so that the total number of parameters effecting ε_t^{crit} increases to 6. Therefore in case of buried defects a 3^6 factorial analysis is necessary in order to determine the sensitivity of ε_t^{crit} with respect to each parameter. In a 3^6 factorial analysis there are 729 possible combinations of the low, intermediate and high levels of 6 parameters. Also, there are 243 different combinations of different levels of 5 parameters when one of the parameters is fixed in its low, intermediate or high level. The result of the factorial analysis for the buried defect equation (Eq. 2.5) is plotted in Figure 3.3. Similar to the case of surface defects, the effect of the parameter δ on ε_t^{crit} is seen to be perfectly linear. Also, the effects of the parameters λ and t are close to linear whereas the variation of the average ε_t^{crit} with respect to the changes in the parameters ψ, ξ and η is non-linear. Again the parameter η has the largest difference (5.25%) between the maximum and minimum values that the average ε_t^{crit} takes for any parameter.

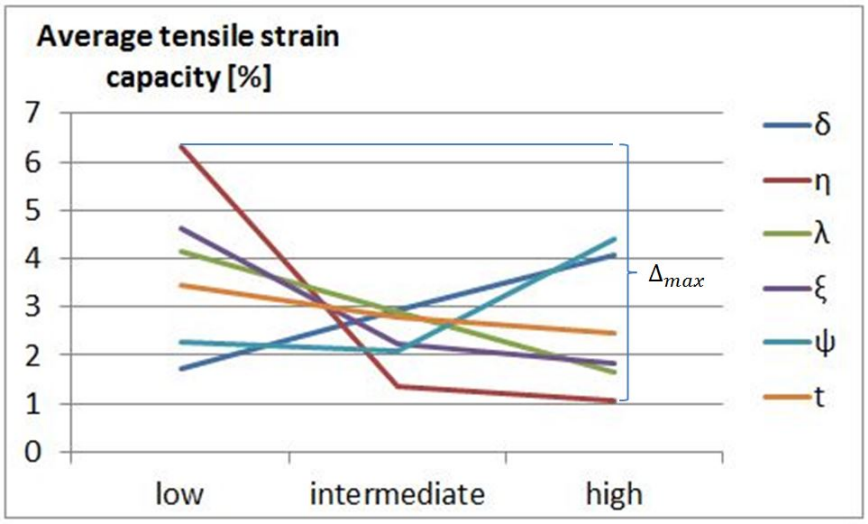

Figure 3.3: Sensitivity analysis for buried defects

3.2 PRCI Equations

The PRCI report[17] presents an equation format which is based on curve fitting procedures and contains different coefficient sets for different welding methods used for the manufacturing of girth welds. One set of coefficients is applicable to gas metal arc welding (GMAW) method whereas the other set of coefficients is applicable to shielded metal arc welding (SMAW) and flux cored arc welding (FCAW) methods. In this section the factorial analysis is applied for both of these coefficient sets. Further details of this method are elaborated in Section 2.2. A total of 7 parameters are included in the PRCI equation which include ξ, η, λ and δ. The remaining three parameters are the girth weld metal strength mismatch ratio (ϕ), the normalized high-low misalignment (ψ_1) and the ratio of the hoop stress caused by the internal pressure to the yield strength of the pipe base metal (f_p). As a result 3^7 factorial analyses are carried out the results of which are plotted in Figure 3.4 and Figure 3.5 for GMAW and SMAW/FCAW respectively.

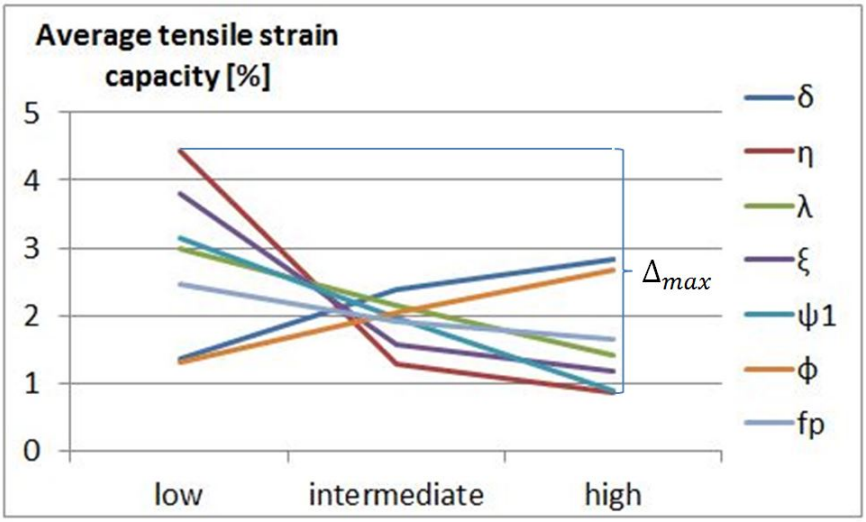

Figure 3.4: Sensitivity analysis for GMAW

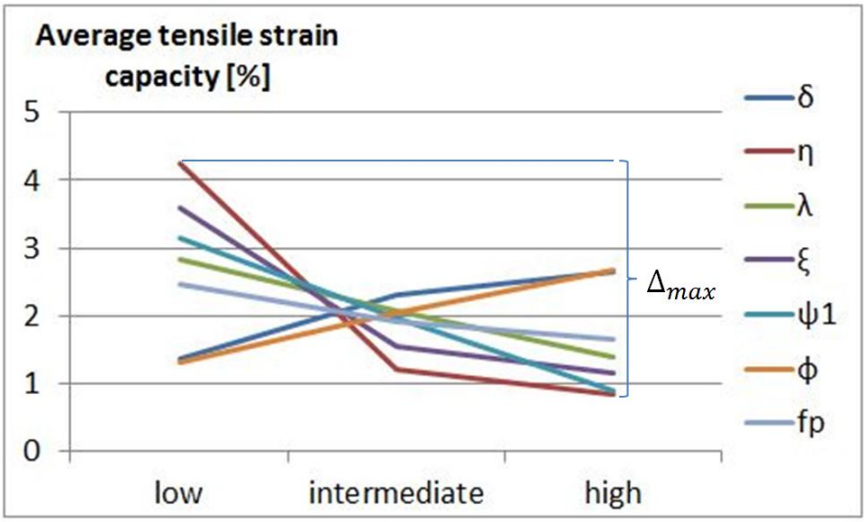

Figure 3.5: Sensitivity analysis for SMAW/FCAW

The results of the factorial analysis for GMAW and SMAW/FCAW plotted in Figure 3.4 and Figure 3.5 show that, the outcome of the strain capacity equation (Eq. 2.7) is similar for both welding types. The highest difference between the maximum and minimum average ε_t^{crit} is again observed for η (3.57% for GMAW and 3.43% for SMAW/FCAW). From Figure 3.4 and Fig-

ure 3.5 it can be reckognized that the parameters having linear and non-linear effect on ε_t^{crit} can be classified in two groups. The group of the parameters having linear effect consists of $f_p, \phi, \psi_1, \lambda$ whereas the group of the parameters having non-linear effect consists of ξ, η, δ. It should be noted that the majority of the parameters considered in Eq. 2.8 to Eq. 2.13 have linear effect on ε_t^{crit} which is not clearly discernable from the format of these equations. The source code of the program used in the factorial analyses of this section is given in Appendix A.4.

3.3 Closing Remarks

The prediction of the tensile strain capacity of pipeline structures is a crucial part of strain based design. Having reliable prediction methods for the maximum strain that a pipe structure can withstand would allow pipeline operators to use the load carrying capacity of their pipeline network more efficiently. In order to achieve that, several prediction equations are proposed in the pipeline literature and two of these equations are also included in the Canadian oil and gas pipeline systems code CSA Z662-11. However, since these equations are developed using curve fitting techniques based on the results of experimental and numerical analyses, they contain a large number of empirical coefficients that obscure the effect of different parameters on the tensile strain capacity.

The parameters that have been included in most of the equations are the dimensions of the flaws in the pipe wall such as circumferential length of a flaw on the pipe wall and the height of a flaw measured from the outer surface of the pipe towards the inner surface. In addition to these parameters also, the equations developed by the Pipeline Research Council International (PRCI) consider the effect of the internal pressure on the tensile strain capacity.

The sensitivity analyses carried out in this chapter aimed at clarifying the effect of different parameters on the tensile strain capacity. In this process the parameters having the largest effect on the tensile strain capacity are identified using factorial analysis. 3^4 and 3^6 factorial analyses are carried out for the surface defect and buried defect prediction equations of CSA Z662-11 respectively. It is found that changing the magnitude of the parameter ξ which is the ratio of the flaw length to pipe wall thickness, while keeping the other parameters constant, causes the largest changes in the average tensile strain capacity for each level of this parameter in case of surface defects. Also, the effect of changing the parameter η (the ratio of the flaw height to pipe wall thickness) is found to be almost equal to but slightly lower than the effect of changing the parameter ξ. The average tensile strain capacity is found to vary non-linearly with respect to both ξ and η. The difference between the maximum and minimum average tensile strain capacity for the three levels of the Y/T ratio is less than the difference observed for ξ and η. Also, the non-linearity of the average tensile strain capacity variation is less than what is observed for ξ and η. It should be noted that the average tensile strain capacity is observed to decrease with increasing values of the Y/T ratio. The parameter δ which represents the fracture toughness of the material is found to affect the tensile strain capacity in a magnitude comparable to ξ and η with a linear variation in case of surface flaws.

The same procedure is repeated for the buried defect equation of the CSA Z662-11 which includes the parameters ψ (the ratio of the flaw depth measured from the inner pipe surface to the pipe wall thickness) and t (the pipe wall thickness) in addition to the parameters included in the equation for surface defects. In case of buried defects, changing the value of the parameter η is found to have clearly the greatest effect on the average value of the

tensile strain capacity followed by the effects of changing the parameters ξ, λ (the Y/T ratio) and δ. Again the Y/T ratio and the average tensile strain capacity are found to be inversely proportional. The variation of the average tensile strain capacity with respect to ψ showed that, increasing the distance of a buried defect from the inner surface of the pipe while keeping all other parameters constant, has a favourable effect on the tensile strain capacity in the interval between the intermediate and high level of this parameter. Finally, changing the wall thickness while keeping the other parameters constant, is found to cause the least changes in the average tensile strain capacity in case of buried defects.

The equations developed by PRCI consider the effect of using different welding procedures in the manufacturing of girth welds on the tensile strain capacity in addition to the effects of the flaw dimensions, the high-low misalignment of the girth weld, the internal pressure and the ratio of the ultimate strength of the girth weld metal to the ultimate strength of the pipe base metal. Two different equations are developed for the cases when the gas metal arc welding (GMAW) technique is utilized and either one of the flux-cored arc welding (FCAW) or shielded metal arc welding (SMAW) technique is utilized. The outcome of the sensitivity analysis for both equations was similar to each other and again the parameter η was found to have the greatest effect on the tensile strain capacity followed by the parameter ξ. The changes in the parameters of the ultimate strength ratio of the weld metal to the pipe base metal (ϕ) and the fracture toughness are found to have an almost equal effect to each other, albeit the effect of δ being non-linear. Similar to the CSA equation results, the increase in the Y/T ratio is found to linearly decrease the average tensile strain capacity. Finally the internal pressure parameter f_p is found to have the least effect on the tensile strain

capacity.

The factorial analyses carried out in this chapter revealed certain properties of the tensile strain capacity prediction equations which are not apparent due to the complex format of the equations. For certain parameters the linear dependence of the predicted strain capacity values on these parameters are shown. Furthermore, different parameters involved in the equations are ordered according to the impact of changing these parameters on the predicted value of the tensile strain capacity. Determining the impact of different parameters such as pipe wall flaw dimensions, on the tensile strain capacity and prioritizing them according to their impact can have significant benefits in the process of pipe inspections.

4 DESIGN OF THE FULL SCALE TESTS

Prior to the start of the full scale experiments, a proper dimensioning of the specimens and other peripheral equipment, like the end plates and the connection pieces, is vital. This section elaborates the process of choosing proper dimensions and materials for these peripheral parts of the experimental setup.

4.1 Test Setup and Instrumentation

The test setup consists of testing pipe segments with girth welds in the middle of the segment. A flaw is machined next to the girth weld. The pipe is positioned vertically in an MTS machine (Figures 4.3, 4.6). Loading is conducted in two steps, the first is by applying an internal pressure using a pneumatic pump. After achieving the desired pressure, eccentric tensile loading is applied using the MTS machine while keeping the pressure constant. The details of the instrumentation, the machining of the flaws, and the test setup components are described in this section.

The most significant variables in this experimental study are the strain distribution on the pipe wall, the internal pressure, the applied tensile force and the applied displacement on the full scale specimens. In order to measure the strain variable two different techniques are utilized. These are strain gauges and digital image correlation.

The internal pressure is applied by filling the pipe specimen with water and pressurizing it. For the application of the internal pressure a pneumatic pump is connected to the water inlet of one of the end plates. At both the water inlet and the air outlet in the two opposite end plates, ball valves are connected. The valve at the air outlet is closed once the pipe is filled with

water prior to the pressurization. In this way the trapping of air within the specimen is prevented. Also, a pressure transducer is connected directly at the water inlet valve which is calibrated such that the pressure would be relieved by letting water out of the pipe in case that the maximum pressure is exceeded.

The tensile force is applied using the MTS machine in the I.F. Morrison Structural Engineering Laboratory with 6000 kN tensile force capacity. The specimens are placed into the machine vertically. The lug pieces (Figure 4.1) bolted to the end plates of the pipes are used in order to bring the specimen to a stable position from which displacement could be applied. These lug pieces are connected to the pin-yoke assemblies (Figure 4.2) fixed to the floor and to the actuator of the MTS machine.

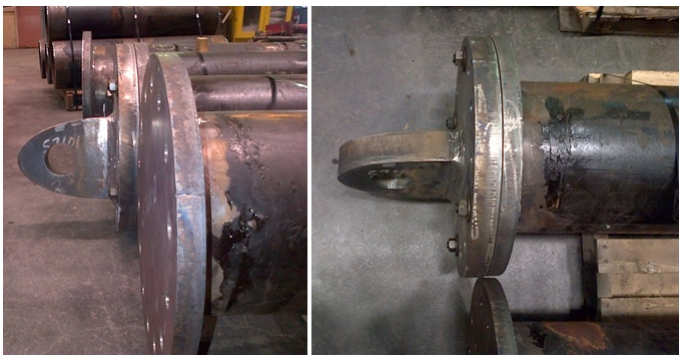

Figure 4.1: End plates and the lug pieces

The digital image correlation (DIC) system and the MTS machine are synchronized so that the force and displacement data are recorded in equal intervals with the pictures taken by the DIC system. In order for the DIC method to function the specimens are painted in white and afterwards speckled with a dark coloured paint. This operation was limited to the areas around the pipe wall crack and the remote strain areas for the first two experiments and later extended to the entire specimen surface facing the DIC

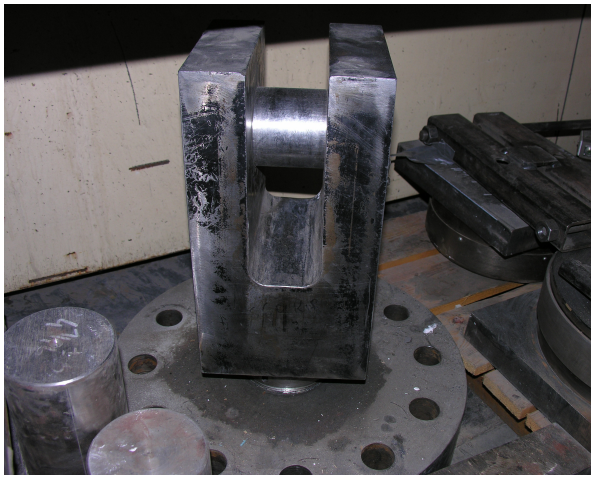

Figure 4.2: Pin-yoke assembly

system. The painted and speckled areas of interest for the DIC method are shown in Figure 4.3.

In the process of speckling the pipe wall one important factor to be considered is the irregularity of the speckle pattern so that the same speckle configuration does not repeat itself at different parts of the pipe wall. Spraying the dark coloured paint from a bottle manually is a suitable method for creating an irregular speckle pattern. Also large white gaps or large speckles should be avoided. Examples of acceptable speckle patterns is given in Figure 4.4.

In addition to the DIC, strain gauges are used in order to have redundant data for the strain measurement. The strain gauges consisted of 350Ω or 120Ω electrical resistors that can be glued to the pipe wall. Prior to the installation of the strain gauges it is important to have a clean and slightly rough surface for a better adhesion between the strain gauge and the pipe surface. Therefore the adhesive coating that covers the pipe surface should be completely removed. Before the application of the glue between the pipe base metal and the strain gauge, the location of the strain gauge is cleaned

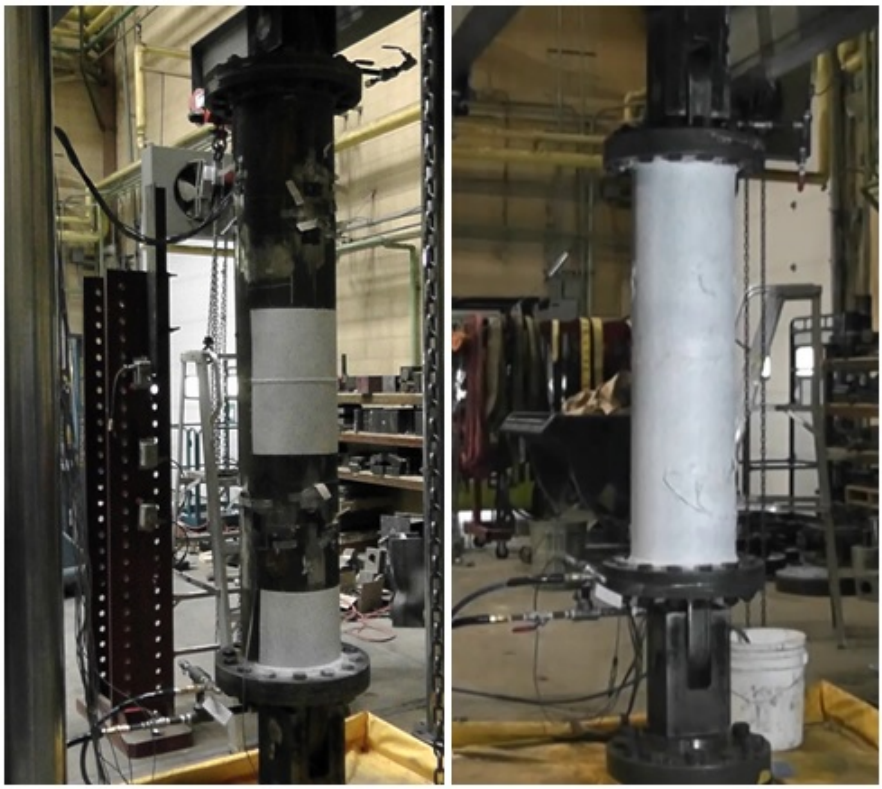

Figure 4.3: DIC areas of interest in the first two tests (left) and in Test 3 to Test 8 (right)

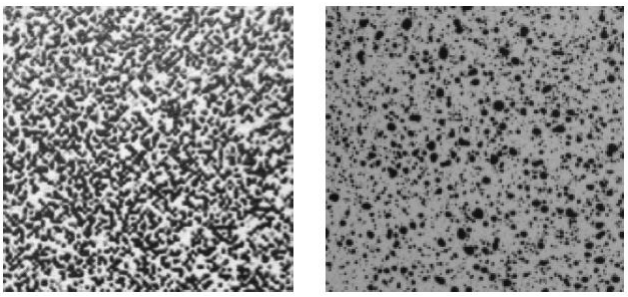

Figure 4.4: Speckle patterns [52]

with a degreaser and roughened with a sand paper. The strain gauges are calibrated in such a way that the data acquisition system can convert the changes in the voltage across the gauges into strain values throughout the test using the gauge factor provided by the manufacturer of the strain gauges.

4.1.1 Positioning of the Strain Gauges

The positioning of the strain gauges varied throughout the testing program. The gauges are positioned in the longitudinal or hoop direction in order to measure the longitudinal and hoop strain respectively. In the first 4 tests with the long specimens the longitudinal gauges are positioned both at the vicinity of the girth weld 1 OD away from it and at the remote strain zone 1 OD away from the end plate. Also, in the mid-length of the pipe at each side of the girth weld strain gauges are installed. On the other hand in the fifth to eighth tests with the shorter specimens, the longitudinal strain gauges are only placed in the mid-length of each half of the specimen. The pipe circumference is divided into four quarters (Figure 4.5) and at each quarter strain gauges are installed. Figure 4.5 shows the naming convention for the strain gauges when looked from the top side of a pipe in the MTS machine, towards the bottom side of the pipe.

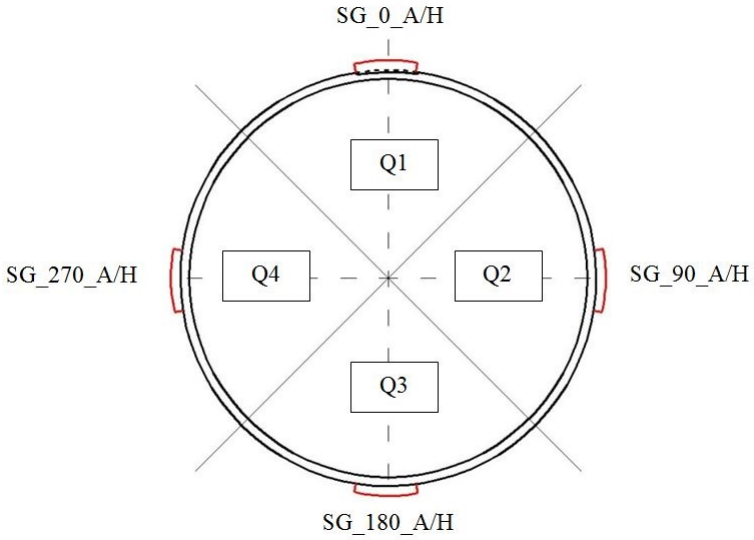

Figure 4.5: Strain gauge positions around the pipe circumference

The four quarter segments of the pipe cross section are denoted with Q1

to Q4 in Figure 4.5. The red lines on the pipe surface in the middle of each quarter show the location of a strain gauge. The strain gauges are positioned with 90 degrees radial distance from each other and are denoted according to their radial distance from the machined flaw in the heat affected zone. The last letter in each strain gauge label in Figure 4.5 indicates the direction of the strain gauge. This letter can be either 'A' or 'H'. For example the letter 'A' in SG_0_A denotes that the strain gauge is measuring axial strain. Also the number '0' in the strain gauge label denotes that the strain gauge is aligned with the flaw. Similarly, SG_90_H is the strain gauge which is located in a clockwise direction 90 degrees away from the flaw and measures the hoop strain at this location. In order to describe the location of a strain gauge an additional number is included in the labels which is not shown in Figure 4.5. This number takes the values 1/3, 1/2 and 2/3 for the strain gauges 1 OD away from the end plate, the strain gauges at the mid-length of one side of the girth weld and the strain gauges 1 OD away from the girth weld respectively. Another letter used in the actual labels but not included in Figure 4.5 is the letter showing on which side of the girth weld the gauge is located. For the gauges at the bottom side of the girth weld the letter 'A' is used whereas for the gauges at the top side of the girth weld the letter 'B' is used.

The pieces of the experimental setup elaborated in the previous sections are sketched in Figure 4.6. The amount of eccentricity of the applied displacement (50 mm) as well as the remote strain location can be seen in Figure 4.6. The amount of eccentricity of the lug pieces is identical on both sides of the pipe. Also, the pipe lengths on both sides of the girth weld are identical. Using this symmetry, only half of the specimen is shown in Figure 4.6.

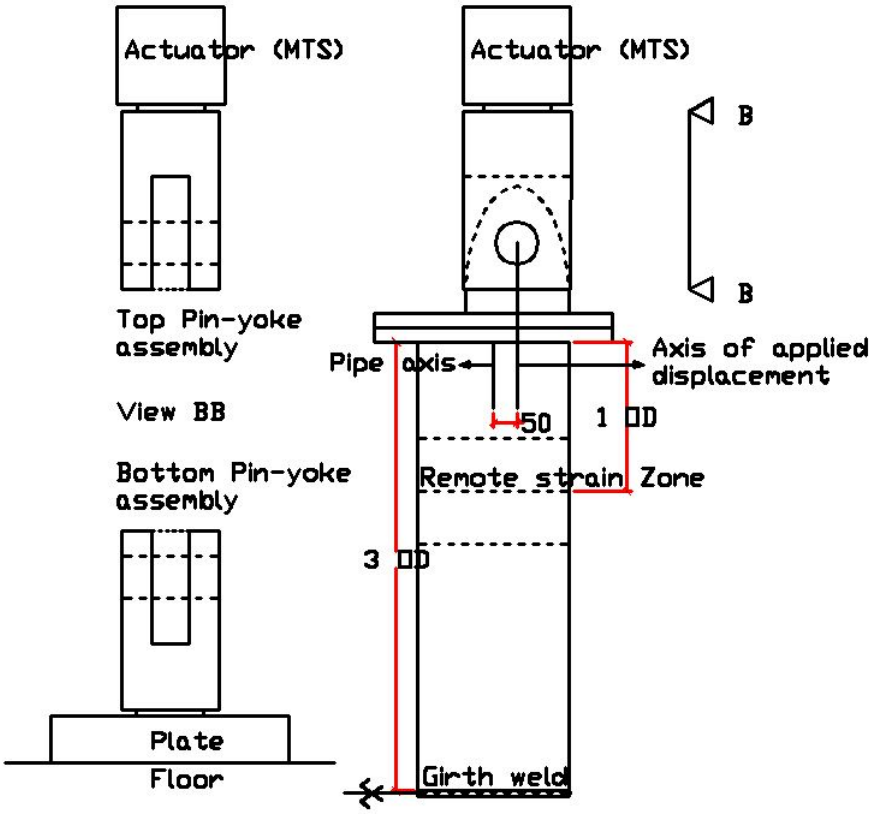

Figure 4.6: Experimental setup

4.2 End Plate Design

In the design of the end plates the factors that have to be considered are the thickness of the end plates, the strength of the material that the end plates are made of and the configuration of the bolt holes that connect the end plates to the testing machine. The design process of the end plates was an iterative process which started with a conservative estimate of the maximum tensile force that the full scale specimen would have to endure. This estimate was based on finite element modelling and simulation of the specimen. The iterative process of choosing proper dimensions for the end plates is illustrated in Figure 4.7. The process illustrated in Figure 4.7 started with the

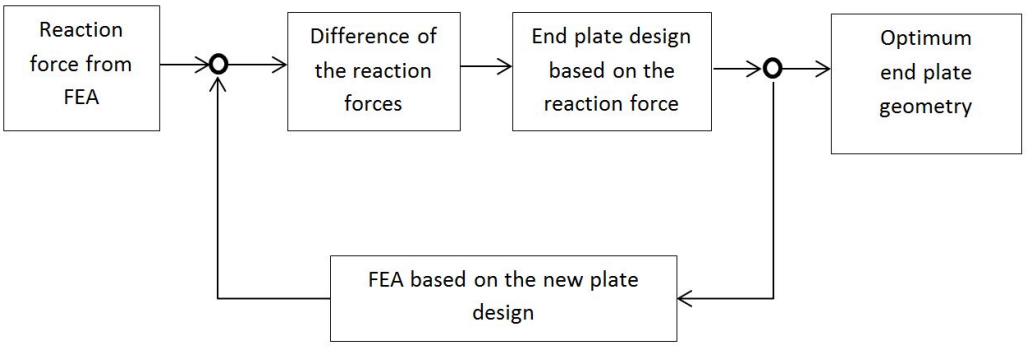

Figure 4.7: Iterative process of end plate dimensioning

simulation of a pipe with 12 in.(305 mm) diameter and 6.9 mm wall thickness connected to a rectangular 30 mm thick end plate without bolt holes. X52 steel grade material properties are used for both the pipe and the end plate. Since the tensile forces in the experiments were planned to be applied eccentrically, the effect of tensile load eccentricity is taken into account by introducing a load eccentricity which is about one quarter of the pipe diameter. An assumption had to be made for the amount of eccentricity since at that stage of the project a final decision for the eccentricity was not made. The maximum reaction force that could be carried by the pipe−end plate assembly is found to be 2878 kN in the absence of bolt holes. An observation of the experimental results in the later sections of this text can confirm that this value is a very close estimate of the actual maximum reaction force values observed in most of the tests. Especially in the first four tests of the experimental program where the crack height is shallow (25% of the wall thickness) the observed reaction forces were close to but less than 2878 kN. One exception to this trend occurred in the second experiment where the experiment was prolonged due to a material yielding at the connection piece between the testing machine and the end plate. In this prolonged experiment the maximum reaction force exceeded 3000 kN.

In order to have a safe bolt hole configuration, the maximum reaction force obtained from the finite element simulation is multiplied by a safety factor of 1.4. The resulting reaction force of $4029kN$ is used in the first attempt to design the bolt configuration.

4.2.1 First iteration of bolt design calculations based on an initial assumption for the number of bolts and their diameter

4.2.1.1 Calculations for pure tension

In the first attempt to design the bolt configuration, the diameter of each bolt hole is assumed to be 0.875 in (22.22 mm) and the number of the bolt holes is assumed to be 12. The shape of the end plates and the configuration of the bolt holes is decided to be circular to conform with the circular pipe geometry. The initial total diameter of the end plate is in this case 464 mm, leaving 30 mm distance between the pipe outer edge and the edge of one bolt hole. The tensile stress per bolt due to pure tension resulting from the maximum tensile force, is calculated as follows[46]:

$$f_t = \frac{\sum RF}{n \cdot A_b} \tag{4.1}$$

where $\sum RF$ is the total axial tensile force, n is the number of bolts and A_b is the cross section area of one bolt. According to ASTM A490[49], f_t has to be less than 1040 MPa which is the allowable unit tensile stress for A490 high−strength bolts. Using $A_b = 380mm^2$ and $RF_{max} = 4029kN$ the maximum tensile stress per bolt is calculated as:

$$(f_t)_{max} = \frac{RF_{max}}{n \cdot A_b} = \frac{4029kN}{12 \cdot 380mm^2} = 884MPa < 1040MPa \tag{4.2}$$

Therefore the design with 12 bolts of diameter 0.875 in.(22.22 mm) each is safe under concentric tensile loading.

4.2.1.2 Calculations for eccentric tension

In case of eccentric loading, the bolts are subjected to an additional amount of tensile force due to the applied moment caused by the eccentricity[46]. In this case the following equation can be used in order to determine the additional tensile stress in each bolt caused by the bending moment:

$$(f_t)_{max} = \frac{M \cdot c}{I} = \frac{\sum RF \cdot e \cdot c}{I} \tag{4.3}$$

where e is the amount of eccentricity, c is the distance from the pipe axis to the centre of a bolt and I is the total moment of inertia of the bolt cross section areas. In this case $\sum RF = 4029kN$, $c = 191mm$ and $e = 0.5 \cdot c = 95.5mm$. Since the bolt holes are designed in a circular pattern, they have equal distance from the pipe axis and equal moment of inertia such that $I = \sum A_b c^2 = 12 \cdot (380mm^2) \cdot (191mm)^2 = 1664 \cdot 10^5 mm^4$. The maximum tensile stress in a bolt caused by the bending moment is therefore

$$(f_t)_{max} = \frac{(4029kN) \cdot (95.5mm) \cdot (191mm)}{1664 \cdot 10^5 mm^4} = 442MPa \tag{4.4}$$

The total maximum tensile stress acting on a bolt is calculated as follows:

$$\sum f_t = (f_t)_{BM} + (f_t)_T = 442MPa + 884MPa = 1325MPa > 1040MPa \tag{4.5}$$

This calculation shows that the number and diameter of bolts in the first iteration is not in the allowable range to satisfy the safety criterion in ASTM A490.

4.2.2 Second iteration of bolt design calculations

Since the quantity and diameter of bolts assumed in the first iteration did not satisfy the allowable stress requirement of ASTM A490, a larger bolt diameter and number of bolts is assumed in the second iteration. According to ASTM A490, The distance between bolt hole centers must not be less than 2.67 times diamater of a single bolt. In order to satisfy this condition, the end plate diameter is also increased as listed in Table 4.1.

Table 4.1: Comparison of the bolt hole configurations of the first and second iterations

	First iteration	Second iteration
End plate radius [mm]	232	252
Number of bolt holes	12	14
Bolt diameter [mm]	22.22 (0.875 in.)	25.8 (1 in.)

The increased bolt and end plate diameters result in a bolt area of $A_b = 523mm^2$ and a pipe axis to bolt center distance of $c = 203mm$ respectively. The increase in the value of c also results in an increase in the load eccentricity which is calculated as $e = c/2 = 102mm$. The total moment of inertia of the bolt cross section areas is calculated as $I_2 = 14 \cdot (523mm^2) \cdot (203mm)^2 = 3013 \cdot 10^5 mm^4$ where the subscript 2 denotes the second iteration. Using the above mentioned values the tensile stresses per bolt resulting from pure tension and bending, are calculated as in Eq. 4.6 and Eq. 4.7.

$$(f_t)_T = \frac{\sum RF}{n \cdot A_b} = \frac{4029kN}{14 \cdot 523mm^2} = 551MPa \tag{4.6}$$

$$(f_t)_{BM} = \frac{\sum RF \cdot e \cdot c}{I_2} = \frac{4029kN \cdot (102mm) \cdot (203mm)}{3013 \cdot 10^5 mm^4} = 275MPa \tag{4.7}$$

$$\sum f_t = (f_t)_T + (f_t)_{BM} = 826MPa < 1040MPa \tag{4.8}$$

It follows that the bolt hole and end plate configuration of the second iteration satisfies the per bolt hole maximum allowable stress requirement of ASTM A490.

4.2.2.1 Re-modelling the end plate

Once a satifactory bolt hole and end plate size is achieved, the next step is to simulate this new configuration with finite element analysis. In this way the effect of introducing bolt holes into the end plate and changing its size, on the maximum reaction force that can be carried by the pipe is analyzed. In this finite element analysis, the von Mises stress distribution on the pipe is observed and once the von Mises stress reaches the ultimate stress for X52 steel grade($452MPa$) anywhere on the pipe or end plate, the simulation is aborted. In the finite element model (Figure 4.9), the effect of a shallow crack was approximated by decreasing the element thickness to 75% of overall pipe wall thickness at the crack location. Using the symmetry of the pipe geometry about the crack location, one half of an entire full scale specimen was modelled. As Figure 4.9 shows, the location on the pipe with reduced wall thickness reached the ultimate stress first. Figure 4.10 shows the force−displacement curve of the simulation with a bolt hole configuration of 14 holes having 1 in. (25.4 mm) diameter. In the finite element analysis, the internal pressure and the tensile force were applied in two separate steps using the software Abaqus. In the first step a pressure of $12.7MPa$ was applied to the internal walls of the pipe as well as the part of the end plate that is subject to internal pressure. This amount of internal pressure causes a hoop direction stress on the pipe wall which is equivalent to 80% of the specified minimum yield stress (SMYS). This internal pressure level was chosen since 80 % SMYS is the maximum amount of internal pressure that

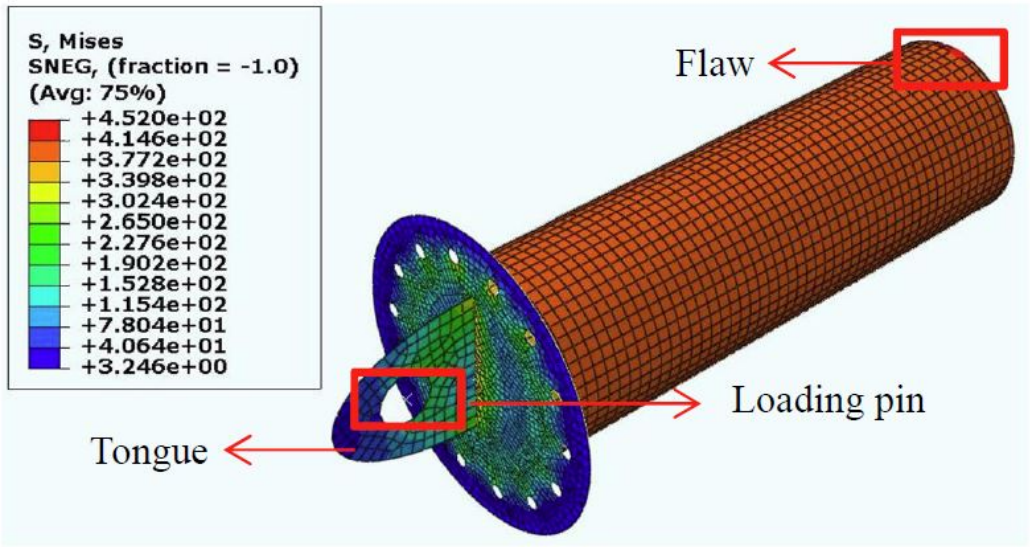

Figure 4.8: Distribution of the von Mises stress on the finite element model

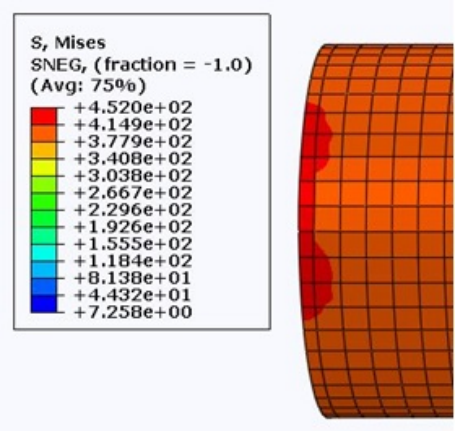

Figure 4.9: Von Mises stress distribution at the crack location with the end plate configuration with 14 bolt holes and 1 in. (25.4 mm) bolt hole diameter

is tested in this experimental program. In the second step the longitudinal force was applied in a displacement controlled way such that a total of $50mm$ displacement was applied in the axial direction. The maximum reaction force obtained from this simulation was $2880kN$. This result is almost identical with the maximum reaction force obtained from the model without bolt holes. Therefore the number and size of the bolts and the end plate described in

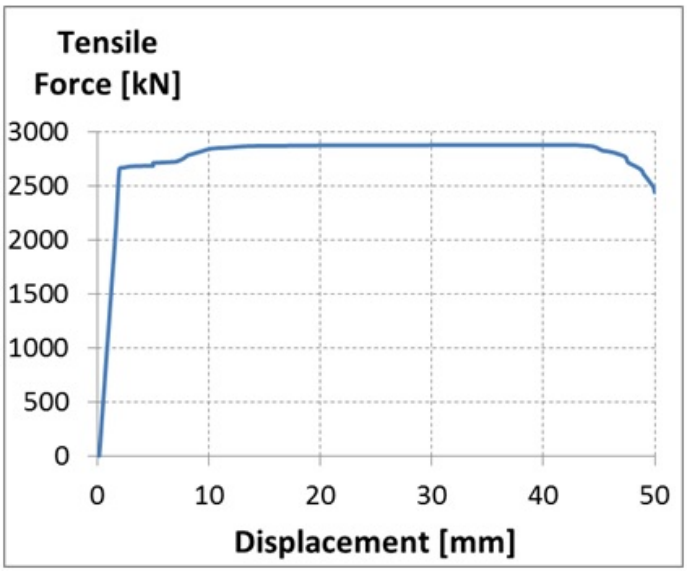

Figure 4.10: Force−displacement response with 14 bolts of 1 in. (25.4 mm) diameter

the previous section are accepted as the optimum end plate configuration.

4.3 Finite Element Analysis and Machining of Flaws in the Pipe Wall

Flaws in the pipe wall in the vicinity of the girth weld are expected due to the imperfect welding procedures applied in situ. One of the major goals of this experimental study is to investigate the effect of flaws of different sizes on the tensile strain capacity of pipelines. This section elaborates the machining procedure utilized in the creation of the pipe wall flaws and the numerical study of the effect of changing the flaw geometry on the stress distribution around the flaw.

In order to quantify the effect of the flaw size, flaws of different height and length are machined into the pipe wall using jewelry blades of two different thicknesses. A 0.012 in. (0.3048 mm) thick blade is used to create the initial

1 mm height of the shallow flaws and the initial 1.7 mm height of the deep flaws. Afterwards the remaining height is machined up to 25% wall thickness or 50% wall thickness for shallow and deep flaws respectively, using a 0.006 in. (0.1524 mm) thick blade. The second variable defining the geometry of a flaw is the circumferential length of the flaw. Two different groups of length are machined in this study having 50 mm and 150 mm length. The flaws are machined into the heat affected zone (HAZ) within the 5 mm proximity of the girth weld since it is known that the HAZ has reduced material strength and flaws in this area are more critical compared to the rest of the pipe. The equipment used in the flaw machining is shown in Figure 4.11.

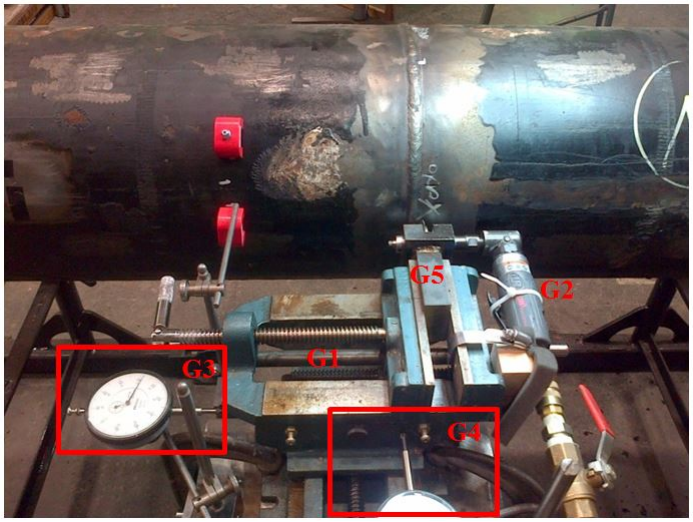

Figure 4.11: Flaw machining equipment

Different parts of the flaw cutting setup are denoted by different numbers following the letter G in Figure 4.11. The blades are driven by an air motor(G2) which is fixed in position in the axial and circumferential directions of the pipe using an x-y table (G1). In order to hold the blade in a fixed position, a steel block(G5) is machined and clamped in the x-y table which is connected to a mandrel building the connection between the air mo-

tor and the blade. In order to keep the blades attached to the mandrel, two clamping plates are placed on both sides of the blade. Figure 4.12 presents a close up of the blade assembly in the process of cutting the flaw for the third full scale experiment. The dial indicator denoted with (G3) is used in order to control the position of the blade/air motor assembly with respect to the pipe in the axial direction of the pipe. Since the blade position is fixed in the circumferential direction, the circumferential length of the flaw is controlled by the rotation of the pipe using the rollers of the pipe stand and the help of the two red stopper magnets on the pipe wall marking the two ends of the flaw. On the other hand the position of the blade with respect to the pipe wall in the direction perpendicular to the pipe wall is not fixed and can be manually adjusted using the x-y table. For this purpose a dial indicator(G4) is brought into contact with the x-y table and its position is zeroed at the point where the blade comes into contact with the pipe surface. From this point onwards, moving the blade/air motor assembly towards the pipe increases the displacement shown by the dial indicator. The flaw height is thus controlled by incrementally moving the blade towards the pipe wall. The blade is moved 0.05 mm towards the pipe after each circumferential pass of the blade through the flaw path. The small size of the increments is due to the limited torque of the air motor used in this process. Once the first 1 mm height of the flaw is completed, the 0.012 in. (0.3048 mm) thick blade is replaced by the 0.006 in. (0.1524 mm) thick one. During this replacement, the dial indicator (G3) is used in order to move the new blade 0.003 in. (0.0762 mm) towards the middle of the flaw path in order to prevent an unsymmetric flaw geometry(Figure 4.13 left) that would result from the difference in the blade thicknesses.

Since the machining of the flaws is done manually, differences between the

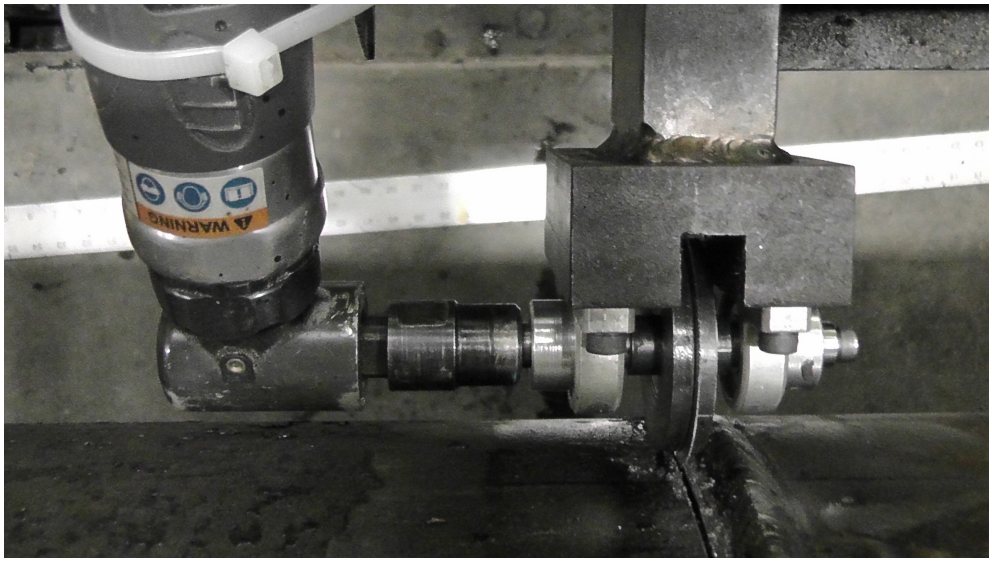

Figure 4.12: A close-up of the blade assembly

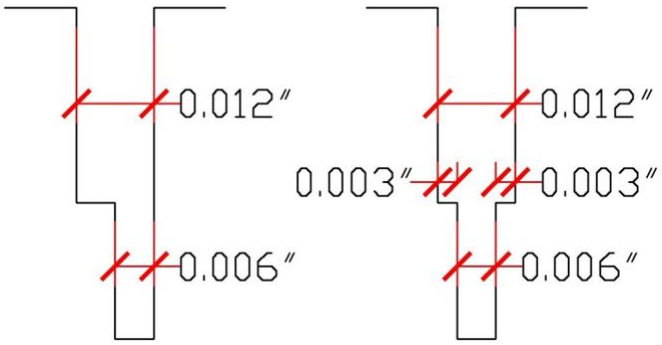

Figure 4.13: Flaw dimensions (height), undesired (left), desired (right)

planned crack geometry and the actual machined geometry are inevitable. One of the difficulties associated with the manual operation of the machining blade is that the width of the flaw can be greater than the planned width since multiple passes of the blade are necessary in order to reach the planned flaw height. However since the stress concentration is at the tip of the flaw, the inaccuracies in the width of the initial part of the flaw do not affect the tensile strain capacity of the pipe. In order to clarify this situation, finite element models are created for three different possible configurations of the

initial wider part of both the shallow (1.7mm height) and the deep(3.4mm height) flaws. For each one of these configurations, the von Mises stress distribution around the flaw is visualized in Figure 4.14 to Figure 4.19 at the point where the material starts to fail at the tip of the flaw. This starting point is determined using Eq. 2.17. It is found that the starting point of failure predicted by Eq. 2.17 is the same point where the element at the flaw tip reaches the ultimate strength of the material.

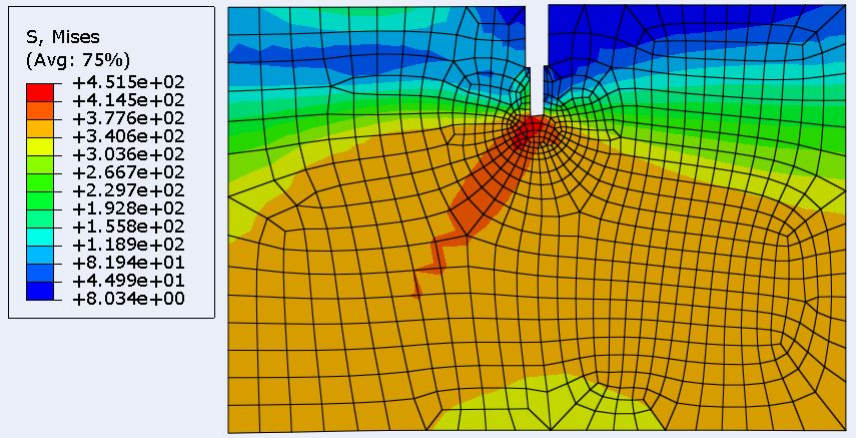

Figure 4.14: Von Mises stress distribution for 1.7 mm crack height

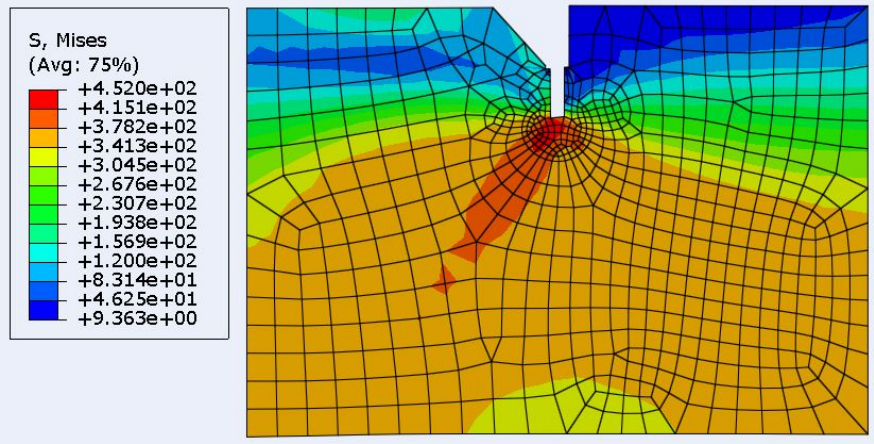

Figure 4.15: Von Mises stress distribution for 1.7 mm crack height with the initial 1 mm cut wider on one side

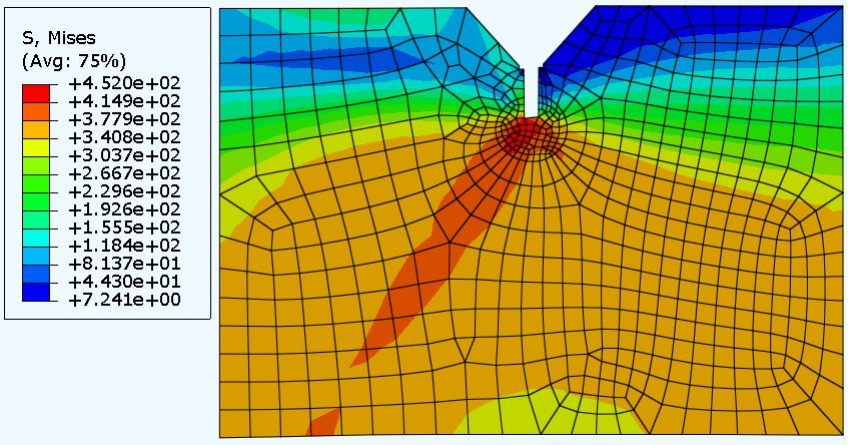

Figure 4.16: Von Mises stress distribution for 1.7 mm crack height with the initial 1 mm cut wider on both sides

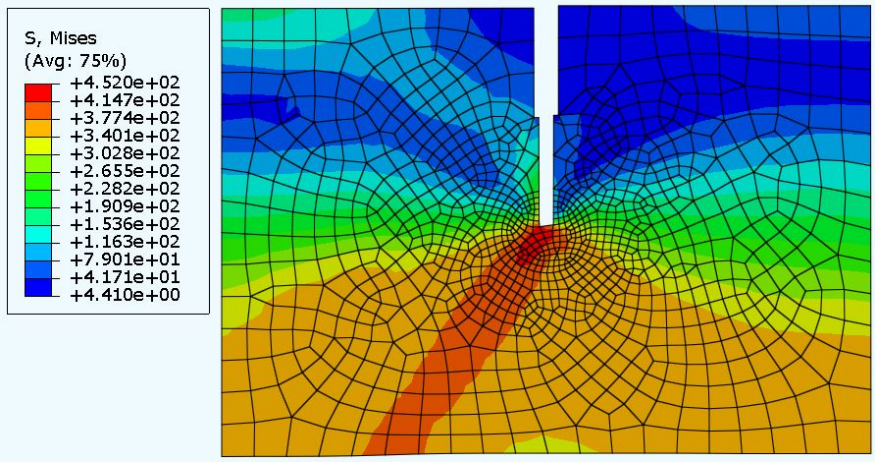

Figure 4.17: Von Mises stress distribution for 3.4 mm crack height

The von Mises stress distribution is widely used in the industry in order to visualize the structural response under various loading conditions since the von Mises stress relates to the distortion energy required to initiate the yielding of the material. It is well known that the strain energy U stored in a solid body can be expressed as in Eq. 4.9 where V denotes the total volume of the solid body[50].

$$U = \frac{1}{2}\int_V \sigma : \varepsilon dV \tag{4.9}$$

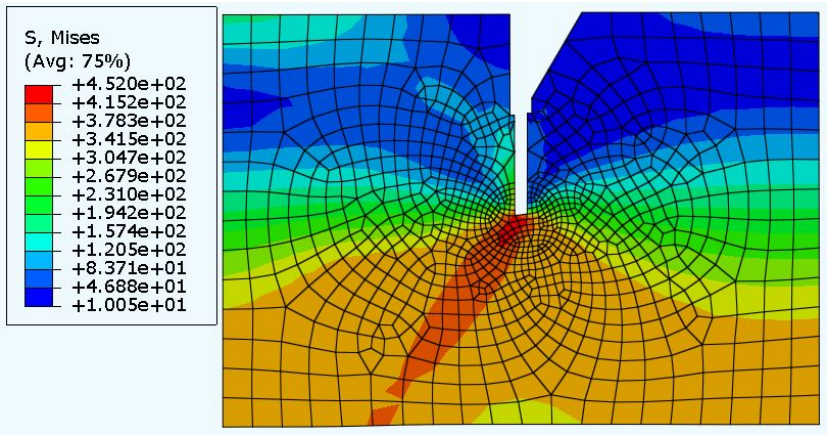

Figure 4.18: Von Mises stress distribution for 3.4 mm crack height with the initial 1.7 mm cut wider on one side

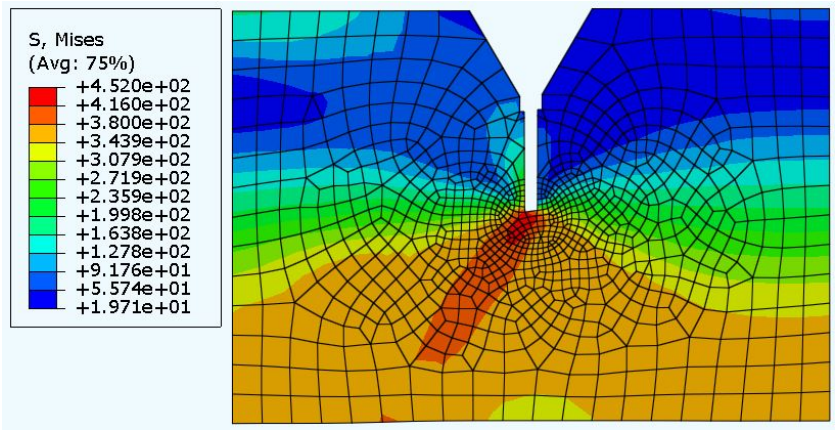

Figure 4.19: Von Mises stress distribution for 3.4 mm crack height with the initial 1.7 mm cut wider on both sides

Choosing a coordinate system aligned with the principal directions cancels out the shear stress components. Expressing the principal strains in terms of the principal stresses using Eq. 4.10 we obtain Eq. 4.11 where ν denotes

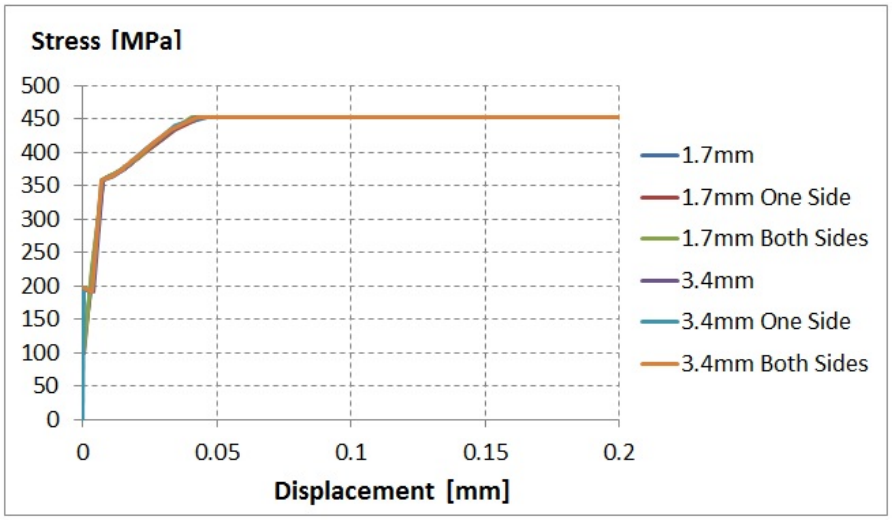

Figure 4.20: The variation of the flaw tip von Mises stress with respect to the applied displacement

the Poisson's ratio of the material.

$$\begin{aligned} \varepsilon_1 &= \frac{1}{E}(\sigma_1 - \nu\sigma_2 - \nu\sigma_3) \\ \varepsilon_2 &= \frac{1}{E}(\sigma_2 - \nu\sigma_1 - \nu\sigma_3) \\ \varepsilon_3 &= \frac{1}{E}(\sigma_3 - \nu\sigma_1 - \nu\sigma_2) \end{aligned} \tag{4.10}$$

$$U = \frac{1}{2E}\int_V \sigma_1^2 + \sigma_2^2 + \sigma_3^2 - 2\nu(\sigma_1\sigma_2 + \sigma_2\sigma_3 + \sigma_1\sigma_3)dV \tag{4.11}$$

Using the decomposition of the stress tensor into its hydrostatic (σ_h) and deviatoric stress components ($\sigma_{d1}, \sigma_{d2}, \sigma_{d3}$), the strain energy expression in Eq. 4.11 can also be decomposed into its volumetric strain energy and

distortion energy components.

$$\begin{aligned} \sigma_h &= \frac{\sigma_1 + \sigma_2 + \sigma_3}{3} \\ \sigma_{d1} &= \sigma_1 - \sigma_h \\ \sigma_{d2} &= \sigma_2 - \sigma_h \\ \sigma_{d3} &= \sigma_3 - \sigma_h \end{aligned} \tag{4.12}$$

Plugging the deviatoric stress components in Eq. 4.12 in Eq. 4.11 yields the distortion energy U_d as in Eq. 4.13.

$$U_d = \frac{1+\nu}{3E} \int_V \frac{(\sigma_1 - \sigma_2)^2 + (\sigma_2 - \sigma_3)^2 + (\sigma_3 - \sigma_1)^2}{2} dV \tag{4.13}$$

Since the expression inside the integral in Eq. 4.13 is equivalent to the square of the von Mises stress (σ_{VM}), the relationship between the distortion energy and the von Mises stress can be established as in Eq. 4.14.

$$U_d = \frac{1+\nu}{3E} \int_V \sigma_{VM}^2 dV \tag{4.14}$$

In the finite element models of the pipe wall cross section around a machined flaw(Figure 4.14 to Figure 4.19) an internal pressure corresponding to 80%SMYS hoop stress is applied at the bottom part of the model while a total of 1 mm displacement is applied to the right hand side of the model and the left side of the model is held fixed. The wall thickness is modeled as 6.95 mm which is identical with the wall thickness of the full scale specimens and the total length of the model is 10 mm.

For both the shallow and the deep flaw the von Mises stress distributions at the flaw tip are identical for the three different initial flaw widths. Furthermore, as it can be seen in Figure 4.20 the curves showing the variation

of the von Mises stress at the flaw tip element with respect to the applied displacement are overlapping each other for all flaw configurations. Therefore, it is clear that the variations in the initial width of the flaw do not have a considerable effect on the tensile strain capacity.

4.4 High-Low Misalignment Measurements

In the strain based design literature the high−low misalignment of girth welds is occasionally considered as one of the parameters affecting the tensile strain capacity of pipes. Therefore prior to the first and second full scale tests the high−low misalignment of the girth weld is examined using a 3D laser scanner and reverse engineering software Geomagic. The outcome of the scanning procedure is a three dimensional respresentation of the outside pipe surface in the computer environment. The method utilized for the determination of the high−low misalignment is based on a comparison of the scanned pipe surface with a perfect cylinder having the radius of the best-fit cylinder to the scanned pipe surface. This radius value is obtained from Geomagic which determines the closest perfect cylinder to the scanned geometry.

Geomagic contains a functionality specifically developed for geometric comparison of three dimensional objects. Using this functionality the scanned pipe surface and the perfect cylinder are overlapped and a colour map is generated showing the deviations of the scanned geometry from the perfect cylinder(Figure 4.21). In this colour map, locations of the scanned surface where the scanned surface is above the perfect cylinder are coloured in the tones of red and yellow, whereas locations where the scanned surface is below the surface of the perfect cylinder are coloured in the tones of blue and green. This colour convention can also be recognized from the fact that in Figure 4.21 the girth weld location is coloured in dark red since this part of the pipe has significantly greater diameter than the rest of the pipe. Once the colour map of the deviations given in Figure 4.21 was obtained, it was clear that at certain locations the scanned surface is above the perfect cylinder

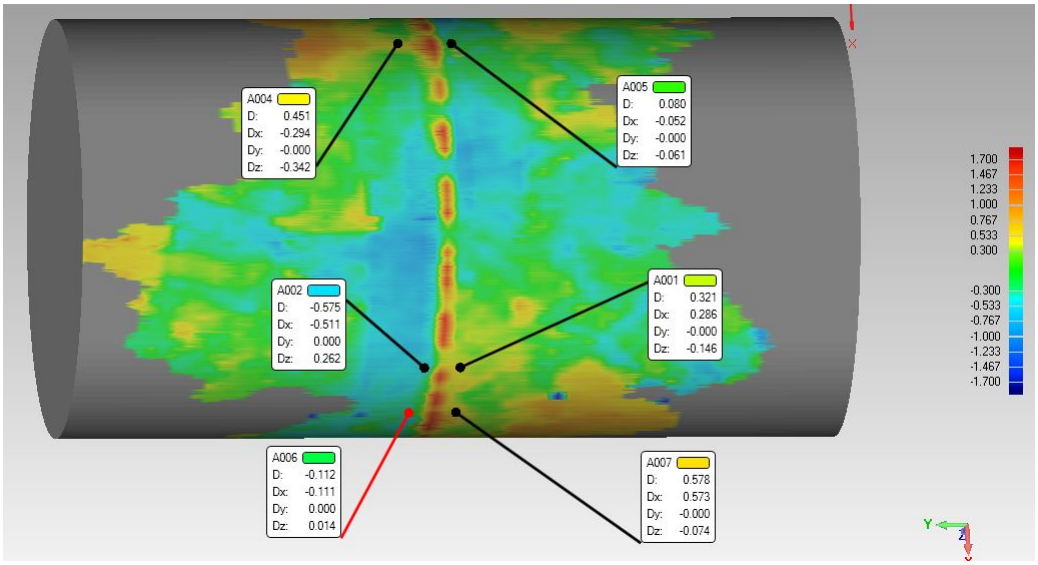

Figure 4.21: Determination of the high−low misalignment for the first full scale specimen

on one side of the girth weld and below the perfect cylinder on the other side. Three of these locations where the difference in the shade of colours on both sides of the girth weld is most obvious, are selected. The deviations at these locations are shown in Figure 4.21 where D denotes the magnitude of the deviation and D_x, D_y, D_z denote the deviations in x, y, z directions respectively. A minus sign in Figure 4.21 indicates that the scanned surface is below the perfect cylinder surface and a positive deviation indicates that the scanned surface is above the perfect cylinder surface. All deviation values in Figure 4.21 are in millimeters. Based on the deviation measurements in Figure 4.21, the greatest magnitude of misalignment is observed as 0.896 mm. This procedure is repeated for the second specimen and as expected the high-low misalignments are found to be minor since the girth welds of this experimental program are manufactured in a machine shop and have only minor imperfections compared to girth welds manufactured in situ. The process is not repeated for the rest of the specimens.

5 RESULTS OF THE FULL SCALE TESTS

In this chapter the measurements made by the DIC system, the strain gauges and the MTS system are presented. The cross correlation coefficients of the measurements from different strain gauges is computed separately for each test. The similarities between the strain developments at different locations of the pipe can be reckoned from the cross correlation matrices presented in this section. Also, the load-displacement response is presented for each test using the data collected by the MTS system.

5.1 Material properties of the X52 Specimens

In order to determine the material properties of the pipe specimens as well as the girth welds, tension tests have been conducted with specimens cut out of the pipes in longitudinal and circumferential direction. Furthermore, Charpy V-Notch impact tests are conducted in order to determine the fracture toughness of the pipe base metal, weld metal and the heat affected zone. After the arrival of the NPS12 pipes in the I.F. Morrison Structural Laboratory and the removal of the yellow jackets only one girth weld could be located on the pipes. In order to carry out the full scale tests a new set of girth welds are manufactured using the same welding procedures as the old girth weld. In the scope of the material test program both the old and the new girth welds are tested under uniaxial tension according to the ASTM E8/E8M-11 standard. The outcome of this tension test program was that in all of the tensile tests the measured yield strength of the of the pipe base metal exceeded the specified minimum yield strength of 360 MPa for X52 steel grade. The average value of the measured yield strength for the pipe base metal was 411 MPa. Also the ultimate strength of the pipe base

metal was measured higher than the specified minimum value of 460 MPa for this variable. The average of the measured ultimate strength values was 573 MPa in terms of true stress and 501 MPa in terms of engineering stress. The stress-strain behaviour of the tension coupons is shown in Figure 5.1. In Figure 5.1, 1A, 1B and 1C show the stress-strain response in three different coupon tests and the average values of these curves are shown with circles.

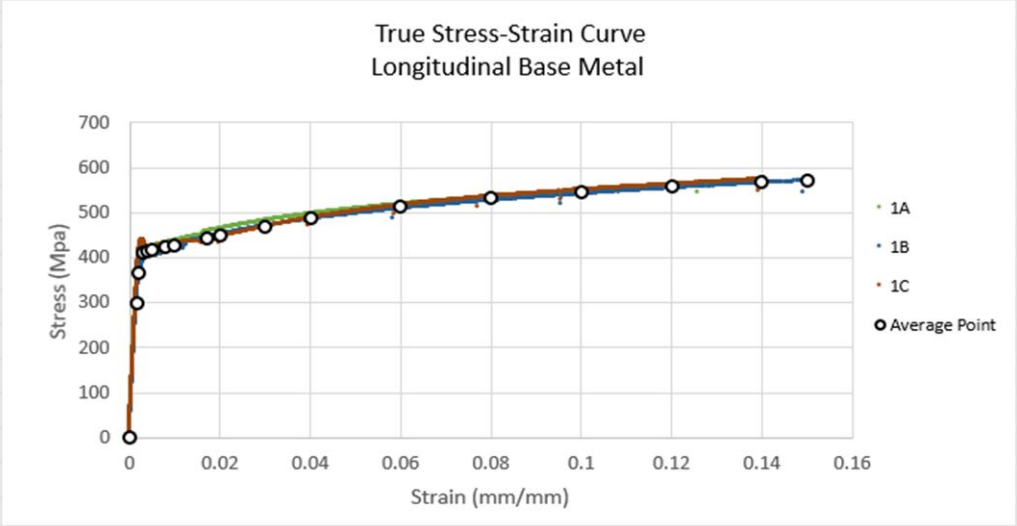

Figure 5.1: X52 pipe base metal stress-strain variation [51]

In addition to the pipe base metal also, the stress-strain behaviours of the old and the new girth welds are measured. The yield stresses of the new and old girth welds were measured as 428 MPa and 438 MPa respectively. The ultimate stresses of the new and old girth welds were measured as 531 MPa and 518 MPa in terms of engineering stress and 607 MPa and 561 MPa in terms of true stress respectively.

A total of 24 Charpy impact tests are carried out according to ASTM E 23-07 code in order to determine the variation of the absorbed energy during the impact with respect to the temperature. It is known that the fracture mode of metals can change from brittle to ductile with increasing

temperatures. Therefore the Charpy impact tests are carried out at two different temperature ranges (room temperature and a temperature below -21°). It was found that the new weld metal and both old and new heat affected zones have higher fracture toughness than the base metal. Also, the pipe base metal was found to be highly ductile based on the observation of the fracture surfaces of the specimens. Table 5.1 provides a list of the average Charpy impact energies of base metal, weld metal and HAZ at room temperature and low temperature [51].

Table 5.1: Average Charpy impact energies [51]

	Average Charpy Impact Energy at Low Temperature [J]	Average Charpy Impact Energy at Room Temperature [J]
Base metal	150	167
Old weld metal	92	94
Old HAZ	193	202
New weld metal	179	182
New HAZ	216	220

5.2 Strain Measurements and their Cross Correlation

Strain gauge measurements are proven to be a reliable method of monitoring the strain development on steel pipes. However their usage is limited to small strain values. At strain values larger than 1.5 %, strain gauge measurements cease to be reliable and often strain gauges fail by debonding due to large displacements. In the first two tests, due to the small size of the machined flaws, large displacements were necessary in order to cause the rupture of the pipe at the flaw location. As a result, many of the strain gauges failed before the rupture happened and erratic measuremets were observed in some others.

The method of cross correlation helps to identify the erratic measurements especially in the first two tests, since those measurements have very low cross correlation coefficients compared to the correct measurements.

The cross correlation of two discrete-time signals is a measure of similarity between these two signals. The formal definition of cross correlation between two discrete-time signals $x(n), y(n)$ is shown in Eq. 5.1 where ρ_{xy} is the cross correlation coefficient between $x(n)$ and $y(n)$, μ_x, μ_y are the mean values of $x(n)$ and $y(n)$ and σ_x, σ_y are the standard deviations of $x(n)$ and $y(n)$[47].

$$\rho_{xy} = \frac{\lim_{N\to\infty} \frac{1}{2N+1} \sum_{n=-N}^{N} (x(n) - \mu_x)(y(n) - \mu_y)}{\sqrt{\sigma_x^2 \sigma_y^2}} \tag{5.1}$$

In this section the cross correlation coefficients of the strain gauges are calculated using the 'corrcoef' function in Matlab and listed in table format in Table 5.2 to Table 5.13. In these tables the cross correlation between any two strain gauges is listed only once in order to save space using the symmetric property of the cross correlation coefficient. Also the cross correlation of any gauge with itself is not listed since this coefficient is known to be always equal to 1. In the cross correlation matrices only coefficients greater than or equal to 0.9 are listed as an indication of a good correlation between any two strain gauges. As mentioned earlier, in the first two tests a great number of strain gauges could not capture the strain development for the entire test because of the large strain values observed in these tests. Also, the failure of different strain gauges occured at different stages of the experiments which prevents a cross correlation analysis using all of the measured strain values. In order to compensate for this condition, the strain gauge cross correlation analysis of the first two experiments is carried out using the strain measurements up to the first strain gauge failure during the test.

In Table 5.2 to Table 5.13 each strain gauge is denoted with a number. In order to clarify to which part of the pipe these numbers belong, for each experiment a separate strain gauge map is drawn (Figures 5.2, 5.3, 5.11, 5.12, 5.17, 5.18, 5.24, 5.25, 5.31, 5.32). For the locations of the strain gauges in tests 5 to 8 one drawing was sufficient since in all of the last four tests the same strain gauge configuration was used.

5.2.1 Analysis of the Strain Measurements for the First Full Scale Experiment

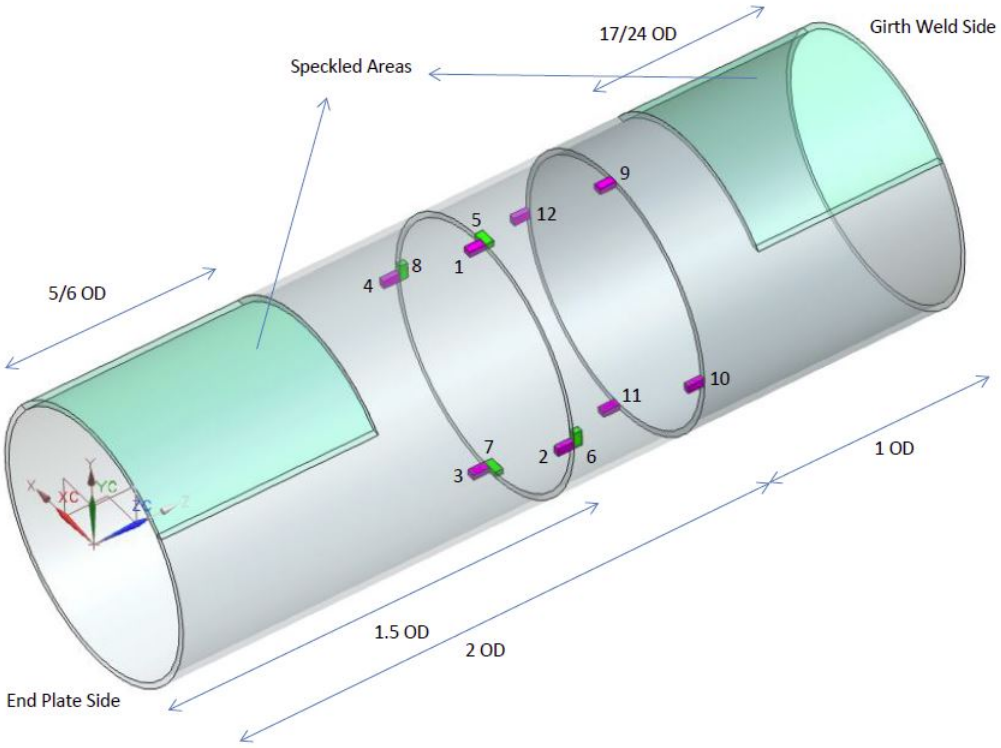

Figure 5.2: Bottom side of the pipe in the first test

The position of each strain gauge number in Tables 5.2 and 5.3 is shown in Figures 5.2 and 5.3. Figure 5.2 shows only the strain gauge positions at the bottom part of the specimen whereas Figure 5.3 shows only the positions

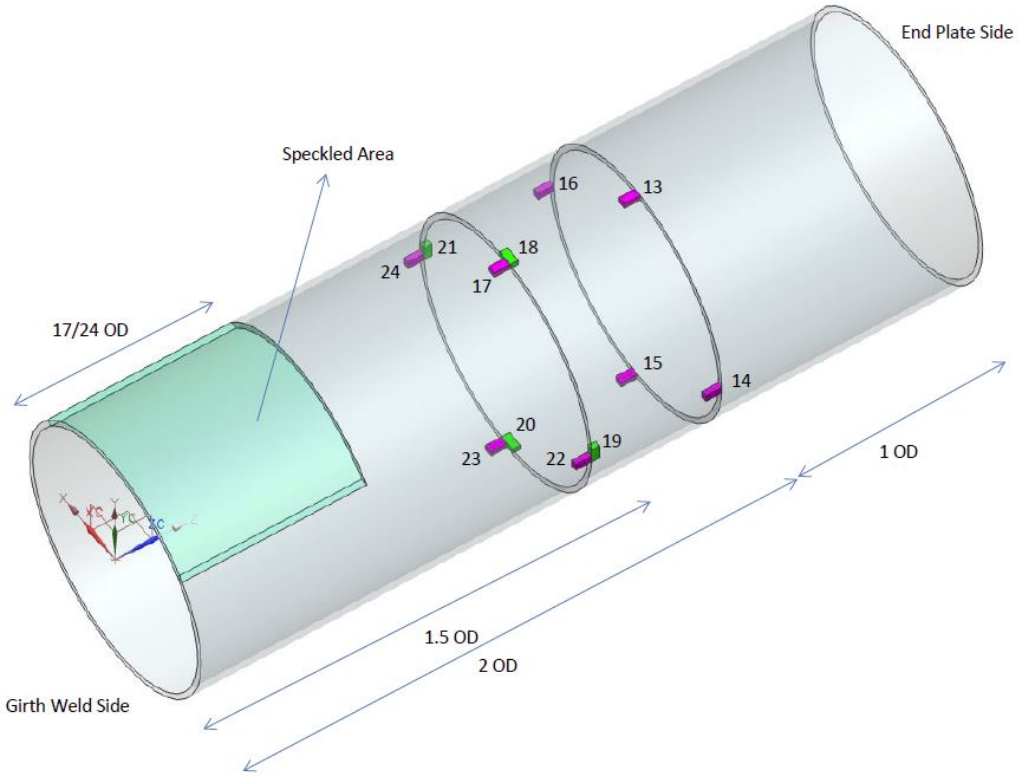

Figure 5.3: Top side of the pipe in the first test

of the strain gauges at the top part of the specimen. In Figure 5.2 and Figure 5.3 the locations of the longitudinal and hoop direction strain gauges are marked with purple and green colours respectively. The main difference in the locations of the strain gauges between the top and bottom parts of the specimen is that in the bottom part there is a ring of strain gauges 1 OD away from the girth weld flaw whereas in the top part there is a ring of strain gauges 1 OD away from the top end plate (The term 'ring' is used in order to facilitate the explanation referring to any group of strain gauges having equal distance from an end plate). The reason for this is the difference between the positions of the speckled areas at the top and bottom parts in the first two experiments. On the top side of the girth weld the only speckled area was

adjacent to the girth weld due to the height limitation of the camera system in the first two tests. The longitudinal strain values on the top part of the specimen close to the top end plate, which is the remote strain area at the top side of the girth weld, are measured using the ring of strain gauges 1 OD away from the top end plate (gauges number 13, 14, 15 and 16 in Figure 5.3). On the other hand the remote strain at the bottom side of the girth weld is measured using digital image correlation in the first two experiments.

Table 5.2: Cross correlation of strain gauge measurements from Test 1

Gauge no	8	9	10	11	12	14	16
2		0.92					
3				0.99			
4			0.93		0.99	0.99	0.99
6	0.96						
7							
8							
9			0.92				
10					0.9	0.93	0.96
11					0.91		
12						0.99	0.97
13							0.99
14							0.99

From Table 5.2 and Table 5.3 it is clear that the strain gauges 4, 10, 12, 16, 22, 24 have good correlation with at least six other strain gauges whereas the strain gauges 1, 5, 15, 18, 21 have no correlation with any of the strain gauges in test 1. The measurements of these two groups of strain gauges are plotted separately in Figure 5.7 and Figure 5.8. The results of the cross correlation analysis combined with the strain variations in Figure 5.7 and Figure 5.8 clearly show that, the strain gauges having no correlation with any other strain gauge are also observed to have erratic behaviour. This condition justifies the usage of the cross correlation coefficients in the detection

Table 5.3: Cross correlation of strain gauge measurements from Test 1

Gauge no	17	19	20	22	23	24
2						
3					0.99	
4				0.98		0.99
6		0.97				
7			0.91			
8		0.95				
9				0.9		
10				0.98		0.94
11					0.99	
12				0.96	0.9	0.99
13	0.97				0.96	0.9
14				0.98		0.99
16				0.99		0.99
22						0.99

of the strain gauge data which should not be used in order to make a judgement about the structural response of the specimen. The unexpected strain variations of the gauges in Figure 5.8 indicate a higher likelihood of unreliable measurements for gauges having lower cross correlation coefficients. In addition to the strain gauge measurements plotted in Figure 5.7 and Figure 5.8, the gauges number 9, 13 and 16 measured high strain values. The strain development measured by these gauges is plotted in Figure 5.9. According to Figure 5.9, the axial direction strain gauge at the top side of the first specimen 1 OD away from the top end plate and aligned with the flaw, measured the highest strain values in this experiment (3.41%) before it failed due to large displacements.

In order to visualize the variation of the axial strain along the length of the pipe surface, a combination of the digital image correlation measurements and the strain gauge measurements is used in the first two tests. This was necessary for the first two experiments since at least three strain values are

needed in order to capture the non-linearity of the strain variation along the pipe length. However, the strain gauges as well as the digital image correlation method can measure the strain at only two different locations on each side of the girth weld along the specimen length in the first two experiments. In order to eliminate this deficiency, the strain measurements of the digital image correlation at the remote strain zone (Figure 5.4) and at the vicinity of the girth weld (Figure 5.5) are combined with the strain measurement of either the axial direction strain gauge at the mid-length of the bottom side of the specimen or the axial strain gauge 2 OD away from the bottom end plate. Using this combination the development of the strain along one side of the girth weld, referred to as 'strain profile' in the rest of this text, is plotted at different stages of the first and second experiment.

The strain fields in Figure 5.4 and Figure 5.5 are shown in terms of the Lagrangian strain. The Lagrangian strain tensor ε is defined as in Eq. 5.2 where $\mathbf{F}$ is the deformation gradient and $\mathbf{I}$ is the identity tensor[48].

$$\varepsilon = \frac{1}{2}(\mathbf{F}^T\mathbf{F} - \mathbf{I}) \tag{5.2}$$

The deformation gradient $\mathbf{F}$ can be expressed in terms of the displacement vector $\mathbf{u}$ as in Eq. 5.3 where $\mathbf{X}$ denotes the initial position of a material point and $\mathbf{x}$ denotes the position of a material point after deformation.

$$\begin{aligned} \mathbf{u} &= \mathbf{x} - \mathbf{X} \\ \mathbf{F} &= \nabla_{\mathbf{X}}\mathbf{u} + \mathbf{I} \end{aligned} \tag{5.3}$$

Inserting the expression for $\mathbf{F}$ in Eq. 5.3 into Eq. 5.2 yields the expression in

Eq. 5.4 for the Lagrangian strain tensor.

$$\varepsilon = \frac{1}{2}\Big((\nabla \mathbf{u})^T \nabla \mathbf{u} + (\nabla \mathbf{u})^T + \nabla \mathbf{u}\Big) \tag{5.4}$$

In the process of the digital image correlation, the pictures of the speckled side of the pipe are taken with certain time intervals. The usage of the Lagrangian strain in the visualizations of the strain field indicates that at each one of these time instances the strain field is computed with respect to the initial undeformed configuration of the speckles on the pipe wall.

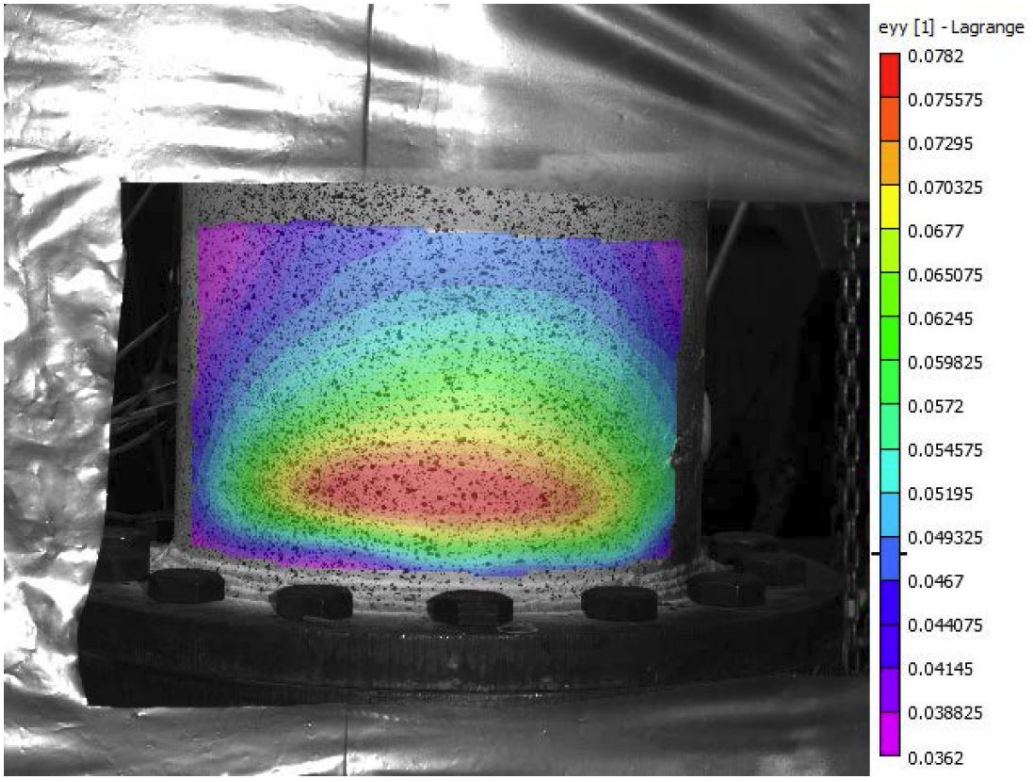

Figure 5.4: Digital image correlation showing the critical strain distribution close to the bottom end plate (Test 1)

In the first test, the strain gauge 1.5 OD away from the bottom end plate is the gauge number 1 (Figure 5.2) which is assumed to be unreliable according

to the cross correlation analysis. Therefore for the middle strain value of the bottom side of the first specimen, the strain gauge 2 OD away from the bottom end plate is used. This strain gauge has the number 9 in Figure 5.2. However the measurements from gauge number 9 have a sudden drop towards the end of the test from 1.6 % to 1 %. This sudden strain drop indicates the possibility of debonding of the gauge number 9 towards the end of the test. Therefore the measurements of gauge number 9 are deemed unreliable at the late stages of the test. In order to obtain the critical strain profile that occurs immediately before the pipe rupture, an extrapolated strain value is adopted instead of the strain measurement of gauge number 9. The extrapolated value is calculated based on the ratio between the strain gauge measurement and the image correlation strains in the earlier stages of the test. Table 5.4 and Table 5.5 demonstrate the steps of calculating the extrapolated strain value for the frames 1300 and 1382. In Table 5.4 the extrapolated strain values at the gauge 9 location are coloured in red. The frames in Table 5.4 and Table 5.5 correspond to time instances when the DIC system captured the state of the strain distribution. The frame 1382 is the closest time instance to the rupture of the flaw in the first experiment among a total of 1457 measurement instances. During experiments, all data is recorded every 10 seconds and each frame represents one sample of recordings. In Table 5.4 and Table 5.5 'remote strain measurement' denotes the strain measured by the image correlation method close to the bottom end plate. From Figure 5.4 it is clear that adjacent to the end plate there is a strain concentration. This condition is caused by the constraints put on the pipe by the end plate and does not correspond to the usual operating conditions of the pipe. Therefore for the remote strain measurements, the longitudinal strain value farthest away from the end plate is chosen in Figure 5.4 in order to minimize the

effect of the end plate on the strain profile. The location of the girth weld side strain measurements in Table 5.4 is the uniform strain zone closest to the surface defect in Figure 5.5.

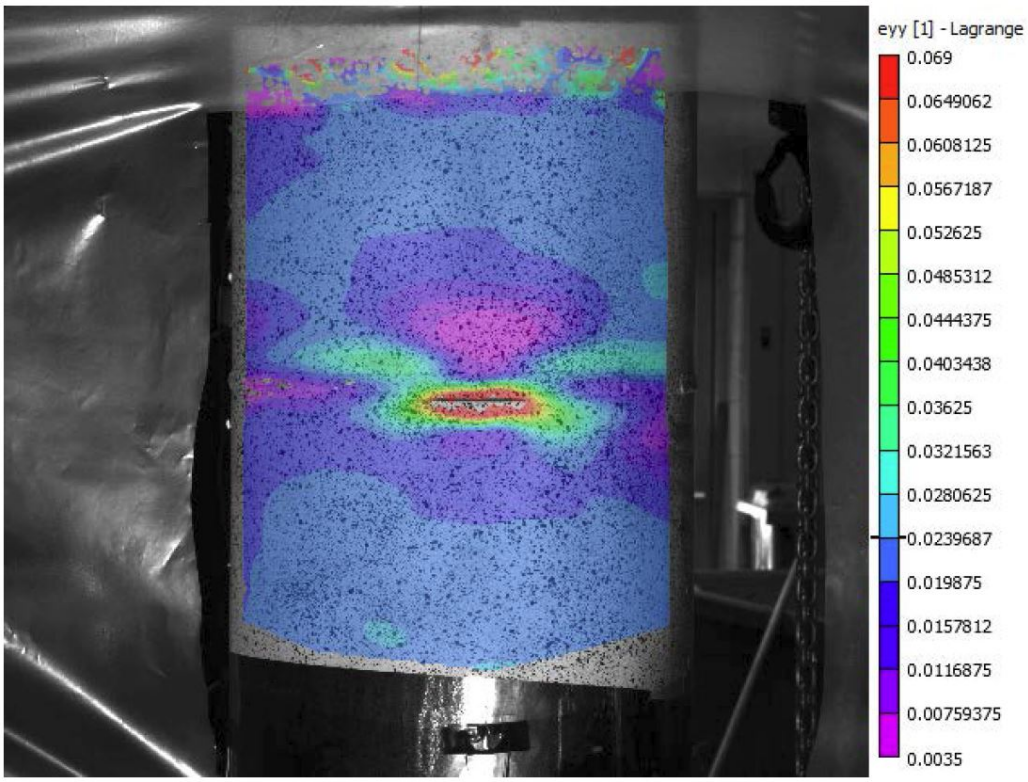

Figure 5.5: Digital image correlation showing the critical strain distribution close to the heat affected zone (Test 1)

Table 5.4: Development of the strain profile in Test 1

Frame	**Remote strain measurement**	**Gauge 9 reading**	**Girth weld side strain measurement (%)**
600	0.0477	0.03115	0.03566
800	0.2496	0.22352	0.2265
1000	0.6781	0.68817	0.6731
1200	2.099	1.31304	1.44583
1300	3.4	1.97407	1.86875
1382	4.8013	2.72061	2.39687

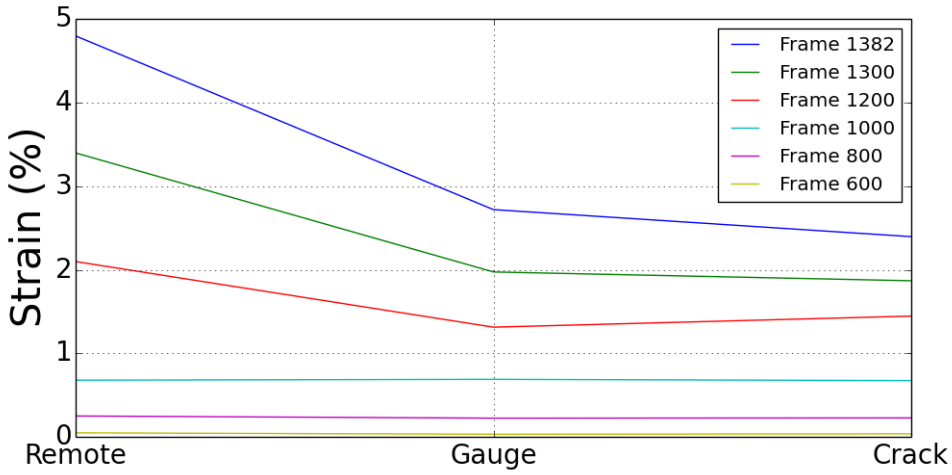

Figure 5.6: Development of the strain profile in the first full scale test

Table 5.5: The ratio between the strain gauge measurement and the image correlation strains

Frame	Remote strain increase(%)	Ratio (left/right)	Gauge 9 reading increase	Ratio (left/right)	crack side strain increase (%)
800	0.2019	1.04954	0.19237	1.008017	0.19084
1000	0.4285	0.922199	0.46465	1.040417	0.4466
1200	1.4209	2.273938	0.62486	0.808644	0.77273
1300	1.301	NA	NA	NA	0.42292
1382	1.40125	NA	NA	NA	0.52812
	Average	**1.415226**		**0.952359**	

In Table 5.5 the columns denoted with 'ratio (left/right)' show the ratios between the increases in the image correlation strains and the increases in the gauge 9 readings. Since the gauge 9 readings are assumed to be unreliable for frames 1300 and 1382, they are not included in Table 5.5. The gauge 9 readings in Table 5.4 for the frames 1300 and 1382 are calculated using the average value of the strain increases calculated using the strain increase ratios in the last row of Table 5.5. Eq. 5.5 and Eq. 5.6 demonstrate this calculation for frame 1300:

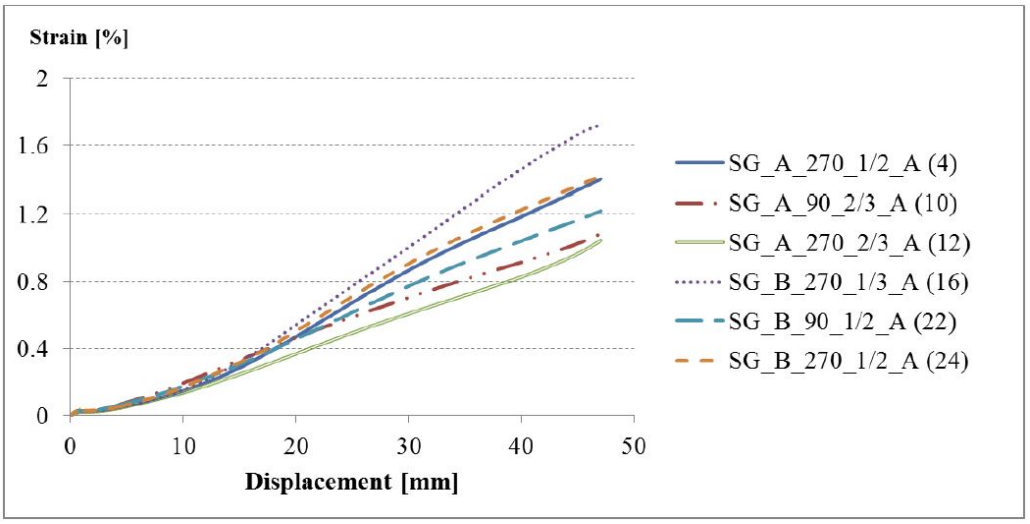

Figure 5.7: Measurements of the strain gauges with good correlation (Test 1)

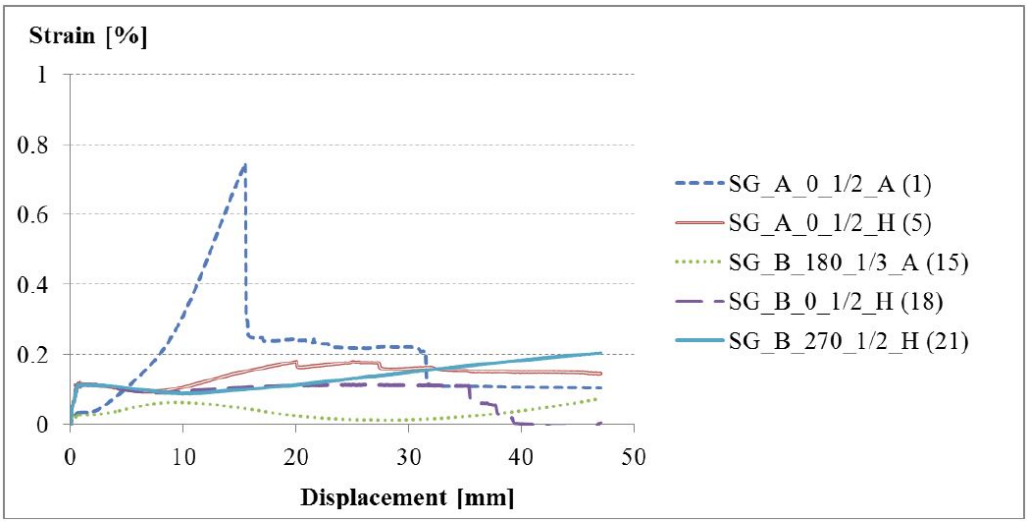

Figure 5.8: Measurements of the strain gauges with no correlation (Test 1)

$$\Delta\varepsilon_{gauge9,frame1300} = \frac{1}{2}\left(\frac{1.301}{1.415226} + 0.42292 \cdot 0.952359\right) = 0.66103 \qquad (5.5)$$

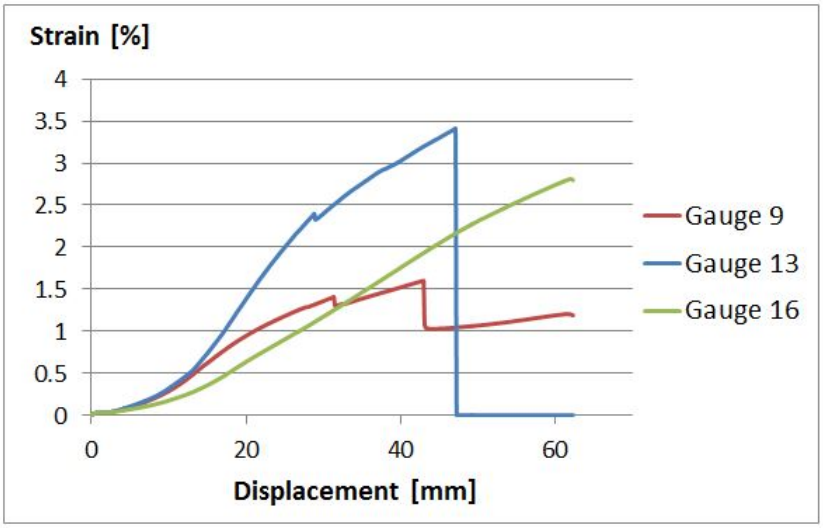

Figure 5.9: Highest axial strain gauge measurements in Test 1

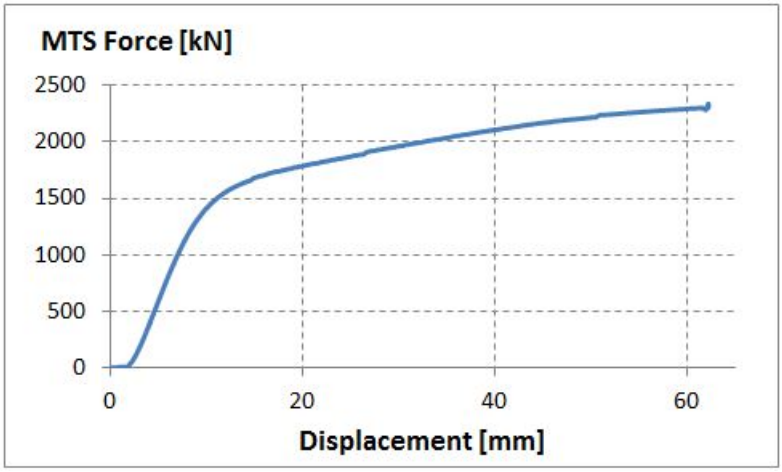

Figure 5.10: Load-displacement response of the first test

$$\varepsilon_{gauge9,frame1300} = 1.31304 + 0.66103 = 1.97407 \tag{5.6}$$

In Figure 5.6, the strain profiles at different stages of the first test are demonstrated using different colours. The labels 'remote', 'gauge', 'crack' for the horizontal axis of Figure 5.6 denote the locations of the 'remote strain measurement', 'gauge 9' and 'girth weld side strain measurement' respec-

tively. Since adjacent to the top end plate no image correlation was applied, the strain profiles are only generated for the bottom part of the first specimen. From Figure 5.6 and Figure 5.4 it can be clearly observed that towards the end of the first test in the vicinity of the bottom end plate significantly large strains are present. These large strain values are mainly due to the constraints applied by the end plate and do not reflect the actual strain capacity of the pipe. In order to have a conservative estimate of the tensile strain capacity in the first experiment, the smallest strain value in Frame 1382 of Figure 5.6 is assigned as the tensile strain capacity according to DIC (2.4%).

5.2.2 Analysis of the Strain Measurements for the Second Full Scale Experiment

According to Table 5.6 and Table 5.7, in test 2 all strain gauges are highly correlated to at least two other strain gauges. Gauges number 2, 4, 6, 7, 9, 10, 11, 13, 14, 15, 17 are correlated to at least 6 other strain gauges. The gauges 8 and 12 are only correlated to each other and gauge 16. Although the gauges 8, 12 and 16 are not correlated to a large number of the rest of the gauges, Figure 5.11 and Figure 5.12 show that all of these three gauges are longitudinal gauges 180° away from the surface defect. Since this part of the specimen experiences relatively low levels of strain during the test, these strain gauges are expected to measure strains uncorrelated with the rest of the gauges. Therefore it is assumed that the measurements of gauges 8, 12, 16 are reliable in the second test.

Figure 5.13 shows the strain measurements of the gauges number 8, 12 and 16 up to the point of gauge failure. It is clear that despite being on the opposite side of the pipe relative to the flaw, these gauges have measured tensile strain values above 2.5%. However it should be noted that in the

Table 5.6: Cross correlation of strain gauge measurements from Test 2

Gauge no	2	3	4	5	7	9	10	11
1	0.91		0.91	0.93				
2		0.95	0.99	0.99				
3			0.95	0.91				
4				0.99				
5								
6					0.99	0.99	0.99	0.99
7						0.99	0.99	0.99
8								
9							0.99	0.99
10								0.99

Table 5.7: Cross correlation of strain gauge measurements from Test 2

Gauge no	12	13	14	15	16	17	18	19
1							0.94	
2							0.99	0.9
3								0.99
4							0.99	0.9
5							0.99	
6		0.99	0.99	0.99		0.99		
7		0.99	0.99	0.99		0.99		
8	0.96				0.96			
9		0.99	0.99	0.99		0.99		
10		0.99	0.99	0.99		0.99		
11		0.99	0.99	0.99		0.99		
12					0.99			
13			0.99	0.99	0.91	0.99		
14				0.99		0.99		
15						0.99		
16						0.91		

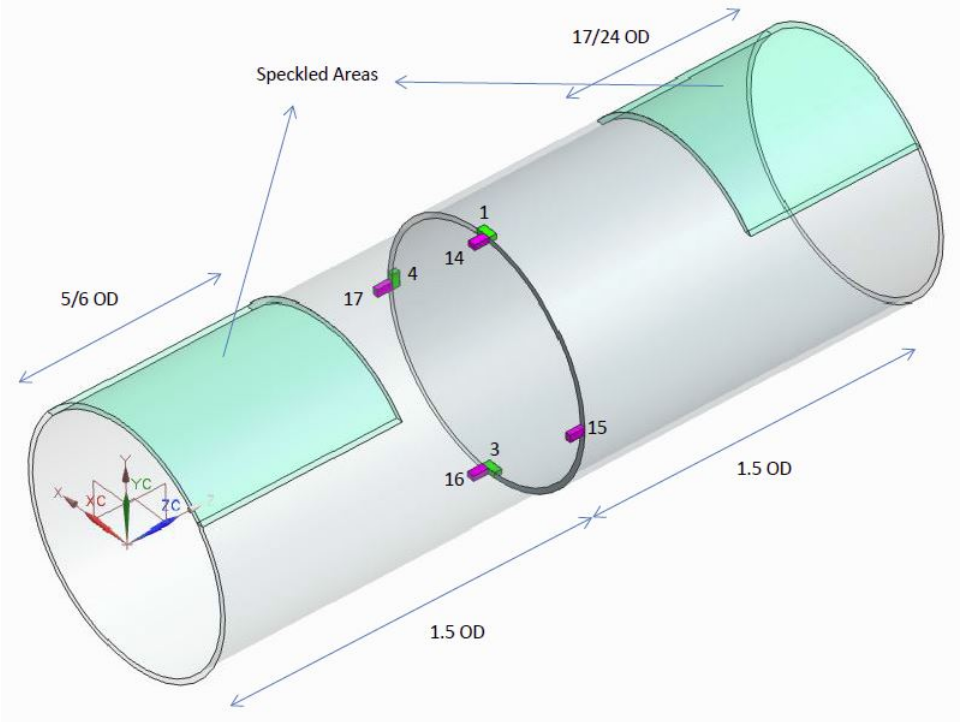

Figure 5.11: Bottom side of the pipe in the second test

second experiment the highest strain values are observed among all experiments. A comparison with the strains measured by the gauges at the tension side reveals that the measurements of the compression side gauges are still relatively low. A comparison of gauges number 12 and 16 shows that at the bottom side of the specimen larger strain values are measured at the compression side, since both of these gauges are 1.5 OD away from end plates. A comparison of gauge number 12 and 8 shows that the strain values are decreasing towards end plates at the compression side of the pipe.

Table 5.6 and Table 5.7 show that all of the three strain gauges measuring the axial tensile strain at the tension side of the second specimen (gauges number 6, 10 and 14), have good correlation with each other. However due to the large displacements in the second experiment, all of these gauges failed

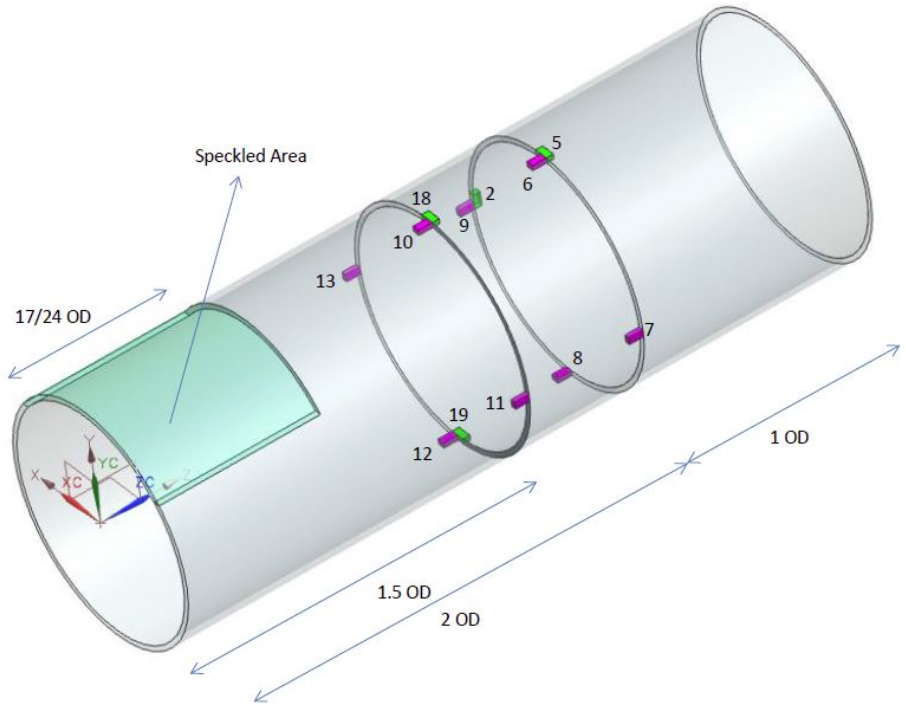

Figure 5.12: Top side of the pipe in the second test

before the pipe reached its rupture state. Figure 5.14 shows the measurements of the strain gauges aligned with the flaw in the second experiment. Clearly, none of the strain gauges could capture the strain values beyond 3.7%. Considering that the failure strain values of all gauges were close to each other, it can be reckoned that the location of the gauge number 6 which is 1 OD away from the top end plate, experienced the highest strain values in the second experiment followed by the gauges number 14 and 10.

In the second test, gauge 14 is aligned with the mid-line of the surface defect on the tension side of the specimen 1.5 OD away from the bottom end plate. According to Table 5.6 and Table 5.7, gauge 14 is highly correlated with 8 other strain gauges. Therefore the measurements from gauge number 14 are assumed to be reliable and this strain gauge is used for the

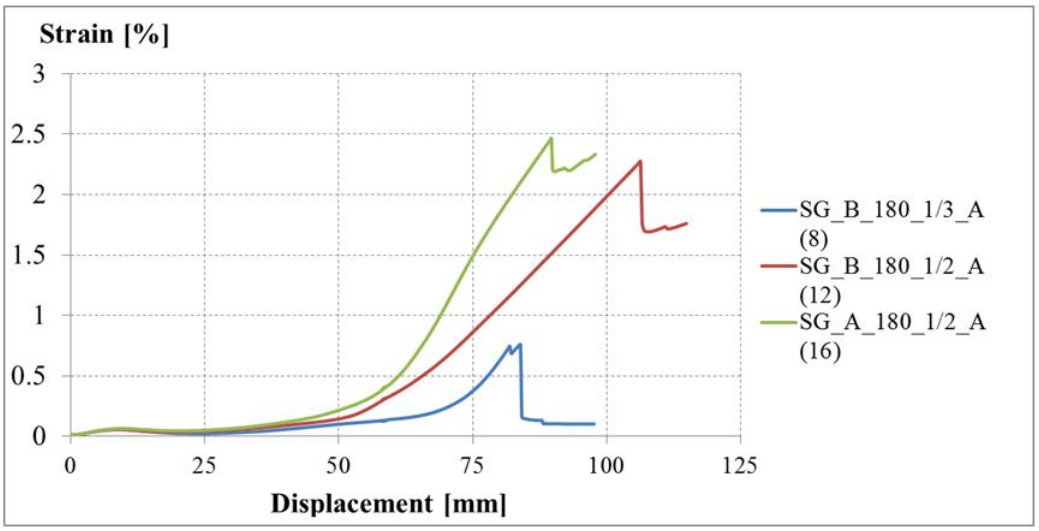

Figure 5.13: Strain measurements of the gauges 180° away from the flaw in Test 2

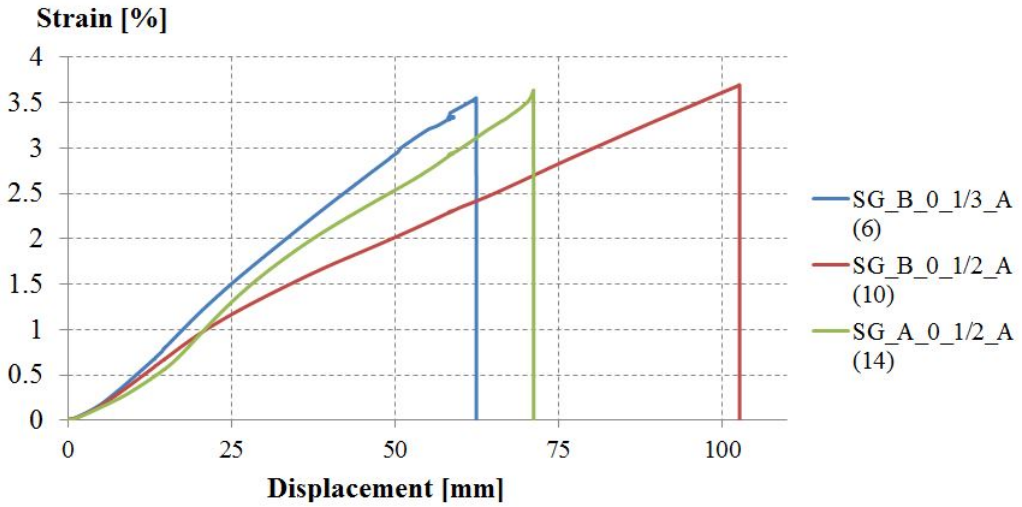

Figure 5.14: Strain measurements of the gauges aligned with the flaw in Test 2

strain profiles of the second test. However for this strain gauge erroneous measurements were observed starting from frame 1592. Similar to the first experiment, the strain profiles of the second experiment at different stages of the test are created using a combination of DIC measurements at both

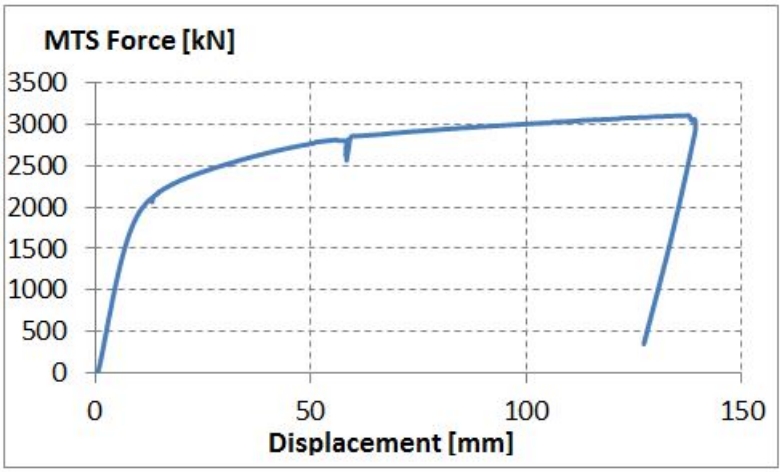

Figure 5.15: Load-displacement response of the second test

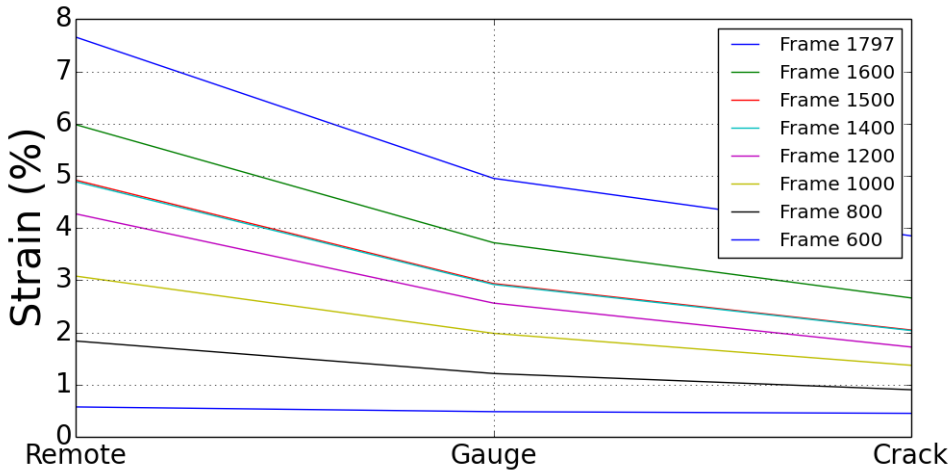

Figure 5.16: Development of the strain profile in the second full scale test

sides of the bottom side of the girth weld and the measurements of a strain gauge at the mid-length of the bottom side of the girth weld (gauge number 14). Since the measurements of the gauge number 14 are observed to be erroneous towards the end of the test, the gauge strain values of the strain profiles for frame 1600 and frame 1797 in Figure 5.16 are extrapolated values calculated using the same method as in test 1. In test 2 a total of 1818 data frames are recorded with 10s intervals and the data frame closest to the pipe

rupture is frame number 1797. Similar to Test 1, significantly large strains are measured by the DIC at the end plate side of the specimen which can not be representative for the overall strain capacity of the pipe. According to Figure 5.16 the minimum strain observed in Frame 1797 is 3.8%. This strain value is assigned as an acceptable conservative estimation of the strain capacity in the second experiment based on the DIC.

5.2.3 Analysis of the Strain Measurements for the Third Full Scale Experiment

In the third full scale test a total of twelve strain gauges are installed. At the mid-length of the bottom part of the girth weld, aligned with the flaw, two axial direction strain gauges are installed for the sake of having redundancy in the number of strain gauges, since larger strains are expected at this location. The strain gauge configurations for the bottom and top parts of the specimen are given in Figure 5.17 and Figure 5.18 respectively for the third test. Also, the cross correlation coefficients of the strain gauges are listed in Table 5.8. In all images showing the strain gauge configurations of test 3 to test 8, the parts of the pipe painted for DIC are coloured in green.

Table 5.8: Cross correlation of strain gauge measurements from Test 3

Gauge no	2	4	5	6	7	8	9	10	11
1	0.94			0.98					
2				0.96		0.99			
3		0.99	0.99		0.99		0.99	0.99	0.99
4			0.99		0.99		0.99	0.99	0.99
5					0.99		0.99	0.99	0.99
6						0.9			
7							0.99	0.99	0.99
9								0.99	0.99
10									0.99

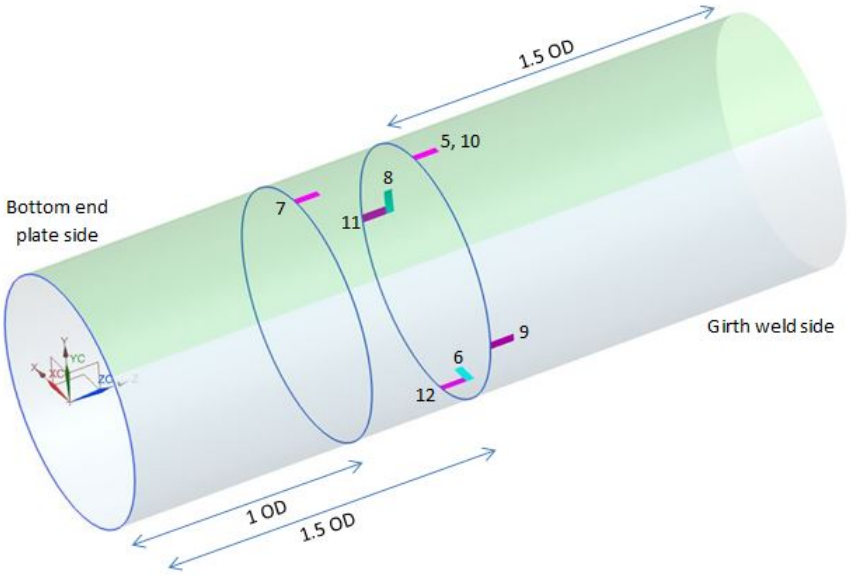

Figure 5.17: Bottom side of the pipe in the third test

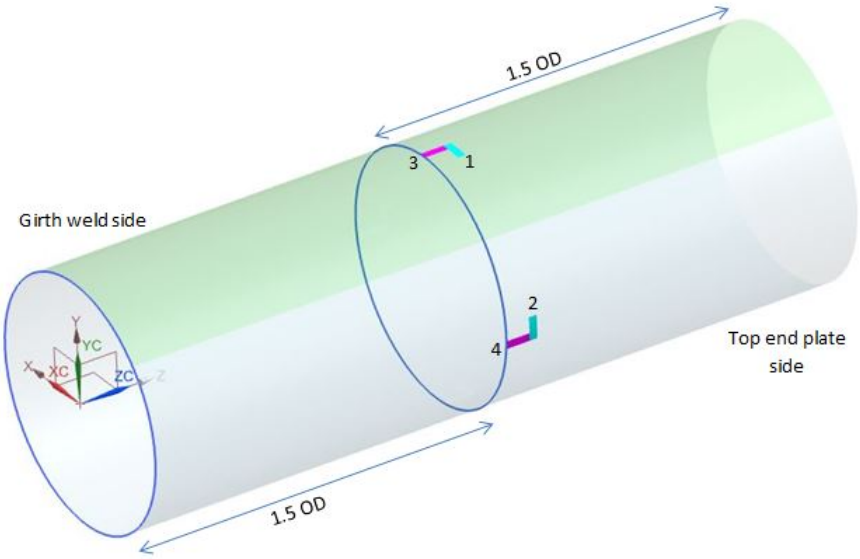

Figure 5.18: Top side of the pipe in the third test

From Table 5.8 it can be reckoned that the strain gauges number 1, 2 and 6 have a good correlation with each other. Figure 5.17 and Figure 5.18 show that, all of these three gauges are measuring the hoop direction strain.

Furthermore, the gauges 1 and 2 are measuring the hoop direction strain at the mid-length of the top side of the girth weld and gauge number 6 is measuring the hoop direction strain at the mid-length of the bottom side of the girth weld. In addition to that, there is a high correlation between the gauge number 2 and gauge number 8 which is a hoop direction strain gauge 90 degrees away from the girth weld at the bottom side of the specimen.

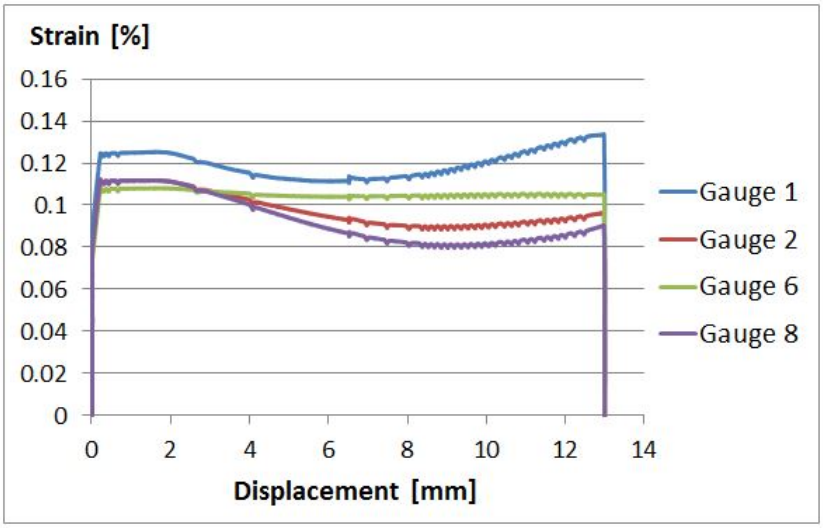

Figure 5.19: Hoop strain measurements in Test 3

The strain measurements of the gauges 1, 2, 6 and 8 are plotted against the applied displacement in Figure 5.19. From Figure 5.19 it is clear that the biggest part of the hoop strain is measured by these gauges in the beginning of the experiment where the internal pressure is increased from zero to 1.7 ksi (80 % SMYS hoop stress). The hoop strain at the compression side of the specimen, measured by the gauge number 6, has not changed for the entire test. At the point of 2 mm displacement, the measured values of the gauges 1,2 and 8 slightly dropped. Figure 5.20 shows that this is the point where the tensile force starts being applied on the specimen. The constant value of the gauge number 6 indicates that at the mid-length of the compression

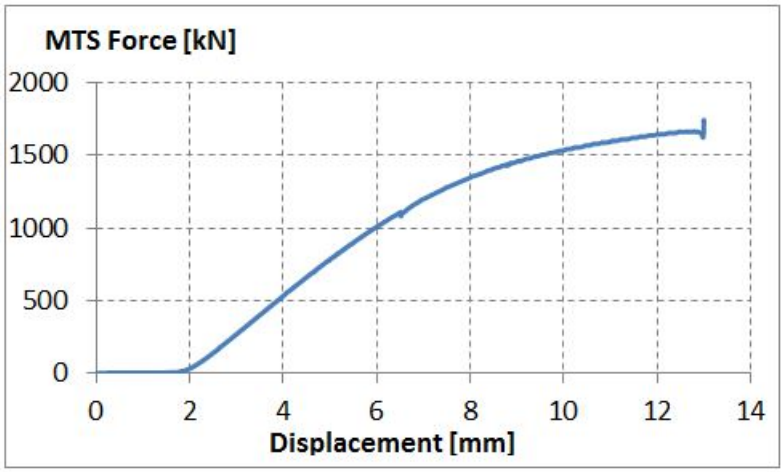

Figure 5.20: Load-displacement response of the third test

side of the specimen at the bottom side of the girth weld, the effect of the compression due to the eccentricity and the tendency of the pipe diameter to decrease due to tension balanced out. On the other hand the increase of the strain measurements of the gauges 1, 2 and 8 towards the end of the test implies that increasing the rotation of the top end plate caused a tendency in the pipe diameter to expand.

Further analysis of the cross correlation coefficients in Table 5.8 shows that, all of the axial direction strain gauges have good correlation with each other except gauge number 12 which is the only axial direction strain gauge at the compression side of the pipe 180° away from the flaw. Figure 5.21 shows the variation of all axial strain gauge measurements with respect to the applied displacement.

From Figure 5.21 the axial strain gauge measurements of the third test can be categorized in three groups. The first group consists of the gauges number 3, 5, 7 and 10. All of these gauges are aligned with the flaw. It can be observed that gauges number 5 and 7 measured almost equal strain values throughout the test with the measurement of gauge number 5 slightly

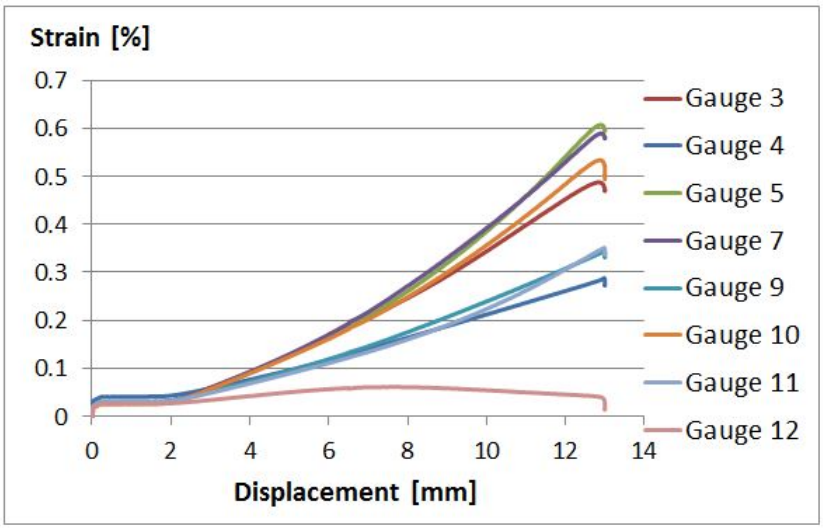

Figure 5.21: Axial strain measurements in Test 3

exceeding that of gauge 7 at the end of the experiment. The gauge number 3 which is the only top side gauge in the first group, measured the lowest strain values among this group. The second strain gauge group consists of gauges number 4, 9 and 11 where gauges number 9 and 11 measured almost equal strain values. Figure 5.17 and Figure 5.18 show that all three of these gauges are 90° away from the flaw. As expected, the strain gauges in this group measured lower strain values compared to the gauges in the first group. Finally, the last group of gauges consists only of gauge number 12 which is the only axial strain gauge 180° away from the flaw confirming the result of the cross correlation analysis. As expected this strain gauge measured the lowest strain values among all strain gauges.

Starting from Test 3, the pipe wall is completely painted and speckled where it is facing the DIC system. As a result for Test 3 to Test 8 it was possible to calculate the strain profiles using only the DIC measurements. Figure 5.23 shows the strain profiles at three different stages of the experiment corresponding to 599 kN, 1203 kN and 1647 kN axial tensile force where

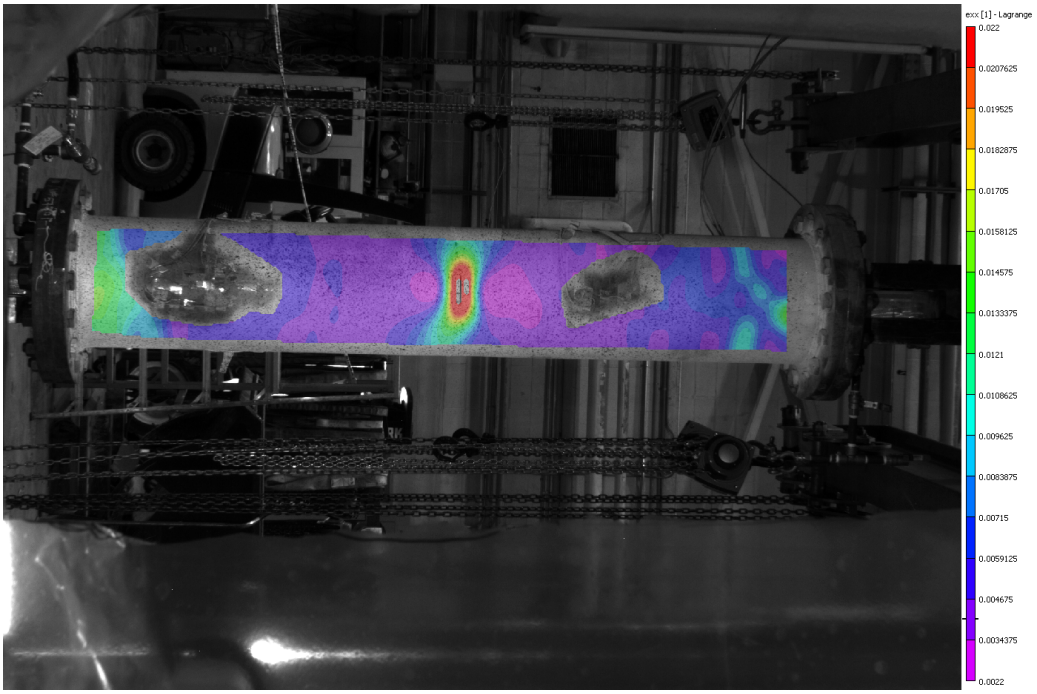

Figure 5.22: Axial strain field prior to rupture in Test 3

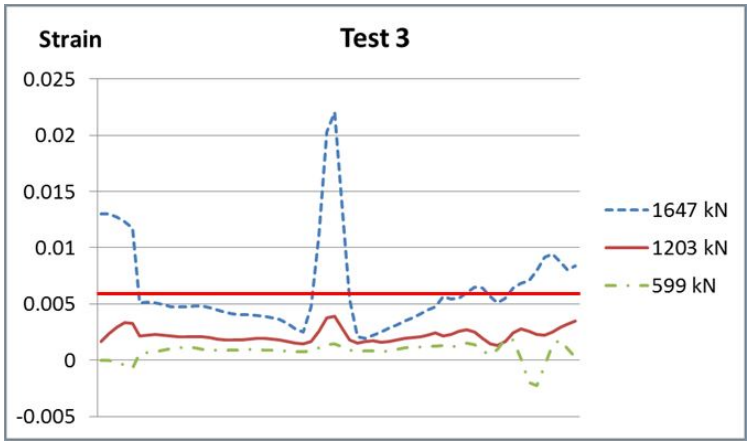

Figure 5.23: Development of the strain profile in the third full scale test

1647 kN corresponds to the maximum tensile force prior to the pipe rupture (Figure 5.20). In Figure 5.23 the horizontal axis represents the axial length of the pipe such that the starting point of each curve in Figure 5.23 shows the axial strain at the bottom end plate and the ending point shows the ax-

ial strain at the top end plate. In the middle part of each curve there is an abrupt increase in strain which does not correspond to the actual strain value since this middle part is at the location where the flaw is. As a result this middle part is not painted or speckled in a way suitable for DIC calculations. Therefore the large strains in the middle of each curve are interpolated values. Figure 5.22 shows the distribution of the axial strain on the pipe wall at the point where the axial tensile force reaches its peak value. The horizontal red line in Figure 5.23 shows the average value of strain along the pipe length at the point of peak tensile force. The interpolated large strain values at the mid-length of the pipe are not included in this average value. For Test 3 the average DIC strain at the point prior to rupture is 0.6%

5.2.4 Analysis of the Strain Measurements for the Fourth Full Scale Experiment

The configuration of the strain gauges in the fourth experiment is similar to the configuration in the third experiment with some reduction in the number of the strain gauges. In this test the hoop direction strain gauge at the top side 90° away from the flaw is omitted. In the fourth experiment a total of eleven strain gauges are used. Similar to the third experiment, aligned with the flaw and at the mid-length of the bottom half of the specimen, two longitudinal strain gauges are installed. Both of these strain gauges are shown as a single strain gauge in Figure 5.24.

The cross correlation analysis of the strain gauges in test 4 shows that, the gauges number 1 and 7 have a good correlation with each other. Gauge number 1 has no correlation with the rest of the strain gauges whereas gauges number 7 and 5 have a good correlation. Figure 5.24 and Figure 5.25 show that all three of these strain gauges are hoop direction strain gauges and

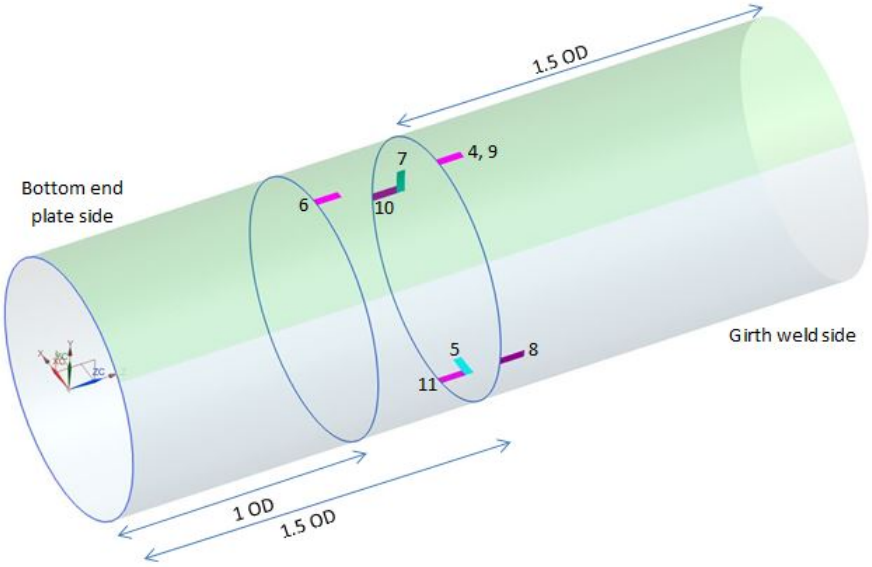

Figure 5.24: Bottom side of the pipe in the fourth test

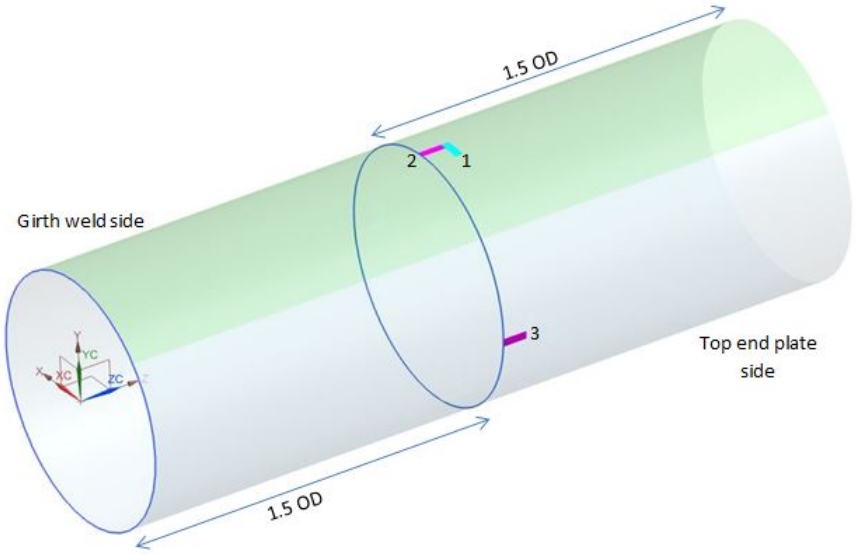

Figure 5.25: Top side of the pipe in the fourth test

Table 5.9 shows that none of the axial direction strain gauges has a good correlation with any of the hoop direction strain gauges.

The variation of the hoop strain measurements in the fourth test with

Table 5.9: Cross correlation of strain gauge measurements from Test 4

Gauge no	3	4	6	7	8	9	10
1				0.98			
2	0.99	0.99	0.99		0.99	0.99	0.99
3		0.99	0.99		0.99	0.99	0.99
4			0.99		0.99	0.99	0.99
5				0.91			
6					0.99	0.99	0.99
8						0.99	0.99
9							0.99

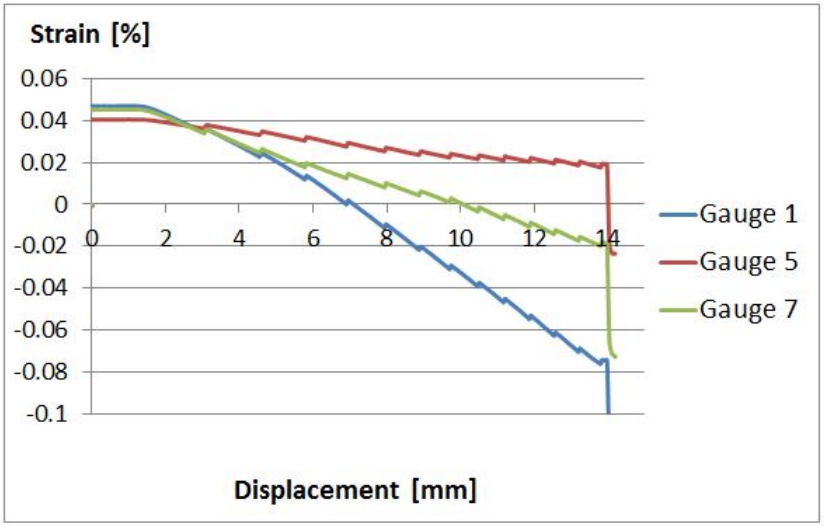

Figure 5.26: Hoop strain measurements in Test 4

respect to the applied displacement is plotted in Figure 5.26. A comparison between Figure 5.26 and Figure 5.19 clearly shows the effect of decreasing the internal pressure from 80 % SMYS (Test 3) to 30% SMYS (Test 4). Similar to Test 3, the application of the internal pressure expands the pipe diameter in the elastic range up to the point of 1.5 mm displacement which is the point where the tensile force starts being applied on the pipe as shown in Figure 5.27. Decreasing the internal pressure from 1.7 ksi (11.72 MPa) (Test 3) to 0.7 ksi (4.83 MPa) (Test 4) results in a reduction of the maximum hoop

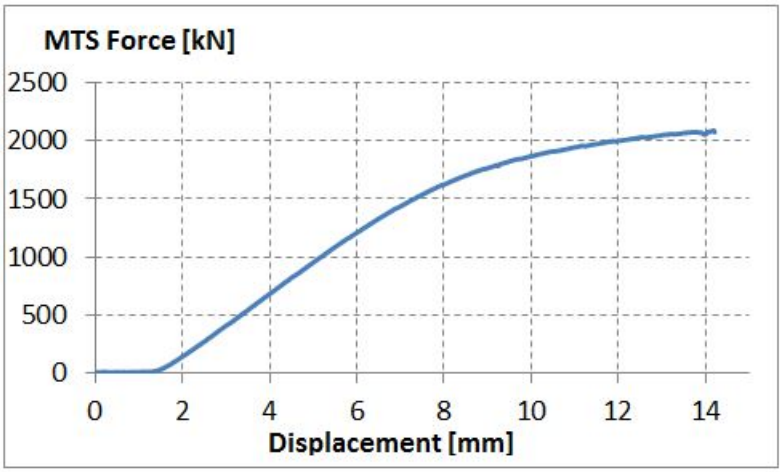

Figure 5.27: Load-displacement response of the fourth test

direction tensile strain from 0.125% (Figure 5.19) to 0.045% (Figure 5.26). Moreover, it can be observed that in Test 4, the effect of the tensile force on the hoop strain exceeds the effect of the internal pressure at some parts of the pipe, such that starting from an applied displacement of 7 mm, the gauge number 1 starts measuring compressive strains. Also, at 10 mm displacement gauge number 7 starts measuring compressive strains and gauge number 5 measures tensile strains throughout the test. This shows that the effect of the tensile force is greatest at the position of the gauge number 1 as expected, since this gauge is aligned with the flaw and experiences the maximum amount of axial tensile force among all hoop direction strain gauges. On the other hand, at the compression side of the pipe, where gauge number 5 is located, the axial tensile force is not sufficient to balance out the effect of the internal pressure on the hoop strain.

Further analysis of Table 5.9 shows that all of the axial direction strain gauges have good correlation with each other. The variation of the strain values measured by the axial direection strain gauges in the fourth test is plotted in Figure 5.28.

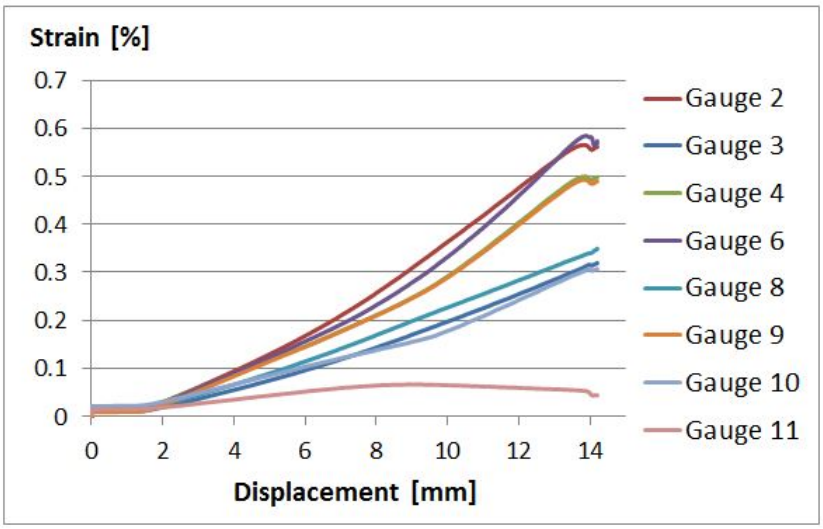

Figure 5.28: Axial strain measurements in Test 4

According to Figure 5.28 the axial strain measurements can be classified in three groups. The first of these groups consists of the gauges 2, 4, 6 and 9. The highest strain values are measured by this group of gauges (0.57%). All of the gauges in the first group are aligned with the flaw. The second group consists of gauges number 3, 8 and 10. All of the second group gauges are 90° away from the flaw. As expected the gauges in this group measured lower strain values (0.35% maximum strain) compared to the first group. Similar to Test 3, gauge number 11, which is the only axial direction strain gauge 180° away from the flaw, measured the lowest strain values and is not correlated with any of the rest of the gauges.

Figure 5.29 shows the strain distribution at the point of peak axial tensile force (2075 kN) immediately before the pipe rupture. The strain profile at this stage together with the strain profiles at two earlier stages of the test is plotted in Figure 5.30. Similar to Test 3, the average value of the axial tensile strain (0.65%) is calculated and shown with a horizontal red line using the strain values at the peak axial force point. Clearly both in Test 3 and

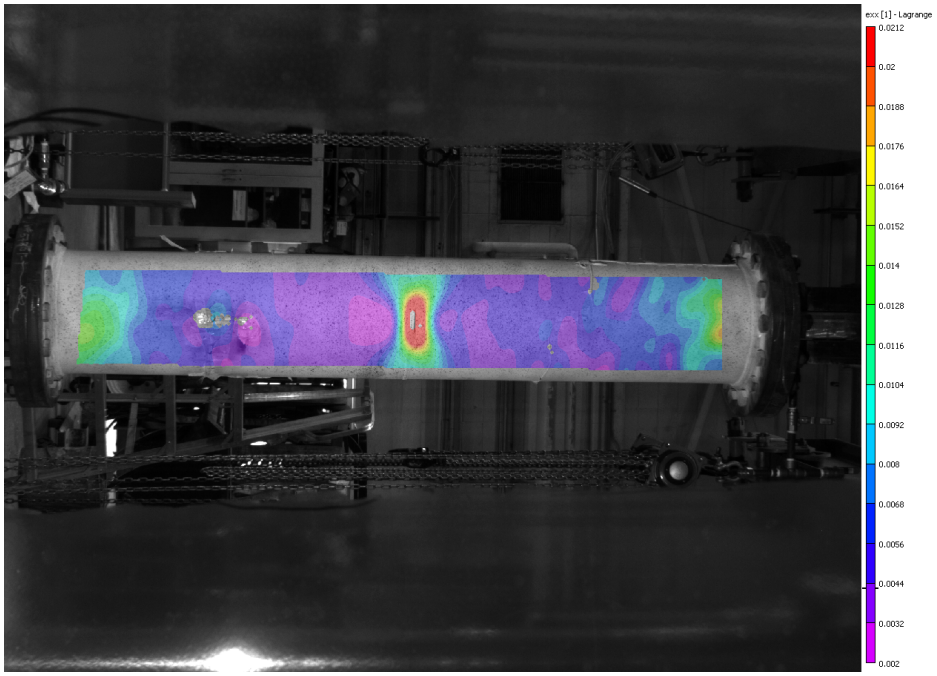

Figure 5.29: Axial strain field prior to rupture in Test 4

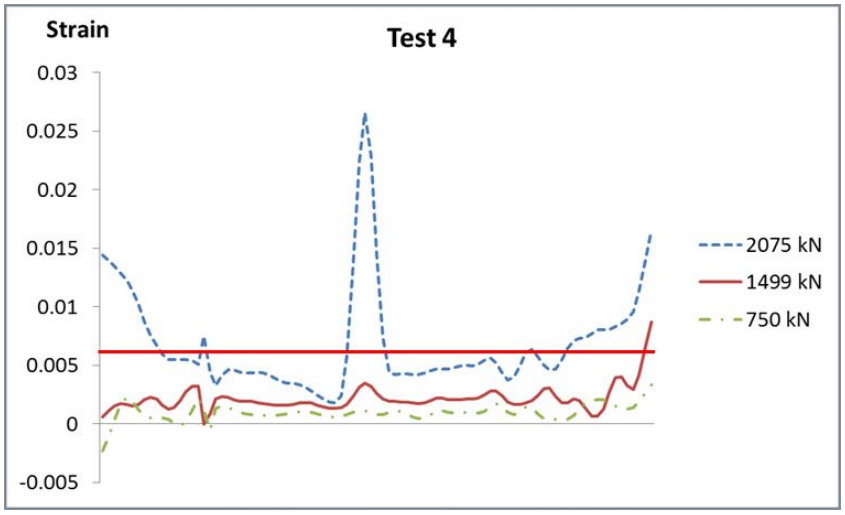

Figure 5.30: Development of the strain profile in the fourth full scale test

Test 4 the average strain calculated using DIC is in good agreement with the maximum axial strain value measured by strain gauges.

5.2.5 Analysis of the Strain Gauge Measurements for the Fifth Full Scale Experiment

From the fifth test onwards, the same strain gauge configuration is applied in all tests (Figure 5.31, Figure 5.32).

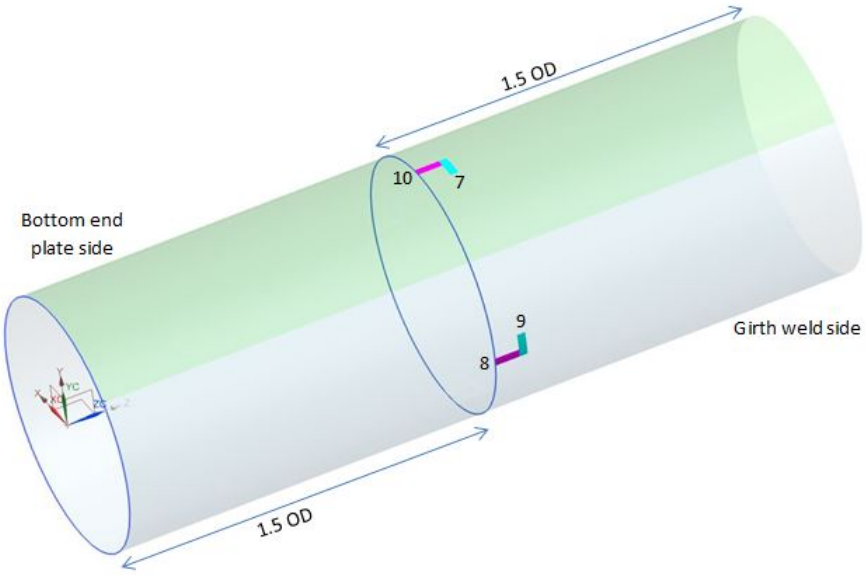

Figure 5.31: Bottom side of the pipe in the fifth to eighth tests

Table 5.10: Cross correlation of strain gauge measurements from Test 5

Gauge no	4	5	7	8	9	10
1			0.93		0.93	
2	0.97	0.97		0.96		0.94
4		0.99		0.99		
5				0.99		

The cross correlation analysis (Table 5.10) shows that, in the fifth test all hoop direction strain gauges (1, 7, 9) except gauge number 6 have good correlation with each other. The gauge number 6 is at the mid-length of the top side of the girth weld (Figure 5.32). Similar to Test 3, with the

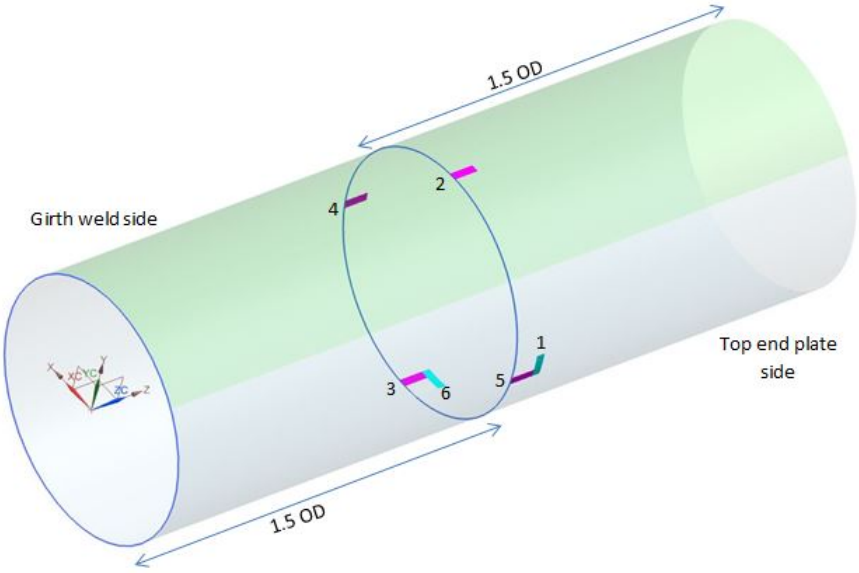

Figure 5.32: Top side of the pipe in the fifth to eighth tests

difference that gauge number 6 is this time at the top side of the specimen, the value of gauge 6 stays constant after reaching its maximum value (around 0.1 % neglecting slight fluctuations) at the point where the pipe is fully pressurized. Among the rest of the hoop direction gauges, gauge number 1 measured the highest tensile strain values (0.16%). However it should be noted that at certain phases of the experiment, gauge number 7 measured higher strain values than gauge number 1 and started to fluctuate at 15 mm applied displacement. Therefore it could be assumed that the measurements of gauge number 7 are not as reliable as gauges number 1 and 9 from 15 mm displacement onwards. The positive strain values measured by all hoop direction strain gauges in this experiment imply that at no stage of the test the tensile forces had a greater effect on the hoop direction strains than the internal pressure in order to cause compressive hoop strain.

According to Table 5.10 all of the axial direction strain gauges have good correlation with each other in Test 5 except the gauges number 3 and 10.

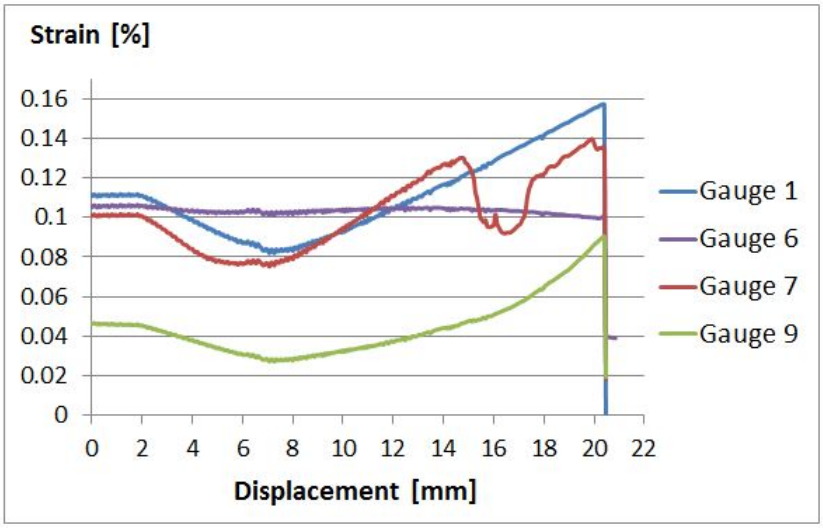

Figure 5.33: Hoop strain measurements in Test 5

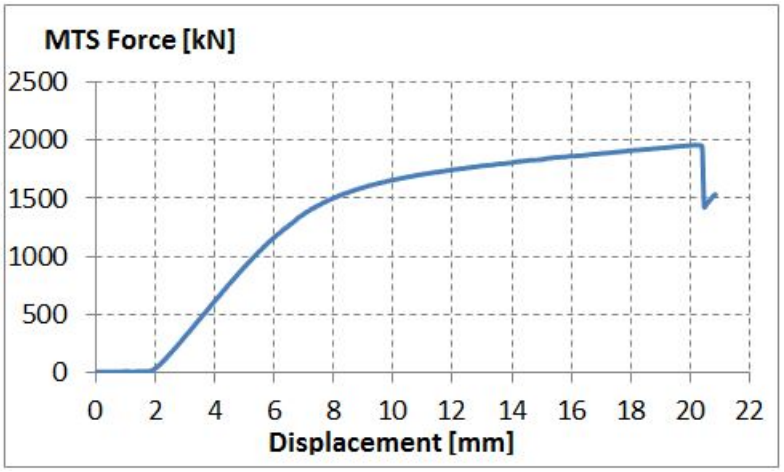

Figure 5.34: Load-displacement response of the fifth test

Gauge number 10 is aligned with the flaw and in a location expected to undergo the highest strain values whereas gauge number 3 is at the compression side of the pipe and is therefore expected to measure significantly lower tensile strain values compared to the rest of the gauges. The variation of all axial strain gauge measurements with respect to the applied displacement is plotted in Figure 5.35.

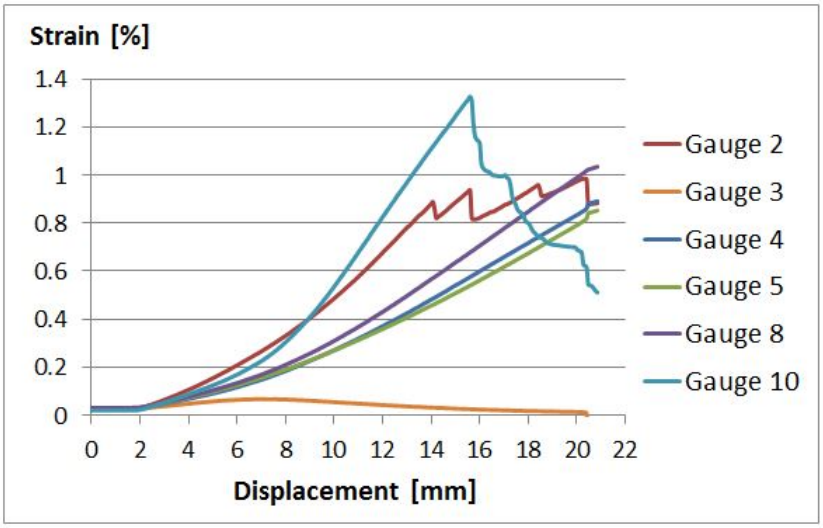

Figure 5.35: Axial strain measurements in Test 5

Figure 5.35 shows that the gauge number 10 measured the highest strain values among all axial direction strain gauges in Test 5 up to 15 mm applied displacement. At this stage of the test there is a sudden drop in gauge 10 which indicates a possible failure of this gauge around 15 mm applied displacement and 1.3% axial tensile strain. This condition also explains the low cross correlation coefficient of gauge 10. Also starting from 14 mm applied displacement and 0.9% axial tensile strain, the measurements of the gauge number 2, which measured the second highest strain values up to that point, severely fluctuate. Both gauge 2 and 10 are aligned with the flaw and at the mid-lengths of the top and bottom sides of the specimen respectively. Three of the remaining four axial strain gauges are 90° away from the flaw and therefore expected to measure lower strain values compared to the gauges number 2 and 10. Among them the gauge number 8 measures the highest strain values and slightly exceeds 1% strain towards the end of the test. The gauge number 3 is the only strain gauge 180° away from the flaw and as expected measures much lower strain values than all of the other axial direction

strain gauges.

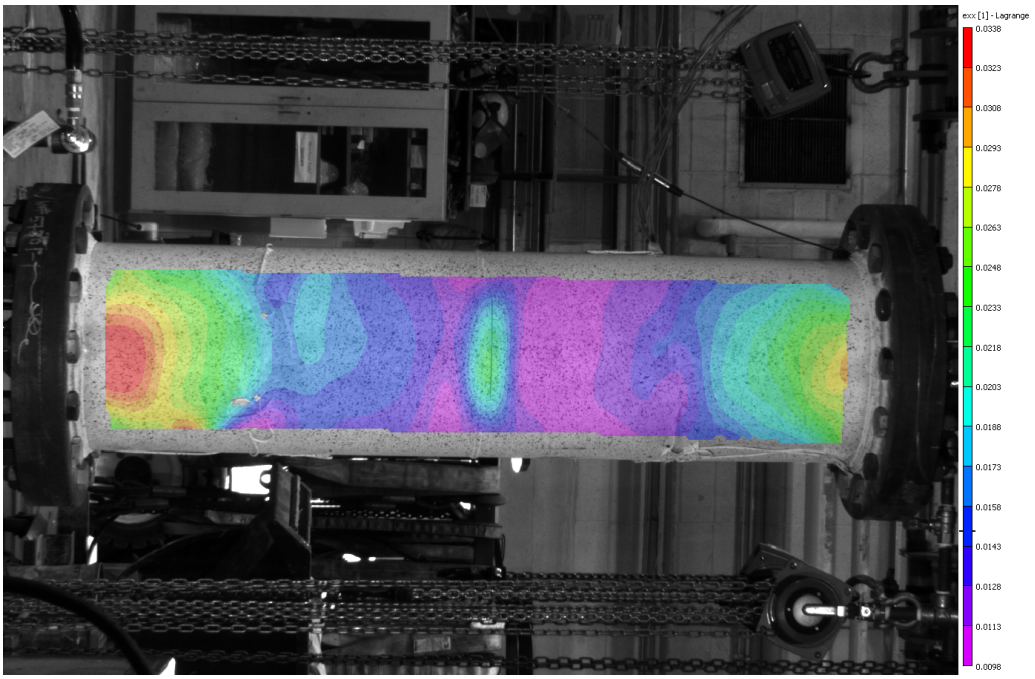

Figure 5.36: Axial strain field prior to rupture in Test 5

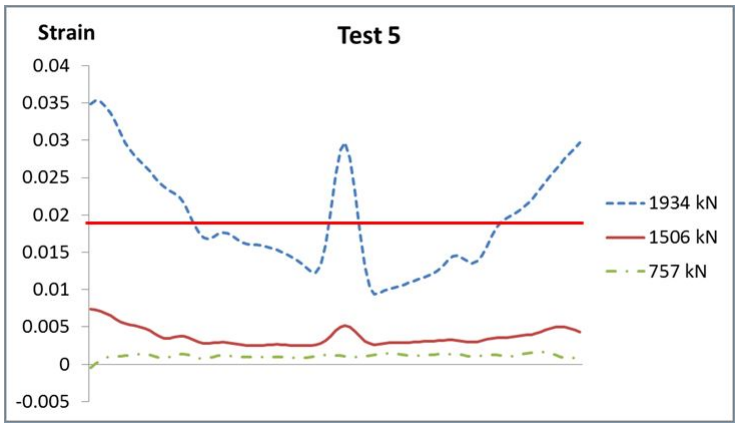

Figure 5.37: Development of the strain profile in the fifth full scale test

The axial strain field and the strain profiles for Test 5 are plotted in Figure 5.36 and Figure 5.37 respectively. The tensile strain capacity of the fifth specimen is estimated using the strain profile at the point of peak axial

tensile force (1934 kN) which occurs immediately before the pipe rupture. The average axial tensile strain value at the point of rupture is calculated as 1.85% and shown with a horizontal red line in Figure 5.37. A comparison with the maximum strain value in Figure 5.35 shows that the DIC method estimates 33% higher tensile strain capacity compared to the strain gauges in Test 5.

5.2.6 Analysis of the Strain Gauge Measurements in the Sixth Full Scale Experiment

In the sixth experiment, two of the hoop direction strain gauges (number 1 and 7 in Figure 5.31, Figure 5.32) have good correlation with each other whereas with the remaining two hoop direction strain gauges (number 6 and 9) no measurements could be made due to a connectivity problem in these gauges. The strain gauges of Test 6 having good correlation with at least one other strain gauge are listed in Table 5.11.

Table 5.11: Cross correlation of strain gauge measurements from Test 6

Gauge no	4	5	7	8	10
1			0.98		
2	0.99	0.99		0.99	0.99
4		0.99		0.99	0.99
5				0.99	0.99

Figure 5.38 shows that the low internal pressure in Test 6 effected the hoop direction strains so that starting from a certain level of applied displacement both hoop strain gauges started to measure compressive strain values. This condition is similar to what is observed in Test 4 (Figure 5.26) with the difference that in Test 6 the compressive hoop strain values start to be measured earlier than in Test 4. In Test 4 the first compressive hoop

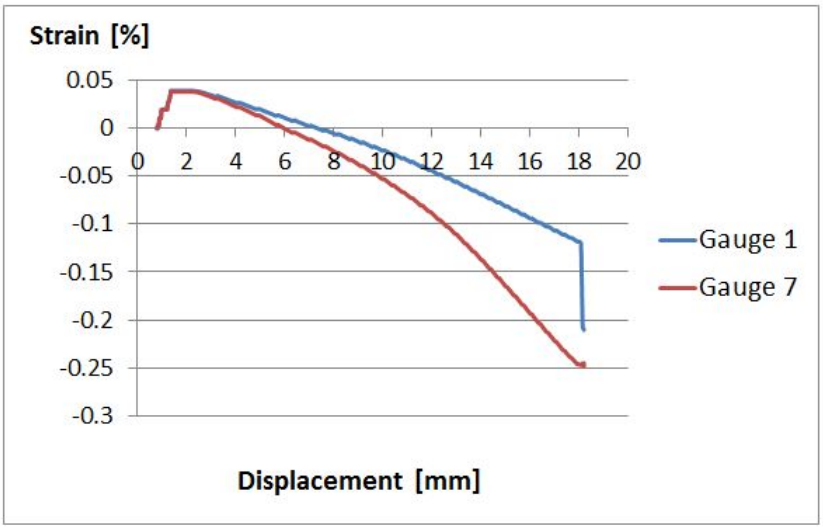

Figure 5.38: Hoop direction strain gauge measurements in Test 6

Figure 5.39: Load-displacement response of the sixth test

strain value is measured at an applied displacement of 7 mm whereas this displacement decreased to 6 mm in Test 6. A possible cause of that behaviour is the three times longer flaw size in Test 6 compared to Test 4.

According to Table 5.11, in Test 6 all of the axial direction strain gauges have good correlation with each other except the gauge number 3. The gauge number 3 is the compression side strain gauge at the mid-length of the top

side and expected to measure an order of magnitude lower tensile strain values as observed in the previous tests.

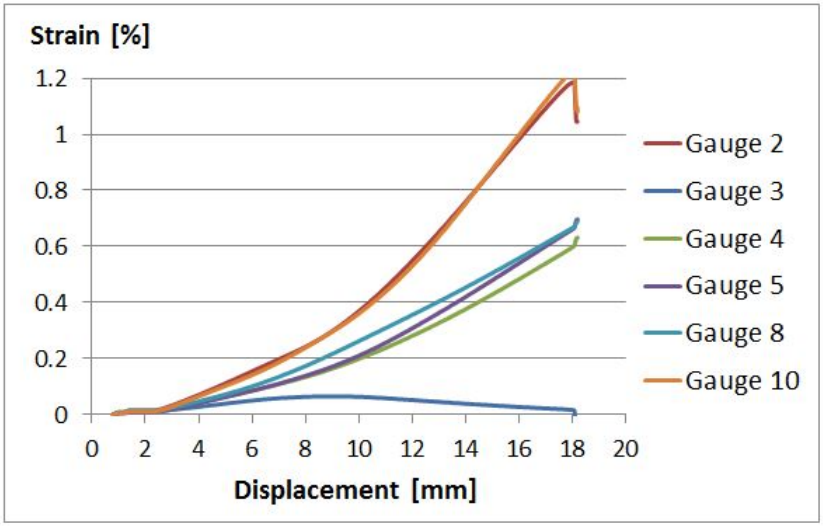

Figure 5.40: Axial strain gauge measurements in Test 6

According to Figure 5.40 the axial strain gauge measurements can be classified in three groups. The first of these groups consists of the gauges number 2 and 10. The gauges number 2 and 10 are located at the mid-lengths of the top and bottom side of the specimen respectively and both of them are aligned with the flaw. Clearly these gauges measured equal amounts of strain throughout the test which indicates that in Test 6 there was no significant difference in the strain developments of the top and bottom parts of the specimen at the tension side. The gauges 2 and 10 measured 1.2% maximum axial tensile strain in Test 6. The second group of the axial strain gauges consists of the gauges number 4, 5 and 8. Figure 5.31 and Figure 5.32 show that all of the gauges in this group are 90° away from the flaw. The gauges 4 and 5 are at the top side of the girth weld whereas the gauge 8 is at the bottom side. The average maximum axial tensile strain measured by the gauges of the second group is around 0.65%. A comparison

between the axial strain gauge measurements of Test 4 and Test 6 shows that in both experiments the average strain measured 90° away from the flaw is about half of what is measured by the gauges aligned with the flaw. Finally, the third group of the axial strain gauges consists of gauge 3 which is 180° away from the flaw and as expected, measured an order of magnitude lower strain values ($\backsim$0.05%) compared to the rest of the axial strain gauges.

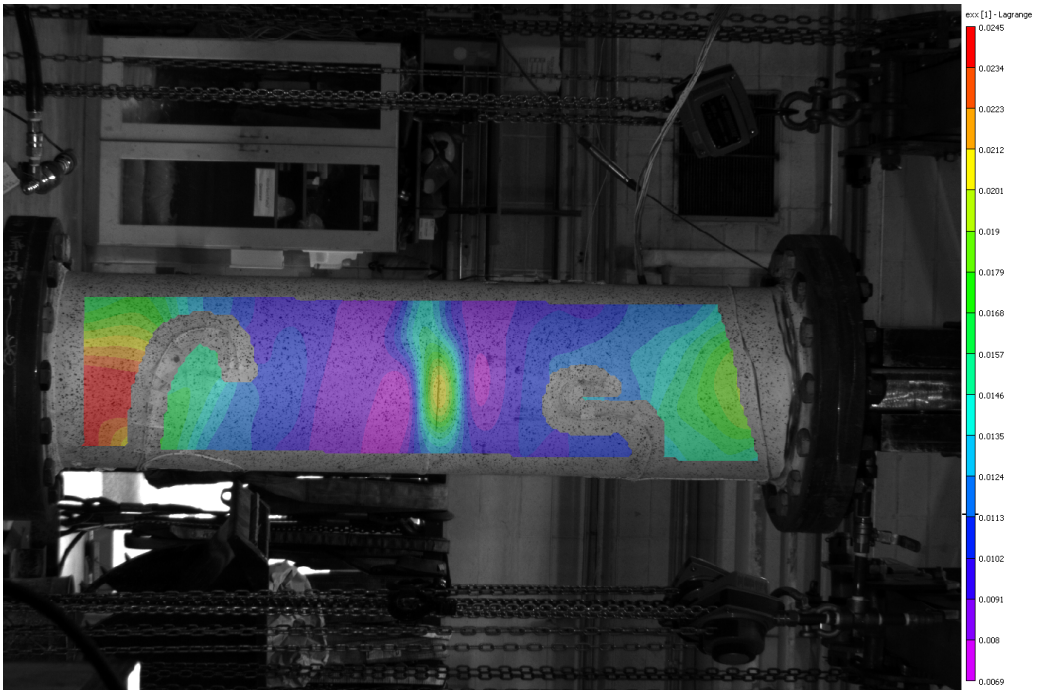

Figure 5.41: Axial strain field prior to rupture in Test 6

According to Figure 5.42 in the sixth test the average axial tensile strain prior to pipe rupture can be calculated as 1.3%. A comparison with Figure 5.40 shows that this value is with 6% difference in agreement with the maximum axial tensile strain measured by the strain gauges. The strain distribution on the pipe wall at 2268 kN axial tensile force is plotted in Figure 5.41.

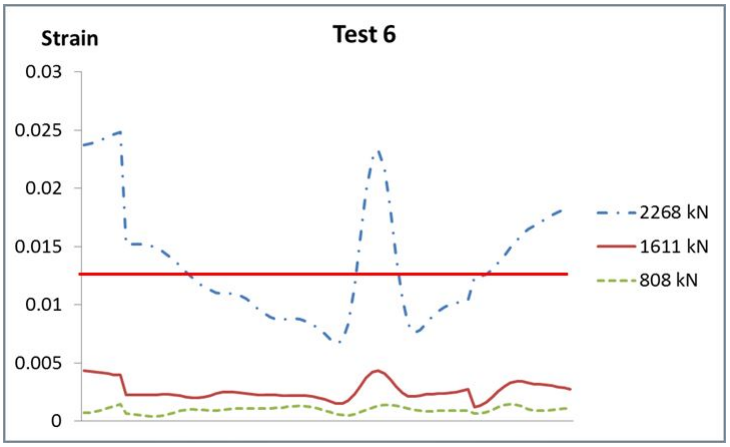

Figure 5.42: Development of the strain profile in the sixth full scale test

5.2.7 Analysis of the Strain Gauge Measurements in the Seventh Full Scale Experiment

In the seventh test all of the four hoop direction strain gauges (1, 6, 7, 9) except gauge number 6, have good correlation with each other whereas the gauge number 6 has only good correlation with gauge number 7 (Table 5.12).

Table 5.12: Cross correlation of strain gauge measurements from Test 7

Gauge no	4	5	7	8	9	10
1			0.93		0.99	
2	0.92	0.92		0.91		0.99
4		0.99		0.99		
5				0.99		
6			0.98			
7					0.94	

Similar to the previous tests, the hoop strain gauges reached their maximum strain values at the point where the pipe was fully pressurized (1.7 ksi) with the difference that in Test 7, towards the end of the test, the gauge number 6 measured increasing amounts of strain. According to Figure 5.43, the tensile hoop strains measured by the gauges 1, 7 and 9 start to decrease at

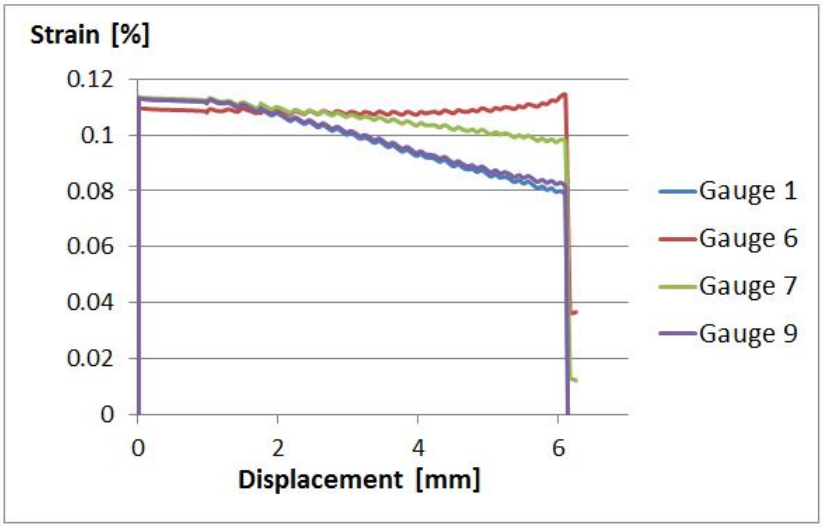

Figure 5.43: Hoop strain gauge measurements in Test 7

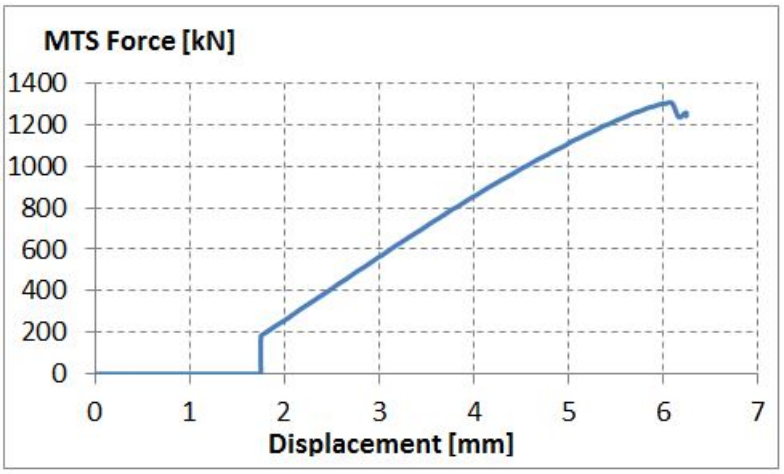

Figure 5.44: Load-displacement response of the seventh test

1.7 mm applied displacement. The load-displacement curve of Test 7 plotted in Figure 5.44 shows that, at 1.7 mm displacement the tensile force begins to act on the specimen which implies that the applied tensile force counteracts the hoop direction tensile force caused by the internal pressure. On the other hand, the hoop direction tensile strain measured by gauge 6 stayed constant for most part of the test up until the 4 mm applied displacement

point. Starting from this point, the gauge number 6 measured increasing amounts of strain. This behaviour is slightly different from the behaviour of the compression side strain gauge in Test 3 and Test 5 where the value of the strain measured by this gauge stayed almost constant throughout the test. One possible reason for this difference is that the specimen of Test 7 has the largest flaw size among all the specimens (together with the specimen of Test 8) and is pressurized with high pressure. Since Test 7 is one of the experiments with high pressure, the reducing effect of the tensile force on the tensile hoop strains did not exceed the increasing effect of the internal pressure on the hoop strains throughout the test. As a result, the strain values in Figure 5.43 stay positive during the entire test.

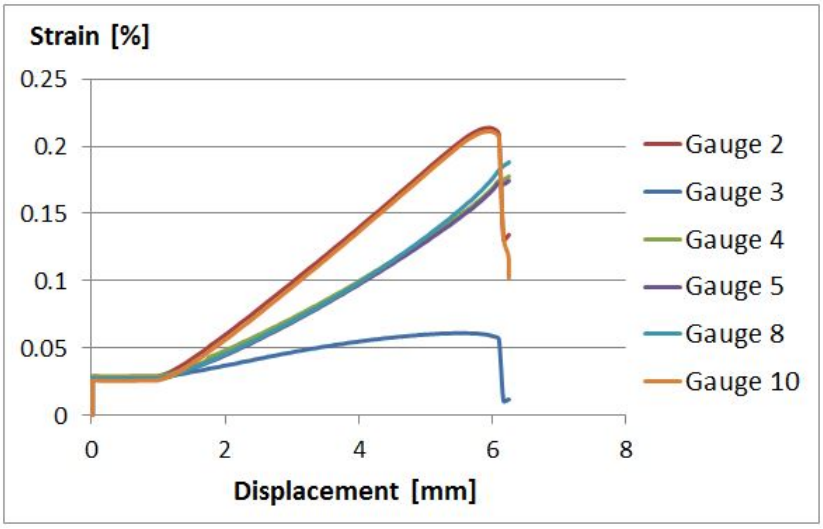

Figure 5.45: Axial strain gauge measurements in Test 7

The development of the axial strain in Test 7 is similar to the previous tests such that the gauges can be classified in three groups. The gauges number 2 and 10 measure the highest strain values as expected whereas the gauges 4, 5, 8 measure lower strain values and the compression side axial strain gauge (gauge 3) measured the lowest strain values. The main

difference of Test 7 from the previous tests in terms of the axial strain is that in Test 7 the lowest strain values (0.22% maximum strain) are measured due to the large flaw size and high internal pressure. Another difference is that the strain values measured by the axial strain gauges of the second group are closer to the values measured by the first group compared to the previous tests.

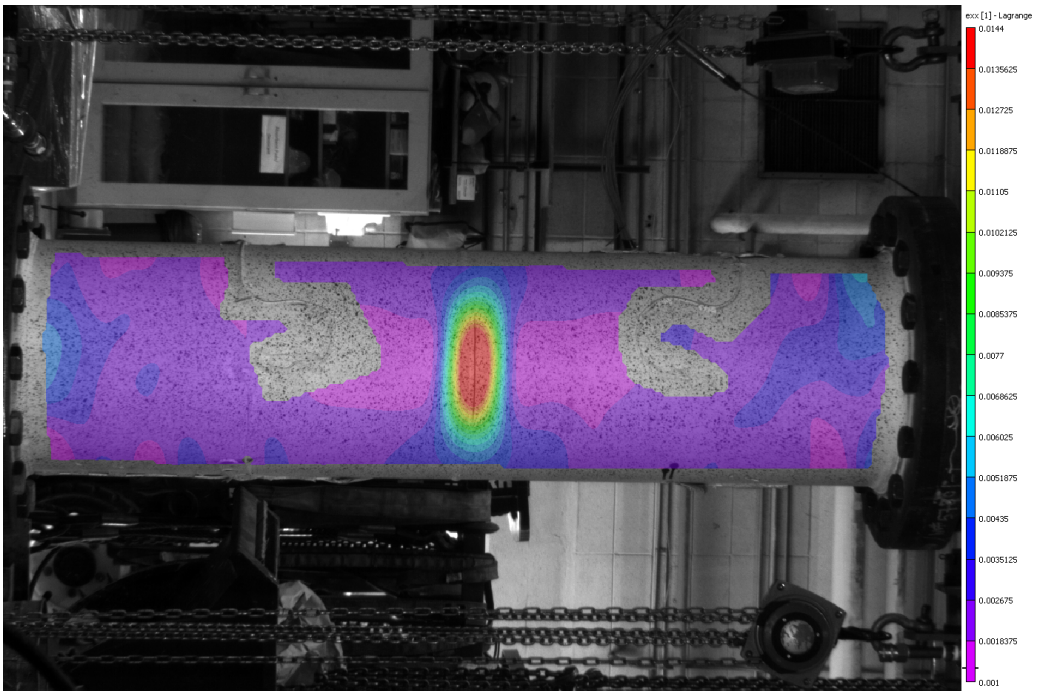

Figure 5.46: Axial strain field prior to rupture in Test 7

In Test 7 the average strain prior to rupture is calculated as 0.2% as shown in Figure 5.47. This value is in well agreement with the maximum axial tensile strain measured by the strain gauges in Test 7 (Figure 5.45).The strain distribution on the pipe wall at the peak axial tensile force (1301 kN) is shown in Figure 5.46.

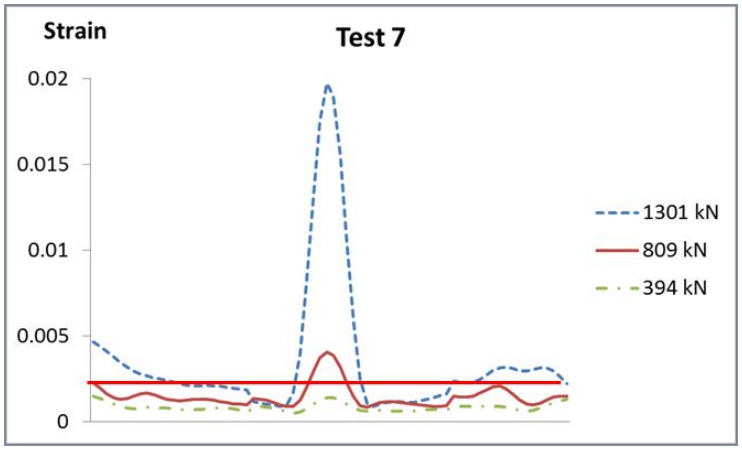

Figure 5.47: Development of the strain profile in the seventh full scale test

5.2.8 Analysis of the Strain Gauge Measurements in the Eighth Full Scale Experiment

In the eighth experiment all of the hoop direction strain gauges except gauge number 6 have good correlation with each other.

Table 5.13: Cross correlation of strain gauge measurements from Test 8

Gauge no	4	5	7	8	9	10
1			0.93		0.99	
2	0.9	0.91				0.99
3				0.92		
4		0.99				0.93
5						0.94
7					0.93	

According to Figure 5.48, similar to the previous tests with low pressure, the effect of the axial force on the hoop strains exceeded the effect of the internal pressure in the later stages of the experiment. In Test 8, the first negative hoop strain value occurs at 7.5 mm applied displacement. This value is larger than the displacement at which the first negative hoop strain is observed in Test 6 (6 mm) which has the same internal pressure and flaw

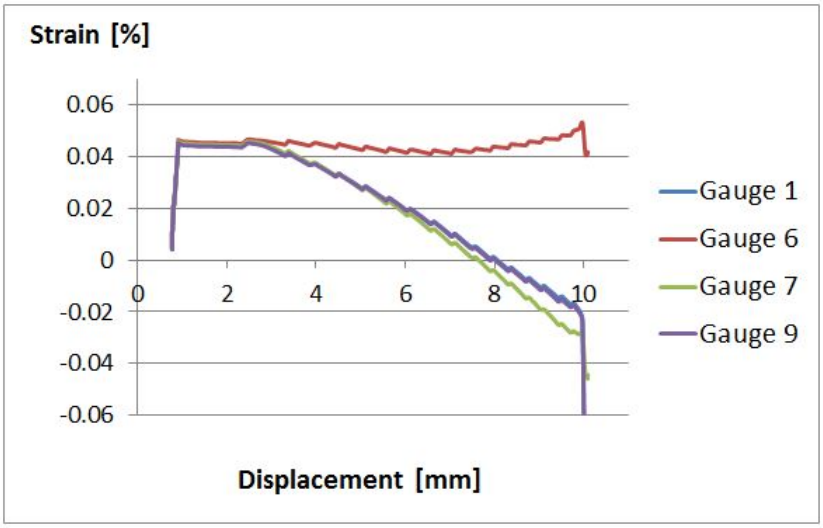

Figure 5.48: Hoop strain gauge measurements in Test 8

Figure 5.49: Load-displacement response of the eighth test

length as Test 8 but has a shallow flaw height. Also, similar to Test 7, the increase of the strain measured by gauge 6 towards the end of the experiment is repeated. The common attribute of Test 7 and Test 8 can be related to both tests having the same flaw size which is the largest among all tests.

The development of the axial strain measurements in Test 8 is plotted in Figure 5.50. According to Figure 5.50, the maximum axial tensile strain mea-

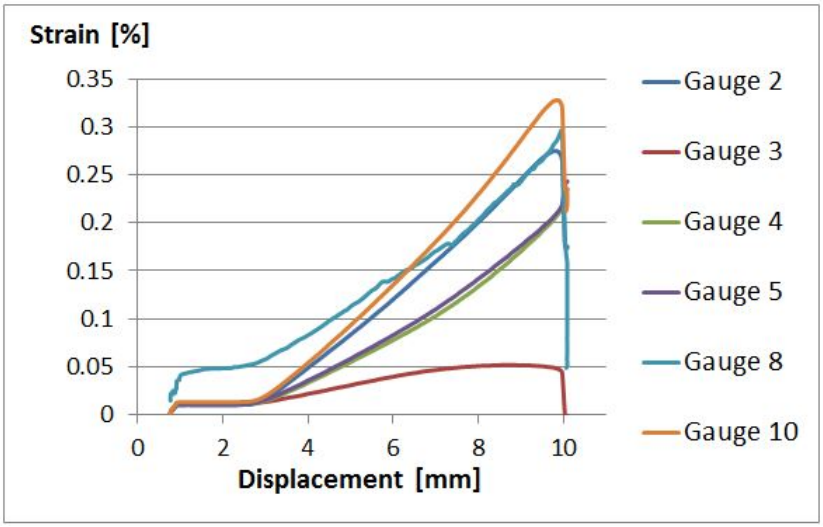

Figure 5.50: Axial strain gauge measurements in Test 8

sured in this experiment is about 0.33% which is higher than the maximum strain measured in Test 7. Again, the axial strain gauges can be classified in three groups. However this time, instead of only the gauges number 2 and 10, also the gauge number 8 is in the first group of gauges measuring the highest strain values. This result is contrary to the expectation since gauge number 8 is 90° away from the flaw whereas gauges 2 and 10 are aligned with the flaw. The other 2 gauges 90° away from the flaw (gauges 4 and 5) constitute the second group. The gauges in the second group measured a maximum strain of about 0.22%. The ratio of this value to the maximum strain value measured by the gauges in the first group, is in agreement with the results of the previous tests. Finally, the gauge number 3 measured at the compression side an order of magnitude lower strain values throughout the eighth experiment.

Figure 5.52 shows that the average axial tensile strain at the peak axial tensile force is calculated as 0.3% in Test 8. Again this value is in good agreement with the maximum tensile strain measured by the strain gauges

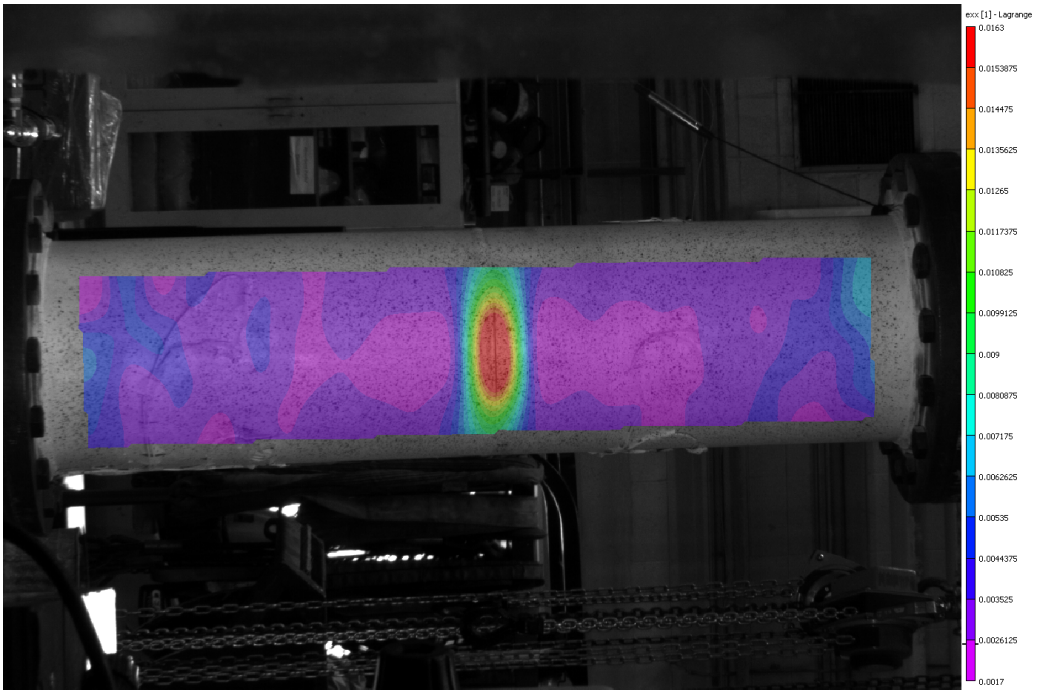

Figure 5.51: Axial strain field prior to rupture in Test 8

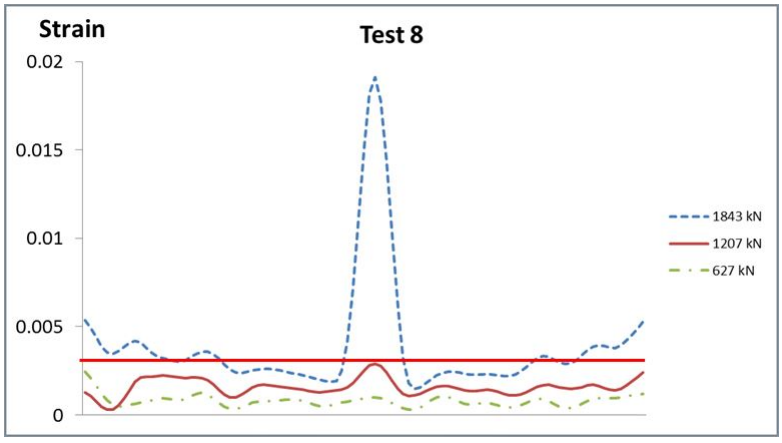

Figure 5.52: Development of the strain profile in the eighth full scale test

(0.33%). Overall, the DIC method and the strain gauge measurements provided close estimations. In all experiments with the exception of Test 5, the difference between the measurements of the DIC system and the strain gauge measurements were within 10%. Table 5.14 shows a list of all experiments

with the corresponding tensile strain capacity measurements by DIC and strain gauges.

Table 5.14: The comparison of the tensile strain capacity measurements by the DIC and the strain gauges

	Flaw length [mm]	Flaw height [mm]	Internal pressure (% SMYS)	Maximum strain (% by gauges)	Maximum strain (% by DIC)
Test 1	50	1.7	80	3.41	2.40%
Test 2	50	1.7	30	3.69	3.80%
Test 3	50	3.4	80	0.61	0.6
Test 4	50	3.4	30	0.58	0.65%
Test 5	150	1.7	80	1.33	1.85%
Test 6	150	1.7	30	1.22	1.30%
Test 7	150	3.4	80	0.21	0.20%
Test 8	150	3.4	30	0.33	0.30%

5.3 Load-Displacement Response

This section summarizes the behaviour of the load-displacement response in all of the eight full scale experiments of this research program. In Figure 5.53 the load-displacement responses in all of the eight experiments are plotted together. Although it is not clearly visible in Figure 5.53, from the separate load-displacement curves plotted in section 5.2 it can be reckoned that, in all experiments the load-displacement curve has an initial flat part where the load does not increase. This is due to the fact that different parts of the connections between pipe end plates, the actuator of the MTS machine and the bottom pin-yoke assembly are not perfectly tight in the beginning of the test so that a certain amount of displacement needs to be applied in order to tighten these connections. In all of the experiments except Test 7 and Test 8, there is a clearly recognizable linear initial part of the load-displacement curves followed by a decrease in the stiffness of the specimen. Due to the relatively early pipe rupture in Test 7 and Test 8, the load-displacement response could not be developed far beyond the initial linear phase (Figure 5.44, Figure 5.49) in these experiments.

Table 5.15: Maximum tensile force and strain in the experiments

	Flaw length [mm]	Flaw height [mm]	Internal pressure (% SMYS)	Maximum Tensile Force [kN]	Maximum Strain (% by gauges)
Test 1	50	1.7	80	2339	3.41
Test 2	50	1.7	30	3105	3.69
Test 3	50	3.4	80	1742	0.61
Test 4	50	3.4	30	2089	0.58
Test 5	150	1.7	80	1958	1.33
Test 6	150	1.7	30	2269	1.22
Test 7	150	3.4	80	1304	0.21
Test 8	150	3.4	30	1844	0.33

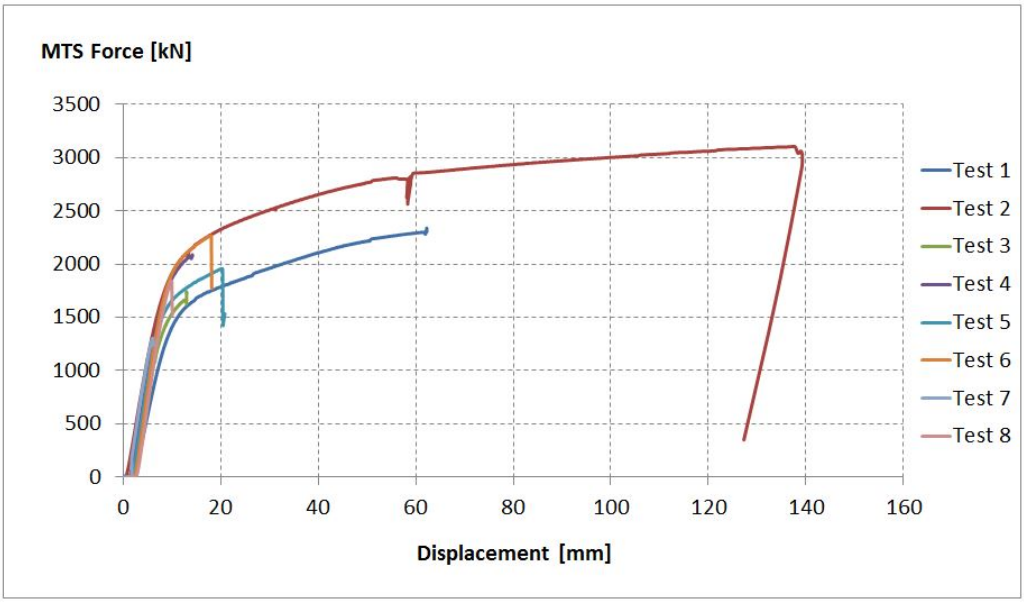

Figure 5.53: Load-displacement response of all full scale tests

Figure 5.53 and Table 5.15 clearly show that the highest amount of tensile force was applied in Test 2. In addition to having the highest tensile force among all experiments it can be seen from Figure 5.53 that in Test 2 significantly large amounts of displacement had to be applied in order to bring about the pipe rupture. One reason for that is the yielding and elongation of the connection part during the test. This connection part is replaced with one having higher yield strength in the following tests. In Test 2, the drop in force at 59 mm applied displacement is caused by a pause in the test due to high tensile forces. The oil pressure of the MTS 6000 had to be increased at this point in order to apply forces beyond 3000 kN. Also, the initial part of the curve in Test 2 overlaps with the curve of Test 6 up to the 18 mm displacement point where Test 6 is terminated due to pipe rupture. It should be noted that Test 2 and Test 6 have all their parameters identical except the flaw length. It follows that the earlier rupture in Test 6 can be attributed entirely to the 3 times longer flaw in this test. Similarly, the initial part

of the curve of Test 2 overlaps with the curve of Test 4 up to the 14 mm displacement point where Test 4 is terminated due to pipe rupture. Again, those two tests differ in only one of the parameters. The only difference between the configurations of Test 2 and Test 4 is that Test 4 has a 2 times greater flaw height compared to Test 2. According to Table 5.15 this increase in the flaw height resulted in a 39% decrease in the maximum tensile force of Test 4 compared to Test 2. A similar reduction in the maximum tensile force due to the increase in the flaw height can also be observed in Test 8. A comparison between Test 6 and Test 8 shows that these two tests have all of their parameters identical except that Test 8 has two times greater flaw height. Table 5.15 shows that this increase in the flaw height resulted in a 21% reduction in the tensile force necessary to bring about the pipe rupture. A list of all the reductions in maximum tensile force due to increasing the flaw height is given in Table 5.16.

Table 5.16: Difference in the maximum tensile force due to increasing flaw height

Test pair	Internal pressure [% SMYS]	Flaw length [mm]		Difference [%]
Test 1 - Test 3	80	5	0	29
Test 2 - Test 4	30	5	0	39
Test 5 - Test 7	80	1	50	40
Test 6 - Test 8	30	1	50	21

In order to analyse the effect of increasing only the flaw length while keeping the rest of the parameters constant, either one of the pairs of Test 1 and Test 5, Test 2 and Test 6, Test 3 and Test 7 or Test 4 and Test 8 can be compared. The comparison between Test 1 and Test 5 yields 18% reduction of the maximum tensile force whereas the comparison between Test

3 and Test 7 yields 29% reduction of the maximum tensile force. It should be noted that both of Test 1 and Test 5 have specimens with shallow flaw whereas both of Test 3 and Test 7 have specimens with deep flaw. On the other hand the tensile force reduction due to lengthening of the flaw in the pair of Test 2 and Test 6 (31 %) is greater than the reduction in the pair of Test 4 and Test 8 (12%) which implies that there is no direct relationship between the magnitude of the reduction in the maximum tensile force due to the lengthening of the flaw and the flaw height. A list of all the reductions in maximum tensile force due to increasing the flaw length is given in Table 5.17.

Table 5.17: Difference in the maximum tensile force due to increasing flaw length

Test pair	Internal pressure [% SMYS]	Flaw height [mm]	Difference [%]
Test 1 - Test 5	80	1.7	18
Test 2 - Test 6	30	1.7	31
Test 3 - Test 7	80	3.4	29
Test 4 - Test 8	30	3.4	12

Another factor which has an influence on the maximum tensile force in an experiment is the internal pressure. The comparison between any two tests in Table 5.15 where the only changing input variable is the internal pressure, shows that the test with the lower internal pressure has the greater maximum tensile force. The differences in the maximum tensile force due to changing internal pressure are listed in Table 5.18 for all tests.

Table 5.18: Difference in the maximum tensile force due to internal pressure

Test pair	Flaw height [mm]	Flaw length [mm]	Difference [%]
Test 1 - Test 2	1.7	50	28
Test 3 - Test 4	3.4	50	18
Test 5 - Test 6	1.7	150	15
Test 7 - Test 8	3.4	150	34

5.4 Closing Remarks

Flaws in the pipe wall can lead to structural failure and the loss of containment capability of pipelines. These pipe wall flaws can be caused not only due to imperfect manual or automatic welding procedures on the field but also due to corrosion. Pipe wall defects caused by corrosion become a major concern especially in case of pipelines built in the 1950s and 1960s that constitute a large portion of the Canadian pipeline network. In order to have a better understanding of the capacity of vintage pipes to withstand operational loads in the presence of pipe wall defects, experimental studies play a crucial role. In the scope of this research project, eight full scale tests are carried out with vintage pipes having X52 steel grade and 12 in. (305 mm) nominal diameter. Each test specimen contained a unique combination of pipe wall defect length, defect height and internal pressure. In all of the full scale tests the specimen has ruptured at the location of the machined pipe wall flaw. The major outcome of the full scale tests is the tensile strain capacity which is the maximum amount of the axial strain that a specimen can withstand before it ruptures. In order to determine the tensile strain capacity of each test specimen, strain gauges and digital image correlation techniques are used. The distribution of the axial strain along the longitudinal axis of each specimen prior to the pipe rupture is plotted using the

outcome of the image correlation method. Furthermore, the strain gauge readings at the critical locations are plotted and compared to the DIC results. A list of the tensile strain capacity values obtained from DIC and the strain gauges can be seen in Table 5.19.

Table 5.19: The comparison of the tensile strain capacity measurements and the predicted values

	Flaw length [mm]	Flaw height [mm]	Internal pressure (% SMYS)	Maximum strain (% by gauges)	Maximum strain (% by DIC)	CSA (%)	PRCI (GMAW) (%)	PRCI (SMAW) (%)
Test 1	50	1.7	80	3.41	2.40	0.94	0.6	0.6
Test 2	50	1.7	30	3.69	3.80	0.94	0.67	0.67
Test 3	50	3.4	80	0.61	0.6	0.45	0.44	0.47
Test 4	50	3.4	30	0.58	0.65	0.45	0.49	0.53
Test 5	150	1.7	80	1.33	1.85	0.79	0.33	0.35
Test 6	150	1.7	30	1.22	1.30	0.79	0.36	0.39
Test 7	150	3.4	80	0.21	0.20	0.27	0.16	0.14
Test 8	150	3.4	30	0.33	0.30	0.27	0.18	0.16

The list of the measured strain values in Table 5.19 shows that the DIC and strain gauge methods delivered fairly close results. It can be observed that the specimens with the smallest flaw sizes (Test 1, Test 2) were able to withstand the highest amounts of strain whereas the lowest strain capacities are observed for Test 7 and Test 8 having the largest flaw sizes.

In order to investigate the applicability of the strain capacity prediction equations in the literature, the predictions of different equations are compared to the strain capacities measured in the experiments. It is known that the equations in the literature have limitations for the ranges of parameters in which they can be applied. As an example the equations developed by PRCI have an applicability range for the pipe base metal yield strength between 56 ksi (386 MPa) and 100 ksi (690 MPa) such that the vintage pipe with 52 ksi (359 MPa) yield strength remains outside of the applicability range. Nevertheless, in similar situations where the actual pipe parameters remained outside of the applicability ranges, the lower or upper bounds of the given applicability ranges are used in order to compute the predicted tensile strain capacity values. In case of the CSA equation, from the values listed in Table 5.19 it can be reckoned that the equations predict closer values to the actual measured strain capacities for larger flaw sizes. For Test 7 and Test 8 where the flaw sizes are the largest, the equations predicted higher strain capacities than the measured capacities. However it should be noted that the values listed in Table 5.19 are unfactored values. In contrast to the cases of Test 7 and Test 8, the CSA predictions for the tensile strain capacity in Test 1 and Test 2 are significantly lower than the measured strain capacities. This condition can be attributed to the small flaw sizes in the first two tests which resulted in excessive deformations in the pipe wall prior to rupture. Another shortcoming of the CSA equation is that it predicts

the same strain capacities for tests where the only changing parameter is the internal pressure. The strain predictions of the PRCI equations are in general more conservative than the CSA equation except in Test 3 and Test 4. Overall, it can be inferred that the CSA equation predictions are closer to the actual strain capacities albeit being significantly smaller in cases with small flaw sizes.

The main purpose of strain based design of pipelines is to use the strain capacities of pipe structures in a more effective way. Experimental studies showed that pipes can withstand large amounts of strain in the inelastic range of the pipe material. However, traditional allowable stress design methods only address situations where the pipe material stays in the elastic range. On the other hand, in order to economically operate the pipeline network, the post-yield capacity of pipeline structures should not be ignored. Therefore, it is imperative to have a sound understanding of the tensile strain capacity of steel pipes in order to guarantee the safe and economic operation of a pipeline network.

6 TENSION SIDE FRACTURE OF PIPES

Pipeline structures can undergo large strains due to various geotechnical factors like seismic activity, slope instability or discontinuous permafrost. These factor often cause bending of the pipeline structure which can result in the formation of large wrinkles at the compression side of the pipe in the post-buckling phase. Once large wrinkles are formed in the compression side (intrados), the pipe is expected to fail at this location due to large strains followed by leaking of the pipe contents. This form of local failure is less hazardous and preferred over a tension side fracture because of the explosion associated with tension side fractures. In practice often pipes are observed to fail in the compression side because of the aforementioned wrinkling phenomenon and the associated large strains. However experimental studies carried out in the University of Alberta [1], [16], [21] showed that the tension side fracture also has a considerable likelihood of occurrence. Therefore it is crucial to have a sound understanding of this structural behaviour and conditions leading to it. This chapter elaborates the comprehensive numerical analyses of this structural behaviour that were carried out in order to identify to conditions that may lead to a tension side fracture of pipelines.

6.1 TENSION SIDE FRACTURE OF COLD BENDS

Cold bending is a procedure that is applied in the field using cold bending machines in order to change the direction of a pipeline in a horizontal or vertical plane. The process of cold bending usually results in residual stresses as well as changes in the material properties at the vicinity of the cold bent location which makes the study of the mechanical behaviour of cold bends indispensable.

One of the major differences between straight and cold bent pipes is the changes in the material properties of the cold bend at the intrados and extrados due to the Bauschinger effect and work hardening respectively. In the process of cold bending the extrados of the cold bend can be strained beyond its elastic limit in tension whereas the intrados can undergo compressive strains which exceed the elastic limit. As a result of the Bauschinger effect and work hardening the tensile and compressive yield strengths of the pipe material decrease at the intrados and extrados of the cold bend respectively.

Sen et al.[53] conducted tension coupon tests with specimens taken from intrados and extrados of cold bends as well as from straight pipes. In all of the tension coupon tests with specimens from the extrados the measured yield stresses were greater than the yield strength of the straight pipe as a result of work hardening that takes place once the extrados is loaded beyond its yield strength during the cold bending procedure. On the other hand the ultimate stresses of the extrados specimens were found to be close to the ultimate stresses of the specimens taken from a straight pipe since the residual strains due to cold bending are small compared to the ultimate strain. The tension coupon tests with specimens taken from the pipe intrados revealed that the yield strength of these specimens were significantly less than the yield strength of a straight pipe due to the Bauschinger effect. In this current work for the sake of simplicity the differences in the stress-strain responses of the intrados and the extrados of the cold bend are neglected. The post-yield material behaviour is implemented in Abaqus using the Ramberg-Osgood material model whose details are given in Section 2.1.1.

Another difference between straight and cold bent pipes is that the peak moment and corresponding curvature at the point of buckling are lower in case of cold bends compared to straight pipes as shown by the experimen-

tal study of Sen[1]. Particularly the amount of critical buckling strain was observed to decrease 48% due to cold bending.

The experimental studies of Sen et al.][1],[16],[21] which resulted in a tension side fracture, were carried out with cold bent pipes. In these experiments the curvature of the cold bend is increased in the presence of a constant internal pressure. In their experimental study a total of 8 full scale tests were conducted with a variety of pipe diameters, diameter to wall thickness ratio and steel grade. The setup of these tests is illustrated in Figure 6.1. The specimen shown in Figure 6.1 is fixed at the left hand side and connected to a jack on the right hand side with a pin connection allowing the rotation of the end plate. The right hand side jack applies horizontal displacement in an eccentric way such that the curvature of the specimen increases throughout the test. The collar pieces on both sides of the specimen adjacent to the end plates strenghten the pipe at these locations of high stress concentration in order to prevent the buckling of the specimen in these locations because of the pipe - end plate interaction. Specimen failure due to the interaction with the end plate is highly undesirable since the end plates only serve the purpose of load application and pressurization and do not represent the in situ conditions of the line pipe.

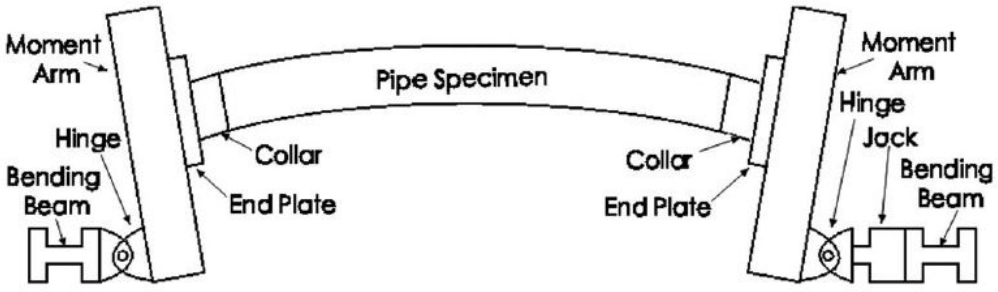

Figure 6.1: Test setup used in the cold bend experiments[16]

In this set of full scale tests one of the pipes with steel grade X65 and an

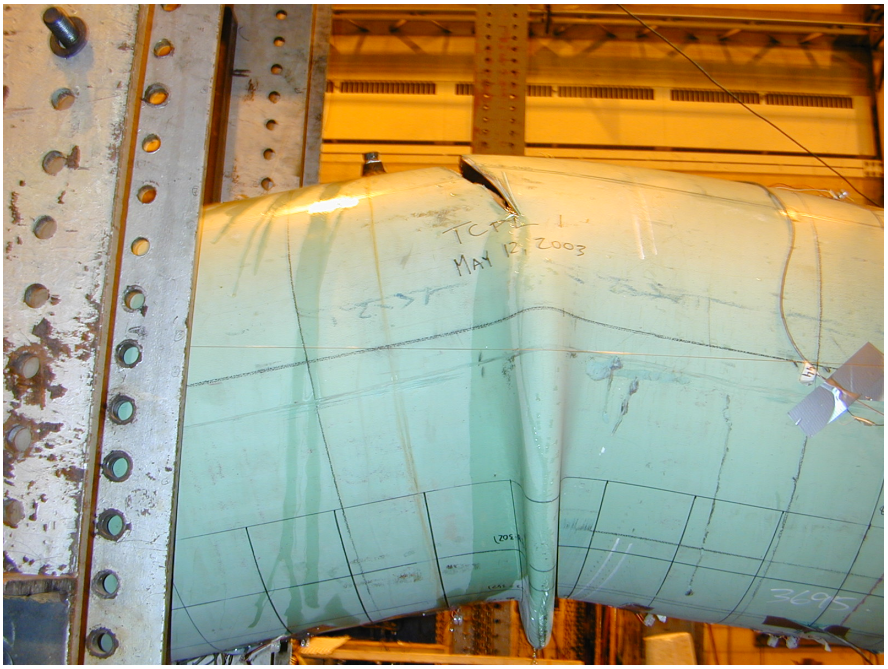

Figure 6.2: Tension side fracture[54]

Modulus of Elasticity [MPa]	201530
SMYS [MPa]	448
Ultimate strength [MPa]	531
Pipe outer diameter (OD) [mm]	762
Thickness of collar reinforced sections [mm]	16
Length of the collar reinforced sections [mm]	237
Diameter to wall thickness ratio	93
Initial radius of curvature [mm]	17796
Initial curvature [1/mm]	$5.62 \cdot 10^{-5}$
Pipe total length [mm]	7454
Pipe horizontal length [mm]	7400

Figure 6.3: Material and geometic properties of the specimen in Figure 6.2[55]

internal pressure causing 80% SMYS hoop stress, failed due to fracture at the extrados (Figure 6.2) after buckling and formation of wrinkles at the intrados. The detailed material and geometric properties of this particular specimen configuration are listed in Figure 6.3. The initial bend angle of the specimen

in Figure 6.2 was 8.0 degrees. In order to understand the conditions leading to the tension side fracture of this particular pipe configuration, a finite element model of the experimental setup is built using Abaqus. The finite element simulations take advantage of the symmetry of the specimen with respect to two planes. One of these planes is perpendicular to the longitudinal axis of the pipe (neglecting the curvature of this axis) and cuts the specimen in half at its mid-length. On the other hand, the second symmetry plane divides the pipe cross section vertically in two equal parts. As a result, it is sufficient to model one quarter of the entire specimen in order to simulate the structural behaviour. Shell elements with reduced integration (S4R) are used in order to mesh the model. At the location of the loading jack (Figure 6.1) a reference point is created in order to apply the eccentric displacement. This reference point is called the 'loading pin' throughout the rest of this text. For the modelling of the material non-linearity, the stress-strain variation between the yield strength and ultimate strength points is modelled either by a linear isotropic hardening model or by Ramberg-Osgood material model as described in Section 2.1.1.

In the post-processing phase of the simulations, the main focus was on the distribution of the equivalent plastic strain on the pipe wall. It is observed that the variation of this parameter in case of unpressurized specimens is significantly different from the distribution in case of pressurized specimens. The distribution of the equivalent plastic strain on the pipe wall for the model of the specimen in Figure 6.2 is shown in Figure 6.4 and Figure 6.5 for un-pressurized and pressurized load cases respectively.

From Figure 6.4 and Figure 6.5 it can be observed that in both un-pressurized and pressurized load cases the compression side of the cold bend becomes highly deformed prior to the abortion of the simulations due to

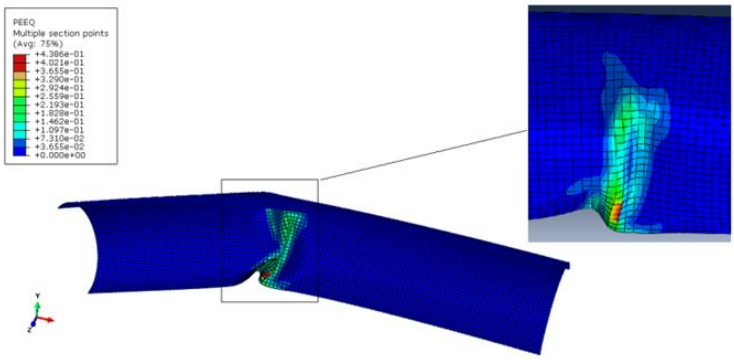

Figure 6.4: Distribution of the equivalent plastic strain for un-pressurized X65 cold bend

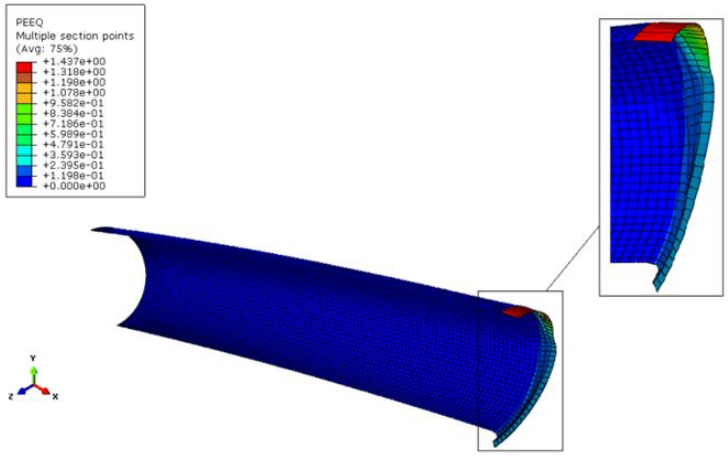

Figure 6.5: Distribution of the equivalent plastic strain for pressurized X65 cold bend

excessive displacements. However the deformed configuration of the un-pressurized case has a wrinkle formed at the intrados where the highest equivalent plastic strains are concentrated. On the other hand, the deformed configuration of the pressurized case has a bulge at the intrados and the highest equivalent plastic strains are concentrated at the tension side where the elements also seem to be highly distorted. The high distortion of the elements at the tension side can be interpreted as being a result of high tensile strain values beyond what the material can withstand. Based on this

observation it is assumed that the internal pressure can significantly change the structural behaviour of the cold bends. In order to better understand the effect of the internal pressure, a parametric study is carried out for the cold bend with X65 steel grade. In the scope of this parametric study, 10 different levels of the internal pressure are simulated. The internal pressure is varied between values causing 20% SMYS and 80% SMYS hoop stress. In all simulations of this parametric study, in addition to the internal pressure also, displacement controlled bending load is applied by pushing the loading pin in horizontal direction and increasing the curvature of the cold bend.

The applied displacement in an experiment has an effect on the structure only relative to the total length of it. Therefore the variation of a parameter such as equivalent plastic strain with respect to the applied displacement obtained from a particular experiment could not be compared to the result of another experiment with completely different specimen dimensions. Therefore there is a need to visualize the test result using a more general parameter instead of the applied displacement. For this purpose, the applied displacement values throughout the experiment are converted to the changes in the curvature of the specimen. The curvature of the cold bend is calculated based on the assumption that as the displacement of the loading pin (u) is applied, the cold bend deforms into a circular arc with a radius of curvature (R). Although in practice cold field bends do not have perfect curvature because of being progressively kinked, this assumption allows to approximate the overall curvature of the cold bend. More details about the concept of curvature are given in Appendix A.5. The non-linear relationship between u and R is a function of the total length of the cold bend (L), the bend angle (θ=L/2R) and the initial horizontal length of the cold bend (H_0)

as follows:

$$2R\sin\left(\frac{L}{2R}\right) = H_0 - u \tag{6.1}$$

Using the data output of Abaqus for the applied displacement u, the corresponding values of the radius of curvature are calculated using an iterative algorithm to solve Eq. 6.1. The pseudocode for this algorithm is given in Listing 1.

Listing 1: Pseudocode for the computation of the radius of curvature

```
Subroutine radius of curvature (displacement)
  Horizontal length = Initial Horizontal Length  − displacement
  Radius = initial estimate
  Horizontal Length Iteration =
  2·radius·sin((total length)/(2·radius))
  Do while | horizontal length−
  horizontal length iteration |>tolerance
     Radius = radius − step size
     Horizontal length iteration =
     2·radius·sin(totallength/(2·radius))
  Loop
  Return radius
End subroutine
```

The output of the algorithm in Listing 1 is inserted into the equation $\kappa = 1/R$ where κ is the curvature of the cold bend axis and R is the radius of curvature. The algorithm makes use of the fact that the initial radius of curvature is known and the radius of curvature after increasing the curvature is expected to be less than the initial radius of curvature. The algorithm reduces an initial estimate for the radius of curvature until Eq. 6.1 is satisfied. Therefore the initial estimate for the radius of curvature is supposed to be a real num-

ber greater than or equal to the initial radius of curvature in order for this algorithm to yield correct results. The conversion of all applied displacement values to a curvature value makes the comparison of the obtained results to other pipe geometric configurations possible. The relationship between the initial horizontal length H_0, the applied displacement u, the radius of curvature R and its initial value R_0 is also illustrated in Figure 6.6.

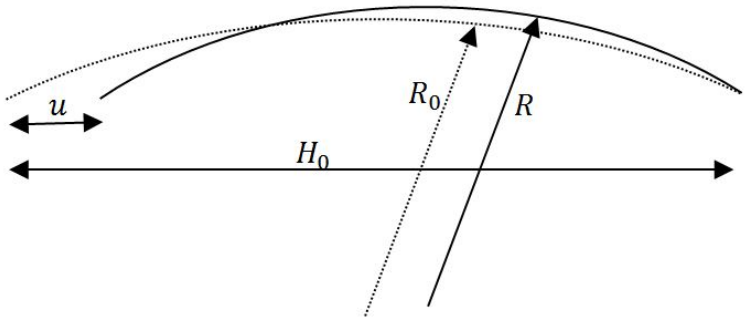

Figure 6.6: The original (undeformed) cold bend with an initial radius of curvature R_0 (dotted lines) versus the deformed cold bend after applying a horizontal displacement u and the new radius of curvature R[55].

The obtained relationship between the applied displacement u and the curvature of the pipe κ is illustrated in Figure 6.7. Clearly, the variation of the curvature with respect to the applied diaplacement is slightly nonlinear which is caused by the sinus term in Eq. 6.1. In the rest of this chapter, for each displacement of the loading pin the corresponding curvature value is used as a measure of deformation since the applied displacement value is dependent on a specific pipe configuration but the usage of the curvature value generalizes the obtained results.

Once the parametric study of the internal pressure is completed, the variation of the equivalent plastic strain (PEEQ) is visualized for both the intrados and the extrados of the cold bend. This visualization is repeated for all internal pressure values of the parametric study and plotted in Figure 6.8

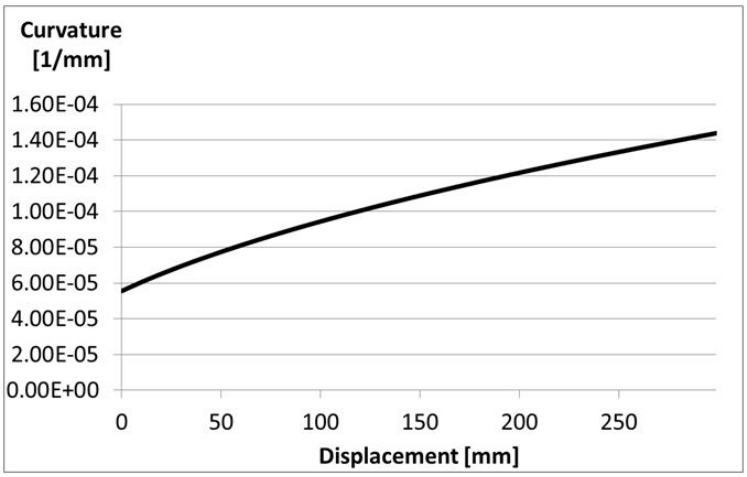

Figure 6.7: The relationship between the curvature κ and the applied displacement u

and Figure 6.9.

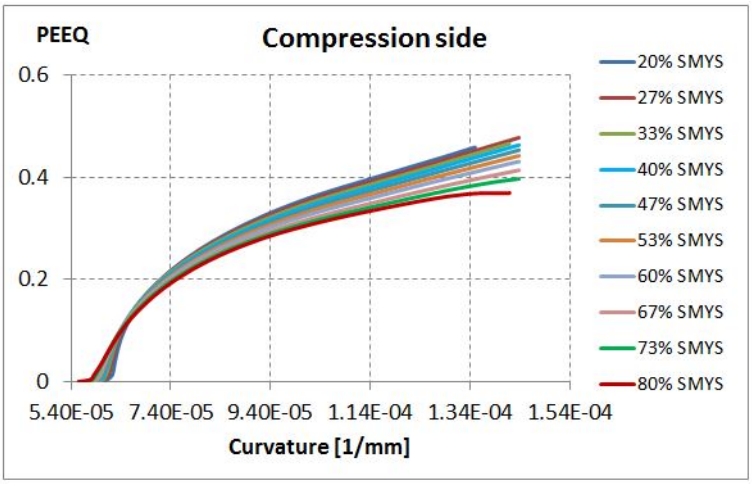

Figure 6.8: Development of the equivalent plastic strain at the intrados (X65)

From Figure 6.8 it can be deduced that in case of X65 steel grade, the development of the equivalent plastic strain at the intrados has a similar pattern for all levels of internal pressure with a slight reduction of the maximum strain value with increasing levels of internal pressure. A comparison of the 20% SMYS internal pressure curve with the 80% SMYS internal pressure

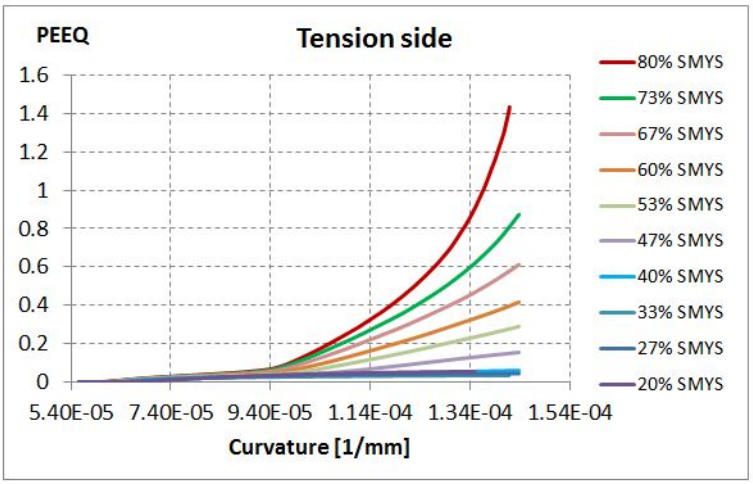

Figure 6.9: Development of the equivalent plastic strain at the extrados (X65)

curve in Figure 6.8 shows that there is about 24% decrease in the maximum equivalent plastic strain at the intrados as the internal pressure increases from 20% SMYS to 80% SMYS. On the other hand in the initial part of the curves up to the point of about $6.5 \cdot 10^{-5}$[1/mm] curvature, the amount of equivalent plastic strain is largest for the case of 80% SMYS internal pressure. It can be observed that at this particular curvature level, the same amount of PEEQ ($\sim$ 10%) is reached for all levels of internal pressure. Starting from this 10% strain point, those models having lower internal pressure value seem to have higher PEEQ values. Furthermore, in the later parts of the simulation, the behaviour of the PEEQ curves is such that they are asymptotically converging to values in the vicinity of 40%. In those simulations having internal pressure causing a hoop stress less than or equal to 67% SMYS, the PEEQ curves are converging to values above 40% whereas in case of internal pressures higher than 67% SMYS the PEEQ curves converge to values slightly below 40%. The 40% PEEQ level is designated as the threshold strain value for local failure in the rest of this chapter.

An analysis of the visualization in Figure 6.9 shows that the internal pres-

sure has greater effect on the PEEQ development in the pipe extrados. For internal pressure levels up to 47% SMYS the PEEQ value at the extrados stays below 5% throughout the simulations. On the other hand, for internal pressure levels equal to or greater than 47% SMYS, the PEEQ curves consist of two different parts exhibiting different behaviours. The initial parts of the curves up to a curvature level of $9.4 \cdot 10^{-5}$[1/mm] show almost identical behaviour for all levels of internal pressure. However starting from this curvature level, pipes with 47% SMYS or higher internal pressure have rapidly increasing PEEQ at the extados. Furthermore, the rate of increase of the PEEQ at the extrados for these high pressure load cases is getting larger with the internal pressure. This condition indicates that there is a transition in the structural behaviour as a result of increasing the internal pressure beyond a certain level. Also, for internal pressure values of 53% SMYS or less, the PEEQ at the extrados stays below 40% throughout the simulations whereas for internal pressures corresponding to 60% SMYS and above, the PEEQ at the extrados increases beyond 40%. Therefore, for the case of cold bends with X65 steel grade, the transition pressure could be located between 60% SMYS and 53% SMYS. However from the results of the parametric study the exact point where this transition takes place is hard to spot. For this purpose an alternative approach is devised which makes use of the amount of curvature at which the local failure occurs. In order to have a more accurate estimate of the exact transition point, two more simulations are carried out at 55% SMYS and 58% SMYS internal pressure levels. It is observed that at 55% SMYS internal pressure the local failure occurs at the compression side whereas at 58% SMYS internal pressure the local failure occurs at the tension side. The development of the PEEQ for 55% SMYS and 58% SMYS is shown in Figure 6.10 and Figure 6.11 for both the intrados and the extrados.

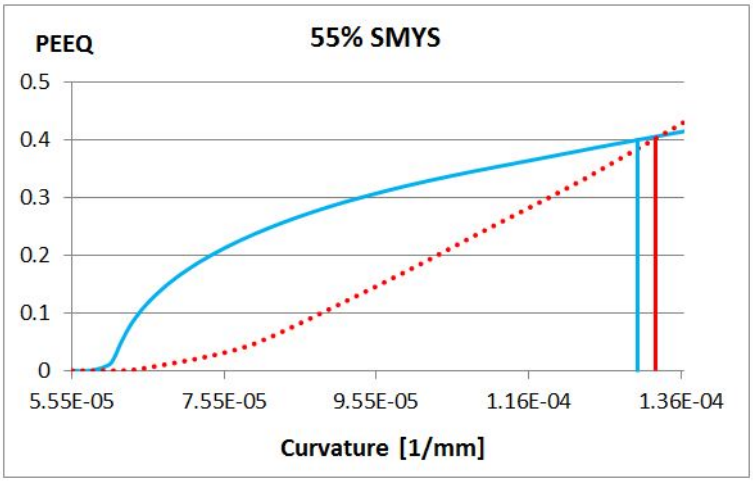

Figure 6.10: Compression side (solid) and tension side (dotted) variations of PEEQ (X65, 55% SMYS)

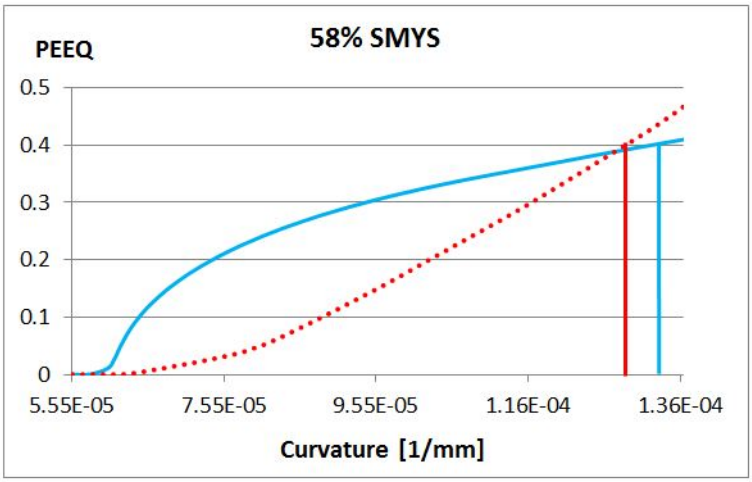

Figure 6.11: Compression side (solid) and tension side (dotted) variations of PEEQ (X65, 58% SMYS)

Observing the visualizations in Figure 6.10 and Figure 6.11, the exact point of transition should be expected to be located between 55% SMYS and 58% SMYS internal pressure levels. As mentioned before, with the aid of the level of curvature the exact transition point is spotted. The graphical procedure (Figure 6.12) is based on a two dimensional plot where the vertical

axis is used to show the difference of curvature values necessary to cause local failure at the intrados and the extrados. From Figure 6.10 and Figure 6.11 it can be reckoned that at 55% SMYS internal pressure the intrados local failure occurs earlier whereas at 58% SMYS internal pressure the extrados local failure occurs earlier. Therefore the difference of the failure curvature values of the intrados and the extrados have different signs for 55% SMYS and 58% SMYS internal pressure. The horizontal axis of the same two dimensional plot is used to show the level of internal pressure. In case of X65 steel grade the internal pressure levels 55% SMYS and 58% SMYS are marked on the horizontal axis. For each of these internal pressure levels the corresponding curvature difference is marked on the vertical axis. In this way the 55% SMYS and 58% SMYS load cases are located on the two dimensional space of curvature difference ($\Delta\kappa$) and internal pressure (p_i). Since the curvature differences for 55% SMYS and 58% SMYS have different signs, a straight line joining these points in the $(\Delta\kappa, p_i)$ space must intersect the pressure axis. This intersection point is assigned as the transition point of the failure mode from compression side fracture to tension side fracture.

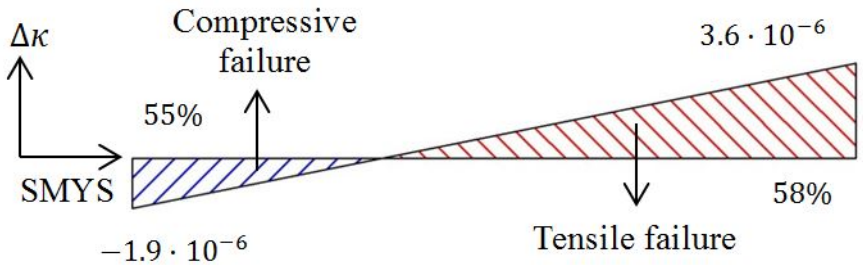

Figure 6.12: Transition of the failure mode in the $(\Delta\kappa, p_i)$ space (X65)

The curvature values that cause intrados and extrados fracture corresponding to 10 different internal pressure levels for X65 steel grade are listed in Table 6.1. In Table 6.1 the curvature values at which the local failure oc-

curs, are coloured in red. The internal pressure levels in Table 6.1 are chosen in such a way that the intervals between the pressure levels are smaller in the vicinity of the threshold pressure. According to Figure 6.12, the threshold internal pressure value for the transition of the failure mode from intrados side failure to extrados side failure for X65 steel grade is $p_{th,X65} = 56\%$ SMYS.

Table 6.1: Failure curvature values for X65

Internal pressure (%SMYS)	κ at intrados fracture [1/mm]	κ at extrados fracture [1/mm]	$\Delta\kappa$
20	1.16E-4	-	-
35	1.21E-4	-	-
53	1.28E-4	1.35E-4	-7.0E-6
55	1.30E-4	1.32E-4	-2.0E-6
58	1.32E-4	1.28E-4	4.0E-6
60	1.33E-4	1.27E-4	6.0E-6
67	1.40E-4	1.21E-4	1.9E-5
70	1.44E-4	1.20E-4	2.4E-5
75	-	1.17E-4	-
80	-	1.15E-4	-

6.1.1 Extension of the Parametric Study to X60 and X80 Steel Grades

In order to analyze the effect of the steel grade on the structural behaviour and the failure mode, the parametric study of the internal pressure is extended to X60 and X80 steel grades thereby extending the parametric study to all steel grades tested in the experimental study of Sen et al[1]. The geometric configuration of the cold bend is kept unchanged.

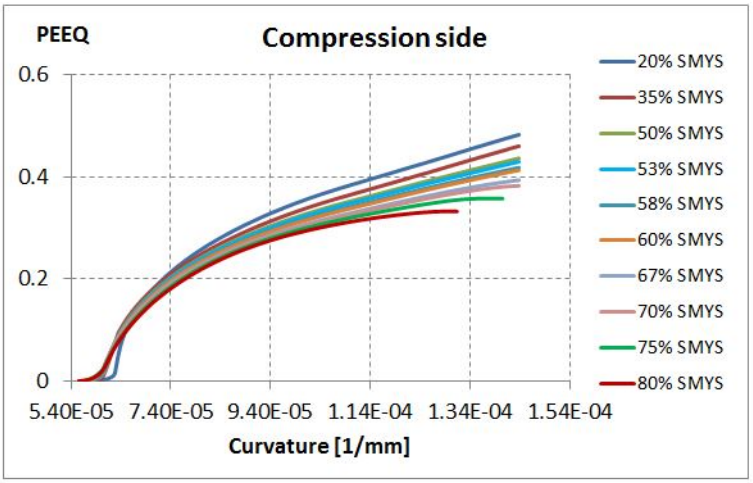

Figure 6.13: Development of the equivalent plastic strain at the intrados (X60)

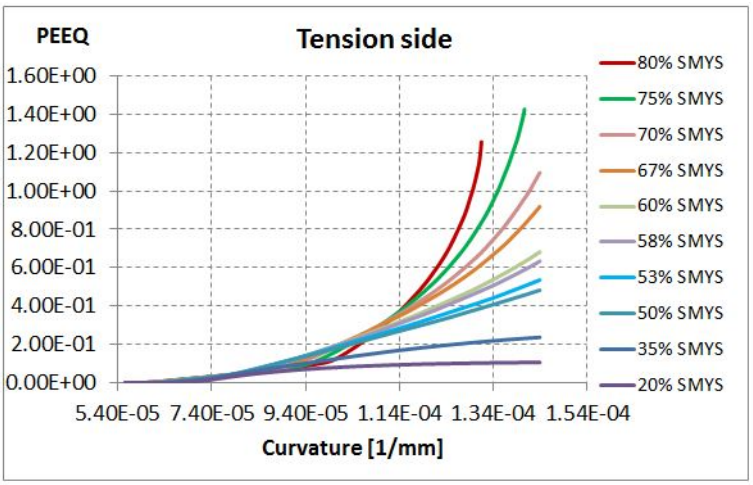

Figure 6.14: Development of the equivalent plastic strain at the extrados (X60)

6.1.1.1 Analysis of the X60 Steel Grade

Figure 6.13 and Figure 6.14 show the variation of the PEEQ at the intrados and extrados of a cold bend with X60 steel grade respectively. Clearly, the development of PEEQ at the intrados has a similar pattern to the development in case of X65 steel grade. Again, in the initial part of the curves the

curve for the 80% SMYS internal pressure case exhibits the highest PEEQ values although in case of X60 steel grade no single curvature level exists where all curves intersect at a certain value of PEEQ in the initial parts from where onwards the curves for the lower internal pressure cases have higher PEEQ values. As the internal pressure increases from 20% SMYS to 80% SMYS, a 36% decrease is observed at the maximum PEEQ value, which indicates that the curves are wider apart from each other compared to the case of X65 steel grade. The average PEEQ value to which the intrados curves asymptotocally converge towards the end of the simulations is again around 40%. Similar to the X65 steel grade case, for internal pressure values of 67% SMYS and above, the intrados PEEQ curves stay below the 40% level whereas for internal pressure levels less than 67% SMYS the PEEQ curves exceed 40%. Overall it can be inferred that the change in the level of internal pressure does not effect the PEEQ development at the intrados as much as it effects the PEEQ development at the extrados. Similar to the case of X65, the curves showing the PEEQ development at the extrados of the pipe with X60 steel grade (Figure 6.14) can be classified in two groups. In the first of these groups there are the curves for 20% SMYS and 35% SMYS internal pressure. These two low pressure curves stay below the 40% PEEQ threshold throughout the simulations. On the other hand the curves for 50% SMYS or greater internal pressure values, exceed 40%. This level of internal pressure is less than what was needed in case of X65 steel grade in order to make the extrados PEEQ exceed 40% (Figure 6.9). Based on this condition relative to the X65 case also, the level of the transition pressure is expected to be less than the X65 case. In order to spot the exact level of transition pressure, the first two internal pressure levels in Figure 6.14 which exceed the 40% strain level are compared to each other. The variations of the PEEQ at the

intrados and extrados of the 50% SMYS and 53% SMYS internal pressure cases are shown in Figure 6.15 and Figure 6.16.

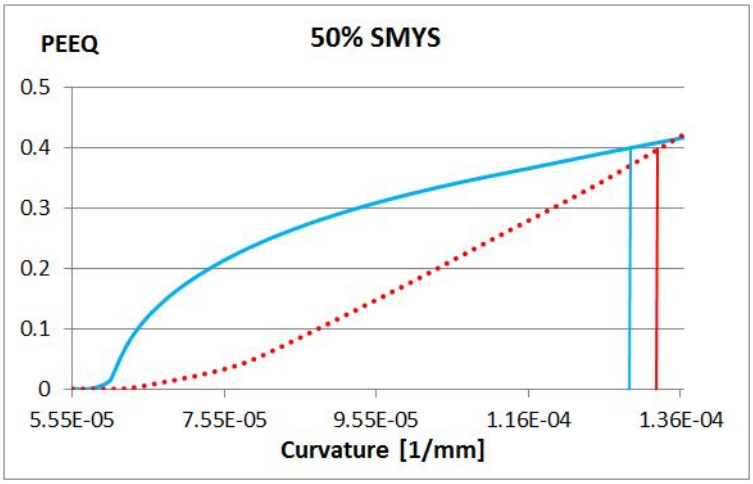

Figure 6.15: Compression side (solid) and tension side (dotted) variations of PEEQ (X60, 50% SMYS)

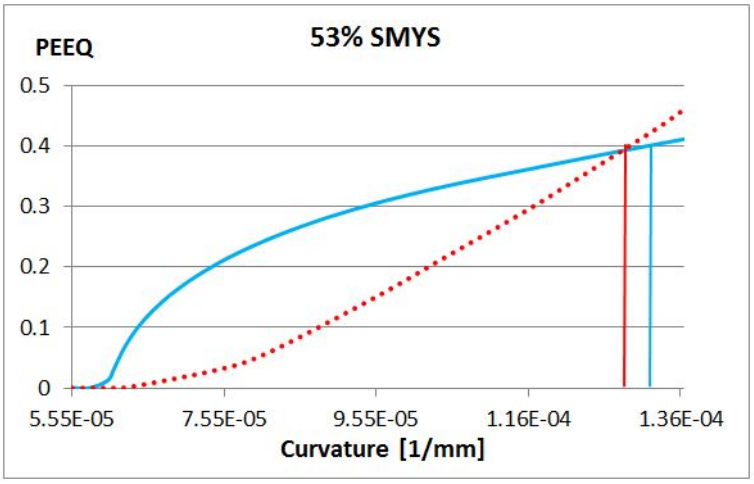

Figure 6.16: Compression side (solid) and tension side (dotted) variations of PEEQ (X60, 53% SMYS)

The intrados and extrados PEEQ curves in Figure 6.15 and Figure 6.16 show that, in case of 50% SMYS internal pressure the intrados of the pipe

reaches 40% PEEQ earlier than the extrados while for the case of 53% SMYS internal pressure the extrados of the pipe reaches 40% PEEQ earlier than the intrados. This condition confirms that indeed the transition pressure value is shifted to a lower internal pressure level in case of X60 steel grade compared to the X65 steel grade case. In order to identify the exact transition level, the same graphical procedure used for the X65 case is repeated using the failure curvature differences of the 50% SMYS and 53% SMYS load cases as shown in Figure 6.17. It should be noted that for all internal pressure levels less than 50% SMYS the intrados fracture takes place earlier whereas for all internal pressure levels greater than 53% SMYS the extrados fracture takes place earlier (Table 6.2).

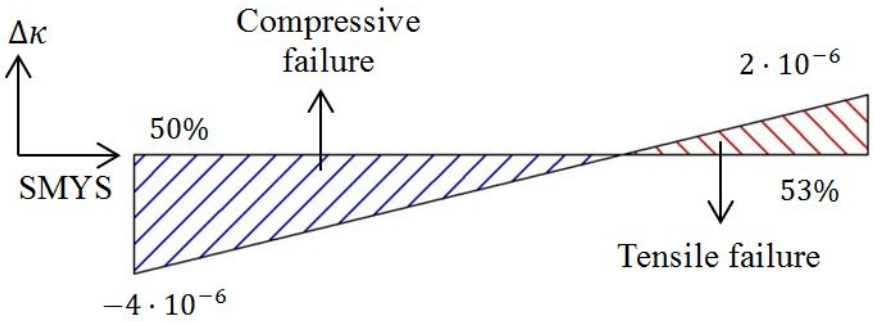

Figure 6.17: Transition of the failure mode in the $(\Delta\kappa, p_i)$ space (X60)

The curvature values that cause intrados and extrados fracture for 10 different values of internal pressure for X60 steel grade are listed in Table 6.2. According to Figure 6.17, the threshold internal pressure value for the transition of the failure mode from intrados side failure to extrados side failure for X60 steel grade is $p_{th,X60} = 52\%$ SMYS.

Table 6.2: Failure curvature values for X60

Internal pressure (%SMYS)	κ at intrados fracture	κ at extrados fracture	$\Delta\kappa$
20	1.16E-4	-	-
35	1.23E-4	-	-
50	1.29E-4	1.33E-4	-4E-6
53	1.31E-4	1.29E-4	2E-6
58	1.35E-4	1.23E-4	1.20E-5
60	1.37E-4	1.22E-4	1.50E-5
67	-	1.18E-4	-
70	-	1.16E-4	-
75	-	1.15E-4	-
80	-	1.15E-4	-

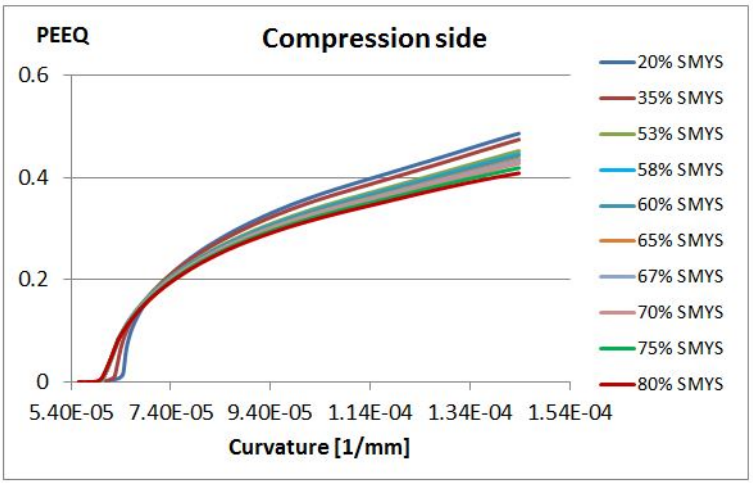

Figure 6.18: Development of the equivalent plastic strain at the intrados (X80)

6.1.1.2 Analysis of the X80 Steel Grade

Finally, Figure 6.18 and Figure 6.19 show the variation of PEEQ in case of X80 steel grade for the intrados and the extrados of the pipe respectively. From Figure 6.18 it can be observed that the PEEQ development at the intrados of the pipe with X80 steel grade has a similar pattern to the case

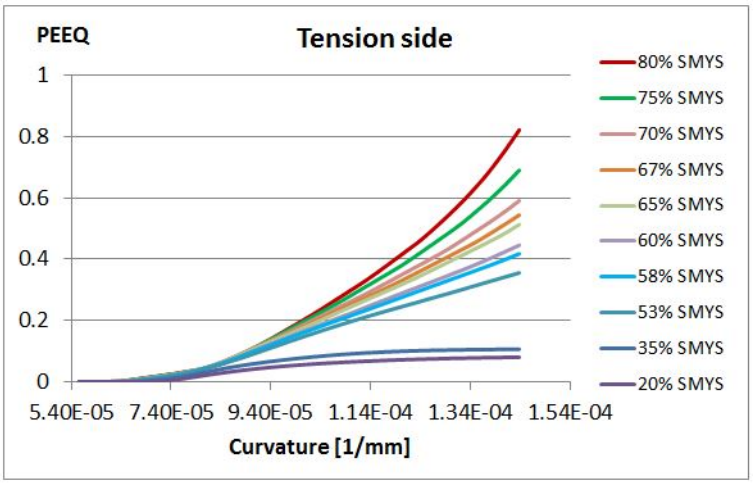

Figure 6.19: Development of the equivalent plastic strain at the extrados (X80)

with X65 steel grade. However in case of X80 steel grade, for all levels of internal pressure above 35% SMYS the PEEQ curves exceed the 40% level which is not the case for X65 steel grade. The maximum PEEQ value reached at the intrados for the load case with 20% SMYS internal pressure is 18% higher than the maximum PEEQ value reached at the intrados for the load case with 80% SMYS internal pressure. This difference is smaller than what was observed for X60 and X65 steel grades. This observation leads to the inference that the PEEQ variation at the intrados becomes less affected by the changes in the internal pressure as the steel grade increases from X60 to X80.

While the increase in the steel grade causes the PEEQ values at the intrados to increase, at the extrados the lowest PEEQ values of all three steel grades are observed for X80. Figure 6.19 shows that the lowest internal pressure level at which the 40% PEEQ level could be reached at the extrados is 58% SMYS for X80. This internal pressure level is higher than both of the levels at which the extrados of the X60 and X65 pipes reached the 40%

PEEQ level. Figure 6.20 shows the PEEQ variation at the intrados and the extrados for X80 steel grade at 65% SMYS internal pressure. According to Figure 6.20, the compression and tension sides reach 40% PEEQ simultaneously under 65% SMYS internal pressure. Therefore the transition internal pressure can be estimated as $p_{th,X80} = 65\%$ SMYS for X80 steel grade without further approximations. It should be noted that for all internal pressure levels less than 65% SMYS the intrados fracture occurs earlier than the extrados fracture whereas for all internal pressure levels above 65% SMYS the extrados fracture occurs earlier than the intrados fracture. This is also confirmed by the list of curvature values for the intrados and extrados fracture in Table 6.3.

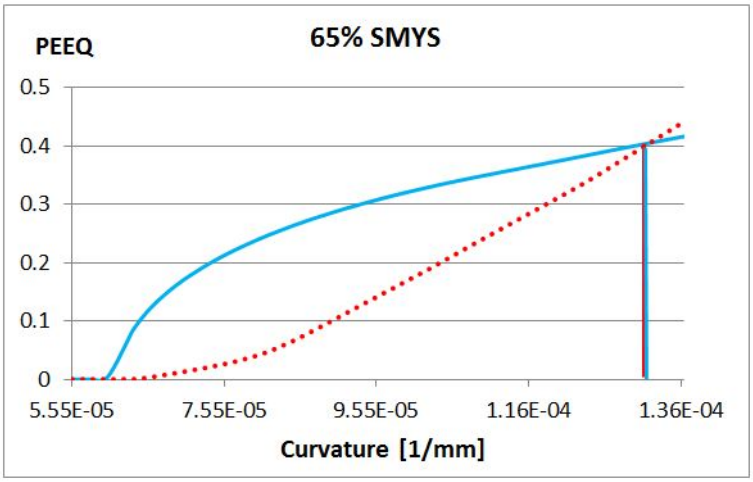

Figure 6.20: Compression side (solid) and tension side (dotted) variations of PEEQ (X80, 65% SMYS)

6.2 CLASSIFICATION OF FAILURE MODES

In this section the load cases analyzed in the previous sections are classified into two groups according to their corresponding mode of failure. The outcome of the simulations in the previous sections showed that, pipes may

Table 6.3: Failure curvature values for X80

Internal pressure (%SMYS)	κ at intrados fracture	κ at extrados fracture	$\Delta\kappa$
20	1 .14E-4	-	-
35	1 .19E-4	-	-
53	1 .25E-4	-	-
58	1 .26E-4	1.41E-4	-1.5E-5
60	1 .27E-4	1.38E-4	-1.1E-5
65	1 .298E-4	1 .298E-4	0
67	1.31E-4	1 .28E-4	3.01E-6
70	1.32E-4	1 .26E-4	6.08E-6
75	1.35E-4	1 .22E-4	1.35E-5
80	1.40E-4	1 .20E-4	2.0E-5

fail under excessive tensile strain, bending and internal pressure either at the extrados or at the intrados. Based on this observation, the intrados and extrados failure scenarios are defined as two different classes of pipe structural behaviour. The parametric studies showed that both internal pressure and the grade of pipe steel play a decisive role in determining to which class a particular pipe configuration belongs. Therefore in this current section, each load case is described as a 2 dimensional vector $\mathbf{x}_t \in \mathbb{R}^2$ that contains the level of internal pressure and the grade of steel for each pipe configuration. The classification is carried out using a classifier function $f(\mathbf{x}_t)$ that is defined as follows:

$$f(\mathbf{x}_t) = \begin{cases} 1 & \text{if } \langle \mathbf{w}, \mathbf{x}_t \rangle + b > 0 \\ -1 & \text{else} \end{cases} \tag{6.2}$$

In Eq. 6.2, $\mathbf{w} \in \mathbb{R}^2$ is the weight vector and $b \in \mathbb{R}$ is the bias coefficient. The symbol $\langle \cdot, \cdot \rangle$ denotes the scalar product of two vectors. The classifier function can be obtained using the perceptron algorithm. The perceptron

algorithm was proposed by Frank Rosenblatt in 1956 and builds the foundation of modern machine learning algorithms. The algorithm uses a training set $T = \{(\mathbf{x}_t, y_t) : \mathbf{x}_t \in \mathbb{R}^2, y_t \in \{-1, 1\}\}$ of pipe configurations with known behaviour in order to obtain a proper weight vector and bias coefficient. The letter t in the notation for a training sample $\mathbf{x}_t$ is the index of the training sample and belongs to the set $\{1, ..., l\}$ where l is the total number of training samples. For each training sample $\mathbf{x}_t$ in the training set, a label y_t is assigned according to the known behaviour of the sample. If the sample $\mathbf{x}_t$ is known to be in the intrados fracture class, then its label y_t is equal to 1 and if it is known to be in the extrados fracture class then its label is equal to -1.

The classifier function in Eq. 6.2 makes a decision about the class of a vector $\mathbf{x}_t$ which depends on the expression $\langle \mathbf{w}, \mathbf{x}_t \rangle + b$ having a value greater than 0 or not. Therefore the set of vectors $\mathbf{x}$ in the $\mathbb{R}^2$ space for which this expression is equal to 0 builds the decision boundary of the training set. Formally the decision boundary is defined as $DB = \{\mathbf{x} \in \mathbb{R}^2 : \langle \mathbf{w}, \mathbf{x} \rangle + b = 0\}$. The weight vector $\mathbf{w}$ determines the orientation of the decision boundary and is perpendicular to it. In order to show this, let $\mathbf{v}_1$ and $\mathbf{v}_2$ be any two vectors in DB. Then $\langle \mathbf{w}, \mathbf{v}_1 \rangle + b = \langle \mathbf{w}, \mathbf{v}_2 \rangle + b = 0$ and $\langle \mathbf{w}, \mathbf{v}_1 - \mathbf{v}_2 \rangle = 0$. Therefore any vector lying within DB is perpendicular to $\mathbf{w}$. This can be easily visualized in $\mathbb{R}^2$ (Figure 6.21).

In Figure 6.21 the symbols 'x' and 'o' represent the samples of two different classes and γ_G denotes the geometric margin of the decision boundary DB between these two classes. The geometric margin is the smallest distance between any sample in the training set and the hyperplane that separates the two classes in the training set (the decision boundary). An expression to compute the magnitude of the geometric margin can be obtained as follow: Let $\mathbf{x}_t$ be the training sample having the least distance to the decision

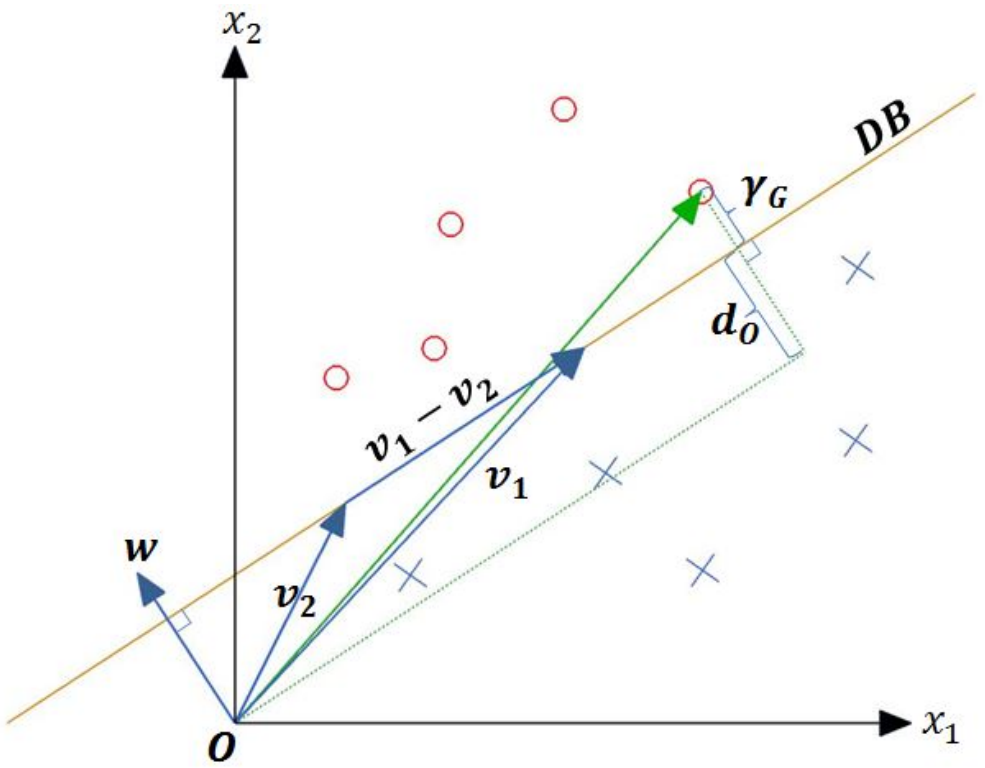

Figure 6.21: Geometry of the training set and the decision boundary in $\mathbb{R}^2$

boundary. Then, $\mathbf{x}_t$ can be expressed as the sum of its orthogonal projection on DB ($(\mathbf{x}_t)_\perp$) and another vector which is parallel to the weight vector $\mathbf{w}$ as in Eq. 6.3:

$$\mathbf{x}_t = (\mathbf{x}_t)_\perp + (\gamma_G + d_O)\frac{\mathbf{w}}{\|\mathbf{w}\|} \tag{6.3}$$

In Eq. 6.3, d_O is the distance of the decision boundary from the origin and is closely related to the bias coefficient b first introduced in Eq. 6.2. In order to see that, let $\mathbf{x}_0$ be a vector that is perpendicular to the decision boundary and has a magnitude equal to the distance of the decision boundary from the origin such that $\|\mathbf{x}_0\| = d_O$. Then $\mathbf{x}_0$ has the same direction as $\mathbf{w}$ and can be written as $\mathbf{x}_0 = \|\mathbf{x}_0\|\frac{\mathbf{w}}{\|\mathbf{w}\|}$. Clearly, $\mathbf{x}_0$ is also in the decision boundary and therefore $\langle \mathbf{w}, \mathbf{x}_0 \rangle + b = \frac{\|\mathbf{x}_0\|}{\|\mathbf{w}\|}\langle \mathbf{w}, \mathbf{w} \rangle + b = \|\mathbf{x}_0\|\|\mathbf{w}\| + b = 0$. Therefore

d_O can be computed as in Eq. 6.4.

$$d_O = -\frac{b}{\|\mathbf{w}\|} \tag{6.4}$$

Plugging the expression for d_O from Eq. 6.4 into Eq. 6.3 and taking the scalar product of both sides of the equation with $\mathbf{w}$ we obtain Eq 6.5.

$$\langle \mathbf{w}, \mathbf{x}_t \rangle = \langle \mathbf{w}, (\mathbf{x}_t)_\perp \rangle + \frac{\gamma_G}{\|\mathbf{w}\|} \langle \mathbf{w}, \mathbf{w} \rangle - \frac{b}{\|\mathbf{w}\|^2} \langle \mathbf{w}, \mathbf{w} \rangle \tag{6.5}$$

Since $\mathbf{w}$ and $(\mathbf{x}_t)_\perp$ are perpendicular to each other, the $\langle \mathbf{w}, (\mathbf{x}_t)_\perp \rangle$ term in Eq. 6.5 vanishes. After adding b to both sides of Eq. 6.5, we obtain Eq. 6.6 which shows the expression for the geometric margin γ_G [59].

$$\langle \mathbf{w}, \mathbf{x}_t \rangle + b = \gamma_G \|\mathbf{w}\| \Rightarrow \boxed{\gamma_G = \frac{\langle \mathbf{w}, \mathbf{x}_t \rangle + b}{\|\mathbf{w}\|}} \tag{6.6}$$

The perceptron algorithm starts with the initialization of $\mathbf{w}$ and b as $\mathbf{w}^{(0)} = \mathbf{0}$, $b^{(0)} = 0$. In the next step the algorithm traverses the training set. For each pipe sample $\mathbf{x}_t$ in the training set, if the product $y_t(\langle \mathbf{w}^{(k)}, \mathbf{x}_t \rangle + b^{(k)})$ is less than or equal to zero, then this would imply that the actual label of the training sample and the predicted label have opposite signs and the training sample is misclassified. In this case, $\mathbf{w}^{(k)}$ and $b^{(k)}$ are updated as follows:

$$\mathbf{w}^{(k+1)} = \mathbf{w}^{(k)} + y_t \mathbf{x}_t \tag{6.7}$$

$$b^{(k+1)} = b^{(k)} + y_t R^2 \tag{6.8}$$

where $R = \max \|\mathbf{x}_t\|$ and the symbol $\|\cdot\|$ denotes the Euclidean norm of a vector. It can be proven that the above updates improve the weight vector and the bias coefficient as follows[57]: Assume that after the updates, another

attempt is made in order to classify the same training sample $\mathbf{x}_t$. Then Eq. 6.9 shows that the new product $y_t(\langle \mathbf{w}^{(k+1)}, \mathbf{x}_t \rangle + b^{(k+1)})$ is closer to a positive value compared to $y_t(\langle \mathbf{w}^{(k)}, \mathbf{x}_t \rangle + b^{(k)})$.

$$\begin{aligned} y_t(\langle \mathbf{w}^{(k+1)}, \mathbf{x}_t \rangle + b^{(k+1)}) &= y_t(\langle \mathbf{w}^{(k)} + y_t \mathbf{x}_t, \mathbf{x}_t \rangle + b^{(k)} + y_t R^2) \\ &= y_t(\langle \mathbf{w}^{(k)}, \mathbf{x}_t \rangle + y_t \|\mathbf{x}_t\|^2 + b^{(k)} + y_t R^2) \\ &= y_t(\langle \mathbf{w}^{(k)}, \mathbf{x}_t \rangle + b^{(k)}) + \|\mathbf{x}_t\|^2 + R^2 \\ &\geq y_t(\langle \mathbf{w}^{(k)}, \mathbf{x}_t \rangle + b^{(k)}) \end{aligned} \tag{6.9}$$

It can also be proven that after a finite number of updates a proper classifier function can be obtained as long as the samples in the training set are linearly separable with a functional margin $\gamma_F > 0$. The functional margin γ_t of a training sample $\mathbf{x}_t$ with respect to a separating hyperplane (decision boundary)$(\mathbf{w}, b)$ is defined as[58]:

$$\gamma_t = y_t(\langle \mathbf{w}, \mathbf{x}_t \rangle + b) \tag{6.10}$$

and the functional margin γ_F of a separating hyperplane $(\mathbf{w}, b)$ is defined as the minimum of all functional margins associated with a training set. A larger functinal margin implies that the training samples are geometrically farther away from the separating hyperplane and therefore the two classes are more distinctly separated. The relationship between the functional margin and the geometric separateness of the classes can be reckoned by comparing the expressions for the geometric margin (Eq. 6.6) and the functional margin (Eq. 6.10).

In order to prove that the perceptron algorithm converges to a solution after a finite number of iterations, the following new weight vectors $\widetilde{\mathbf{w}}$ and training samples $\widetilde{\mathbf{x}}_t$ are defined by appending R to every training sample and

$b^{(k)}/R$ to every weight vector $\mathbf{w}^{(k)}$:

$$\widetilde{\mathbf{x}}_t = (\mathbf{x}_t^T, R), \quad \widetilde{\mathbf{w}}^{(k)} = ({\mathbf{w}^{(k)}}^T, b^{(k)}/R) \tag{6.11}$$

Given that the training samples are linearly separable, there exists a separating hyperplane $(\mathbf{w}^*, b^*)$ such that for any $(\mathbf{x}_t, y_t) \in T$, $y_t(\langle \mathbf{w}^*, \mathbf{x}_t \rangle + b^*) = y_t \langle \widetilde{\mathbf{w}}^*, \widetilde{\mathbf{x}}_t \rangle \geq \gamma^*$ where γ^* is the functional margin of $(\mathbf{w}^*, b^*)$.

Assume that the weight vector $\widetilde{\mathbf{w}}^{(k-1)}$ resulted in a misclassification of the sample $\widetilde{\mathbf{x}}_t$ and is therefore updated to $\widetilde{\mathbf{w}}^{(k)}$. $\widetilde{\mathbf{w}}^{(k)}$ and $\widetilde{\mathbf{w}}^*$ both belong to the vector space $\mathbb{R}^3$ and the cosine of the angle between them is defined as in Eq. 6.12.

$$\cos(\widetilde{\mathbf{w}}^*, \widetilde{\mathbf{w}}^{(k)}) = \frac{\langle \widetilde{\mathbf{w}}^*, \widetilde{\mathbf{w}}^{(k)} \rangle}{\|\widetilde{\mathbf{w}}^*\| \|\widetilde{\mathbf{w}}^{(k)}\|} \leq 1 \tag{6.12}$$

In Eq. 6.12, the expression for $\widetilde{\mathbf{w}}^{(k)}$ can be expanded as follows.

$$\begin{aligned} \widetilde{\mathbf{w}}^{(k)} &= \left({\mathbf{w}^{(k)}}^T, \frac{b^{(k)}}{R} \right) = \left({\mathbf{w}^{(k-1)}}^T + y_t \mathbf{x}_t^T, \frac{b^{(k-1)} + y_t R^2}{R} \right) \\ &= \left({\mathbf{w}^{(k-1)}}^T + y_t \mathbf{x}_t^T, \frac{b^{(k-1)}}{R} + y_t R \right) \\ &= \widetilde{\mathbf{w}}^{(k-1)} + y_t \widetilde{\mathbf{x}}_t \end{aligned} \tag{6.13}$$

It can also be shown that the scalar product term in Eq. 6.12 is greater than or equal to $k\gamma^*$. In order to show this let $k = 1$, then $\langle \widetilde{\mathbf{w}}^*, \widetilde{\mathbf{w}}^{(1)} \rangle = \langle \widetilde{\mathbf{w}}^*, \widetilde{\mathbf{w}}^{(0)} + y_t \widetilde{\mathbf{x}}_t \rangle = y_t \langle \widetilde{\mathbf{w}}^*, \widetilde{\mathbf{x}}_t \rangle \geq \gamma^*$ since $\widetilde{\mathbf{w}}^{(0)}$ is initialized as the zero vector. If for some $n \in \mathbb{N}$, $\langle \widetilde{\mathbf{w}}^*, \widetilde{\mathbf{w}}^{(n)} \rangle \geq n\gamma^*$, then $\langle \widetilde{\mathbf{w}}^*, \widetilde{\mathbf{w}}^{(n+1)} \rangle = \langle \widetilde{\mathbf{w}}^*, \widetilde{\mathbf{w}}^{(n)} + y_t \widetilde{\mathbf{x}}_t \rangle = y_t \langle \widetilde{\mathbf{w}}^*, \widetilde{\mathbf{x}}_t \rangle + \langle \widetilde{\mathbf{w}}^*, \widetilde{\mathbf{w}}^{(n)} \rangle \geq \gamma^* + n\gamma^* = (n+1)\gamma^*$. By induction it follows that for any $k \in \mathbb{N}$, $\langle \widetilde{\mathbf{w}}^*, \widetilde{\mathbf{w}}^{(k)} \rangle \geq k\gamma^*$. Using this result the inequality in Eq. 6.14 is established.

$$\frac{k\gamma^*}{\|\widetilde{\mathbf{w}}^*\| \|\widetilde{\mathbf{w}}^{(k)}\|} \leq 1 \tag{6.14}$$

Furthermore, the boundedness of the norm $\|\widetilde{\mathbf{w}}^{(k)}\|$ can be shown as follows:

$$\begin{aligned}\|\widetilde{\mathbf{w}}^{(k)}\|^2 &= \langle \widetilde{\mathbf{w}}^{(k-1)} + y_t \widetilde{\mathbf{x}}_t, \widetilde{\mathbf{w}}^{(k-1)} + y_t \widetilde{\mathbf{x}}_t \rangle \\ &= \|\widetilde{\mathbf{w}}^{(k-1)}\|^2 + 2y_t \langle \widetilde{\mathbf{w}}^{(k-1)}, \widetilde{\mathbf{x}}_t \rangle + \|\widetilde{\mathbf{x}}_t\|^2\end{aligned} \tag{6.15}$$

Since the weight vector $\widetilde{\mathbf{w}}^{(k-1)}$ resulted in a misclassification, it is known that $y_t \langle \widetilde{\mathbf{w}}^{(k-1)}, \widetilde{\mathbf{x}}_t \rangle \leq 0$. Therefore,

$$\|\widetilde{\mathbf{w}}^{(k)}\|^2 \leq \|\widetilde{\mathbf{w}}^{(k-1)}\|^2 + \|\widetilde{\mathbf{x}}_t\|^2$$

Using $\|\widetilde{\mathbf{x}}_t\|^2 = \|\mathbf{x}_t\|^2 + R^2$ gives

$$\|\widetilde{\mathbf{w}}^{(k)}\|^2 \leq \|\widetilde{\mathbf{w}}^{(k-1)}\|^2 + 2R^2 \tag{6.16}$$

Eq. 6.16 implies the boundedness of $\|\widetilde{\mathbf{w}}^{(k)}\|$. In order to prove this, consider that for $k = 1$, $\|\widetilde{\mathbf{w}}^{(1)}\|^2 \leq \|\widetilde{\mathbf{w}}^{(0)}\|^2 + 2R^2 = 2R^2 = 2kR^2$. If for some $n \in \mathbb{N}$, $\|\widetilde{\mathbf{w}}^{(n)}\|^2 \leq 2nR^2$ then using Eq. 6.16 we obtain $\|\widetilde{\mathbf{w}}^{(n+1)}\|^2 \leq \|\widetilde{\mathbf{w}}^{(n)}\|^2 + 2R^2 \leq 2nR^2 + 2R^2 = (n+1)2R^2$. By induction it follows that:

$$\forall k \in \mathbb{N}, \|\widetilde{\mathbf{w}}^{(k)}\|^2 \leq k2R^2 \tag{6.17}$$

By plugging Eq. 6.17 in Eq. 6.14, squaring both sides of the inequality and using the boundedness of $\widetilde{\mathbf{w}}^*$, Eq. 6.18 shows that only a finite number of iterations are needed in order to obtain a proper classifier function.

$$\frac{k\gamma^*}{\|\widetilde{\mathbf{w}}^*\| R\sqrt{2k}} \leq 1 \Rightarrow \frac{k^2(\gamma^*)^2}{\|\widetilde{\mathbf{w}}^*\|^2 R^2 2k} \leq 1 \Rightarrow \boxed{k \leq \frac{2R^2\|\widetilde{\mathbf{w}}^*\|^2}{(\gamma^*)^2}} \tag{6.18}$$

The perceptron algorithm is applied to the cold bends using the simulation results for X60, X65 and X80 steel grades as a training set. Two different

classifier functions are obtained for the two cases when the steel grade and the internal pressure have reversed positions in the vectors $\mathbf{x}_t$. In the $\mathbb{R}^2$ space the decision boundary between the two failure modes is computed as

$$DB_1 = \{\mathbf{x} \in \mathbb{R}^2 : x_2 = 0.664x_1 + 0.125\} \tag{6.19}$$

for the case when x_1 stands for the steel grade and x_2 stands for the internal pressure. The internal pressure is described in terms of the ratio of the hoop stress caused by it to the SMYS of the pipe base metal and the steel grades are described by dividing the steel grade numbers by one hundred in order to bring the two parameters to the same order of magnitude. A satisfactory decision boundary with a functional margin of 0.8 is achieved after 2893 iterations. For this order of the parameters, the sample space together with its decision boundary is visualized in Figure 6.22. In Figure 6.22 and in the subsequent images of training sets, intrados fractures are denoted with an 'x' while extrados fractures are denotes with an 'o'.

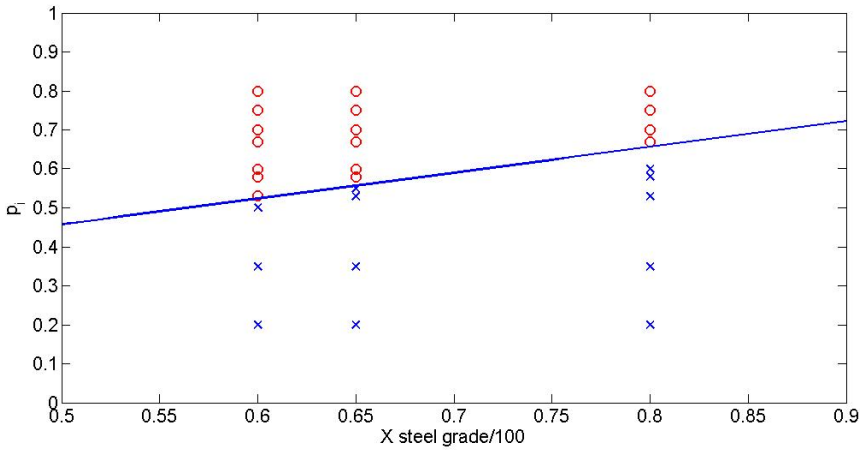

Figure 6.22: Training set of cold bends separated by a decision boundary (x_1 :steel grade, x_2 :internal pressure)

The training set and the decision boundary for the case of reversely ordered sample vectors is plotted in Figure 6.23. In this case the decision boundary is computed as

$$DB_2 = \{\mathbf{x} \in \mathbb{R}^2 : x_2 = 1.352x_1 - 0.1\} \tag{6.20}$$

The source code of the perceptron algorithm used in this section can be

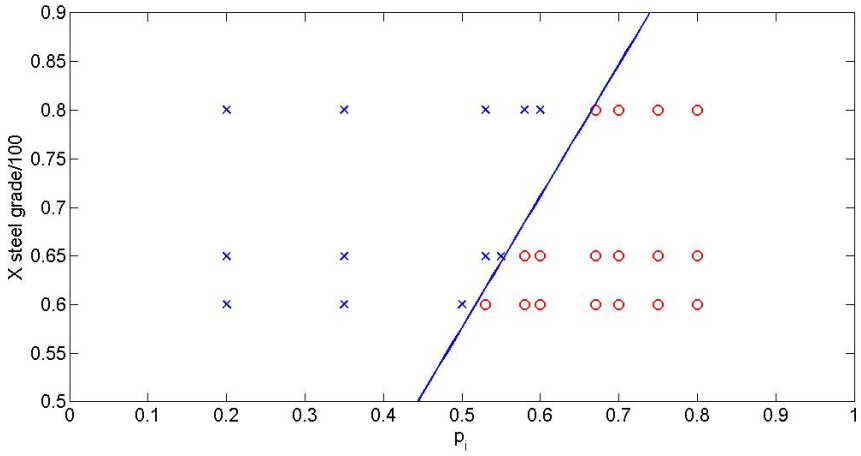

Figure 6.23: Training set of cold bends separated by a decision boundary (x_1 :internal pressure, x_2 :steel grade)

found in the Appendix A.6.

In order to test the obtained classifier function, further simulations are carried out for cold bends having X70 steel grade. The variations of the PEEQ values for a range of internal pressure between 20% SMYS and 80% SMYS at the intrados and extrados of a X70 cold bend are plotted in Figure 6.24 and Figure 6.25 respectively.

The variation of the PEEQ at the intrados and extrados is compared for all the internal pressure levels listed in Figure 6.24 and Figure 6.25. It is found that at 60% SMYS internal pressure, the intrados and extrados of the pipe

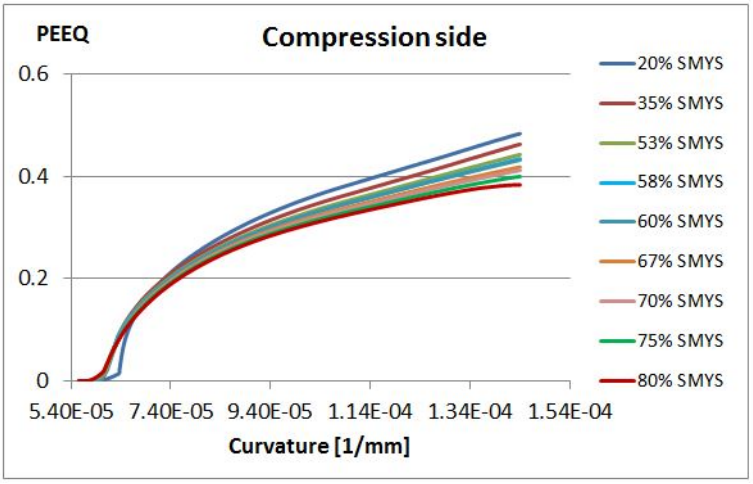

Figure 6.24: Variation of PEEQ at the intrados for X70 steel grade

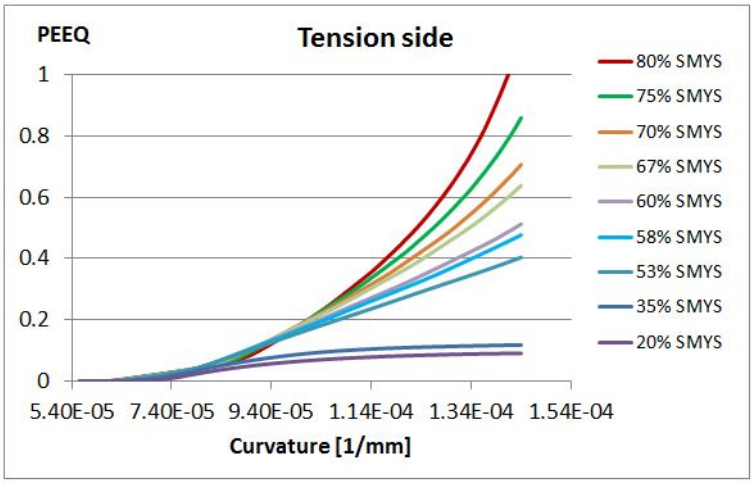

Figure 6.25: Variation of PEEQ at the extrados for X70 steel grade

reach the 40% limit strain value simultaneously (Figure 6.26). Furthermore, for all internal pressure levels below 60% SMYS the intrados reaches the limit strain earlier than the extrados, whereas for all internal pressure levels above 60% SMYS the extrados reaches the limit strain earlier than the intrados (Table 6.4). Based on this observation the threshold internal pressure level for the transition of the failure mode from intrados fracture to extrados fracture is assigned as $p_{th,X70} = 60\%$ SMYS.

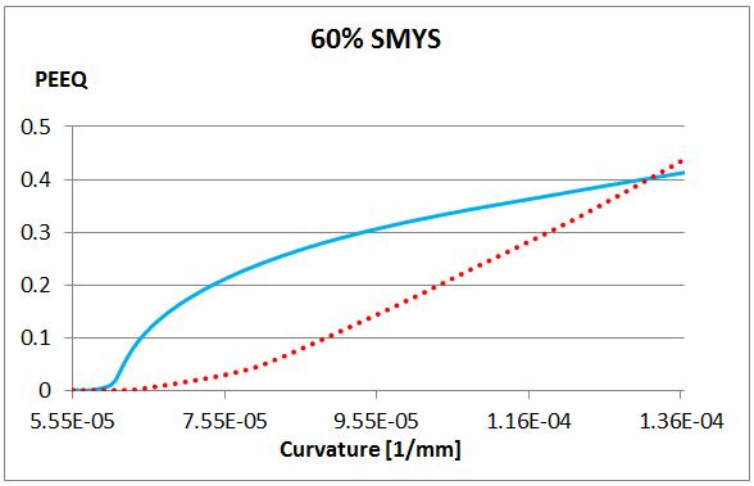

Figure 6.26: Variation of PEEQ at the extrados (dotten) and intrados (solid) for 60% SMYS internal pressure and X70 steel grade

Table 6.4: Failure curvature values for X70

Internal pressure (%SMYS)	κ at intrados fracture [1/mm]	κ at extrados fracture [1/mm]	$\Delta\kappa$
20	1.17E-4	-	-
35	1.22E-4	-	-
53	1.28E-4	1.44E-4	-1.60E-5
58	1.31E-4	1.34E-4	-3.50E-6
60	1.32E-4	1.32E-4	0
67	1.37E-4	1.24E-4	1.22E-5
70	1.38E-4	1.22E-4	1.6E-5
75	1.44E-4	1.19E-4	2.5E-5
80	-	1.17E-4	-

All load cases listed in Table 6.4, could be correctly classified using the decision boundaries DB_1 and DB_2. This can be shown for DB_1 by plugging $x_1 = 0.7$ (X70) in Eq. 6.19. The value of the internal pressure that separates the two failure modes can be thus computed as 0.59 (59% SMYS) so that for an X70 steel grade, any internal pressure level greater than 59% SMYS

would be marked with an 'o' and any internal pressure level less than 59% SMYS would be marked with an 'x' in Figure 6.22. The same result can be obtained by plugging 0.7 for x_2 in Eq. 6.20 which gives the point (0.59, 0.7) on the decision boundary shown in Figure 6.23.

6.3 Closing Remarks

The numerical investigation of cold bends in this current chapter showed that indeed the structural response of cold bends can significantly change not only depending on the operating pressure but also depending on the grade of steel used in pipeline manufacturing. As the decisive parameter in the failure of a pipeline structure, the variations of the equivalent plastic strain (PEEQ) are investigated. The differences between the PEEQ distributions at the intrados and the extrados are visualized for different levels of internal pressure for the steel grades X60, X65, X70 and X80. Using a fixed limit strain failure criterion, it was observed that the mode of failure changes at certain levels of internal pressure from intrados fracture to extrados fracture. Moreover this transition level for the internal pressure increases with the steel grade. In order to clarify this relationship between the steel grade and the level of internal pressure at which the failure mode changes, in Figure 6.27 the transition pressure level is plotted with respect to the grade of steel for all steel grades simulated in this study. According to Figure 6.27, the transition pressure linearly increases from 52% SMYS for X60 steel grade to 65% SMYS for X80 steel grade with a slight deviation from the linear trend at X70 steel grade.

The outcome of the parametric studies was that certain combinations of the steel grade and internal pressure result in intrados fracture of the pipe under excessive tensile strains whereas other combinations result in extrados

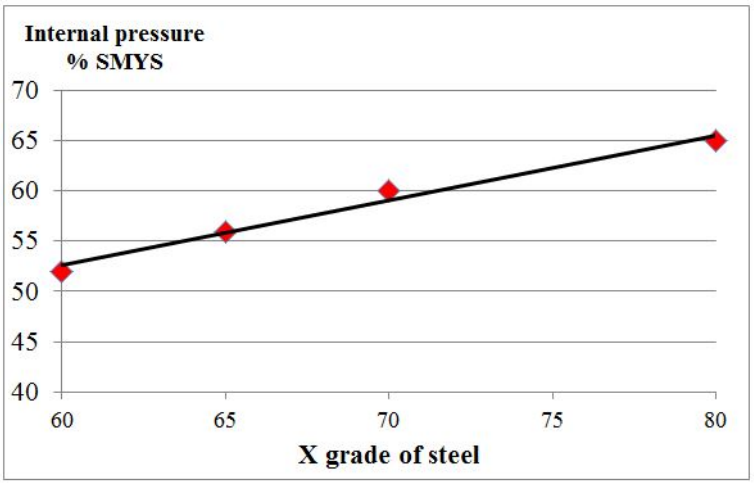

Figure 6.27: Relationship between the steel grade and the transition pressure

fracture. Based on this observation, each load case of the parametric studies is described using a 2 dimensional vector with entries of internal pressure and steel grade. Afterwards each one of these vectors is assigned a label showing to which class the vector belongs. Using the perceptron algorithm for binary classification, the set of all test results is divided with a two dimensional decision boundary. In order to test the validity of the decision boundary an additional steel grade (X70) is simulated for different internal pressure values. The threshold internal pressure determined by the parametric study was close to the predicted threshold internal pressure value within 1%. As a result all of the load cases for the X70 steel grade could be correctly classified. The availability of classification methods for pipeline structures can prevent unexpected conditions on the field such as explosions of gas pipelines due to excessive tensile strain. Future work on this topic can extend the obtained classifier function to more than two parameters so that in addition to the internal pressure and the steel grade also, wall thickness, pipe diameter and dimensions of defects on the pipe wall can be considered in the process of classification.

7 ERROR ANALYSIS AND LIMITATIONS OF THE STUDY

This chapter summarizes the uncertainties and sources of error in the full scale experiments as well as the limitations of the experimental study and the finite element analyses. A major part of the measurements in the full scale experiments were done by the sensors of the MTS(Michigan Testing System) universal testing machine, the pressure transducer connected to the bottom end plate of the specimen and the strain gauges. The MTS machine and the pressure transducer are calibrated in such a way that they are capable of measuring force, displacement and pressure in a confidence range of 0.25 % of their nominal range. The nominal ranges of the MTS force, MTS displacement and the pressure transducer in these experiments were 6625.6 kN, 240 mm and 68.95 MPa respectively. As a result a fluctuation of the measurements in the range of 16.56 kN, 0.6 mm and 0.17 MPa is expected for the MTS force, the MTS displacement and the internal pressure respectively.

The confidence intervals of the strain gauge measurements are also analyzed using the values given by the manufacturer of the strain gauges. According to Showa Measuring Instruments Co., Ltd., the strain gauges used in the full scale experiments have a resistance of 350.0 $\pm 1.05\Omega$ with a relative error of 0.3% and a gauge factor of 2.19 ± 0.0219 with a relative error of 1%. The relationship between the measured strain (ε), the initial resistance of the strain gauge (R_0), the change in the strain gauge resistance due to deformation (ΔR) and the gauge factor (GF) is given in Eq. 7.1.

$$\varepsilon = \frac{\Delta R}{R_0 \cdot GF} \tag{7.1}$$

Adding up the relative errors for the resistance and the gauge factor, the relative error in the measured strain can be calculated as 1.3%[60].

In addition to the confidence intervals given by the manufacturer of the strain gauges also, the comparison of the strain gauge measurements with the theoretical strain values can give an idea about the reliability of the measured values. In order to do this comparison, the strain values measured by the hoop direction strain gauges are compared to the theoretical hoop direction strain values caused by internal pressure. In the absence of a shear force acting on the pipe the stress state on the pipe wall can be fully described by the hoop stress (σ_h) and the longitudinal stress (σ_l) caused by the internal pressure. Assuming plane stress condition and isotropic material behaviour, the hoop direction strain (ε_h) can be computed as in Eq. 7.2.

$$\varepsilon_h = \frac{1}{E}(\sigma_h - \nu\sigma_l) \tag{7.2}$$

Inserting the definitions of σ_h and σ_l as functions of internal pressure (p_i), pipe diameter (D) and wall thickness (t), into Eq. 7.2, Eq. 7.3 can be obtained.

$$\varepsilon_h = \frac{1}{E}\left(\frac{p_i \cdot D}{2 \cdot t} - \nu\frac{p_i \cdot D}{4 \cdot t}\right) \tag{7.3}$$

Using Eq. 7.3, the theoretical hoop strain values and their differences from the experimental values at every internal pressure increment are tabulated in Table 7.1 for Test 1.

In Table 7.1 the experimental hoop strain value is calculated taking the average of four strain gauge measurements in hoop direction at the mid-section of the top side of the pipe. Based on the theoretical hoop strain values, the average relative error of the strain gauges can be calculated as 1.69% which is close to the 1.3% relative error computed based on the tolerance

Table 7.1: Comparison of the theoretical and experimental hoop strain values

Internal pressure [MPa]	Theoretical hoop strain [%]	Experimental hoop strain [%]	Difference [%]
1.38	0.0129	0.0128	0.4
2.76	0.0257	0.0258	0.38
4.14	0.0386	0.0389	0.9
5.52	0.0514	0.0521	1.35
6.9	0.0643	0.0654	1.78
8.27	0.0772	0.079	2.46
9.65	0.09	0.0925	2.83
11.72	0.109	0.113	3.45

intervals specified by the manufacturer of the strain gauges.

An alternative way of measuring the strain would be using cable transducers in order to measure the overall changes in the length of the specimens and compare this change in length to the initial length of the specimen in order to obtain the global strain. Another possibility to capture the strain locally is to cover the pipe wall with a grid and obtain the final strain value based on the distortions of the grid elements. Furthermore, in pipelines subjected to slope instabilities the comparison of the final length of pipe segments to their initial length can provide information about the strain that the pipe undergoes. Remote monitoring of strain using fiber optic sensors is also an accepted method in the field of pipelines [61]. In addition to these methods, ultrasonic measurement [62] and x-ray diffraction measurement are among the in situ strain measurement techniques applicable to pipelines [63].

The marked scale of the dial indicators used in adjusting the flaw height and the errors in the determination of the camera positions relative to each other and relative to the tested specimen in the digital image correlation system used in determining the strain fields as well as the random noise in

the spatial image signal were other limitations on the experimental study.

Another uncertainty in the flaw sizes stems from the initial assumptions made on the pipe wall thickness. The wall thickness was determined using the ultrasonic thickness measurement technique. The measurements are repeated at random locations of the pipe wall. A total of 53 wall thickness measurements are made. The outlier data which lies 3 standard deviations or more away from the average value is replaced with the average wall thickness. The histogram in Figure 7.1 shows the frequency of different wall thickness ranges.

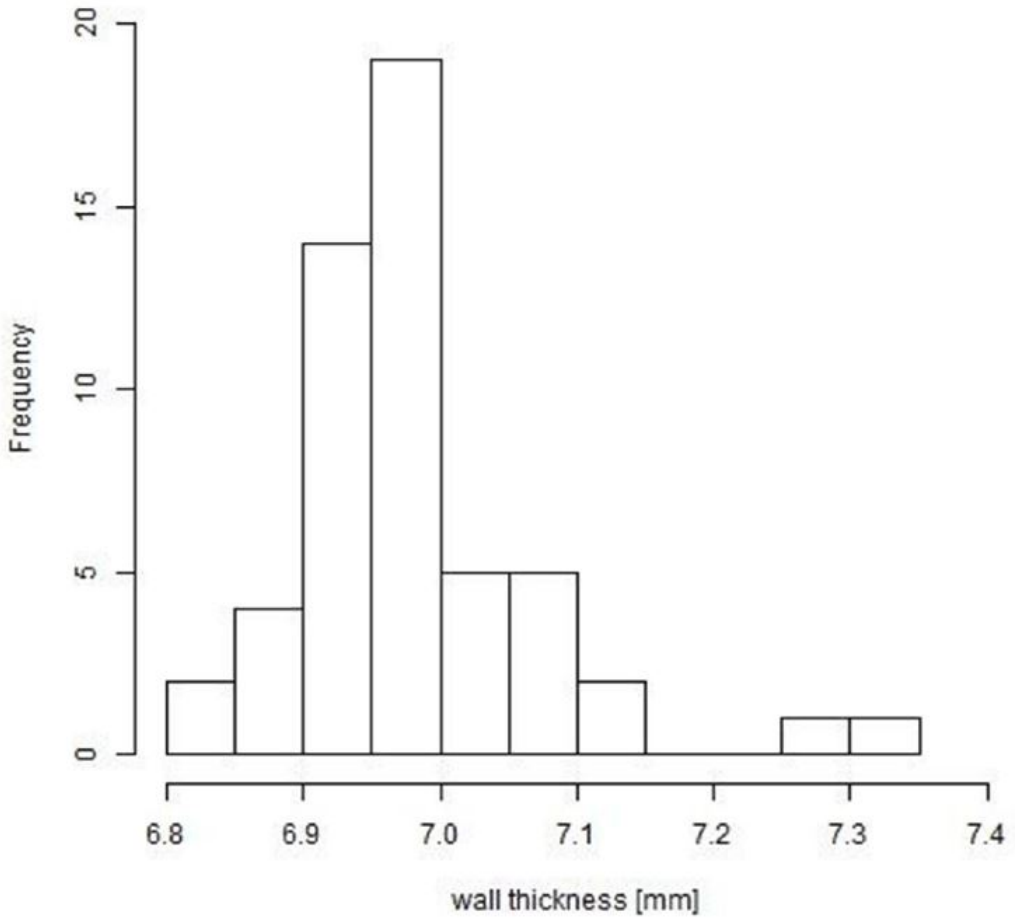

Figure 7.1: Frequency distribution of the wall thickness

According to the histogram in Figure 7.1 a substantial part of the wall thickness measurements fall into the range between 6.9 mm and 7.0 mm. Therefore the average of these two values (6.95 mm) is used as the wall thickness in determining the flaw height as 25% or 50% of the wall thickness. After the removal of the outlier data, a standard deviation of 0.12 mm was observed in the wall thickness measurements which corresponds to 1.7% relative error.

In all of the full scale tests the pipe wall flaws were planned to be machined in the heat affected zone of the girth weld since this part of the pipe wall is expected to have reduced mechanical properties. On the other hand the exact location of the heat affected zone can only be determined after conducting fractography on the specimens cut out of a location of the pipe wall containing the girth weld. Since conducting the metallurgical analysis of the girth weld cross section before the experiments would render the specimens untestable, the fractography of the girth weld is carried out after machining the flaws and testing the specimens.

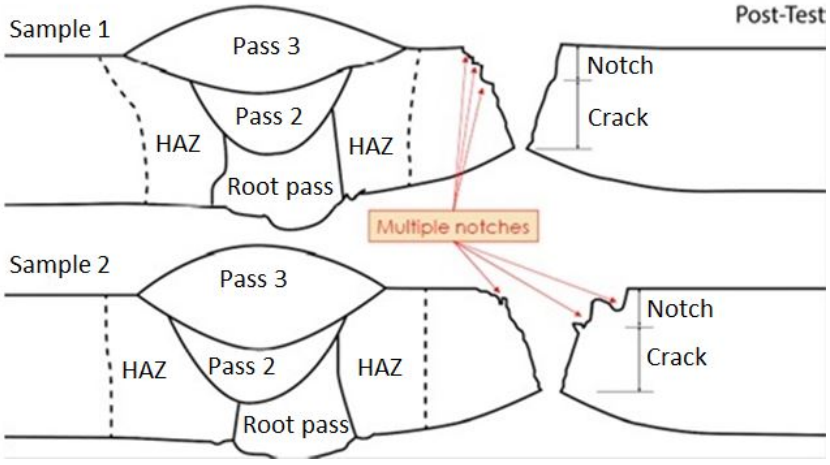

Figure 7.2: Fractography results of the machined flaw

The outcome of the fractography analysis for the second full scale test

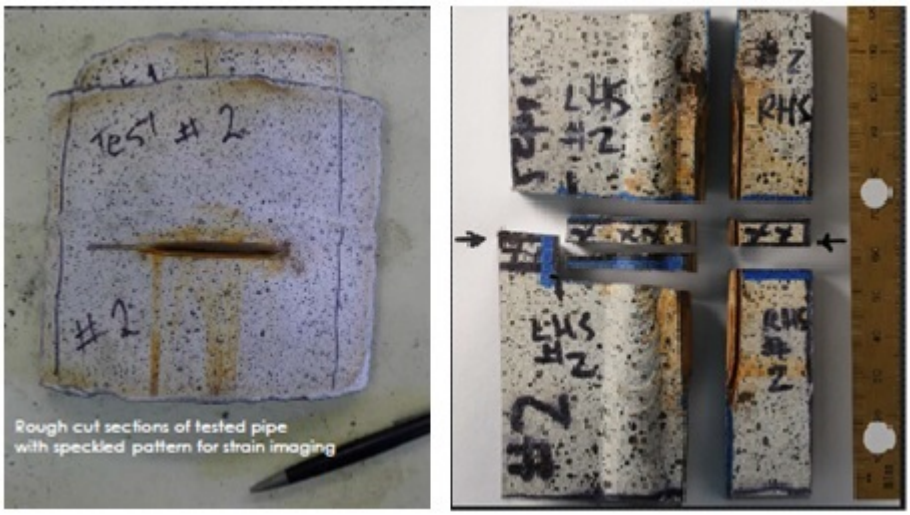

Figure 7.3: Flaw after the rupture (left hand side) and the location of the fractography specimen (right hand side)

where the initial part of the flaw was wider than expected is shown in Figure 7.2 for two different samples. According to Figure 7.2, the machined flaw is a couple of millimeters outside of the heat affected zone. The location where the specimens of Figure 7.2 were cut from are shown in Figure 7.3. The actual notch depths of the first and second fractography specimens were determined as 24% of the wall thickness and 21% of the wall thickness respectively with an average relative error of 10% compared to the planned flaw depth of 25% of the wall thickness. Furthermore it was concluded that the pipe wall plastically deformed during the experiment with a decrease in the pipe wall thickness accompanied with necking down and lengthening of the pipe wall.

Overall the sources of error and limitations in the full scale experiments can be summarized as errors caused by the limited accuracy of the measurement devices and errors caused by the scattering of the measured values around a mean value. Furthermore, in the sections of this work dealing with

the structural behaviour of the cold bends the major limitation is on the modelling of the pipe material. As a future work it is advisable to incorporate the results of the tension coupon tests carried out by Sen et al[53] in the finite element simulations.

8 SUMMARY AND CONCLUSIONS

Experimental studies in the field of pipeline structures showed that, large strains can be sustained without endangering the containment capability of steel pipes. Particularly, the research projects conducted by Wang et al. [4],[5],[6],[7] shed light on the subject of tensile strain capacity of energy pipelines. As a result, the strain based design of pipelines has gained in importance in the recent years in order to guarantee the safe and economic operation of pipeline networks. Various equations have been developed for the prediction of the tensile strain capacity of pipelines some of which are also included in the Canadian Standards Association code for oil and gas pipeline systems (CSA Z662-11). These equations are based on experimental data enriched with finite element analysis results. Some of the factors most prevalently considered in these equations are the dimensions of the flaws in the pipe wall, yield strength to ultimate strength ratio of the pipe base metal and the fracture toughness of the pipe base metal. Flaws in the pipe wall are particularly expected in vintage pipes due to being prone to corrosive degradation over long periods of time. It is known that in Canada an oil pipeline network of 34000 km and a gas pipeline network of 26000 km can be currently classified as vintage pipes[64] out of a pipeline network of 115000 km total length[65]. Another factor that can lead to flaws in the pipe wall is the faulty application of manual or automatic welding procedures during the construction of pipelines.

Despite the corrosion-related critical condition of vintage pipelines with low yield strength, the tensile strain capacity prediction equations currently available in the literature are only applicable to modern high strength steel pipes. Furthermore, a great number of the experiments carried out for the

strain analysis of pipelines, used curved wide plates as test specimens, which prevented the effect of the internal pressure on the tensile strain capacity from being considered in the equations of CSA Z662-11. These conditions lead to a necessity to investigate the structural behaviour of vintage pipes in the presence of internal pressure which is at the focus of this research project.

In order to have a better understanding of the currently available equations in the literature, a sensitivity analysis is carried out in Chapter 3. The sensitivity analysis provided insights about the most significant parameters affecting the tensile strain capacity. In addition to the equations of the CSA Z662-11 code also, tensile strain capacity prediction equations proposed in a report of the Pipeline Research Council International (PRCI) are analyzed. Figure 3.2 to Figure 3.5 of Chapter 3 show the variations of the average tensile strain capacity at different levels of the parameters considered in the equations. For each parameter affecting the tensile strain capacity, the average tensile strain capacity is computed and plotted when this parameter is fixed at its low, intermediate and high level. In these plots a large difference between the maximum and minimum value of the average tensile strain capacity for a certain parameter is an indication of the relatively high sensitivity of the equations with respect to this parameter. The observation of these plots in Figure 3.2 to Figure 3.5 shows that the parameter η which is the ratio of the flaw height to pipe wall thickness, has overall the greatest effect on the tensile strain capacity followed by the flaw length, the Y/T ratio of the base metal and the fracture toughness of the base metal. The effects of changing the wall thickness and the internal pressure are found to be minor relative to the rest of the parameters. Also, the Y/T ratio of the pipe base metal is found to be inversely proportional to the tensile strain capacity. In case of buried flaws, the effect of increasing the distance of the

buried flaw from the inner surface of the pipe is found to have a favourable effect on the tensile strain capacity when the parameter ψ, which is the ratio of the distance of the buried flaw from the inner pipe surface to the pipe wall thickness, varies between its intermediate and high values. The sensitivity analysis of the equations developed by the PRCI showed that the ratio of the weld metal ultimate strength to the pipe base metal ultimate strength has an effect on the tensile strain capacity in a magnitude comparable to the effect of the fracture toughness. Another geometric parameter introduced by the PRCI among the parameters affecting the tensile strain capacity is the high-low misalignment of the girth weld. The sensitivity analysis showed that the effect of this parameter on the tensile strain capacity can be ranked less than the flaw length and height but greater than the material properties of the weld metal and base metal.

Due to the complex format of the tensile strain capacity equations, the effects of different parameters on the tensile strain capacity are obscured. The sensitivity analyses clarified the effect of each parameter to a certain extent by prioritizing the parameters according to their impact on the tensile strain capacity. In addition, it is also revealed that the change of the average tensile strain capacity with respect to certain parameters is linear. Knowing the impact of different parameters relative to each other and having simplified linear relationships between the tensile strain capacity of pipes and affecting parameters can have great benefits for practitioners in the field of inspection and health monitoring of pipeline structures.

In the scope of this research program eight full scale tests are carried out with vintage pipes of X52 steel grade. Prior to the testing of the pipe specimens, the proper dimensioning of end plates and the bolted connections is imperative. In order to have a proper end plate design, the steel grade

and thickness of the end plates as well as the number and diameter of the bolt holes have to be selected with a proper safety margin. An optimum configuration for the end plates and the bolt holes was reached by iteratively increasing the end plate size, the bolt diameter and the number of the bolts up to the point where the factored resistance of the bolted connection exceeds the factored maximum tensile force that the connection should withstand.

After the manufacturing of the end plates and the connection pieces between the end plates and the MTS machine, the next step in the preparation of the specimens was the machining of the flaws in the pipe wall. Jewellery blades of two different thicknesses are used in the machining process creating flaws of two different lengths and two different heights in the heat affected zone within 5 mm proximity of the girth weld. Although the manual machining of the flaws brings certain imperfections in the flaw geometry with itself, the finite element analysis of different flaw geometries showed that, the effect of having a wider than planned initial flaw part on the von Mises stress distribution at the flaw tip is negligible.

In order to collect strain data during the tests, digital image correlation and strain gauge measurements are used. After the machining of the flaw, strain gauges are glued at critical strain points on the pipe wall. Afterwards the pipe surface facing the digital image correlation cameras is painted and speckled. The specimen is vertically placed into the MTS machine using the lug pieces bolted to both end plates and pin-yoke assemblies connected to the ground and the MTS actuator. Finally, the specimen is filled with water and pressurized with a pneumatic pump prior to the application of the tensile force by the MTS actuator.

The most significant outcome of the full scale tests of this research program is the determination of the tensile strain capacity as a function of the

pipe wall flaw dimensions and the internal pressure. In order to test the effects of the flaw length, flaw height and the internal pressure on the tensile strain capacity, a high and a low level of each of these parameters is tested. The tensile strain capacity is defined as the maximum average axial tensile strain observed on the pipe wall before the pipe rupture occurs. In order to determine this strain value, the distribution of the axial strain along the longitudinal axis of each specimen prior to the pipe rupture is plotted using the strain values computed by the digital image correlation method. In order to verify these average strain values also, the strain gauge measurements are plotted and their maximum values are compared to the strain values computed by digital image correlation in Table 5.19 of Section 5.4. The strain capacities determined with both methods are observed to be fairly close to each other. Since each of the three parameters was tested at a high and a low level, 4 different tensile strain capacities are measured corresponding to each level of a parameter. In order to determine the variation of the tensile strain capacity with respect to the flaw length, flaw height and the internal pressure, for each level of these parameters the average value of the 4 tensile strain capacities is computed. The average strain capacities for the low and the high levels of each parameter are plotted in Figure 8.1, Figure 8.2 and Figure 8.3 for the flaw length, the flaw height and the internal pressure respectively.

The tensile strain capacity variation graphs in Figure 8.1 to Figure 8.3 contain besides the test result averages also the averages of the tensile strain capacities predicted by the CSA equation and the PRCI equations (GMAW, SMAW). A comparison of the test results with the predicted values shows that, the actual strain capacities are significantly higher than the predicted values. However, in case of flaw length and flaw height, the difference between

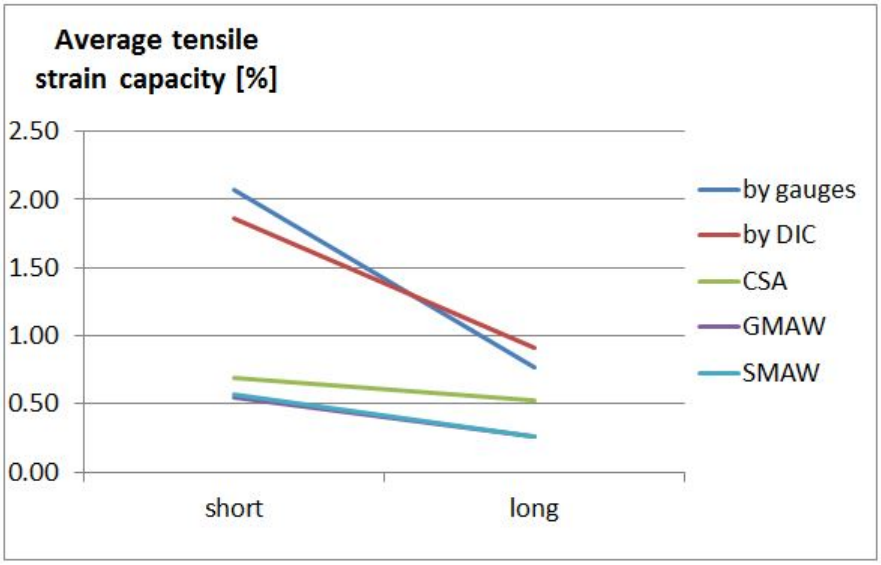

Figure 8.1: Average tensile strain capacities for short and long flaws

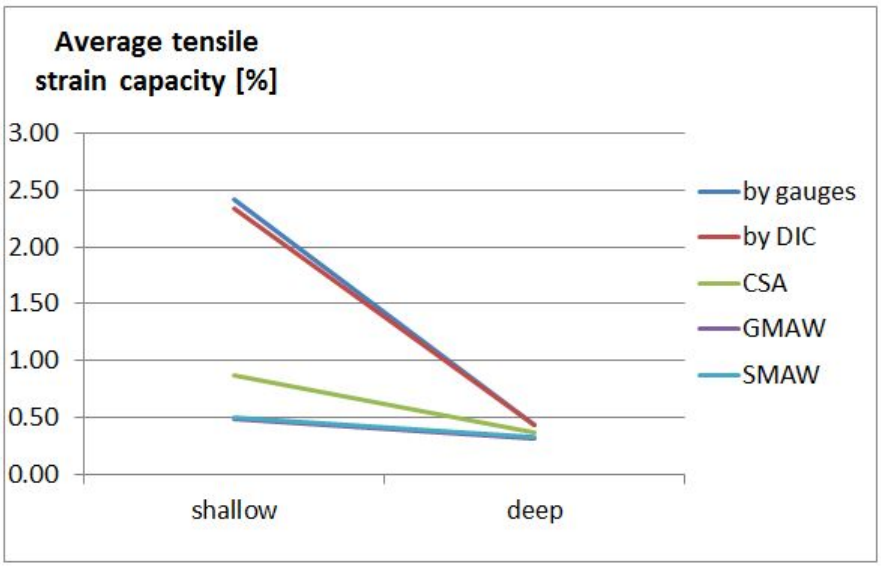

Figure 8.2: Average tensile strain capacities for shallow and deep flaws

the actual strain capacities and the predicted values decreases as the flaw sizes increase. Particularly in case of the flaw height, the difference between the measured and predicted strain capacities decreases significantly for the larger flaw size (deep flaw). On the other hand a similar trend can not be observed

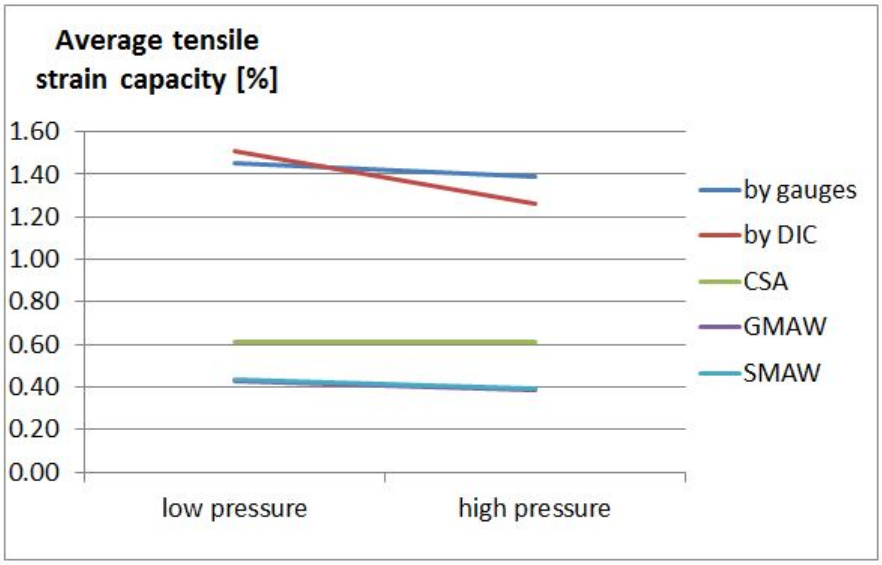

Figure 8.3: Average tensile strain capacities for low and high levels of the internal pressure

with increasing internal pressure for the change in the difference between the measured and predicted strain capacities. It can also be concluded that, for all of the parameters the CSA equation predicts higher strain capacities than the PRCI equations. Also, the difference between the predictions of the PRCI equations for GMAW and SMAW is negligible. It should be noted that the tested specimen configurations have parameters outside the applicability range of the equations such as low yield strength and flaw lengths greater than the upper bound for the equations. Therefore the comparison of the predicted and measured strain capacities in case of this experimental study can only give a rough idea about the behaviour of the equations.

In the next part of this research program the tension side fracture of cold bends is studied numerically in order to gain a better understanding of the causes leading to this highly dangerous pipeline failure mode. The possibility of a pipeline structural failure due to tension side fracture came to attention after the experimental studies of Sen[1] carried out with cold bends. In this

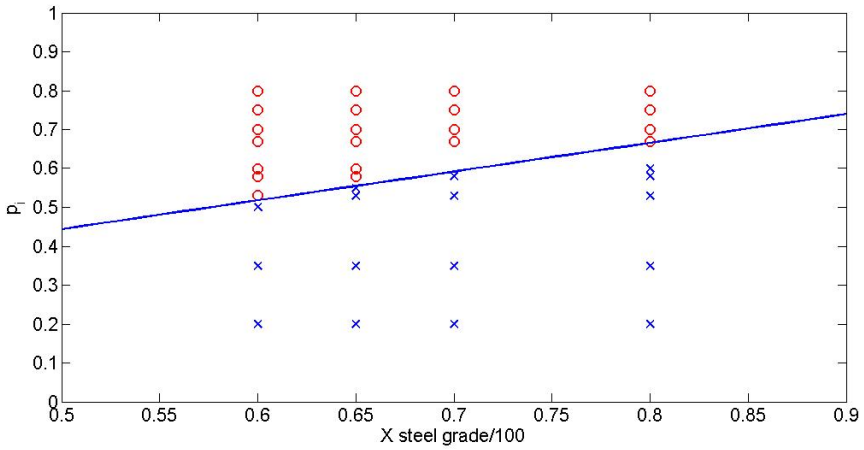

Figure 8.4: Combined training set of the steel grades X60, X65, X70 and X80

current research program the exact cold bend configuration that fractured at the tension side in an experiment carried out by Sen, is modelled and simulated using finite element analysis. The simulation results showed that the level of internal pressure has a decisive effect on the mode of the structural response. Therefore the simulations are extended to a range of internal pressure levels causing hoop stresses between 20% SMYS and 80% SMYS in order to determine a threshold internal pressure at which the transition of the structural behaviour occurs. Furthermore the parametric study of the internal pressure is repeated for X60, X65 and X80 steel grades whereby covering the entire range of steel grades tested in the experimental study of Sen[1]. It was found that the totality of the simulation results can be classified in two classes such that one class contains the cold bend configurations, determined by the internal pressure level and the steel grade, that fail due to intrados fracture and the other class contains the cold bend configurations that fail due to extrados fracture. Based on the parametric study results, a fixed failure criterion of 40% equivalent plastic strain is utilized. The parametric

study results for X60, X65 and X80 are used as a training set in order to obtain a well defined decision boundary between the two failure modes using the perceptron classification algorithm. Afterwards the parametric study of the internal pressure is repeated for X70 steel grade in order to confirm the validity of the decision boundary obtained for X60, X65 and X80 steel grades. The decision boundary was able to correctly separate the two groups of cold bend configurations with X70 steel grade. Finally, the results of the simulations with X70 steel grade are incorporated into the training set in order to obtain a refined decision boundary. The result of this further refinement is shown in Figure 8.4. The formal expression for the decision boundary in Figure 8.4 is given in Eq. 8.1.

$$DB = \{\mathbf{x} \in \mathbb{R} : x_2 = 0.74x_1 + 0.074\} \tag{8.1}$$

The main contributions of this research program to the field of pipeline engineering are the investigation of the structural behaviour of vintage pipes with X52 steel grade and cold bent pipes under tensile strain. In the scope of this investigation also, the applicability of the tensile strain capacity prediction equations currently available in the CSA code for the oil and gas pipeline systems to vintage pipes under internal pressure is analysed. Particularly it is found that as mentioned in CSA Z662-11 Annex C Section C.6.3.1.3.3 (a), the tensile strain capacity prediction equations can be overly conservative for small defects. In general the predicted tensile strain capacities were found to be conservative which is in agreement with CSA Z662-11 Annex C Section C.6.3.1.3.1. According to this section of the CSA code the equations are designed in such a way that they deliver generally conservative predictions for the tensile strain capacity. In addition to the equations in the CSA Z662-11 code also the equations proposed by the Pipeline Research Council

International are found to be significantly conservative in most load cases. This condition can be related to the fact that none of the equations in the literature is designed in order to predict the tensile strain capacity of vintage pipes since they are based on the experimental research programs and parametric studies with finite element simulations carried out with modern high strength steel pipes.

As it was revealed by the sensitivity analyses of Chapter 3, the tensile strain capacity is proportional to the fracture toughness of the base metal and inversely proportional to the Y/T ratio of the base metal. The highly ductile behaviour of X52 vintage pipes leads to a greater fracture toughness and lower Y/T ratio compared to modern pipelines. Therefore vintage pipelines are expected to have greater tensile strain capacities than modern pipelines.

The contribution of this research project to the field of cold bend structural analysis is that the likelihood of a mostly overlooked failure mode is brought into attention. Furthermore using basic methods of artificial intelligence, different failure modes of cold bends are classified according to the steel grade and internal pressure of the cold bend. The experimental and numerical studies carried out with cold bends mostly focus on the compression side fractures of cold bends due to the formation of telescoping wrinkles and tearing of the pipe material in the vicinity of these wrinkles due to large strains. Particularly the reduction of the material yield strength in tension due to Bauschinger effect increases the likelihood of compression side fractures. However as it occurred in the experimental studies of Sen[1], there is also a considerable likelihood of tension side fracture of cold bends. In this current work it is revealed that indeed the variation of different parameters such as the steel grade and the level of the operating pressure can have a crucial effect on the structural behaviour of cold bends. Particularly at high

levels of internal pressure a concentration of equivalent plastic strain at the tension side of the cold bends is observed which indicates an increase in the likelihood of tension side fractures. Future work in the field of the finite element analysis of cold bends can include the effect of different geometric and material parameters such as the D/t ratio, Y/T ratio and length of the modelled specimen and the effect of the initial curvature of the cold bent pipes on the structural response. Particularly for the investigation of the effect of the initial curvature it is beneficial to carry out further parametric studies with straight pipes. Also, as shown by the experimental studies of the cold bend material properties carried out by Sen et al.[53] there are considerable differences between the tension and compression side material properties of cold bends which could be implemented in the future studies of this topic.

The availability of reliable methods for the prediction of the tensile strain capacity and classification of failure modes of pipelines can have great benefits in terms of facilitating the safe and efficient operation of a pipeline network. Having a sound understanding of the post-yield strain capacity of pipelines, can prevent unnecessary replacement of pipeline sections due to the overestimation of the risk of a pipe rupture. Similarly, knowing the conditions that lead to dangerous failure modes such as tension side fracture of gas pipelines and having proper classification methods based on that knowledge can greatly reduce the risk of occurrence of these failure modes. Therefore the experimental study of pipeline structures under critical load combinations causing large strains, augmented with finite element simulations will continue to play a crucial role in an economic and safe design of pipelines.

References

[1] Sen, M. (2006); Behaviour of Cold Bend Pipes Under Combined Loads Ph.D. dissertation, University of Alberta

[2] Das, S. (2003): "Fracture of Wrinkled Energy Pipelines", Ph.D. dissertation, University of Alberta

[3] DelCol P.R., Grondin G.Y., Cheng R.J.J., Murray D.W. (1998);Behaviour of Large Diameter Line Pipe Under Combined Loads, University of Alberta, Department of Civil Engineering, Structural Engineering Report No. 224

[4] Wang Y-Y, Cheng W, Horsley D. (2004); Tensile Strain Limits of Buried Defects in Pipeline Girth Welds Proceedings of IPC2004, International Pipeline Conference, IPC2004-524

[5] Wang Y-Y, Chen Y (2005); Reliability Based Strain Design Gas Research Institute Report 04/0146. Des Plaines, IL.

[6] Wang Y-Y, Cheng W (2004); Guidelines on Tensile Strain Limits Gas Research Institute Report 04/0030. Des Plaines, IL.

[7] Wang Y-Y, et al (2004); Tensile Strain Limits of Girth Welds with Surface-Breaking Defects, Part 1 An Analytical Framework Proceedings of the 4th International Conference on Pipeline Technology, 235249

[8] Wang Y-Y, et al (2004); Tensile Strain Limits of Girth Welds with Surface-Breaking Defects, Part 2 Experimental Correlation and Validation Proceedings of the 4th International Conference on Pipeline Technology, 251 266

[9] CSA Z662-11; Oil and gas pipeline systems - Sixth Edition; Update No. 1: January 2012

[10] http://www.esabna.com/euweb/mig_handbook/592mig7_1.htm

[11] Feng Q., Lin Y., Li B., Song H. (2010); Failure Assessment for Girth Weld Defects of Pipeline, Proceedings of IPC2010, International Pipeline Conference, September 27-October 1, 2010, Calgary, Alberta, Canada, IPC2010 31211

[12] Chen J., Feng Q., Wang F., Zhang H., Song H. (2012); Research on Burst Tests of Pipeline with Spiral Weld Defects, Proceedings of IPC2012, International Pipeline Conference, September 24-28, 2012, Calgary, Alberta, Canada, IPC2012 90089.

[13] Feng Q., Lin Y., Wang F., Li B. (2008); Preliminary Failure Assessment for Spiral Welded Defects of Pipeline, Proceedings of IPC2008, International Pipeline Conference, September 29-October 3, 2008, Calgary, Alberta, Canada, IPC2008-64059

[14] http://www.esabna.com/euweb/mig_handbook/592mig10_3.htm

[15] http://www.esabna.com/euweb/mig_handbook/592mig10_2.htm

[16] Sen, M. , Cheng, J.J.R. , Zhou, J. (2011) ; Behaviour of Cold Bend Pipes under Bending Loads, Journal of Structural Engineering, DOI: 10.1061/(ASCE)ST.1943-541X.0000219. 2011 American Society of Civil Engineers

[17] Wang Y-Y.,et al (2011); Second Generation Models for Strain-Based Design. Contract PR-ABD-1-Project 2. Final Approved Report Prepared for the Design, Materials and Construction Technical Committee of Pipeline Research Council International, (PRCI) Inc.

[18] Liu, M. and Wang, Y.-Y., Significance of Biaxial Stress on the Strain Concentration and Crack Driving Force in Pipeline Girth Welds with Softened HAZ, Proceedings of the 26th International Conference on Offshore Mechanics and Arctic Engineering (OMAS 2007),San Diego, California, USA, June 10-15, 2007.

[19] Caminada S, Cumino G, Cipolla L, Di Gianfrancesco, A (2009). Cold bending of advanced ferritic steels: ASTM grades T23, T91, T92. International Journal of Pressure Vessels and Piping 86 (2009) 853861

[20] Montgomery D.C. (2009); Design and Analysis of Experiments (7th Edition)

[21] Sen, M. , Cheng, J.J.R. , Murray, D. W. (2004) ; Full-Scale Tests of Cold Bend Pipes Proceedings of IPC2004, International Pipeline Conference, IPC2004 743

[22] Miki, C. , Kobayashi, T. , Oguchi, N. , Uchida, T. , Suganuma, A. , Katoh, A. (2000) ; Deformation and Fracture Properties of Steel Pipe Bend with Internal Pressure Subjected to In-Plane Bending, Proceedings of the 12th World Conference on Earthquake Engineering

[23] Spiegel, L., Limbrunner, G.F. (1986); Applied Structural Steel Design

[24] Hertele S., de Waele W., Denys R., Verstraete M. (2012), Investigation of Strain Measurements in (curved) wide plate specimens using digital image correlation and finite element analysis, The Journal of Strain Analysis for Engineering Design, DOI:10.1177/0309324712445121

[25] Wang Y.Y., Rudland D., Denys R., Horsley D. (2002); A Preliminary Strain Based Design Criterion for Pipeline Girth Welds, Proceedings of 4th International Pipeline Conference, Calgary, IPC2002-27169

[26] Pick R. J., Glover A. G., Coote R.I. (1980);Full Scale Testing of Large Diameter Pipelines, Pipeline and Energy Plant Piping, Pages 357-366, DOI: 10.1016/B978-0-08-025368-8.50042-7

[27] Glover A.G., Coote R.I., Pick R.J. (1981); Engineering Critical Assessment of Pipeline Girth Welds, Proceedings of Conference on Fitness for Purpose Validation of Welded Construction, The Welding Institute

[28] Glover A.G., Coote R.I. (1984); Full Scale Fracture Tests of Pipeline Girth Welds , Circumferential Cracks in Pressure Vessels and Piping-Vol.2, PVP Vol.95

[29] Wang X., Kibey S., Tang H., Cheng W., Minnaar K., Macia M.L., Kan W.C., Ford S.J., Newbury B. (2011), Strain based Design Advances in Prediction Methods of Tensile Strain Capacity, Internation Journal of Offshore and Polar Engineering (ISSN 1053-5381) Vol. 21, No. 1, pp.1-7

[30] Kibey S., Wang X., Minnaar K., Macia M.L., Fairchild D.P., Kan W.C., Ford S.J., Newbury B. (2010): Tensile Strain Capacity Equations For Strain-Based Design of Welded Pipelines, Proceedings of the 8th International Pipeline Conference, IPC2010-31661

[31] Wang X., Barbas S.T., Kibey S., Gioielli P.C., Minnaar K. (2009), Validation of Strain Capacity Prediction Comparison of Full-Scale Test Results to Predictions from Tearing Analysis Based on FEA, Presented at 5th Pipeline Technology Conference, Ostend, Belgium

[32] Østby E., Hellesvik A.O. (2007), Fracture Control Offshore Pipelines JIP Results from Large Scale Testing of the Effect of Biaxial Loading on the Strain Capacity of Pipes with Defects, Proceedings of the 17th International Offshore and Polar Engineering Conference, Lisbon, Portugal, July 1-6, 2007ISBN 978-1-880653-68-5

[33] Gioielli P.C., Minnaar K., Macia M.L., Kan W.C. (2007), Large-Scale Testing Methodology to Measure the Influence of Pressure on Tensile Strain Capacity of a Pipeline, Proceedings of the Seventh International Offshore and Polar Engineering Conference, ISBN 978-1-880653-68-5

[34] Igi S., Sakimoto T., Endo S. (2011), Effect of Internal Pressure on Tensile Strain Capacity of X80 Pipeline, Procedia Engineering 10 (2011) 14511456

[35] Fukuda N., Yatabe H., Kawaguchi S., Watanabe T., Masuda T. (2003), Experimental and Analytical Study of Cold Bending Process for Pipelines, Journal of Offshore Mechanics and Arctic Engineering, Vol. 125

[36] Caminada S., Cumino G., Cipolla L., Di Gianfrancesco A. (2009), Cold bending of advanced ferritic steels: ASTM grades T23, T91, T92, International Journal of Pressure Vessels and Piping 86 (2009) 853861

[37] Fatemi A., Kenny S., Sen M., Zhou J., Taheri F., Paulin M. (2008), Investigations on the Local Buckling Response of High Strength Linepipe, Proceedings of the 7th International Pipeline Conference, September 29-October 3, 2008, Calgary, Alberta, Canada, IPC2008-64407

[38] Fatemi A., Kenny S., Sen M., Zhou J., Taheri F., Paulin M. (2009), Parameters Affecting the Buckling and Post-buckling Behaviour of High Strength Pipelines, 28th International Conference on Ocean, Offshore and Arctic Engineering, Honolulu, Hawaii, USA, May 31June 5, 2009, doi:10.1115/OMAE2009-79578, ISBN: 978-0-7918-4343-7 — eISBN: 978-0-7918-3844-0

[39] Fatemi A., Kenny S., Taheri F., Duan D-M., Zhou J. (2010), End Boundary Effects on Local Buckling Response of High Strength Linepipe, Proceedings of the 8th International Pipeline Conference, September 27-October 1, 2010, Calgary, Alberta, Canada, IPC2010-31397

[40] Zimmerman T., Timms C., Xie J., Asante J. (2004), Buckling Resistance of Large Diameter Spiral Welded Linepipe, Proceedings of the 2004 International Pipeline Conference, Calgary, Alberta, Canada, October 48, 2004, doi:10.1115/IPC2004-0364, ISBN: 0-7918-4176-6 — eISBN: 0-7918-3737-8

[41] Suzuki N., Arakawa T., Arabey A.(2014), Strain Based Pipeline Design in Harsh Environments Using Large Diameter High Strain

Line Pipes, Proceedings of the 10th International Pipeline Conference, doi:10.1115/IPC2014-33421, IPC2014-33421

[42] Mitsuya M., Sakanoue T., Motohashi H. (2012);Beam-mode Buckling of Buried Pipeline Subjected to Seismic Ground Motion, Journal of Pressure Vessel Technology 135(2), 021801 (Mar 18, 2013), Paper No: PVT-12-1063; doi: 10.1115/1.4007646

[43] Das S., Cheng J.J.R., Murray D.W. (2002);Fracture In Wrinkled Linepipe Under Monotonic Loading, Proceedings of the 4th International Pipeline Conference, Calgary, Alberta, Canada, doi:10.1115/IPC2002-27097

[44] Ahmed A.U., Das S., Cheng J.J.R.(2010);Numerical Investigation of Tearing Fracture of Wrinkled Pipe, Journal of Offshore Mechanics and Arctic Engineering, February 2010, Vol. 132 / 011302-1

[45] American Petroleum Institute Fitness-For-Service Standard, API 579-1/ASME FFS-1 2007

[46] Spiegel L., Limbrunner G.F. (1986); Applied Structural Steel Design, ISBN:0130415677

[47] Jinfeng Liu, course materials for CHE 573 Digital Signal Processing for Chemical Engineers, Winter 2014, University of Alberta.

[48] Adeeb S. (2011); Introduction to Solid Mechanics and Finite Element Analysis using Mathematica, ISBN 978-0-7575-8879-2

[49] ASTM A490, Standard Specification for Structural Bolts, Alloy Steel, Heat Treated, 150 ksi Minimum Tensile Strength

[50] Nam-Ho Kim, course materials for EAS 4200C Aerospace Structures, Fall 2009. University of Florida (http://web.mae.ufl.edu/nkim/eas4200c/VonMisesCriterion.pdf). Downloaded on [8 August 2015].

[51] Lin, M. (2015); Characterization of Tensile and Fracture Properties of X52 Steel Pipes and Their Girth Welds, master thesis, University of Alberta

[52] Vic-3D 2007 Testing Guide, Correlated Solutions

[53] Sen M., Cheng J.J.R., Murray D.W., Zhou J. (2008); Mechanical Properties of Cold Bend Pipes, Journal of Pressure Vessel Technology, doi:10.1115/1.2892034

[54] Cakiroglu C., Adeeb S., Cheng, J.J.R., Sen M. (2014); Numerical Analysis of Pressurized Cold Bend Pipes Under Bending to Investigate the Transition from Compression to Tension Side Failures, Proceedings of the Structures Congress 2014, Boston, Massachusetts, doi: 10.1061/9780784413357.175

[55] Cakiroglu C., Kainat M., Adeeb S., Cheng, J.J.R., Sen M. (2014); Evaluation of Pressurized Cold Bend Pipe Body Tensile Fractures under Bending Loads, Proceedings of the 10th International Pipeline Conference, IPC2014-33582

[56] Pressley A. (2010); Elementary Differential Geometry. ISBN: 978-1-84882-891-9

[57] Tommi Jaakkola, course materials for 6.867 Machine Learning, Fall 2006. MIT OpenCourseWare (http://ocw.mit.edu/), Massachusetts Institute of Technology. Downloaded on [26 May 2014].

[58] Cristianini N., Shawe-Taylor J. (2000); An Introduction to Support Vector Machines and other kernel-based learning methods, Cambridge University Press, ISBN:0521780195

[59] Bishop C.M. (2006); Pattern Recognition and Machine Learning, Springer; 1st ed., ISBN-10: 0-387-31073-8

[60] Columbia University Error Analysis Tutorial, http://phys.columbia.edu/∼ tutorial/

[61] Cauchi S., Morison W.D. (2009)Remote Monitoring of a Natural Gas Pipeline Using Fiber Optic Sensors, Proceedings of the Rio Pipeline Conference and Exposition 2009, IBP1573-09.

[62] Panetta P., Alers G., Francini B., Diaz A., Johnson K., Morra M., Kerr D. Ultrasonic Measurement of Plastic Strain in Pipelines (http://www.netl.doe.gov/kmd/cds/disk29/1-5.pdf)

[63] Fewster P.F., Andrew N.L. (1998);Strain analysis by X-ray diffraction, Journal of Thin Solid Films, Volume 319, Issues 1-2, 29 April 1998, Pages 1-8.

[64] Sinha S.K., Pandey M.D. (2002); Probabilistic Neural Network for Reliability Assessment of Oil and Gas Pipelines, Computer-Aided Civil and Infrastructure Engineering 17 (2002) 320329

[65] Canadian Energy Pipeline Association, History of Pipelines, http://www.cepa.com/about-pipelines/history-of-pipelines

A APPENDIX

A.1 Matlab code for computing the cross correlation of strain gauges

Listing 2: Matlab code for computing the cross correlation of strain gauges

```
load Test1.txt;
cor_test1=corrcoef(Test1);
for i=1:size(cor_test1,1)
    for j=1:size(cor_test1,1)
        if cor_test1(i,j)>=0.9
            [ num2str(i) ' and ' num2str(j)...
                'are in good correlation: '...
                num2str(cor_test1(i,j))]
        end
    end
end
```

A.2 Matlab code for computing the tensile strain capacity according to the equations of CSA Z662-11

Listing 3: Matlab code for computing the tensile strain capacity according to the equations of CSA Z662-11

```
xsi=69/6.9;
eta=0.25;
delta=0.27;
lambda=0.81;
expr1=delta^(2.36-1.58*lambda-0.101*xsi*eta);
expr2=1+16.1*lambda^(-4.45);
expr3=-0.157+0.239*(xsi^(-0.241))*(eta^(-0.315));
epsilonC=expr1*expr2*expr3;
disp(epsilonC);
```

A.3 Matlab code for computing the tensile strain capacity according to the equations of the PRCI report

Listing 4: Matlab code for computing the tensile strain capacity according to the equations of the PRCI report

```
a1=0.9281;a2=0.09573;a3=-0.5053;a4=0.3718;
a5=-2.023;a6=0.7585;a7=0.6299;a8=0.5168;
a9=0.7168;a10=-0.9815;a11=0.2909;a12=-0.3141;
b1=-0.05578;b2=0.01112;b3=-0.1735;b4=1.675;
b5=0.2603;b6=1.106;b7=-1.073;b8=-1.519;b9=1.965;
c1=1.609;c2=0.1138;c3=0.6729;c4=2.357;c5=1.057;
c6=-4.444;c7=0.01727;c8=-0.01354;c9=-0.01224;c10=8.128;
c11=0.2007;c12=-1.594;
d1=0.006822;d2=1.014;d3=1.746;d4=2.378;d5=0.9434;
d6=-1.243;d7=35.79;d8=7.5;d9=62.94;d10=-6.93;
% Flaw dimensions
xi=150/6.9;eta=0.5;delta=0.27;lambda=0.81;psi=0.1297;phi=1.028;
% Flaw dimensions
fp=0.3;
A=a1*exp(a2/xi)*exp(a3*eta*xi*exp(a4/xi))*...
(1+a5*psi^a6+a7*psi^a8*...
    (eta*xi)^a9)*(1+a10*lambda^a11*phi^a12);
B=xi^b1*eta^(b2*xi^b3/eta)*(b4*phi^b5*(b6*phi^b7)^...
lambda+b8*psi^b9);
C=exp(c1/xi)*exp(c2*xi/((1+c3*xi)*eta))*(1+c4*psi^c5+...
    c6*psi*exp(-eta)+c7*psi*exp(-xi))*...
    (c8+c9*phi^c10+c11*lambda^c12*phi);
D=d1*xi^d2*eta^d3*(1+d4*psi^d5+d6*eta*xi*psi)*...
    (1+d7*lambda^d8+d9*phi^d10);
delta_A=0.2262;
fdelta_A=(C*delta_A)^(B*delta_A^D);
epsilonTCrit=A*fdelta_A/(1+fdelta_A);
epsilonTCrit0=1.5*epsilonTCrit;
t0=15.9;t=6.91;
if (abs(t-t0)>0.00001)
    epsilonTCrit = (t0/t)^(0.8096*(1+1.503*psi^1.229))*...
    epsilonTCrit;
end
if fp > 0.6
    epsilonTCrit = epsilonTCrit;%high pressure
end
if fp < 0.6
    epsilonTCrit = epsilonTCrit0+5*fp*...
    (epsilonTCrit-epsilonTCrit0)/3;
end
disp(epsilonTCrit);
```

A.4 Java code for factorial analysis

```
import java.util.*;
import java.io.*;
import java.lang.Math;
import java.text.DecimalFormat;

class Delta{//The fracture toughness parameter
    private double value;
    private double[] range = new double[3];
    public Delta(){
        range[0]=0.1;range[1]=0.2;range[2]= 0.3;
        value=range[0];
    }
    public Delta(float value){
        this.value=value;
    }
    public Delta(double value, double lowerBound,
        double intermediate, double upperBound){
        value=value;
        range[0]=lowerBound;range[1]=intermediate;
        range[2]= upperBound;
    }
    public double getValue(){
        return this.value;
    }
    public void setValue(double value){
        this.value=value;
    }
    public double[] getRange(){
        return this.range;
    }
    public void setRange(double lowerBound,
        double intermediate, double upperBound ){
        range[0]=lowerBound;range[1]=intermediate;
        range[2]=upperBound;
    }
};
class Eta{//The ratio of the flaw height to wall thickness
    private double value;
    private double[] range=new double[3];
    public Eta(){
        range[0]=0.1;range[1]=0.3;range[2]= 0.5;
        value=range[0];
    }
    public Eta(double value){
        this.value=value;
    }
    public Eta(double value, double lowerBound,
        double intermediate, double upperBound){
```

```
        this.value=value;
        range[0]=lowerBound;range[1]=intermediate;
        range[2]=upperBound;
    }
    public double getValue(){
        return this.value;
    }
    public void setValue(double value){
        this.value=value;
    }
    public double[] getRange(){
        return this.range;
    }
    public void setRange(double lowerBound,
        double intermediate, double upperBound ){
        range[0]=lowerBound;range[1]=intermediate;
        range[2]=upperBound;
    }
};
class Fp{//The ratio of the flaw height to wall thickness
    private double value;
    private double[] range=new double[3];
    public Fp(){
        range[0]=0.0;range[1]=0.4;range[2]= 0.8;
        value=range[0];
    }
    public Fp(double value){
        this.value=value;
    }
    public Fp(double value, double lowerBound,
        double intermediate, double upperBound){
        this.value=value;
        range[0]=lowerBound;range[1]=intermediate;
        range[2]=upperBound;
    }
    public double getValue(){
        return this.value;
    }
    public void setValue(double value){
        this.value=value;
    }
    public double[] getRange(){
        return this.range;
    }
    public void setRange(double lowerBound,
        double intermediate, double upperBound ){
        range[0]=lowerBound;range[1]=intermediate;
        range[2]=upperBound;
    }
```

```
};
class Lambda{//Y/T ratio
    private double value;
    private double[] range=new double[3];
    public Lambda(){
        range[0]=0.7;range[1]=0.825;range[2]=0.95;
        value=range[0];
    }
    public Lambda(double val){
        this.value=val;
    }
    public Lambda(double val, double lowerBound,
        double intermediate, double upperBound){
        this.value=val;
        range[0]=lowerBound;range[1]=intermediate;
        range[2]=upperBound;
    }
    public double getValue(){
        return this.value;
    }
    public void setValue(double val){
        this.value=val;
    }
    public double[] getRange(){
        return this.range;
    }
    public void setRange(double lowerBound,
        double intermediate, double upperBound ){
        range[0]=lowerBound;range[1]=intermediate;
        range[2]=upperBound;
    }
};
class Xi{//The ratio of the flaw length to wall thickness
    private double value;
    private double[] range=new double[3];
    public Xi(){
        range[0]=1.0;range[1]=5.5;range[2]=10.0;
        this.value=range[0];
    }
    public Xi(double value){
        this.value=value;
    }
    public Xi(double value, double lowerBound,
        double intermediate, double upperBound){
        this.value=value;
        range[0]=lowerBound;range[1]=intermediate;
        range[2]=upperBound;
    }
    public double getValue(){
```

```
        return this.value;
    }
    public void setValue(double value){
        this.value=value;
    }
    public double[] getRange(){
        return this.range;
    }
    public void setRange(double lowerBound,
        double intermediate, double upperBound ){
        range[0]=lowerBound;range[1]=intermediate;
        range[2]=upperBound;
    }
};
class Psi{//The ratio of the flaw length to wall thickness
    private double value;
    private double[] range=new double[3];
    public Psi(){
        range[0]=0.1;range[1]=0.3;range[2]=0.5;
        this.value=range[0];
    }
    public Psi(double value){
        this.value=value;
    }
    public Psi(double value, double lowerBound,
        double intermediate, double upperBound){
        this.value=value;
        range[0]=lowerBound;range[1]=intermediate;
        range[2]=upperBound;
    }
    public double getValue(){
        return this.value;
    }
    public void setValue(double value){
        this.value=value;
    }
    public double[] getRange(){
        return this.range;
    }
    public void setRange(double lowerBound,
        double intermediate, double upperBound ){
        range[0]=lowerBound;range[1]=intermediate;
        range[2]=upperBound;
    }
};
class PsiOne{//The ratio of the flaw length to wall thickness
    private double value;
    private double[] range=new double[3];
    public PsiOne(){
```

```
        range[0]=0.0;range[1]=0.1;range[2]=0.2;
        this.value=range[0];
    }
    public PsiOne(double value){
        this.value=value;
    }
    public PsiOne(double value, double lowerBound,
        double intermediate, double upperBound){
        this.value=value;
        range[0]=lowerBound;range[1]=intermediate;
        range[2]=upperBound;
    }
    public double getValue(){
        return this.value;
    }
    public void setValue(double value){
        this.value=value;
    }
    public double[] getRange(){
        return this.range;
    }
    public void setRange(double lowerBound,
        double intermediate, double upperBound ){
        range[0]=lowerBound;range[1]=intermediate;
        range[2]=upperBound;
    }
};
class Phi{//The ratio of the flaw length to wall thickness
    private double value;
    private double[] range=new double[3];
    public Phi(){
        range[0]=1;range[1]=1.15;range[2]=1.3;
        this.value=range[0];
    }
    public Phi(double value){
        this.value=value;
    }
    public Phi(double value, double lowerBound,
        double intermediate, double upperBound){
        this.value=value;
        range[0]=lowerBound;range[1]=intermediate;
        range[2]=upperBound;
    }
    public double getValue(){
        return this.value;
    }
    public void setValue(double value){
        this.value=value;
    }
```

```
    public double[] getRange(){
        return this.range;
    }
    public void setRange(double lowerBound,
        double intermediate, double upperBound ){
        range[0]=lowerBound;range[1]=intermediate;
        range[2]=upperBound;
    }
};
class Thickness{//The ratio of the flaw length to wall thickness
    private double value;
    private double[] range=new double[3];
    public Thickness(){
        range[0]=12.7;range[1]=15.9;range[2]=25.4;
        this.value=range[0];
    }
    public Thickness(double value){
        this.value=value;
    }
    public Thickness(double value, double lowerBound,
        double intermediate, double upperBound){
        this.value=value;
        range[0]=lowerBound;range[1]=intermediate;
        range[2]=upperBound;
    }
    public double getValue(){
        return this.value;
    }
    public void setValue(double value){
        this.value=value;
    }
    public double[] getRange(){
        return this.range;
    }
    public void setRange(double lowerBound,
        double intermediate, double upperBound ){
        range[0]=lowerBound;range[1]=intermediate;
        range[2]=upperBound;
    }
};
class EpsilonTCrit{
private double csaSurfValue;
private double csaBuriedValue;
private double prciValue;
private Delta delta= new Delta();
private Eta eta = new Eta();
private Lambda lambda = new Lambda();
private Xi xi = new Xi();
private Psi psi = new Psi();
```

```
private PsiOne psiOne = new PsiOne();
private Phi phi = new Phi();
private Thickness t = new Thickness();
private Fp fp = new Fp();
//List of all strain capacities when delta has its low value
private List<Double> LowDelta = new ArrayList<Double>();
private List<Double> LowEta = new ArrayList<Double>();
private List<Double> LowLambda = new ArrayList<Double>();
private List<Double> LowXi = new ArrayList<Double>();
private List<Double> LowPsi = new ArrayList<Double>();
private List<Double> LowThickness = new ArrayList<Double>();
private List<Double> LowPsiOne = new ArrayList<Double>();
private List<Double> LowPhi = new ArrayList<Double>();
private List<Double> LowFp = new ArrayList<Double>();
private List<Double> IntDelta = new ArrayList<Double>();
private List<Double> IntEta = new ArrayList<Double>();
private List<Double> IntLambda = new ArrayList<Double>();
private List<Double> IntXi = new ArrayList<Double>();
private List<Double> IntPsi = new ArrayList<Double>();
private List<Double> IntThickness = new ArrayList<Double>();
private List<Double> IntPsiOne = new ArrayList<Double>();
private List<Double> IntPhi = new ArrayList<Double>();
private List<Double> IntFp = new ArrayList<Double>();
private List<Double> HighDelta = new ArrayList<Double>();
private List<Double> HighEta = new ArrayList<Double>();
private List<Double> HighLambda = new ArrayList<Double>();
private List<Double> HighXi = new ArrayList<Double>();
private List<Double> HighPsi = new ArrayList<Double>();
private List<Double> HighThickness = new ArrayList<Double>();
private List<Double> HighPsiOne = new ArrayList<Double>();
private List<Double> HighPhi = new ArrayList<Double>();
private List<Double> HighFp = new ArrayList<Double>();
private List<List<Double>> listOfLists = new ArrayList<>(
    Arrays.asList(
        LowDelta, LowEta, LowLambda, LowXi, LowPsi,
        LowThickness, LowPsiOne, LowPhi, LowFp,
        IntDelta, IntEta, IntLambda, IntXi, IntPsi,
        IntThickness, IntPsiOne, IntPhi, IntFp,
        HighDelta, HighEta, HighLambda, HighXi, HighPsi,
        HighThickness, HighPsiOne, HighPhi, HighFp
    )
);
public EpsilonTCrit(){
}
public String getValues(){
    return delta.getValue()+"   "+eta.getValue()+"  "
    +lambda.getValue()+"    "+xi.getValue()+"   "
    +psi.getValue()+"   "+t.getValue()+"    "
    +psiOne.getValue()+"    "+phi.getValue()+"  "
```

```
    +fp.getValue();
}
//For the surface CSA eqn
public void setValues(double deltaVal, double etaVal,
    double lambdaVal, double xiVal){
    delta.setValue(deltaVal);
    eta.setValue(etaVal);
    lambda.setValue(lambdaVal);
    xi.setValue(xiVal);
}
//For the buried CSA eqn
public void setValues(double deltaVal, double etaVal,
    double lambdaVal, double xiVal, double psiVal,
    double tVal){
    delta.setValue(deltaVal);
    eta.setValue(etaVal);
    lambda.setValue(lambdaVal);
    xi.setValue(xiVal);
    psi.setValue(psiVal);
    t.setValue(tVal);
}
//For the PRCI equations
public void setValues(double deltaVal, double etaVal,
    double lambdaVal, double xiVal, double psiOneVal,
    double phiVal, double fpVal){
    delta.setValue(deltaVal);
    eta.setValue(etaVal);
    lambda.setValue(lambdaVal);
    xi.setValue(xiVal);
    psiOne.setValue(psiOneVal);
    phi.setValue(phiVal);
    fp.setValue(fpVal);
}
public void setDeltaRange(double low, double inter,
    double high){
    delta.setRange(low, inter, high);
}
public void setEtaRange(double low, double inter,
    double high){
    eta.setRange(low, inter, high);
}
public void setLambdaRange(double low, double inter,
    double high){
    lambda.setRange(low, inter, high);
}
public void setXiRange(double low, double inter,
    double high){
    xi.setRange(low, inter, high);
}
```

```
public void setPsiRange(double low, double inter,
    double high){
    psi.setRange(low, inter, high);
}
public void setPsiOneRange(double low, double inter,
    double high){
    psiOne.setRange(low, inter, high);
}
public void setPhiRange(double low, double inter,
    double high){
    phi.setRange(low, inter, high);
}
public void setThickRange(double low, double inter,
    double high){
    t.setRange(low, inter, high);
}
public void setFpRange(double low, double inter,
    double high){
    fp.setRange(low, inter, high);
}
public double calcCsaSurf(){
//Calculates the strain capacity of surface
// flaw according to csa
double expr1=Math.pow(delta.getValue(), 2.36-1.58*
    lambda.getValue()-0.101*xi.getValue()*
    eta.getValue());
double expr2=1+16.1*Math.pow(lambda.getValue(),
 -4.45);
double expr3=-0.157+0.239*Math.pow(xi.getValue(),
 -0.241)*Math.pow(eta.getValue(), -0.315);
this.csaSurfValue=expr1*expr2*expr3;
return csaSurfValue;
    }
    public double calcCsaBuried(){
//Calculates the strain capacity of buried flaw
//according to csa
double expr1=Math.pow(delta.getValue(), 1.08-0.612*
    eta.getValue()-0.0735*xi.getValue()+0.364*
    psi.getValue());
double expr2=12.3-4.65*Math.sqrt(t.getValue())+
0.495*t.getValue();
double expr3=11.8-10.6*lambda.getValue();
double expr4=-5.14+0.992/psi.getValue()+20.1*
psi.getValue();
double expr5=-3.63+11.0*Math.sqrt(eta.getValue())
-8.44*eta.getValue();
double expr6=-0.836+0.733*eta.getValue()+0.0483*
xi.getValue()+(3.49-14.6*eta.getValue()-12.9*
    psi.getValue())/(1+Math.pow(xi.getValue(), 1.84));
```

```
this.csaBuriedValue=expr1*expr2*expr3*expr4*expr5*expr6;
return csaBuriedValue;
    }
public double calcPrciGMAW(){//Gas metal arc welding
    //Calculates the strain capacity according to prci
double a1=2.084, a2=0.2812, a3=-0.495, a4=0.7373;
double a5=-5.005, a6=1.186, a7=1.644, a8=0.7374;
double a9=-0.9829, a10=0.08655, a11=-0.1029, a12=-0.15;
double a13=1.025, a14=5.557;
double b1=-0.05005, b2=-0.005139, b3=0.4485, b4=1.417;
double b5=2.217, b6=1.029, b7=-2.598, b8=-2.679, b9=1.694;
double c1=1.409, c2=0.2345, c3=1.125, c4=4.181;
double c5=1.201, c6=-5.384, c7=2.406, c8=-0.2154;
double c9=-0.005237, c10=9.889, c11=0.3547, c12=-0.7513;
double d1=0.02209, d2=1.156, d3=1.601, d4=0.8964;
double d5=1.383, d6=1.333, d7=0.09313, d8=-2.24;
double d9=8.559, d10=-3.719;
double Aexpr1=a1*Math.exp(a2/xi.getValue())*
Math.exp(a3*eta.getValue()*xi.getValue()*
Math.exp(a4/xi.getValue()));
double Aexpr2=1+a5*Math.pow(psiOne.getValue(),a6)+
a7*psiOne.getValue()*Math.pow(eta.getValue()*
    xi.getValue(),a8);
double Aexpr3=1+a9*Math.pow(lambda.getValue(),a10)*
Math.pow(phi.getValue(),a11)+a12*Math.pow(psiOne.getValue(),
    a13)*Math.pow(lambda.getValue(),a14);
double A=Aexpr1*Aexpr2*Aexpr3;
double Bexpr1=Math.pow(xi.getValue(),b1)*Math.pow(
    eta.getValue(),b2*Math.pow(xi.getValue(),b3)/
    eta.getValue());
double Bexpr2=b4*Math.pow(phi.getValue(),b5)*
Math.pow(b6*Math.pow(phi.getValue(),b7),lambda.getValue())
+b8*Math.pow(psiOne.getValue(),b9);
double B=Bexpr1*Bexpr2;
double Cexpr1=Math.exp(c1/xi.getValue())*
Math.exp(c2*xi.getValue()/((1+c3*xi.getValue())*
    eta.getValue()));
double Cexpr2=1+c4*Math.pow(psiOne.getValue(),c5)+
c6*psiOne.getValue()*Math.exp(-eta.getValue())+c7*
psiOne.getValue()*Math.exp(-xi.getValue());
double Cexpr3=c8+c9*Math.pow(phi.getValue(),c10)+
c11*Math.pow(lambda.getValue(),c12)*phi.getValue();
double C=Cexpr1*Cexpr2*Cexpr3;
double Dexpr1=d1*Math.pow(xi.getValue(),d2)*
Math.pow(eta.getValue(),d3*xi.getValue()/(1+
    d4*xi.getValue()));
double Dexpr2=1+d5*Math.pow(psiOne.getValue(),d6);
double Dexpr3=1+d7*Math.pow(lambda.getValue(),d8)+
d9*Math.pow(phi.getValue(),d10);
```

```
double D=Dexpr1*Dexpr2*Dexpr3;
double TSCp=(A*Math.pow(C*delta.getValue(),B*
    Math.pow(delta.getValue(),D)))/(1+Math.pow(
    C*delta.getValue(),B*Math.pow(delta.getValue(),D)));
double t0=15.9;//mm
double tForEqn=t.getValue();
if(tForEqn<12.7){tForEqn=12.7;}
else if(tForEqn>25.4){tForEqn=25.4;}
double sf=Math.pow(t0/tForEqn,0.8096*(1+1.503*
    Math.pow(psiOne.getValue(),1.229)));
TSCp=TSCp*sf;
double TSC0=1.5*TSCp;
if(fp.getValue()<0.6){
    TSCp=TSC0+(5*fp.getValue()/3)*(TSCp-TSC0);
}
return 100*TSCp;
    }
public double calcPrciSMAW(){//Shielded metal arc welding
//Calculates the strain capacity according to prci
double a1=0.9281, a2=0.09573, a3=-0.5053, a4=0.3718;
double a5=-2.023, a6=0.7585, a7=0.6299, a8=0.5168;
double a9=0.7168, a10=-0.9815, a11=0.2909, a12=-0.3141;
double b1=-0.05578, b2=0.01112, b3=-0.1735, b4=1.675;
double b5=0.2603, b6=1.106, b7=-1.073, b8=-1.519,
b9=1.965;
double c1=1.609, c2=0.1138, c3=0.6729, c4=2.357,
c5=1.057;
double c6=-4.444, c7=0.01727, c8=-0.01354,
 c9=-0.01224, c10=8.128;
double c11=0.2007, c12=-1.594;
double d1=0.006822, d2=1.014, d3=1.746, d4=2.378,
d5=0.9434;
double d6=-1.243, d7=35.79, d8=7.5, d9=62.94, d10=-6.93;
double Aexpr1=a1*Math.exp(a2/xi.getValue())*
Math.exp(a3*eta.getValue()*xi.getValue()*Math.exp(
    a4/xi.getValue()));
double Aexpr2=1+a5*Math.pow(psiOne.getValue(),a6)+
a7*Math.pow(psiOne.getValue(),a8)*Math.pow(
    eta.getValue()*xi.getValue(),a9);
double Aexpr3=1+a10*Math.pow(lambda.getValue(),a11)*
Math.pow(phi.getValue(),a12);
double A=Aexpr1*Aexpr2*Aexpr3;
double Bexpr1=Math.pow(xi.getValue(),b1)*Math.pow(
    eta.getValue(),b2*Math.pow(xi.getValue(),b3)/
    eta.getValue());
double Bexpr2=b4*Math.pow(phi.getValue(),b5)*Math.pow(
    b6*Math.pow(phi.getValue(),b7),lambda.getValue())+
b8*Math.pow(psiOne.getValue(),b9);
double B=Bexpr1*Bexpr2;
```

```
double Cexpr1=Math.exp(c1/xi.getValue())*Math.exp(
    c2*xi.getValue()/((1+c3*xi.getValue())*
        eta.getValue()));
double Cexpr2=1+c4*Math.pow(psiOne.getValue(),c5)+
c6*psiOne.getValue()*Math.exp(-eta.getValue())+c7*
psiOne.getValue()*Math.exp(-xi.getValue());
double Cexpr3=c8+c9*Math.pow(phi.getValue(),c10)+
c11*Math.pow(lambda.getValue(),c12)*phi.getValue();
double C=Cexpr1*Cexpr2*Cexpr3;
double Dexpr1=d1*Math.pow(xi.getValue(),d2)*
Math.pow(eta.getValue(),d3);
double Dexpr2=1+d4*Math.pow(psiOne.getValue(),d5)+
d6*eta.getValue()*xi.getValue()*psiOne.getValue();
double Dexpr3=1+d7*Math.pow(lambda.getValue(),d8)+
d9*Math.pow(phi.getValue(),d10);
double D=Dexpr1*Dexpr2*Dexpr3;
double TSCp=(A*Math.pow(C*delta.getValue(),B*
    Math.pow(delta.getValue(),D)))/(1+Math.pow(
    C*delta.getValue(),B*Math.pow(delta.getValue(),D)));
double t0=15.9;//mm
double tForEqn=t.getValue();
if(tForEqn<12.7){tForEqn=12.7;}
else if(tForEqn>25.4){tForEqn=25.4;}
double sf=Math.pow(t0/tForEqn,0.8096*(1+1.503*
    Math.pow(psiOne.getValue(),1.229)));
TSCp=TSCp*sf;
double TSC0=1.5*TSCp;
if(fp.getValue()<0.6){
    TSCp=TSC0+(5*fp.getValue()/3)*(TSCp-TSC0);
}
return 100*TSCp;
}
private double calculateAverage(List <Double> capacities)
 {
  Double sum = 0.0;
  if(!capacities.isEmpty()) {
    for (Double capacity : capacities) {
        sum += capacity;
    }
    return sum / capacities.size();
  }
  return sum;
}
public void csaSurfFactorial() throws IOException{
    DecimalFormat df = new DecimalFormat("#0.000");
    BufferedWriter output = new BufferedWriter(
        new FileWriter("factorialSurf.txt", false));
    output.append("delta"+" "+"eta"+"   "+"lambda"+
        "   "+"xi"+"    "+"psi"+"   "+"t"+" "+
```

```
        "psiOne"+"  "+"phi"+"   "+"fp"+"    "+"epsilon");
    output.newLine();
for(List<Double> list : listOfLists){list.clear();}
for(double deltaVal : delta.getRange()){
    for(double etaVal : eta.getRange()){
        for(double lambdaVal : lambda.getRange()){
            for(double xiVal : xi.getRange()){
        this.setValues(deltaVal, etaVal,
         lambdaVal, xiVal);
        output.append(this.getValues()+
            "   "+df.format(this.calcCsaSurf()));
        output.newLine();
if(Math.abs(xiVal-xi.getRange()[0])<
    1.0e-5){LowXi.add(this.calcCsaSurf());}
else if(Math.abs(xiVal-xi.getRange()[1])<1.0e-5){
    IntXi.add(this.calcCsaSurf());}
else if(Math.abs(xiVal-xi.getRange()[2])<1.0e-5){
    HighXi.add(this.calcCsaSurf());}
if(Math.abs(lambdaVal-lambda.getRange()[0])<1.0e-5){
    LowLambda.add(this.calcCsaSurf());}
else if(Math.abs(lambdaVal-lambda.getRange()[1])<1.0e-5){
    IntLambda.add(this.calcCsaSurf());}
else if(Math.abs(lambdaVal-lambda.getRange()[2])<1.0e-5){
    HighLambda.add(this.calcCsaSurf());}
if(Math.abs(etaVal-eta.getRange()[0])<1.0e-5){
    LowEta.add(this.calcCsaSurf());}
else if(Math.abs(etaVal-eta.getRange()[1])<1.0e-5){
    IntEta.add(this.calcCsaSurf());}
else if(Math.abs(etaVal-eta.getRange()[2])<1.0e-5){
    HighEta.add(this.calcCsaSurf());}
if(Math.abs(deltaVal-delta.getRange()[0])<1.0e-5){
    LowDelta.add(this.calcCsaSurf());}
else if(Math.abs(deltaVal-delta.getRange()[1])<1.0e-5){
    IntDelta.add(this.calcCsaSurf());}
else if(Math.abs(deltaVal-delta.getRange()[2])<1.0e-5){
            HighDelta.add(this.calcCsaSurf());}
        }}
}}
double aveCapLowXi=calculateAverage(LowXi);
double aveCapIntXi=calculateAverage(IntXi);
double aveCapHighXi=calculateAverage(HighXi);
double aveCapLowLambda=calculateAverage(LowLambda);
double aveCapIntLambda=calculateAverage(IntLambda);
double aveCapHighLambda=calculateAverage(HighLambda);
double aveCapLowEta=calculateAverage(LowEta);
double aveCapIntEta=calculateAverage(IntEta);
double aveCapHighEta=calculateAverage(HighEta);
double aveCapLowDelta=calculateAverage(LowDelta);
double aveCapIntDelta=calculateAverage(IntDelta);
```

```
double aveCapHighDelta=calculateAverage(HighDelta);
output.append("Averages");
output.newLine();
output.append("Low Xi Average Strain Capacity: "+
    aveCapLowXi);output.newLine();
output.append("Intermediate Xi Average Strain Capacity: "+
    aveCapIntXi);output.newLine();
output.append("High Xi Average Strain Capacity: "+
    aveCapHighXi);output.newLine();
output.append("Low Lambda Average Strain Capacity: "+
    aveCapLowLambda);output.newLine();
output.append("Intermediate Lambda Average Strain Capacity: "+
    aveCapIntLambda);output.newLine();
output.append("High Lambda Average Strain Capacity: "+
    aveCapHighLambda);output.newLine();
output.append("Low Eta Average Strain Capacity: "+
    aveCapLowEta);output.newLine();
output.append("Intermediate Eta Average Strain Capacity: "+
    aveCapIntEta);output.newLine();
output.append("High Eta Average Strain Capacity: "+
    aveCapHighEta);output.newLine();
output.append("Low Delta Average Strain Capacity: "+
    aveCapLowDelta);output.newLine();
output.append("Intermediate Delta Average Strain Capacity: "+
    aveCapIntDelta);output.newLine();
output.append("High Delta Average Strain Capacity: "+
    aveCapHighDelta);output.newLine();
output.close();
    }
    public void csaBuriedFactorial() throws IOException{
        DecimalFormat df = new DecimalFormat("#0.000");
        BufferedWriter output = new BufferedWriter(
            new FileWriter("factorialBuried.txt", false));
        output.append("delta"+" "+"eta"+"   "+"lambda"+"    "+
            "xi"+"  "+"psi"+"   "+"t"+" "+"psiOne"+"    "+
            "phi"+" "+"fp"+"    "+"epsilon");
        output.newLine();
for(List<Double> list : listOfLists){list.clear();}
for(double deltaVal : delta.getRange()){
    for(double etaVal : eta.getRange()){
        for(double lambdaVal : lambda.getRange()){
            for(double xiVal : xi.getRange()){
                for(double psiVal : psi.getRange()){
                    for(double tVal : t.getRange()){
                        this.setValues(deltaVal, etaVal,
                         lambdaVal, xiVal, psiVal, tVal);
                        output.append(this.getValues()+
                            "   "+df.format(
                                this.calcCsaBuried()));
```

```
                        output.newLine();
if(Math.abs(tVal-t.getRange()[0])<1.0e-5){
LowThickness.add(this.calcCsaBuried());}
else if(Math.abs(tVal-t.getRange()[1])<1.0e-5){
IntThickness.add(this.calcCsaBuried());}
else if(Math.abs(tVal-t.getRange()[2])<1.0e-5){
HighThickness.add(this.calcCsaBuried());}
if(Math.abs(psiVal-psi.getRange()[0])<1.0e-5){
LowPsi.add(this.calcCsaBuried());}
else if(Math.abs(psiVal-psi.getRange()[1])<1.0e-5){
IntPsi.add(this.calcCsaBuried());}
else if(Math.abs(psiVal-psi.getRange()[2])<1.0e-5){
HighPsi.add(this.calcCsaBuried());}
if(Math.abs(xiVal-xi.getRange()[0])<1.0e-5){
LowXi.add(this.calcCsaBuried());}
else if(Math.abs(xiVal-xi.getRange()[1])<1.0e-5){
IntXi.add(this.calcCsaBuried());}
else if(Math.abs(xiVal-xi.getRange()[2])<1.0e-5){
HighXi.add(this.calcCsaBuried());}
if(Math.abs(lambdaVal-lambda.getRange()[0])<1.0e-5){
LowLambda.add(this.calcCsaBuried());}
else if(Math.abs(
lambdaVal-lambda.getRange()[1])<1.0e-5){
IntLambda.add(this.calcCsaBuried());}
else if(Math.abs(
lambdaVal-lambda.getRange()[2])<1.0e-5){
HighLambda.add(this.calcCsaBuried());}
if(Math.abs(etaVal-eta.getRange()[0])<1.0e-5){
LowEta.add(this.calcCsaBuried());}
else if(Math.abs(etaVal-eta.getRange()[1])<1.0e-5){
IntEta.add(this.calcCsaBuried());}
else if(Math.abs(etaVal-eta.getRange()[2])<1.0e-5){
HighEta.add(this.calcCsaBuried());}
if(Math.abs(deltaVal-delta.getRange()[0])<1.0e-5){
LowDelta.add(this.calcCsaBuried());}
else if(Math.abs(deltaVal-delta.getRange()[1])<1.0e-5){
IntDelta.add(this.calcCsaBuried());}
else if(Math.abs(
deltaVal-delta.getRange()[2])<1.0e-5){
HighDelta.add(this.calcCsaBuried());}
}}}}}}
double aveCapLowT=calculateAverage(LowThickness);
double aveCapIntT=calculateAverage(IntThickness);
double aveCapHighT=calculateAverage(HighThickness);
double aveCapLowPsi=calculateAverage(LowPsi);
double aveCapIntPsi=calculateAverage(IntPsi);
double aveCapHighPsi=calculateAverage(HighPsi);
double aveCapLowXi=calculateAverage(LowXi);
double aveCapIntXi=calculateAverage(IntXi);
```

```
double aveCapHighXi=calculateAverage(HighXi);
double aveCapLowLambda=calculateAverage(LowLambda);
double aveCapIntLambda=calculateAverage(IntLambda);
double aveCapHighLambda=calculateAverage(HighLambda);
double aveCapLowEta=calculateAverage(LowEta);
double aveCapIntEta=calculateAverage(IntEta);
double aveCapHighEta=calculateAverage(HighEta);
double aveCapLowDelta=calculateAverage(LowDelta);
double aveCapIntDelta=calculateAverage(IntDelta);
double aveCapHighDelta=calculateAverage(HighDelta);
output.append("Averages:");
output.newLine();
output.append("Low t Average Strain Capacity: "
    +df.format(aveCapLowT));output.newLine();
output.append("Intermediate t Average Strain Capacity: "
    +df.format(aveCapIntT));output.newLine();
output.append("High t Average Strain Capacity: "
    +df.format(aveCapHighT));output.newLine();
output.append("Low Psi Average Strain Capacity: "
    +df.format(aveCapLowPsi));output.newLine();
output.append("Intermediate Psi Average Strain Capacity: "
    +df.format(aveCapIntPsi));output.newLine();
output.append("High Psi Average Strain Capacity: "
    +df.format(aveCapHighPsi));output.newLine();
output.append("Low Xi Average Strain Capacity: "
    +df.format(aveCapLowXi));output.newLine();
output.append("Intermediate Xi Average Strain Capacity: "
    +df.format(aveCapIntXi));output.newLine();
output.append("High Xi Average Strain Capacity: "
    +df.format(aveCapHighXi));output.newLine();
output.append("Low Lambda Average Strain Capacity: "
    +df.format(aveCapLowLambda));output.newLine();
output.append("Intermediate Lambda Average Strain Capacity: "
    +df.format(aveCapIntLambda));output.newLine();
output.append("High Lambda Average Strain Capacity: "
    +df.format(aveCapHighLambda));output.newLine();
output.append("Low Eta Average Strain Capacity: "
    +df.format(aveCapLowEta));output.newLine();
output.append("Intermediate Eta Average Strain Capacity: "
    +df.format(aveCapIntEta));output.newLine();
output.append("High Eta Average Strain Capacity: "
    +df.format(aveCapHighEta));output.newLine();
output.append("Low Delta Average Strain Capacity: "
    +df.format(aveCapLowDelta));output.newLine();
output.append("Intermediate Delta Average Strain Capacity: "
    +df.format(aveCapIntDelta));output.newLine();
output.append("High Delta Average Strain Capacity: "
    +df.format(aveCapHighDelta));output.newLine();
output.close();
```

```
    }
public void prciGMAWFactorial() throws IOException{
DecimalFormat df = new DecimalFormat("#0.000");
BufferedWriter output = new BufferedWriter(
    new FileWriter("factorialGMAW.txt", false));
output.append("delta"+" "+"eta"+"   "+"lambda"+
    "   "+"xi"+"    "+"psi"+"   "+"t"+" "+
    "psiOne"+"  "+"phi"+"   "+"fp"+"    "+"epsilon");
output.newLine();
for(List<Double> list : listOfLists){list.clear();}
for(double deltaVal : delta.getRange()){
for(double etaVal : eta.getRange()){
    for(double lambdaVal : lambda.getRange()){
        for(double xiVal : xi.getRange()){
            for(double psiOneVal : psiOne.getRange()){
                for(double phiVal : phi.getRange()){
                    for(double fpVal : fp.getRange()){
                        this.setValues(deltaVal, etaVal,
                         lambdaVal, xiVal, psiOneVal,
                          phiVal, fpVal);
                        output.append(this.getValues()
                            +"  "+df.format(
                                this.calcPrciGMAW()));
                        output.newLine();
if(Math.abs(fpVal-fp.getRange()[0])<1.0e-5){
    LowFp.add(this.calcPrciGMAW());}
else if(Math.abs(fpVal-fp.getRange()[1])<1.0e-5){
    IntFp.add(this.calcPrciGMAW());}
else if(Math.abs(fpVal-fp.getRange()[2])<1.0e-5){
    HighFp.add(this.calcPrciGMAW());}
if(Math.abs(phiVal-phi.getRange()[0])<1.0e-5){
    LowPhi.add(this.calcPrciGMAW());}
else if(Math.abs(phiVal-phi.getRange()[1])<1.0e-5){
    IntPhi.add(this.calcPrciGMAW());}
else if(Math.abs(phiVal-phi.getRange()[2])<1.0e-5){
    HighPhi.add(this.calcPrciGMAW());}
if(Math.abs(psiOneVal-psiOne.getRange()[0])<1.0e-5){
    LowPsiOne.add(this.calcPrciGMAW());}
else if(Math.abs(psiOneVal-psiOne.getRange()[1])<1.0e-5){
    IntPsiOne.add(this.calcPrciGMAW());}
else if(Math.abs(psiOneVal-psiOne.getRange()[2])<1.0e-5){
    HighPsiOne.add(this.calcPrciGMAW());}
if(Math.abs(xiVal-xi.getRange()[0])<1.0e-5){
    LowXi.add(this.calcPrciGMAW());}
else if(Math.abs(xiVal-xi.getRange()[1])<1.0e-5){
    IntXi.add(this.calcPrciGMAW());}
else if(Math.abs(xiVal-xi.getRange()[2])<1.0e-5){
    HighXi.add(this.calcPrciGMAW());}
if(Math.abs(lambdaVal-lambda.getRange()[0])<1.0e-5){
```

```
    LowLambda.add(this.calcPrciGMAW());}
else if(Math.abs(lambdaVal-lambda.getRange()[1])<1.0e-5){
    IntLambda.add(this.calcPrciGMAW());}
else if(Math.abs(lambdaVal-lambda.getRange()[2])<1.0e-5){
    HighLambda.add(this.calcPrciGMAW());}
if(Math.abs(etaVal-eta.getRange()[0])<1.0e-5){
    LowEta.add(this.calcPrciGMAW());}
else if(Math.abs(etaVal-eta.getRange()[1])<1.0e-5){
    IntEta.add(this.calcPrciGMAW());}
else if(Math.abs(etaVal-eta.getRange()[2])<1.0e-5){
    HighEta.add(this.calcPrciGMAW());}
if(Math.abs(deltaVal-delta.getRange()[0])<1.0e-5){
    LowDelta.add(this.calcPrciGMAW());}
else if(Math.abs(deltaVal-delta.getRange()[1])<1.0e-5){
    IntDelta.add(this.calcPrciGMAW());}
else if(Math.abs(deltaVal-delta.getRange()[2])<1.0e-5){
    HighDelta.add(this.calcPrciGMAW());}
}}}}}}}
double aveCapLowFp=calculateAverage(LowFp);
double aveCapIntFp=calculateAverage(IntFp);
double aveCapHighFp=calculateAverage(HighFp);
double aveCapLowPhi=calculateAverage(LowPhi);
double aveCapIntPhi=calculateAverage(IntPhi);
double aveCapHighPhi=calculateAverage(HighPhi);
double aveCapLowPsiOne=calculateAverage(LowPsiOne);
double aveCapIntPsiOne=calculateAverage(IntPsiOne);
double aveCapHighPsiOne=calculateAverage(HighPsiOne);
double aveCapLowXi=calculateAverage(LowXi);
double aveCapIntXi=calculateAverage(IntXi);
double aveCapHighXi=calculateAverage(HighXi);
double aveCapLowLambda=calculateAverage(LowLambda);
double aveCapIntLambda=calculateAverage(IntLambda);
double aveCapHighLambda=calculateAverage(HighLambda);
double aveCapLowEta=calculateAverage(LowEta);
double aveCapIntEta=calculateAverage(IntEta);
double aveCapHighEta=calculateAverage(HighEta);
double aveCapLowDelta=calculateAverage(LowDelta);
double aveCapIntDelta=calculateAverage(IntDelta);
double aveCapHighDelta=calculateAverage(HighDelta);
output.append("Averages:");
output.newLine();
output.append("Low Fp Average Strain Capacity: "+
    df.format(aveCapLowFp));output.newLine();
output.append("Intermediate Fp Average Strain Capacity: "+
    df.format(aveCapIntFp));output.newLine();
output.append("High Fp Average Strain Capacity: "+
    df.format(aveCapHighFp));output.newLine();
output.append("Low Phi Average Strain Capacity: "+
    df.format(aveCapLowPhi));output.newLine();
```

```
output.append("Intermediate Phi Average Strain Capacity: "+
    df.format(aveCapIntPhi));output.newLine();
output.append("High Phi Average Strain Capacity: "+
    df.format(aveCapHighPhi));output.newLine();
output.append("Low PsiOne Average Strain Capacity: "+
    df.format(aveCapLowPsiOne));output.newLine();
output.append("Intermediate PsiOne Average Strain Capacity: "+
    df.format(aveCapIntPsiOne));output.newLine();
output.append("High PsiOne Average Strain Capacity: "+
    df.format(aveCapHighPsiOne));output.newLine();
output.append("Low Xi Average Strain Capacity: "+
    df.format(aveCapLowXi));output.newLine();
output.append("Intermediate Xi Average Strain Capacity: "+
    df.format(aveCapIntXi));output.newLine();
output.append("High Xi Average Strain Capacity: "+
    df.format(aveCapHighXi));output.newLine();
output.append("Low Lambda Average Strain Capacity: "+
    df.format(aveCapLowLambda));output.newLine();
output.append("Intermediate Lambda Average Strain Capacity: "+
    df.format(aveCapIntLambda));output.newLine();
output.append("High Lambda Average Strain Capacity: "+
    df.format(aveCapHighLambda));output.newLine();
output.append("Low Eta Average Strain Capacity: "+
    df.format(aveCapLowEta));output.newLine();
output.append("Intermediate Eta Average Strain Capacity: "+
    df.format(aveCapIntEta));output.newLine();
output.append("High Eta Average Strain Capacity: "+
    df.format(aveCapHighEta));output.newLine();
output.append("Low Delta Average Strain Capacity: "+
    df.format(aveCapLowDelta));output.newLine();
output.append("Intermediate Delta Average Strain Capacity: "+
    df.format(aveCapIntDelta));output.newLine();
output.append("High Delta Average Strain Capacity: "+
    df.format(aveCapHighDelta));output.newLine();
output.close();
}
public void prciSMAWFactorial() throws IOException{
DecimalFormat df = new DecimalFormat("#0.000");
BufferedWriter output = new BufferedWriter(
    new FileWriter("factorialSMAW.txt", false));
output.append("delta"+" "+"eta"+"   "+"lambda"+"    "+
"xi"+"  "+"psi"+"   "+"t"+" "+"psiOne"+"    "
+"phi"+"    "+"fp"+"    "+"epsilon");
output.newLine();
for(List<Double> list : listOfLists){list.clear();}
for(double deltaVal : delta.getRange()){
    for(double etaVal : eta.getRange()){
        for(double lambdaVal : lambda.getRange()){
            for(double xiVal : xi.getRange()){
```

```
                for(double psiOneVal : psiOne.getRange()){
                    for(double phiVal : phi.getRange()){
                        for(double fpVal : fp.getRange()){
                            this.setValues(deltaVal,
    etaVal, lambdaVal, xiVal, psiOneVal, phiVal, fpVal);
                            output.append(this.getValues()+
    "   "+df.format(this.calcPrciSMAW()));
                            output.newLine();
if(Math.abs(fpVal-fp.getRange()[0])<1.0e-5)
    {LowFp.add(this.calcPrciGMAW());}
else if(Math.abs(fpVal-fp.getRange()[1])<1.0e-5)
    {IntFp.add(this.calcPrciGMAW());}
else if(Math.abs(fpVal-fp.getRange()[2])<1.0e-5)
    {HighFp.add(this.calcPrciGMAW());}
if(Math.abs(phiVal-phi.getRange()[0])<1.0e-5)
    {LowPhi.add(this.calcPrciGMAW());}
else if(Math.abs(phiVal-phi.getRange()[1])<1.0e-5)
    {IntPhi.add(this.calcPrciGMAW());}
else if(Math.abs(phiVal-phi.getRange()[2])<1.0e-5)
    {HighPhi.add(this.calcPrciGMAW());}
if(Math.abs(psiOneVal-psiOne.getRange()[0])<1.0e-5)
    {LowPsiOne.add(this.calcPrciGMAW());}
else if(Math.abs(psiOneVal-psiOne.getRange()[1])<1.0e-5)
    {IntPsiOne.add(this.calcPrciGMAW());}
else if(Math.abs(psiOneVal-psiOne.getRange()[2])<1.0e-5)
    {HighPsiOne.add(this.calcPrciGMAW());}
if(Math.abs(xiVal-xi.getRange()[0])<1.0e-5)
    {LowXi.add(this.calcPrciGMAW());}
else if(Math.abs(xiVal-xi.getRange()[1])<1.0e-5)
    {IntXi.add(this.calcPrciGMAW());}
else if(Math.abs(xiVal-xi.getRange()[2])<1.0e-5)
    {HighXi.add(this.calcPrciGMAW());}
if(Math.abs(lambdaVal-lambda.getRange()[0])<1.0e-5)
    {LowLambda.add(this.calcPrciGMAW());}
else if(Math.abs(lambdaVal-lambda.getRange()[1])<1.0e-5)
    {IntLambda.add(this.calcPrciGMAW());}
else if(Math.abs(lambdaVal-lambda.getRange()[2])<1.0e-5)
    {HighLambda.add(this.calcPrciGMAW());}
if(Math.abs(etaVal-eta.getRange()[0])<1.0e-5)
    {LowEta.add(this.calcPrciGMAW());}
else if(Math.abs(etaVal-eta.getRange()[1])<1.0e-5)
    {IntEta.add(this.calcPrciGMAW());}
else if(Math.abs(etaVal-eta.getRange()[2])<1.0e-5)
    {HighEta.add(this.calcPrciGMAW());}
if(Math.abs(deltaVal-delta.getRange()[0])<1.0e-5)
    {LowDelta.add(this.calcPrciGMAW());}
else if(Math.abs(deltaVal-delta.getRange()[1])<1.0e-5)
    {IntDelta.add(this.calcPrciGMAW());}
else if(Math.abs(deltaVal-delta.getRange()[2])<1.0e-5)
```

```
    {HighDelta.add(this.calcPrciGMAW());}
}}}}}}}
double aveCapLowFp=calculateAverage(LowFp);
double aveCapIntFp=calculateAverage(IntFp);
double aveCapHighFp=calculateAverage(HighFp);
double aveCapLowPhi=calculateAverage(LowPhi);
double aveCapIntPhi=calculateAverage(IntPhi);
double aveCapHighPhi=calculateAverage(HighPhi);
double aveCapLowPsiOne=calculateAverage(LowPsiOne);
double aveCapIntPsiOne=calculateAverage(IntPsiOne);
double aveCapHighPsiOne=calculateAverage(HighPsiOne);
double aveCapLowXi=calculateAverage(LowXi);
double aveCapIntXi=calculateAverage(IntXi);
double aveCapHighXi=calculateAverage(HighXi);
double aveCapLowLambda=calculateAverage(LowLambda);
double aveCapIntLambda=calculateAverage(IntLambda);
double aveCapHighLambda=calculateAverage(HighLambda);
double aveCapLowEta=calculateAverage(LowEta);
double aveCapIntEta=calculateAverage(IntEta);
double aveCapHighEta=calculateAverage(HighEta);
double aveCapLowDelta=calculateAverage(LowDelta);
double aveCapIntDelta=calculateAverage(IntDelta);
double aveCapHighDelta=calculateAverage(HighDelta);
output.append("Averages:");
output.newLine();
output.append("Low Fp Average Strain Capacity: "+
df.format(aveCapLowFp));output.newLine();
output.append("Intermediate Fp Average Strain Capacity: "+
df.format(aveCapIntFp));output.newLine();
output.append("High Fp Average Strain Capacity: "+
df.format(aveCapHighFp));output.newLine();
output.append("Low Phi Average Strain Capacity: "+
df.format(aveCapLowPhi));output.newLine();
output.append("Intermediate Phi Average Strain Capacity: "+
df.format(aveCapIntPhi));output.newLine();
output.append("High Phi Average Strain Capacity: "+
df.format(aveCapHighPhi));output.newLine();
output.append("Low PsiOne Average Strain Capacity: "+
df.format(aveCapLowPsiOne));output.newLine();
output.append("Intermediate PsiOne Average Strain Capacity: "+
df.format(aveCapIntPsiOne));output.newLine();
output.append("High PsiOne Average Strain Capacity: "+
df.format(aveCapHighPsiOne));output.newLine();
output.append("Low Xi Average Strain Capacity: "+
df.format(aveCapLowXi));output.newLine();
output.append("Intermediate Xi Average Strain Capacity: "+
df.format(aveCapIntXi));output.newLine();
output.append("High Xi Average Strain Capacity: "+
df.format(aveCapHighXi));output.newLine();
```

```
output.append("Low Lambda Average Strain Capacity: "+
df.format(aveCapLowLambda));output.newLine();
output.append("Intermediate Lambda Average Strain Capacity: "+
df.format(aveCapIntLambda));output.newLine();
output.append("High Lambda Average Strain Capacity: "+
df.format(aveCapHighLambda));output.newLine();
output.append("Low Eta Average Strain Capacity: "+
df.format(aveCapLowEta));output.newLine();
output.append("Intermediate Eta Average Strain Capacity: "+
df.format(aveCapIntEta));output.newLine();
output.append("High Eta Average Strain Capacity: "+
df.format(aveCapHighEta));output.newLine();
output.append("Low Delta Average Strain Capacity: "+
df.format(aveCapLowDelta));output.newLine();
output.append("Intermediate Delta Average Strain Capacity: "+
df.format(aveCapIntDelta));output.newLine();
output.append("High Delta Average Strain Capacity: "+
df.format(aveCapHighDelta));output.newLine();
output.close();
}
};
public class Factorial{
    public static void main(String[] args){
        EpsilonTCrit epsCrit=new EpsilonTCrit();
        epsCrit.setDeltaRange(0.2, 1.35, 2.5);
        epsCrit.setEtaRange(0.05, 0.275, 0.5);
        epsCrit.setLambdaRange(0.75, 0.845, 0.94);
        epsCrit.setXiRange(1.0, 10.5, 20.0);
        epsCrit.setPsiRange(0.1, 0.3, 0.5);
        epsCrit.setPsiOneRange(0.0, 0.1, 0.2);
        epsCrit.setThickRange(12.7, 15.9, 25.4);
        epsCrit.setPhiRange(1, 1.15, 1.3);
        epsCrit.setFpRange(0, 0.4, 0.8);
        try{epsCrit.csaBuriedFactorial();}
        catch(IOException e){e.printStackTrace();}
        try{epsCrit.csaSurfFactorial();}
        catch(IOException e){e.printStackTrace();}
        try{epsCrit.prciGMAWFactorial();}
        catch(IOException e){e.printStackTrace();}
        try{epsCrit.prciSMAWFactorial();}
        catch(IOException e){e.printStackTrace();}
    }
};
```

A.5 The Application of the Curvature Concept to Cold Bends

In this section the concept of curvature, its mathematical derivation and its application to the geometry of a cold bend is elaborated. The application of the curvature concept makes it possible to visualize the structural response in a way which is independent of the particular geometric configuration of the cold bend. For any particular cold bend length and cross section diameter, any load/displacement curve visualizes the structural response as a function of these particular length and diameter. However these structural response curves lose their meaning when it is necessary to make the assessment of cold bends with length and diameter of a different order of magnitude. Therefore in this work load/curvature graphs are preferred instead of the traditional load displacement graphs. For this purpose the cold bend axis is assumed to be a partition of a circle whose radius represents the radius of curvature of the cold bend.

In order to derive a formula which describes the curvature as a function of the cold bend geometry the equation of the circle, which contains the cold bend axis, is expressed as a parametrized curve. A parametrized curve on a plane is the image of a vector valued function $f : (a, b) \to \mathbb{R}^2$ where the open interval (a,b) is a subset of the set of real numbers $\mathbb{R}$. The parametrization of a circle centered at the point (x(t)=0,y(t)=0) has the following equation[56]:

$$f(t) = \Big(x(t), y(t)\Big) = \Big(R\cos\frac{t}{R}, R\sin\frac{t}{R}\Big) \tag{A.1}$$

In Eq. A.1, R is the radius of curvature and t is the parameter of the curve which could be any real number since f is a periodic function.

Curvature of a parametrized curve at some point t_0 in its domain, is

defined as the deviation of the image of the curve from $f(t_0)$, when t changes to $t_0 + \Delta t$ for some infinitesimal Δt. In case of a circle which is parametrized as in Eq. A.1, this deviation is expressed as in Eq. (3), [7]:

$$\Big((t_0 + \Delta t) - f(t_0)\Big) \cdot \mathbf{n} \tag{A.2}$$

In Eq. A.2, $\mathbf{n}$ is the unit normal to the tangent curve df/dt at the point $t = t_0$ as illustrated in Figure A.1. Applying the Taylor expansion of $f(t_0 + \Delta t)$ to

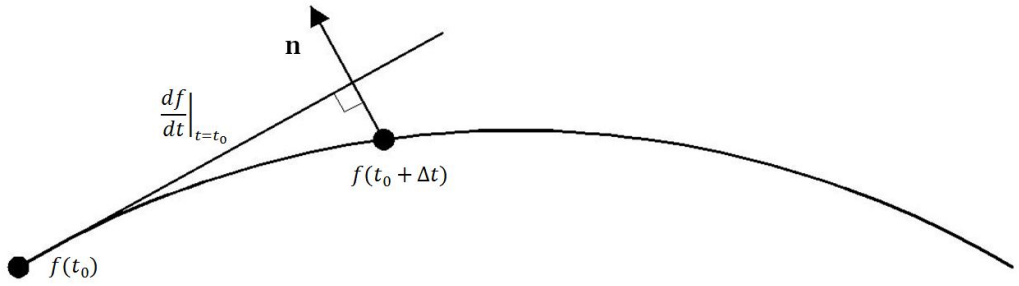

Figure A.1: Description of the curvature as an infinitesimal deviation [56]

Eq. A.2 we obtain:

$$\Big(f(t_0 + \Delta t) - f(t_0)\Big) \cdot n = \Big(\dot{f}(t_0) \cdot n\Big)\Delta t + \frac{1}{2}(\Delta t)^2\Big(\ddot{f}(t_0)\Big) \cdot n + O\Big((\Delta t)^3\Big) \tag{A.3}$$

Since $\dot{f}(t_0)$ and $\mathbf{n}$ are perpendicular to each other, $\dot{f}(t_0) \cdot \mathbf{n} = 0$ and Eq. A.3 becomes:

$$\frac{2}{(\Delta t)^2}\Big(f(t_0 + \Delta t) - f(t_0)\Big) \cdot \mathbf{n} = \Big(\ddot{f}(t_0)\Big) \cdot \mathbf{n} \tag{A.4}$$

where the remainder $O\Big((\Delta t)^3\Big)$ is neglected for infinitesimal Δt. The expression in Eq. A.4 is defined in the literature as the curvature of f at the point $t = t_0$[56]. Considering that $\|\dot{f}\| = 1$ such that $\dot{f} \cdot \dot{f} = 1$, it follows that $\ddot{f} \cdot \dot{f} + \dot{f} \cdot \ddot{f} = 2\dot{f} \cdot \ddot{f} = 0$. In case of the parametrization in Eq. A.1, $\ddot{f} \neq 0$ and therefore $\ddot{f}$ and $\mathbf{n}$ are parallel to each other. It follows that using the

letter κ for curvature, Eq. A.4 can be rewritten as in Eq. A.5[56]:

$$\kappa|_{t=t_0} = \|\ddot{f}(t_0)\| = 1/R \tag{A.5}$$

Since t_0 is an arbitrary point, the curvature of a circle is equal to the reciprocal of its radius at all points.

A.6 Matlab code for the classification of cold bends using the perceptron algorithm

```
ColdBendTraining=[0.6 0.2 1; 0.6  0.35 1;...
     0.6 0.5 1; 0.65 0.2 1;...
     0.65 0.35 1; 0.65 0.53 1;...
     0.65 0.55 1; 0.8 0.2 1; ...
     0.8 0.35 1; 0.8 0.53 1;...
     0.8 0.58 1; 0.8 0.6 1;...
     0.6 0.53 -1; 0.6 0.58 -1;...
     0.6 0.6 -1; 0.6 0.67 -1;...
     0.6 0.7 -1; 0.6 0.75 -1;...
     0.6 0.8 -1;0.65 0.58 -1;...
     0.65 0.6 -1;0.65 0.67 -1;...
     0.65 0.7 -1;0.65 0.75 -1;...
     0.65 0.8 -1; 0.8 0.67 -1;...
     0.8 0.7 -1; 0.8 0.75 -1;...
     0.8 0.8 -1];
yLabels=ColdBendTraining(:,3);
numSamples=size(ColdBendTraining,1);
Norms=zeros([numSamples,1]);
for t=1:numSamples
   Norms(t)=norm(ColdBendTraining(t,1:2));
end
R=max(Norms);
%%%%%%%%%%%%%%%%%%%%%%
%   Iteration part
%%%%%%%%%%%%%%%%%%%%%%
misClas=0;k=0;%k is the total number of updates
w=[0, 0];
b=0;
while (true)
    for t=1:numSamples
        if(yLabels(t)*(dot(w,ColdBendTraining(t,1:2))+b) <=0.8)
```

```
        %Here 0.8 is the minimum margin we want
            w=w+4.0*yLabels(t)*ColdBendTraining(t,1:2);%1.0
            %is the learning rate
            b=b+4.0*yLabels(t)*(R^2);
            misClas=misClas+1;
            k=k+1;
        end
    end
    if (abs(misClas -0)<0.000001)
  % if all samples were classified correctly
        break;
    end
    misClas=0;
end
figure ('Position', [450 391 750 500]);
plot(ColdBendTraining(1:12,1),ColdBendTraining(1:12,2),'X',...
    'MarkerSize', 10);
hold on;
plot(ColdBendTraining(13:29,1),ColdBendTraining(13:29,2),'rO',...
    'MarkerSize', 10);
hold on
disp(k);
x=0.5:0.01:0.9;
y=(-w(1)/w(2))*x-b/w(2);
xlim([0.5 0.9]);
ylim([0 1]);
xlabel('X steel grade/100');
ylabel('p_i');
plot(x,y);
```